OCTOCAM:
Feasibility Study Report

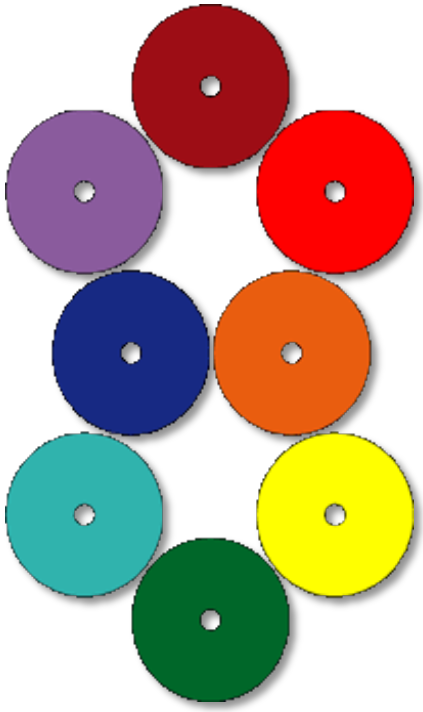

The OCTOCAM consortium

26 October 2015

OCTOCAM

Instrument Overview

OCTOCAM is based on the use of high efficiency dichroics to observe *simultaneously* in 8 channels. It will obtain simultaneous imaging in *g*, *r*, *i*, *z*, *Y*, *J*, *H*, K_S with a field of view of 3'x3', or spectroscopy from 3,700 to 23,500 Å in a single shot, with a long slit of 3'. It can perform high time-resolution observations thanks to the use of state-of-the-art detectors. OCTOCAM will also be equipped with a 9.7"x6.8" Integral Field Unit and a full Stokes spectropolarimeter.

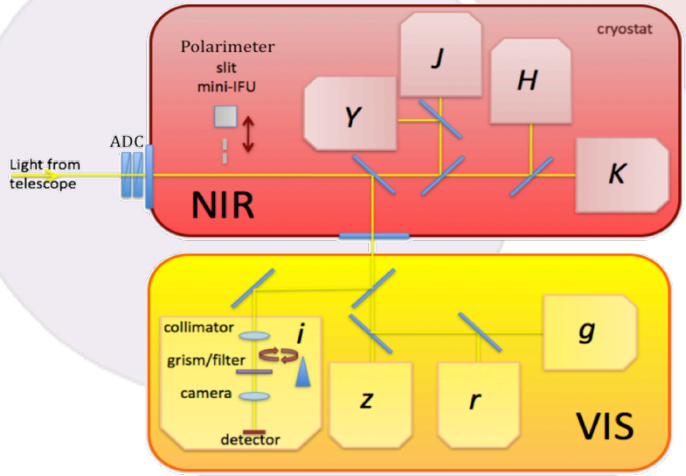

Simultaneous spectral range	Photometry: *grizYJHK* Spectroscopy: 3700-23500 Å
Field of view	Imaging: 3'x3' Spectroscopy: 3' Long slit IFU: 9.7"x6.8"
Plate scale	0.18"/pixel
Spectral resolution	3 000 - 4 000 standard VPH
Average efficiency	Imaging: 41% Spectroscopy: 33%
Maximum frame rate	10 Hz full frame 100 Hz windowed
Observing modes	Multiband imaging Wide band spectroscopy (long slit, IFU) High time-resolution Spectropolarimetry

Science Goals and Objectives

The *efficient, simultaneous multiband observations* obtained by OCTOCAM will give us a new view of the Universe and help to answer many of the questions of Astrophysics in the 2020s. Its capabilities will allow OCTOCAM to do breakthrough science in several fields:

- Characterize *transients* detected by the new generation of surveys, such as LSST, quickly and efficiently.
- Explore *fast changing phenomena* with high time-resolution simultaneously at all wavelengths.
- Study extreme physics near the *event horizon of black holes* and properties of jets at high time-resolution.
- Expand our understanding of *stellar explosions* at all redshifts.
- Use *supernovae* to study the evolution of dust and to push the redshift limits of the Hubble diagram.
- Probe the *very high redshift Universe* and the environment of the *first stars* using as probes the furthest explosions in the Universe.
- Understand the role of *supermassive black holes* in galaxy evolution through detailed observation of active galactic nuclei at all redshifts.
- Observe the *tidal disruption* of stars by supermassive black holes.
- Elucidate the formation and evolution of *neutron stars*, constrain their equation of state, emission mechanisms, and magnetic fields.

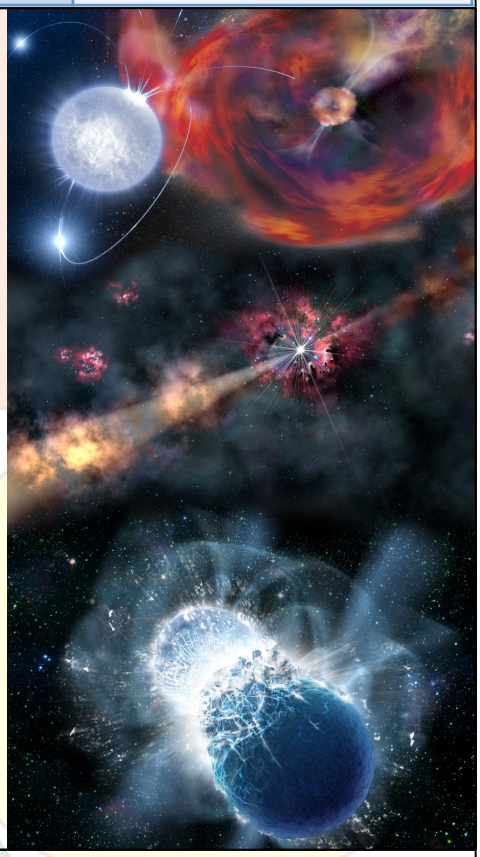

Operations and Performance

Simultaneous multiband observations make OCTOCAM's calibrations robust and fast.

The parameters of each arm can be tuned individually to optimize the performance of OCTOCAM.

Its fast detectors, allow for a very efficient duty cycle, almost eliminating the time lost between exposures, boosting the productivity of the observatory.

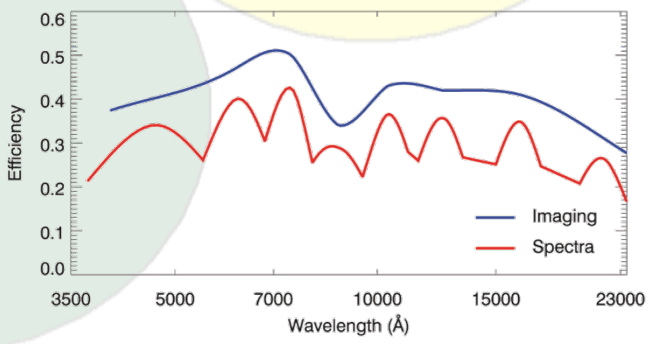

Optics

OCTOCAM uses a single focal plane for all arms. The NIR optics are hosted in a cryogenic chamber while the VIS ones are at room temperature. It is equipped with an atmospheric dispersion corrector. High efficiency dichroics split the light into the eight arms, each optimized for a specific wavelength range to ensure maximum efficiency.

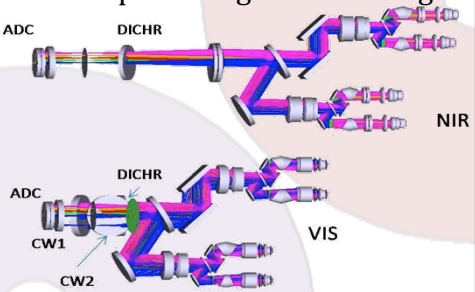

Detectors

OCOTCAM uses e2v frame transfer detectors in the optical and Hawaii 2RG in the NIR. To achieve the required resolution, the region of the detector used for spectroscopy is larger than for imaging. Time resolutions of 10 Hz can be achieved with full frame images, and even higher in windowed modes.

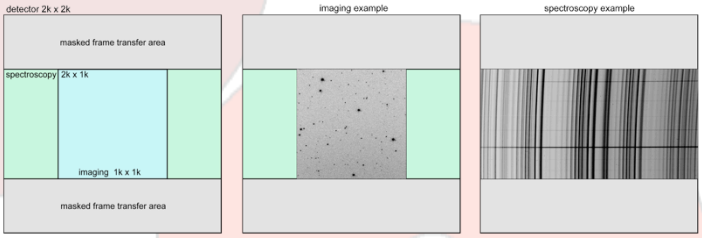

Mechanics

Compactness, light-weight, stiffness, and accessibility have been the main drivers of the mechanical design. A support frame, together with a stiff bench limits the instrument flexures with respect to the telescope. VIS and NIR arms are mounted back-to-back to ensure that any internal flexures are coupled and can be easily dealt with. The instrument benefits from a single focal plane, guaranteeing that the light from the same sky area is delivered to all arms.

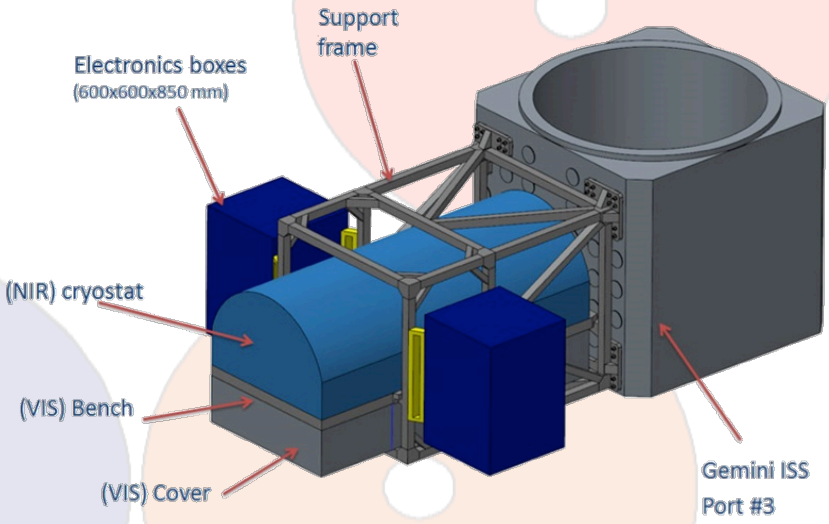

Integral Field Unit

We designed an image-slicer IFU for OCTOCAM with an area of 9.7" x 6.8" in 17 slices of 0.4".

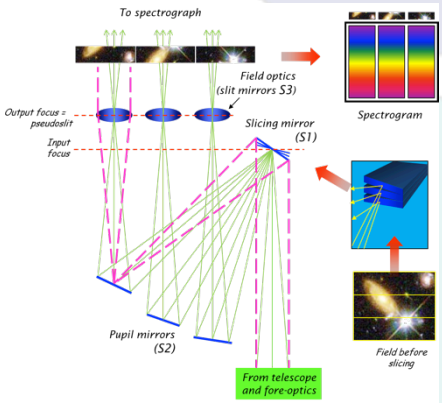

As the only large area IFU simultaneously covering this wavelength range on an 8 m telescope, it will be a unique asset for Gemini, opening the window for new science niches.

Spectropolarimeter

OCTOCAM will have the first broadband spectropolarimeter on an 8 m telescope. An additional high resolution mode for continuum spectropolarimetry at high cadence will be included.

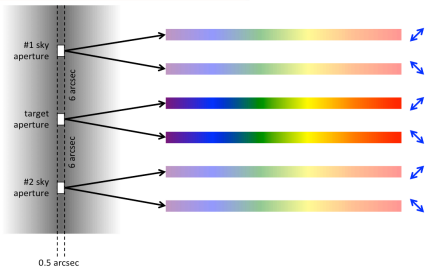

Cost

The total cost of OCTOCAM, including reserves, is $11.98M in FY2016 ($12.56M in RY$ assuming 3% inflation per year). This includes all elements shown here (i.e. IFU and spectropolarimeter).

OCTOCAM Core Team

Instituto de Astrofísica de Andalucía (IAA-CSIC):
Principal Investigator: A. de Ugarte Postigo
Project Manager Spain: C. Thöne

Soutwest Research Institute (SwRI):
Co-PI and Project Manager: P. Roming
Systems Engineer: S. Pope

George Washington University (GWU):
Instrument Scientist: A. van der Horst

Timeline

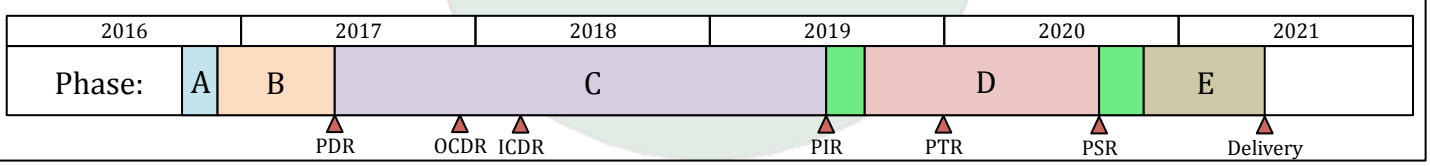

Table of Contents

ACRONYMS 5

EXECUTIVE SUMMARY 8

1. SCIENCE OBJECTIVES AND SCIENCE CASES 11

1.1. SCIENCE TEAM 11
1.2. SCIENCE TEAM SURVEYS 12
1.3. SCIENCE CASES 13
1.3.1. TRANS-NEPTUNIAN OBJECTS 14
1.3.2. EXTRASOLAR PLANETS 16
1.3.3. ASTEROSEISMOLOGY & PULSATING VARIABLE STARS 17
1.3.4. MASSIVE STARS 18
1.3.5. BROWN DWARFS 20
1.3.6. LOW-MASS BINARIES 22
1.3.7. LOW-METALLICITY STARS 24
1.3.8 ISOLATED NEUTRON STARS 25
1.3.9. MAGNETARS 26
1.3.10. INTERACTING BINARIES 28
1.3.11. MILLISECOND PULSAR BINARIES 29
1.3.12. X-RAY BINARIES 30
1.3.13. SUPERNOVAE 32
1.3.14. SUPERNOVA REMNANTS 34
1.3.15. GAMMA-RAY BURSTS 36
1.3.16. ACTIVE GALACTIC NUCLEI 39
1.3.17. TIDAL DISRUPTION EVENTS 41
1.3.18. GALAXY CLUSTERS 42
1.4. SCIENCE REQUIREMENTS 44
1.4.1. INCLUDING THE *U*-BAND 44
1.4.2. FAST RESPONSE MODE 45
1.4.3. PRIORITIZING CAPABILITIES 46
1.4.4. SCIENCE-DRIVEN REQUIREMENTS 53
1.4.5. OBSERVING TIME 53
1.5. CONCEPT OF OPERATIONS 57

2. TECHNICAL REQUIREMENTS AND INSTRUMENT DESIGN 63

2.1. TOP LEVEL REQUIREMENTS AND FLOW-DOWN 63
2.1.1. REQUIREMENTS GENERATION AND VERIFICATION PROCESS 65
2.1.2. REQUIREMENTS FLOW-DOWN 66
2.1.3. TOP LEVEL REQUIREMENTS COMPLIANCE 66
2.2. INSTRUMENT DESIGN 67
2.2.1. DESIGN SUMMARY 67
2.2.2. TRADE STUDY 69
2.2.3. SYSTEMS ENGINEERING AND INTERFACE REQUIREMENTS 72
2.3. OPTICAL DESIGN 74
2.3.1. GENERAL LAYOUT 74
2.3.2. ATMOSPHERIC DISPERSION CORRECTOR 75
2.3.3. CRYOSTAT WINDOWS AND DICHROIC 77
2.3.4. NIR ARM 78
2.3.5. VIS ARM 81
2.3.6. PERFORMANCE ANALYSIS 88
2.3.7. ALTERNATIVE OPTICAL DESIGN 101

2.4. MECHANICAL DESIGN **111**
2.4.1. SPACE FRAME 113
2.4.2. CRYOSTAT AND NIR BENCH CONFIGURATION 115
2.4.3. VISIBLE CHANNEL 120
2.4.4. MECHANISMS 122
2.4.5. ACCESSIBILITY 126
2.4.6. INSTALLATION OF THE INSTRUMENT 128
2.4.7. CONCLUSIONS 129
2.5. CRYOGENICS **130**
2.6. DETECTORS **133**
2.6.1. E2V CCD DESCRIPTION AND PERFORMANCE 133
2.6.2. TELEDYNE H2RG NEAR INFRARED FOCAL PLANE ARRAY DESCRIPTION AND PERFORMANCE 137
2.6.3. E2V CCD COOLING AND PACKAGING, BASELINE CONCEPT 141
2.6.4. E2V CCD COOLING AND PACKAGING, DEVELOPMENTAL TEC-VERSION CONCEPT 142
2.7. ELECTRICAL DESIGN **143**
2.7.1. LOCAL PC 143
2.7.2. IR CONTROLLER BOARD 144
2.7.3. ARCHON CCD CONTROLLER 144
2.7.4. MOTOR AND CRYOCOOLER CONTROLLER (MCC) 144
2.8. INSTRUMENT SOFTWARE **145**
2.8.1. SOFTWARE REQUIREMENTS 145
2.8.2. SOFTWARE DESIGN AND INTERFACES 145
2.8.3. SOFTWARE DEVELOPMENT ENVIRONMENT 147
2.9. DATA REDUCTION PIPELINE **147**
2.9.1. REQUIREMENTS 148
2.9.2. DESIGN AND INTERFACES 148
2.9.3. PIPELINE SOFTWARE ENVIRONMENT 149
2.9.4. PIPELINE TASKS 149
2.10. INTEGRAL FIELD UNIT **152**
2.10.1. REQUIREMENTS 153
2.10.2. BASIC DESIGN 153
2.10.3. LENGTH OF SLICER SYSTEM ALONG FOCAL PLANE 155
2.10.4. LENGTH OF SLICER SYSTEM ALONG OPTICAL AXIS 155
2.10.5. OTHER SLICER SYSTEMS 156
2.10.6. MANUFACTURING 157
2.11. SPECTROPOLARIMETER **158**
2.11.1. GOALS & REQUIREMENTS 158
2.11.2. DESIGN CHOICES 159
2.11.3. OPTICAL PERFORMANCE 165
2.11.4. MITIGATION OF INSTRUMENTAL POLARIZATION EFFECTS 168

3. INSTRUMENT PERFORMANCE AND OPERATIONS **169**

3.1. EFFICIENCY **169**
3.2. LIMITING MAGNITUDE **171**
3.3. SPECTRAL RESOLUTION **172**
3.4. INSTRUMENT OPERATIONS **173**
3.4.1. IMAGING MODES 173
3.4.2. SPECTROSCOPIC MODES 174
3.4.3. CALIBRATION PLAN 175
3.4.4. OVERHEADS 178
3.4.5. A RAPID RESPONSE MODE FOR GEMINI? 179

4. PROJECT MANAGEMENT 180

4.1 TEAM AND MANAGEMENT STRUCTURE 180
4.1.1. ORGANIZATIONAL CHART 180
4.1.2. TASKS OF THE MANAGEMENT TEAM 181
4.1.3. PROJECT MANAGEMENT TOOLS AND PROCESSES 182
4.2. COSTING OF THE INSTRUMENT 183
4.2.1. TRAVEL & SHIPPING 184
4.2.2. RESERVES 184
4.2.3. PERSONNEL 185
4.3. SCHEDULE OF DESIGN AND CONSTRUCTION 185
4.4. WORK BREAKDOWN STRUCTURE 188
4.5. POTENTIAL MANAGEMENT RISKS 190
4.5.1. RISK MANAGEMENT PROCESS SUMMARY 190
4.5.2. RISK MANAGEMENT ORGANIZATION 191
4.5.3. RISK ATTRIBUTES, CLASSIFICATION, & PRIORITIZATION 192
4.5.4. RISK BUY DOWN/TREND REPORT 193
4.5.5. RISK MITIGATION PLAN CONTENT 193
4.5.6. RISK MANAGEMENT PROCESS DETAILS 193
4.5.7. OCTOCAM RISKS 194
4.6. UNIQUE FACILITIES REQUIRED TO EXECUTE THE PROJECT 195
4.7. SPECIAL SKILLSETS REQUIRED TO EXECUTE THE PROJECT 195
4.8. MAJOR LONG LEAD PROCUREMENT ITEMS 199
4.9. DESCOPES 199
5. PROJECT REVIEW REPORT 200
5.1. COMPARISON BETWEEN ORIGINAL SCOPE, SCHEDULE AND COST AND THE ACTUAL ACCOMPLISHED WORK 200
5.1.1. SCOPE 200
5.1.2. GIFS BUDGET 201
5.1.3. GIFS SCHEDULE 202
5.1.4. MANAGEMENT AND COMMUNICATION 203
5.1.5. PERSONNEL 204
5.2. LESSONS LEARNED 204

Acronyms

Acronym	Description
ADC	Atmospheric Dispersion Corrector
AIS	Advanced Image Slicer
AO	Adaptive Optics
AOI	Angle Of Incidence
AR	Anti-Reflection
ASIC	Application Specific Integrated Circuit
AXP	Anomalous X-ray Pulsars
BSP	Beam Splitter
CCD	Charge Coupled Device
CHA	Core Half Angle
CI	Cost Instructions
CMOS	Complementary Metal Oxide Semiconductor
COTS	Commercial Off-The-Shelf
CR	Change Requests
CRM	Continuous Risk Management
CRMP	Continuous Risk Management Plan
CSCI	Computer Software Configuration Items
CSIC	Conseco Superior de Investigaciones Científicas
CTE	Coefficient of Thermal Expansion
CVD	Chemical Vapor Deposition
CW1/2	Cryostat Window 1/2
DPM	Deputy Project Manager
DSE	Deputy Systems Engineer
EB	Error Budget
EED	Encircled Energy Diameter
EER	Encircled Energy Radius
ELT	Extremely Large Telescope
EPC	External PC
ESO	European Southern Observatory
FFT	Fast Fourier Transformation
FITS	Flexible Image Transport System
FoV	Field of View
FPA	Focal Plane Array
FPGA	Field Programmable Gate Array
FS	Fused Silica
FTE	Full Time Equivalent
FWHM	Full Width Half Maximum
GDSN	Gemini Data Storage Network
GE	Gigabit Ethernet
GEFWHM	Gaussian Equivalent Full Width Half Maximum
GIAPI	Gemini Instrument Application Programmer Interface
GIFS	Gemini Instrument Feasibility Studies
GM	Gifford McMahon
GPS	Global Positioning System
GRB	Gamma-Ray Burst
HDL	Hardware Description Language

HTR	High Time-Resolution
IAA	Institutor de Astrofísica de Andalucía
ICD	Interface Control Document
ICDR	Instrument Critical Design Review
IFU	Integral Field Unit
IMS	Integrated Master Schedule
IR	Infrared
IRCB	IR Controller Board
ISS	Instrument Support Structure
I&T	Integration and Testing
JWST	James Webb Space Telescope
LN2	Liquid Nitrogen
LOE	Level Of Effort
LPC	Local Instrument PC
LS	Long Slit
NIR	Near Infrared
MCC	Motor and Cryo-cooler Controller
MLI	Multilayer Insulation
MPSR	Monthly Project Status Report
NRE	Non Recurring Engineering
OB	Observing Block
OCDR	Optical Critical Design Review
ORR	Operations Readiness Review
PCB	Printed Circuit Board
PDR	Preliminary Design Review
PI	Principal Investigator
PIMS	Project Information Management System
PIR	Pre-Integration Review
PM	Project Manager
PMP	Project Management Professional
PR	Problem Reports
PSF	Point Spread Function
PSR	Pre-Ship Review
PT	Pulse Tube
PTR	Pre-Test Review
QE	Quantum Efficiency
RIDM	Risk Informed Decision Making
RMB	Risk Management Board
RMS	Root Mean Square
RPM	Revolutions Per Minute
RV	Radial Velocity
SAM	SIDECAR Acquisition Module
SGR	Soft Gamma-ray Repeater
SE	Systems Engineer
SIDECAR	System for Image Digitalization Enhancement Control And Retrieval
SN	Supernova
SNR	Supernova Remnant
SRR	Systems Requirements Review
STA	Semiconductor Technology Associates

STAC	Science and Technology Advisory Committee
TEC	Thermoelectric
TIMs	Technical Interchange Meetings
TIS	Teledyne Imaging Sensors
SwRI	Southwest Research Institute
VIS	Visible
VLT	Very Large Telescope
VPH	Volume Phase Hologram
WBS	Work Breakdown Structure
WCS	World Coordinate System
WP	Work Package
WPM	Work Package Manager

Executive summary

The decade of the 2020s will be marked by the advent of large surveys and giant telescopes. Many interesting objects will be identified daily by high-cadence surveys, such as the Large Synoptic Survey Telescope (LSST) and the Zwicky Transient Facility (ZTF) at optical and near-infrared wavelengths, and the Square Kilometer Array (SKA) in the radio regime. Only a very small fraction of these objects will be studied with the three planned extremely large telescopes (ELTs). It will be a great time for 8-meter class telescopes that are prepared to efficiently follow up and study exciting phenomena. To take advantage of this opportunity, we envision a highly efficient instrument that will stand apart in looking into the time domain window with simultaneous broad-wavelength coverage.

OCTOCAM has been envisioned as a workhorse instrument that optimizes the use of Gemini for broadband single-target observations, both for imaging and spectroscopy. The instrument design is science driven, and it enables answering fundamental questions for a very broad range of science topics. A large science team has identified the most exciting science cases within their fields, making sure that OCTOCAM delivers the most interesting scientific output. The science requirements to answer the big questions have resulted in technical requirements. In this process, most of the different science cases have been accommodated, but the focus has been on the cases that make optimal use of the combination of high temporal resolution, broad spectral coverage, good spectral resolution, the great sensitivity of Gemini, and synergies with the new facilities coming online in the 2020s. The technical requirements have resulted in the specifications shown in Table 1 and the design shown schematically in Figure 1.

Table 1 – OCTOCAM specifications.

OCTOCAM Specifications	
Simultaneous spectral range	400 to 2,350 nm (*g', r', i', z', Y, J, H* and K_S) in imaging 370 to 2,350 nm in spectroscopy
Field of view	Imaging 3'×3', integral field spectroscopy over an area of 9.7"x6.8"
Plate scale	0.18"/pixel
Spectral resolution	~3,000 – 4,000, depending on the arm and slit width
Maximum full-frame rate	*griz* ~ 10 Hz, Y*JHK*$_S$ ~ 76 Hz
Average efficiency	41 % imaging, 33% spectroscopy
Observing modes	Multiband imaging Broad-band spectroscopy (long slit, and IFU) High-time-resolution (both imaging and spectroscopy) Spectropolarimetry

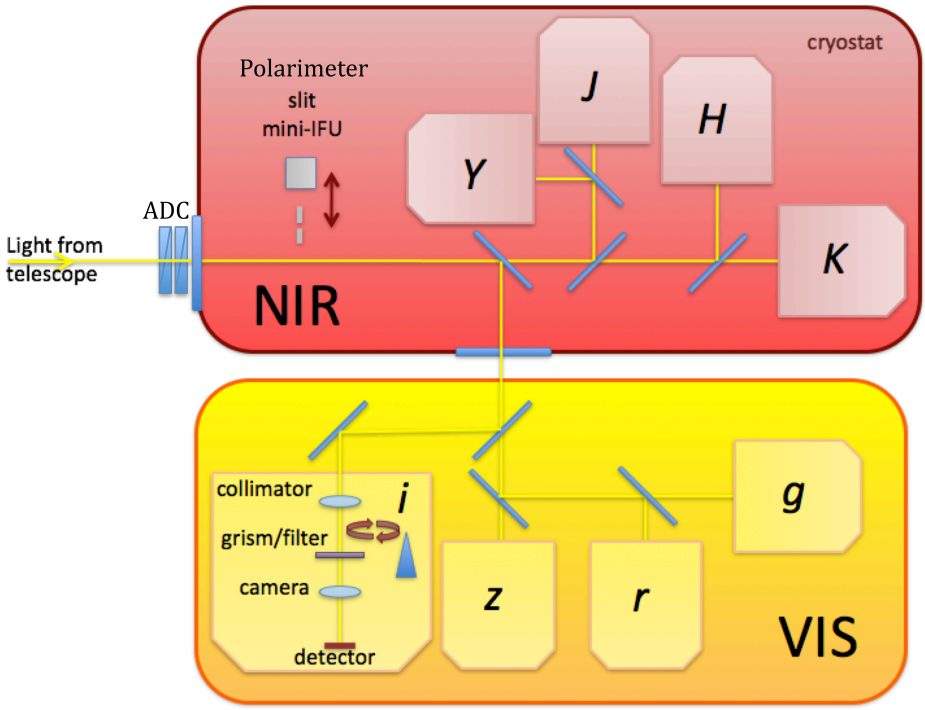

Figure 1 – OCTOCAM schematic layout. The optical arms (*g*, *r*, *i*, *z*) are located outside of the cryostat, reserved for the near-infrared channels (*Y*, *J*, *H*, K_S).

OCTOCAM is based on the use of high-efficiency dichroics to divide the light into eight different arms, four optical, and four near-infrared. It has the advantage of simultaneity, as it is capable of observing at the same time in the *g*, *r*, *i*, *z*, *Y*, *J*, *H*, and K_S bands, with a field of view of 3'x3'. In its spectroscopic mode, it will obtain spectra covering from 370 to 2,350 nm in a single shot. It will use long slit observations to provide spectral resolutions of ~3,000-4,000. Using the Integral Field Unit that we propose, it will perform spatially resolved spectroscopic studies in an area of 9.7" x 6.8", with the full spectral coverage and resolution. OCTOCAM will be capable of obtaining full-Stokes spectropolarimetry simultaneously in the range 370 to 2,200 nm to study geometry and magnetic fields of astrophysical phenomena. Furthermore, thanks to the use of state of the art detectors, it will be able to reach high readout speeds, allowing science cases aimed at high time-resolution. Depending on the detector of each arm, we expect full frame rates reaching speeds of 10 to 76 Hz, which will be even higher for windowed modes. Its detector technology will virtually eliminate dead times in most observing modes, allowing duty cycles of roughly 100%.

OCTOCAM will efficiently cover a region of the *(spectral-resolution)-(spectral-coverage)-(temporal-resolution)* observational space that is not covered, and will not be covered, by any single instrument worldwide in the 2020s, giving the Gemini community a leading position in several fields of astrophysics. While the scientific scope of OCTOCAM is extremely broad, making it a true workhorse instrument, the science cases that make most optimal use of the characteristics of OCTOCAM within the observational landscape of the 2020s are transient phenomena, such as gamma-ray bursts, supernovae, X-ray binaries, neutron stars, active galactic nuclei, and tidal disruption events. Large survey instruments in various spectral regimes will provide an enormous amount of triggers, and OCTOCAM on Gemini will allow detailed studies of the most

interesting sources that cannot be observed by smaller telescopes. OCTOCAM will also identify the most interesting sources for which follow-up observations with one of the ELTs or the James Webb Space Telescope are warranted.

The scientific advantages of the OCTOCAM design are that Gemini can be used efficiently over its full spectral range simultaneously, and that consistent data can be obtained for the full range and at any time, which is particularly relevant for transient phenomena. The extension of the spectral coverage from the optical far into the near-infrared, both in imaging and spectroscopy, is crucial for high-redshift sources in general and high-redshift transients in particular. With OCTOCAM we can use gamma-ray bursts to explore the Universe up to the very beginning of stellar formation, within the epoch of reionization. By studying active galactic nuclei at different redshifts we can acquire fundamental clues on the role of supermassive black holes in galaxy evolution. We can also study active galactic nuclei and X-ray binaries to obtain new insights into accretion physics near the black hole event horizon and properties of jets. The tidal disruption of stars by supermassive black holes allows for the measurement of black hole mass and spin. Studies of different types of supernovae probe their progenitors, the explosion physics, the evolution of dust in the Universe, and push current redshift limits in the Hubble diagram to further constrain the cosmological parameters. OCTOCAM will also enable to elucidate the formation and evolution of neutron stars, and constrain their equation of state, emission mechanisms, and properties of their atmospheres and magnetospheres.

While these are the most exciting science cases that make use of all the OCTOCAM characteristics while at the same time being prime sources of interest for the large surveys of the 2020s, there are several other science cases that make use of the temporal and spectral characteristics of OCTOCAM as well, for instance the identification and characterization of transiting extrasolar planets, to determine their mass and density, and the composition of their atmospheres; the search for ices on the surface of Trans-Neptunian objects, unveiling their surface composition, structure, and potential companions and atmospheres; and asteroseismology to unveil the internal structure and radii of stars.

The addition of spectropolarimetry provides complimentary information besides imaging and spectroscopy. In some research areas, spectropolarimetry is the most important diagnostic technique, e.g., stellar magnetic fields, and other where spectropolarimetry is used frequently, e.g., studies of supernovae, solar system objects, and circumstellar environments. High-impact science will come from exploiting the spectropolarimetric capabilities in the continuum, spanning the entire spectral range from the optical to the near-infrared. This would be a unique capability in the world, also enabling lots of discovery science.

This document presents the science cases driving the design of this high-performance workhorse instrument, and shows that it is feasible both technically and financially, as well as attractive and competitive for the Gemini scientific community. It discusses several trade-offs related to the optical and mechanical design, detectors, spectral coverage, and resolution, evaluating their impact on the project. Several alternatives to the design are also presented.

1. Science objectives and science cases

1.1. Science team

We have put together a strong and diverse science team, with expertise in many different science areas, to understand the science requirements for an instrument like OCTOCAM on Gemini. The science team consists mainly of scientists within the Gemini community, but also some who are not based in Gemini-participating countries but are world experts in scientific areas that are relevant to an instrument like OCTOCAM. For the scientific feasibility study we present here, the starting point has been an instrument that can do imaging in eight bands and wide band spectroscopy from the optical to the near-infrared, and all of this at high time-resolution. The science team has been asked to propose science cases and big science questions in their areas of interest and expertise that could be answered by such an instrument, and what the requirements would be to answer those questions. This has resulted in the scientific requirements for the OCTOCAM design that we present here. The science team has also considered the implications of possible additions to the instrument concept, such as an Integral Field Unit (IFU) or spectropolarimetry.

The scientific part of the original OCTOCAM proposal covered 11 broad topics, and during this feasibility study this has been expanded to 18. We have also expanded the science team from 24 in the original proposal to 46 for this study. The latter was done not only to add new topics, but also to strengthen some of the science cases and broaden the support within the Gemini community, making sure that an instrument like OCTOCAM delivers the science that the community is most interested in. To streamline the process of defining science cases, and determining the instrument requirements and resources necessary to reach the scientific goals, we have performed two surveys within the full science team, and had discussions with subgroups and individual scientists to obtain a clear picture of their scientific needs. The science team surveys are described in section 1.2. The big scientific questions relevant for the Gemini community and the different science cases are presented in section 1.3. The science requirements and amount of observing time necessary to answer the fundamental questions are given in section 1.4.

The science team of OCTOCAM is composed of the following people (in alphabetical order):

- Álvaro Álvarez-Candal, Observatório Nacional, Brazil
- Rodolfo Angeloni, Gemini Observatory, Chile
- Stefano Bagnulo, Armagh Observatory, UK
- Franz Bauer, Pontificia Universidad Católica, Chile
- Amanda Bayless, Southwest Research Institute, USA
- Melina Bersten, Universidad de la Plata, Argentina
- Marcelo Borges Fernandes, Observatório Nacional, Brazil
- Tom Broadhurst, Universidad del País Vasco, Spain
- Nat Butler, Arizona State University, USA
- Brad Cenko, NASA Goddard Space Flight Center, USA
- Lydia Cidale, Observatorio Astronomico de la Plata, Argentina
- Jesus Corral-Santana, Pontificia Universidad Católica, Chile
- Peter Curran, International Center for Radio Astronomy Research, Australia

- Vik Dhillon, University of Sheffield, UK
- René Duffard, Instituto de Astrofísica de Andalucía - CSIC, Spain
- Robert Fesen, Dartmouth College, USA
- Gastón Folatelli, Universidad de la Plata, Argentina
- Jonathan Fortney, University of California Santa Cruz, USA
- Ori Fox, University of California Berkeley, USA
- Anna Frebel, Massachusetts Institute of Technology, USA
- Lluís Galbany, Universidad de Chile, Chile
- Rafael Garrido Haba, Instituto de Astrofísica de Andalucía - CSIC, Spain
- Daryl Haggard, Amherst College, USA
- Eric Hintz, Bringham Young University, USA
- David Kaplan, University of Wisconsin-Milwaukee, USA
- Oleg Kargaltsev, George Washington University, USA
- Chryssa Kouveliotou, George Washington University, USA
- Adam Kraus, University of Texas at Austin, USA
- Michaela Kraus, Astronomický ústav, Akademie věd České republiky, Czech Republic
- Ho-Gyu Lee, Korea Astronomy and Space Science Institute, South Korea
- Chris Lidman, Australian Astronomical Observatory, Australia
- Teo Muñoz-Darias, Instituto de Astrofísica de Canarias, Spain
- Jerome Orosz, San Diego State University, USA
- Thomas Pannuti, Morehead State University, USA
- Jennifer Patience, Arizona State University, USA
- Daniel Perley, California Institute of Technology, USA
- Noemí Pinilla-Alonso, University of Tennessee, USA
- Brian Schmidt, Australian National University, Australia
- Steve Schulze, Pontificia Universidad Católica, Chile
- Denise Stephens, Brigham Young University, USA
- Juan Carlos Suárez, Universidad de Granada, Spain
- Nial Tanvir, University of Leicester, UK
- Ezequiel Treister, Universidad de Concepción, Chile
- Daniel Vanden Berk, St. Vincent College, USA
- Sjoert van Velzen, Johns Hopkins University, USA
- Stefanie Wachter, Max-Planck-Institut für Astronomie, Germany

1.2. Science Team Surveys

We performed three surveys within the science team to define the biggest scientific questions in the many areas that our team covers, and what is necessary to answer those questions; and to define the possible characteristics and features of an instrument like OCTOCAM. These are the questions we asked, distributed over the three surveys:

1. What are the most important scientific questions that an instrument like OCTOCAM would be able to answer in the 2020s astronomical/ instrumentation landscape? And what would the potential impact be if those questions were being answered?
2. What is the estimated number of hours needed to complete your science cases?
3. What kind of observing conditions are necessary for your science?

4. How short would the response time have to be for you to do your science?
5. What is the minimum time-resolution you need to do your science?
6. What is the optimal spectral resolution for your science: ~4000-5000 or higher/lower?
7. Is *u*-band spectroscopy necessary for your science? Or would *g*-band spectroscopy, going down to 370 or 400 nm, be sufficient?
8. Which imaging bands are relevant/crucial for your science?
9. Which wavelength range for spectroscopy is relevant/crucial for your science?
10. How relevant/crucial would adding echelle grisms be for your science?
11. How relevant/crucial would adding a spectropolarimetry unit be for your science?
12. How relevant/crucial would adding an Integral Field Unit of ~10"x10" be for your science?
13. What would be the ideal field of view and platescale for your science?
14. Indicate the importance of the following capabilities of an instrument like OCTOCAM by giving a grade between 1 and 5, and motivate your grades:
    - Multi-band imaging
    - Time resolution
    - Multi-wavelength spectroscopy
    - Spectropolarimetry
    - Integral Field Unit spectroscopy

These questions have provided the base for focusing the science cases in section 1.3 and defining the science requirements in section 1.4. Therefore, the results of these surveys are provided and integrated in these two sections.

1.3. Science Cases

The aim of this scientific feasibility study was to identify the characteristics of a new instrument on Gemini that will be able to address fundamental questions in as many research areas as possible. This was done within the context of the instrumentation and capabilities that will be available in the 2020s. As mentioned before, the starting point was an instrument that can do simultaneous optical to near-infrared photometry and optical to near-infrared spectroscopy, and has high time resolution capabilities, which allowed us to explore a large number of topics in time domain astronomy, but also cover many other interesting science topics. In this section we present the different science cases, and these are the main objectives we would like to address:

- *Search for ices on the surface of Trans-Neptunian objects, unveiling their surface composition, structure, and potential companions and atmospheres.*
- *Identify and characterize transiting extrasolar planets, to determine their mass and density, and the composition of their atmospheres.*
- *Unveil the internal structure and radii of stars with asteroseismology.*
- *Pin down the origin and time development of variability and mass loss in specific short-lived phases in the evolution of massive stars.*
- *Investigate the composition of brown dwarf atmospheres and the role of clouds on their opacity.*
- *Verify stellar evolution by accurately measuring the masses and radii of stars in eclipsing low-mass binary systems.*

- *Ascertain the nature of carbon-enhanced low-metallicity stars and their connection with the first stars in the Universe.*
- *Elucidate the formation and evolution of neutron stars, and constrain the properties of their atmospheres and magnetospheres.*
- *Determine the emission origin and mechanisms of magnetars.*
- *Study the physics of accretion streams and disks in interacting binary systems.*
- *Constrain the equation of state of neutron stars by determining their maximum mass in binary millisecond pulsars.*
- *Obtain new insights into accretion physics near the black hole event horizon and properties of jets by studying X-ray binaries and active galactic nuclei.*
- *Probe supernova progenitors and explosion physics, and evolution of dust in the Universe.*
- *Push current redshift limits in the Hubble diagram and further constrain the cosmological parameters.*
- *Explore the Universe up to the very beginning of stellar formation, within the epoch of reionization, with gamma-ray bursts.*
- *Acquire fundamental clues on the role of supermassive black holes and their formation in galaxy evolution.*
- *Measure the mass and spin of supermassive black holes with tidal disruption events.*
- *Shed light on the content of dark matter and the energy density of the Universe through lensing by galaxy clusters.*
- *Characterize transient sources detected and/or newly discovered with high-cadence optical, radio, X-ray, and gamma-ray surveys.*

1.3.1. Trans-Neptunian Objects

Search for ices, unveiling surface composition, structure, and potential companions and atmospheres (Álvarez-Candal, Duffard, Pinilla-Alonso, Stephens)

Trans-Neptunian objects are among the most primitive objects found in today's Solar System, and are widely considered as carrying the clues that could explain its origin. They orbit around the Sun at large distances, mostly over 30 AU, where the reining temperatures are below 50 K. Therefore, the surfaces of Trans-Neptunian objects are covered by ices (depending on the size of the object, i.e., on their ability to retain light molecules that are otherwise lost to space) such as H_2O, CH_4, N_2, CO, CO_2, as well as silicates and residuals due to space weathering (collisions of micrometeorites and energetic particles with the soil) which reddens and darkens the surfaces. Most of these ices have wide, up to a few hundred angstroms, absorption features from the visible to the near-infrared, due to overtones of fundamental vibrational transitions. The existence of ices is indicative of surface composition, and their observation helps to study the evolution of possible atmospheres. With help of other available data, one can also infer the internal structure, such as the layered distribution of ices. The final goal is to understand where, how, and when these bodies formed, and use them as tracers of the evolution of the Solar System.

Apart from a handful of large bodies (Pluto, Eris, Haumea, and Makemake, all with diameters larger than 1000 km), most Trans-Neptunian objects are relatively small and faint. Therefore, high quality data are quite scarce and detailed studies are currently limited to about 50 to 60 objects with high (> 20)

signal-to-noise spectra (for examples, see Barkume et al. 2008, AJ, 135, 55; Guilbert et al. 2009, Icarus, 201, 272). To improve our understanding of the surface composition of Trans-Neptunian objects, the niche of an instrument like OCTOCAM is in the combination of high time resolution with broadband photometry or spectroscopy.

First of all, simultaneous visible to near-infrared spectroscopy with medium resolution will help put constraint on the existence of volatile ices without relying on extra calibrations and avoiding rotational uncertainties. Pioneer work on Trans-Neptunian objects relied on spectra obtained with different instruments (for instance FORS and ISAAC at the VLT) and joining them. As the spectra did not overlap and were not flux calibrated, it was necessary to use photometric data to join the different pieces, resulting in large uncertainties because the different spectra and the photometric data were not necessarily simultaneous. Therefore, some of these early results could never be confirmed (e.g., the spectra presented in de Bergh et al. 2004, A&A, 416, 791). Prism spectroscopy (for instance NICS at the TNG) partially helps, as it provides wide spectral coverage, but this is limited by low resolving power.

Secondly, a possibility to increase the sample of studied objects, without the time budget of spectroscopy, is relying on photometric data covering from the optical up to the near-infrared. As noted above, simultaneity is critical to avoid rotational uncertainties (rotational periods usually between 8 and 11 h, see e.g., Thirouin et al. 2010, A&A, 522, A93). Using multi-filter photometry will permit the detection of possible broad absorption features, such as H_2O at ~1,400 nm in the *H* filter or ~2,000 nm in the K_S filter (Figure 2). As a side product the *Y* filter will be extremely useful for studies of other minor body populations, for instance objects showing absorption features due to silicates at ~1,000 nm.

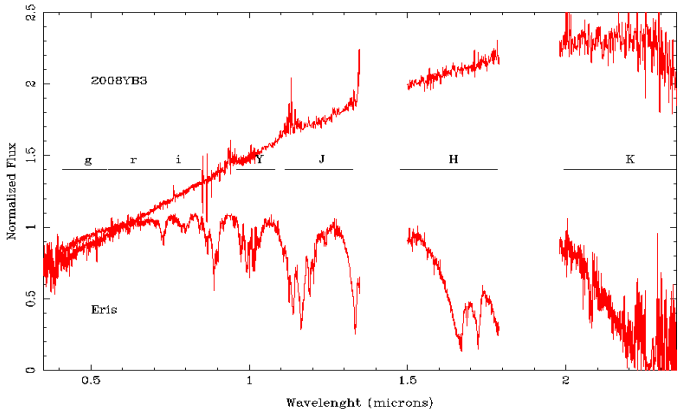

Figure 2 - Spectra of the dwarf planet Eris with deep absorption features due to CH_4 ice (Alvarez-Candal et al. 2011, A&A, 532, A130), and the centaur 2008YB3 with no apparent features (Pinilla-Alonso et al. 2013, A&A. 550, A13). Also shown are approximate positions and widths of some photometric filters proposed for OCTOCAM.

Finally, the high temporal resolution of an instrument like OCTOCAM can provide unique data on very different topics. Studies of stellar occultations by planets, from which an enormous amount of information on the planets' atmospheres can be gathered, like the pressure-temperature profile (e.g. Hubbard et al. 1972, AJ, 77, 41; Lellouch et al 1986, Nature, 424, 6945), requires very fast imaging. An instrument that can deliver images in eight bands at a fast rate can provide an unprecedented wealth of information never obtained before. The atmospheric structure can be resolved to a greater detail so that even planetary or gravity waves can be detected together with other fine scale phenomena. The occultation technique is also used to detect faint discs or rings

around different solar system objects (Uranus rings were discovered that way) and even satellites like Rhea might possess several rings (Jones et al. 2008, Science, 319, 1380). Recently, the first ring around a minor body was discovered (Braga-Ribas et al. 2014, Nature, 508, 72).

1.3.2. Extrasolar Planets

Identify and characterize transiting exoplanets, to determine their mass, density, and composition of their atmospheres (Fortney, Patience, Stephens)

The transiting method to study extrasolar planets (see Figure 3) is the only method that allows us to directly measure the size of the planets, assuming that the host star radius is known. In combination with radial velocity data, they can constrain the planet mass and density. The intervals between individual transits of known transiting planets vary when additional planets are present in the system. This is known as the transit timing method to search for extrasolar planets, and it is potentially sensitive to Earth-size planets. Such planets are too light-weight to be detected via radial velocity measurements, but in a fortuitous resonant orbit can lead to deviation in the transit timing of other planets in the system of the order of 1 to 10 minutes. An instrument like OCTOCAM, with sub-second time resolution, will take these planet detection techniques to the next level. Simultaneous multi-wavelength observations over a wide wavelength range can allow a reliable verification of the nature of the transits, since geometric phenomena are achromatic. Such observations will improve the accuracy of the timing of individual transits because of the large number of bands, which is critical for detecting low mass planets in the systems of known transiting planets.

Besides detecting extrasolar planets, an instrument like OCTOCAM can contribute significantly to studies of the composition of exoplanet atmospheres. Simultaneous multi-wavelength photometric monitoring represents an important probe of their atmospheres, since the different wavelengths are sensitive to different depths in the atmosphere. Comparisons with the atmospheres of brown dwarfs are an important component of this, since the atmospheres of brown dwarfs have overlapping temperatures to the ones of both transiting and directly imaged exoplanets. An example aspect under investigation is the comparison of the carbon/oxygen ratios of brown dwarfs that are thought to form like stars and exoplanets that are thought to form in circumstellar disks, with the carbon/oxygen ratio providing an indication of the formation scenario. Furthermore, for gas giant planets, an instrument like OCTOCAM can provide abundances of carbon and oxygen, and determine if they are enriched in metals compared to their parent stars; and do

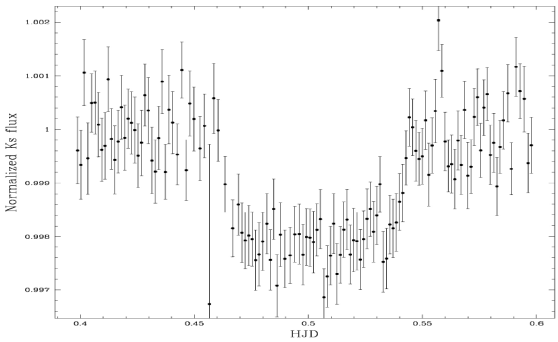

Figure 3 - Secondary transit of WASP-4b in K-band, observed with ISAAC at the ESO VLT (Caceres et al. 2011, A&A, 530, 5). Each data point is an average of 200 measurements with integration time of 0.5 seconds each.

this for a large statistical sample, to answer key questions regarding planet formation.

1.3.3. Asteroseismology & Pulsating Variable Stars

Unveil the internal structure and radii of stars (Garrido Haba, Hintz, Suárez)

The study of pulsating variable stars has a long history starting with the discovery of pulsations in Omicron Ceti (Mira) in 1596. This was followed in 1784 with John Goodricke's discovery of pulsations in delta Cephei. We now know of a large variety of pulsating variable stars that range from supergiant stars down to white dwarf objects, and in theory neutron stars. They can have periods from seconds to years, and each provides a unique set of challenges and opportunities. Sometimes we use pulsating variables as a tool to study other objects, as is the case with a variety of period-luminosity relations that have been discovered and applied. Or we can use techniques such as asteroseismology to probe environments that are accessible in no other way. Below we will discuss the application of the unique capabilities of an instrument like OCTOCAM to a number of approaches to pulsating variable star research.

Traditional Asteroseismology: Asteroseismology is the best technique to test numerical models of stellar structure. Nevertheless, its application needs previous identification of the oscillation mode being detected, usually as a statistically significant peak in the power spectrum of a photometric/radial velocity time series of a given pulsating star. Unambiguous global identification only has been achieved for the Sun although a clear signature of rotationally splitting is lacking.

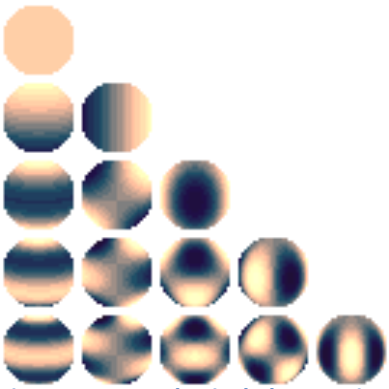

Figure 4 - Spherical harmonics (https://commons.wikimedia.org/wiki/File:Rotating_spherical_harmonics.gif).

Reliable mode identification is essential in order to apply the potential of this technique. Usually this identification is made to observed regular patterns in the peak distribution of the power spectra. For stars more massive than the Sun, it is critical to have long records of time series in order to get a reliable discrimination (e.g., García Hernández et al. 2009, A&A, 506, 79). However, as the amplitudes and phases of those non-radial modes depend critically on wavelength, simultaneous multiband observations can give hints in order to identify the spherical harmonics of the pulsation modes considered (in Figure 4 spherical harmonics up to l=5 are depicted).

Due to the small phase differences predicted by theory for the different wavelengths (Garrido 2000, ASPC, 210, 67), large signal-to-noise ratios are required, which is what an instrument like OCTOCAM is expected to provide. This can be performed by using not necessarily long time series since the frequency solution have been provided by the analysis of space observations from CoRoT or *Kepler*. Multi-band photometric sequences observed with an instrument like OCTOCAM would allow us to obtain oscillation frequency solutions as a function of the wavelength for the highest frequency fitting of a given target already observed by *Kepler* or CoRoT. Once the modes are identified, theoretical stellar structure modeling including second-order rotational

perturbations can be developed further (Suárez et al. 2006 A&A 449, 673; Suárez 2014, A&A, 563, 7). The final objective would be to construct realistic stellar structures (including atmospheric effects, convection, differential rotation and non-adiabatic treatment), fitting the observed frequencies and satisfying the wavelength dependencies. For the most common targets of asteroseismology, delta Scuti variables, frame rates of 1 Hz or less will be sufficient. The cadence rate would need to be increased for asteroseismology studies of white dwarf objects.

Baade-Wesselink method: There are a variety of different approaches that are all known as the Baade-Wesselink method as applied to pulsating variable stars. The basic idea of all the approaches is to determine fundamental parameters such as the radius of a star. Given the radius and temperature for a given star, one can then determine the luminosity or absolute magnitude. The application of this approach to delta Scuti variables can be seen in a number of studies (Laney et al. 2002, ASPC, 259, 112; Laney et al. 2003, ASPC, 292, 203). The Baade-Wesselink method can be used to give luminosities and distances to pulsating stars independent of measured parallaxes (for application to classical variables, see Gieren 2012, IAU Symp., 289). It should be noted that the near-infrared capabilities of the proposed OCTOCAM instrument are ideal for this type of work (see Laney & Stobie, 1995, MNRAS, 274, 337).

Given ESA's *GAIA* mission to measure parallaxes for about 1 billion stars, an instrument like OCTOCAM could be used to determine radii for pulsating variables over a range of distances, which could then be used as an independent check of the *GAIA* results. The Baade-Wesselink techniques can be applied to Cepheids, RR Lyrae and delta Scuti variables. This would also allow us to refine the period-luminosity relation for Cepheid variables, which has an impact upon the overall scale of the Universe.

Combination of both techniques: In theory these two approaches could be done at the same time given the right set of data. OCTOCAM would be the only instrument that could be used to get the simultaneous data needed for a combined approach. Using spectroscopic and photometric data, we could determine a baseline radius for the star and then examine changes over the course of specific pulsation cycles. With an FFT approach for radial velocity determinations, the velocities would be of sufficient quality to see changes. Doing this would provide an additional piece of information that does not exist yet. Although it would be possible to examine stars with a variety of amplitudes, the ideal targets would be medium to high amplitude delta Scuti variables. These would have a large enough radial velocity range to allow a reasonable radius determination, and the pulsations are fast enough to get a sufficient number of cycles for asteroseismology work.

1.3.4. Massive Stars

Pin down the origin and time development of variability and mass loss in specific short-lived evolutionary phases (Borges Fernandes, Cidale, M. Kraus, Wachter)

Massive stars (more than 8 solar masses) play a major role in the evolution of their host galaxies. Via stellar winds they strongly enrich the interstellar medium with chemically processed material, and deposit large amounts of momentum and energy into their surroundings during their entire lifetime. Despite their

great importance, stellar evolution theory is most uncertain for massive stars due to the still poor understanding of some physical processes in the stellar interiors, as well as the amount of mass loss via stellar winds and (irregular) mass ejections. In the recent years, parameters obtained from stellar variability, extracted from multi-epoch and multi-wavelength high-quality photometric and spectroscopic observations, were found to be extremely reliable when confronting theoretical results with observations.

The physical origin of variabilities changes with the evolutionary phase, so that quite different variability patterns are expected for a massive star in distinct stages. The situation is particularly complex beyond the main sequence. Blue supergiants display strong photometric and spectroscopic variability, which is linked to pulsations (Moravveji et al. 2012, ApJ, 749, 74). As massive stars can cross the blue supergiant domain more than once during the evolution, the pulsation activity of a blue supergiant can change drastically. Saio et al. (2013, MNRAS, 433, 1246) demonstrated that blue supergiants evolving blue-ward undergo numerous pulsations, including radial strange modes that facilitate enhanced mass loss. However, observational investigations, aimed at searching for these pulsation modes, exist for only a few objects so far (e.g., Aerts et al. 2013, A&A, 557, A114).

Other phases in the evolution of massive stars, displaying variability in both spectroscopy and photometry, are B[e] supergiants, luminous blue variables, and yellow hypergiants. Stars in these phases experience strongly enhanced mass loss, often connected with eruptions, which were recently suggested to be related to stellar strange mode pulsations (Aerts et al. 2010, A&A, 513, L11).

An instrument like OCTOCAM is ideal to address the important yet unsolved issue of the origin and time development of variability and mass loss in specific, short-lived phases in the evolution of massive stars. Stars in the (pulsating) blue supergiant phase can be studied, utilizing the excellent photometric facilities of an instrument like OCTOCAM for Gemini. Based on high-quality time series, it is possible to determine precise pulsation periods and modes, which help classify each star according to its evolutionary phase, and help to improve our understanding of physical processes inside the star.

Very broad wavelength coverage in spectroscopy and multi-wavelength imaging capabilities provide excellent tools to study the large-scale structure and temporal evolution of the ejecta of stars in the (eruptive) luminous blue variable, B[e] supergiant, and yellow hypergiant transition phases. The circumstellar material of these stars has typically a complex structure, displaying rings, shells, bipolar nebulae, etc., with a mixture of gas in different ionization stages, as well as condensation products (molecules, dust). The structure of the ionized circumstellar medium regions can be retrieved from strategic emission features. Particularly important are the emission lines from the optical and near-infrared hydrogen recombination series, which trace distinct regions within the ionized wind (Granada et al. 2010, AJ, 139, 1983). Furthermore, the gas dynamics can be obtained from the profile shapes of various forbidden emission lines tracing regions of different temperature and density (Kraus et al. 2010, A&A, 517, A30). Permitted lines, such as, e.g., the CaII IR triplet, are composite, possessing contributions from both the less dense wind and the dense shell or disk (Aret et

al. 2012, MNRAS, 423, 284). All these lines were reported from a variety of evolved massive stars and thus serve as ideal indicators for their circumstellar medium.

Moreover, molecules condensate in the ejected material, and several strategic molecules (e.g., CO, TiO, water, etc.) with transitions in the optical and near-infrared regimes were observed in B[e] supergiants and yellow hypergiants (Torres et al. 2012, MNRAS, 427, L80; Oksala et al. 2013, A&A, 558, A17). Tracing different temperature and density regimes, these molecules provide complimentary information on the structure and kinematics of the hot molecular circumstellar medium (see Figure 5).

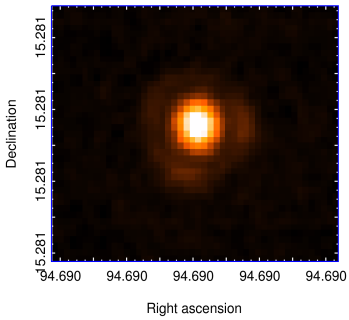

Figure 5 - IFU image of the continuum subtratced pure CO band emission at 2.3 micron of the B[e]SG MWC 137 (Kraus et al., in prep.). Data were obtained with the ESO SINFONI spectrograph. The CO emission displays a clumpy double-ring structure.

Massive stars in transition phases are rare. To study their evolutionary connections, which are still not well known, improved number statistics are vital. These can only be obtained from resolving massive star populations in other galaxies. However, identifying these objects has proven to be a difficult task, because hot luminous blue variables and B[e] supergiants, as well as cool luminous blue variables and yellow hypergiants, are indistinguishable upon their pure optical spectra. The breakthrough in classification came from a recent near-infrared survey, in which Oksala et al. (2013, A&A, 558, A17) discovered that stars in different transition phases display distinct emission features, based on which massive stars can be identified and unambiguously classified. The possibility to simultaneously obtain optical-to-near-infrared spectra, combined with the expected limiting magnitudes of OCTOCAM will greatly advance the identification of new members of evolved massive stars in transition phases in other Local Group galaxies. Reliable number statistics of populations of stars in diverse transition phases can be obtained over a large range of metallicities, allowing us to draw conclusions on the overall impact of mass ejections on the properties of stellar populations, chemical enrichment, and galactic evolution in general.

1.3.5. Brown Dwarfs

Investigate the composition of brown dwarf atmospheres and the role of clouds on their opacity (Fortney, Patience, Stephens)

Brown dwarfs, which form like stars, lack the necessary mass to sustain hydrogen fusion in their cores. This means that their atmospheres are slowly evolving as they age and cool. Higher-mass brown dwarfs will have spectral features in common with the lowest-mass M dwarfs when they first form, but as they age over time they will end up looking very much like a gas giant planet with cloud features and broad molecular bands dominating their spectral energy distribution. Spectral types for the brown dwarfs (L, T, Y) roughly correlate with temperature as they do for stars. But at the transition between the L to T spectral types the temperature will remain roughly constant for the late-L and early-T dwarfs and the observed differences in their spectral energy distributions will be

due more to variations in cloud opacity and gravity than temperature (for a discussion on L-T transition objects, see Stephens et al. 2009, ApJ, 702, 154).

As a brown dwarf transitions from a late-L to an early-T spectral type, the clouds, which dominated the spectral energy distribution when the object was a hotter L dwarf, will begin to drop below the photosphere. This will result in either a non-uniform thinning of the clouds (Marley et al. 2010, ApJL, 723, L117) or possibly a fragmentation of the clouds with the development of holes between the clouds (Burgasser et al. 2002, ApJL, 571, L151). Either effect will result in a spectral energy distribution for the object that is a unique combination of flux from deeper, hotter regions of the atmosphere (holes or thinner clouds) combined with flux from the cooler cloudy regions. The location and extent of the thinner clouds or holes is not expected to be uniform across the surface of the brown dwarf and this should result in spectral variability as the brown dwarf rotates and the relative percentage of flux contributed by different layers of the atmosphere changes (Burgasser 2013, AN, 334, 32). The amplitude of the variability will not be uniform across the optical and near-infrared wavelengths since clouds tend to dominate the spectral energy distribution in the near-infrared more than the optical. For example, Jupiter can show photometric variation of up to 0.2 magnitudes in the near-infrared, where flux from deep in its atmosphere is able to escape, but it only varies by 0.04 magnitudes in the optical (Gelino & Marley 2000, ASP Conf. Ser. 212, 322).

While fragmentation or thinning of clouds may be the source of variability for some late-L and early-T dwarfs, it cannot be the only process through which variability occurs. Many L/T transition objects show no significant variability in large photometric and spectroscopic surveys, and there are cloudy L-dwarfs and clear T-dwarfs that do show variability (Girardin et al. 2013, ApJ, 767, 61; Buenzli et al. 2014, ApJ, 782, 77; Marti & Osorio 2014, A&A, 568, A87; Radigan

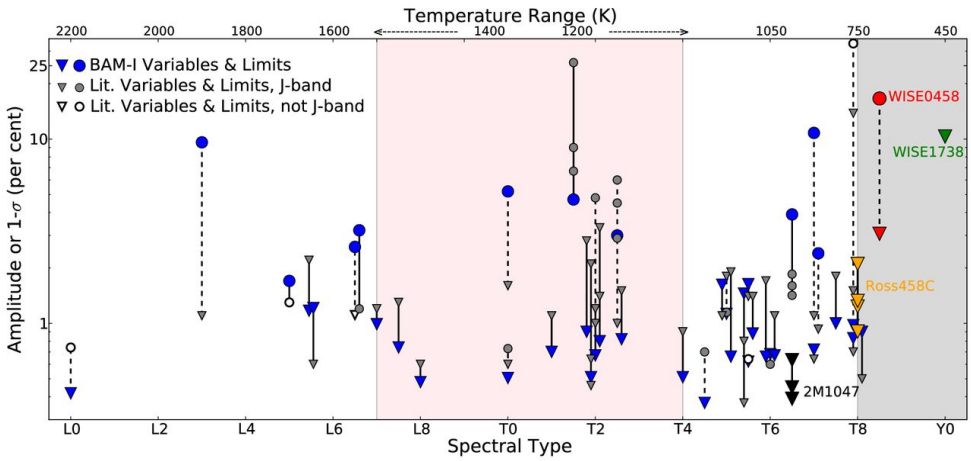

Figure 6 – Variability amplitude as a function of spectral type for several brown dwarfs (Rajan et al. 2015 and references therein). Each vertical line corresponds to a unique object and shows the amplitude of variability that was observed. A solid line indicates that the brown dwarf remained consistently variable or constant at more than one epoch, while the dashed lines identify objects that switched between variable and constant states. This shows that the source of variability must be dynamic to explain the large range of amplitudes for a given object as well as the number of objects that alternate between variable and constant states. This sample is still too small and biased to identify the fraction of highly variable objects as a function of spectral type.

2014, ApJ, 797, 120; Radigan et al. 2014, ApJ, 793, 75; Wilson et al. 2014, A&A, 566, A111; Heinze et al. 2015, ApJ, 801, 104; Metchev et al. 2015, ApJ, 799, 154). These large surveys do not agree as to whether variability is more common at the L/T transition or is uniform across spectral type for the brown dwarfs. They also find that the amplitude of variation for a given brown dwarf can change significantly with time and that variability at one wavelength can be out of phase with variability measured simultaneously at other wavelengths. Figure 6, from Rajan et al. (2015, MNRAS, 448, 3775), presents all the known variable brown dwarfs that have been observed more than once, and it is clear that variability is not constant and can appear at almost any spectral type. The current observations of variability, taken at different times with different telescopes and at different wavelengths, are just too sparse to definitively identify the source of variability for the L and T dwarfs. While the measured variability might be due to cloud fragmentation or patchy clouds, it could also be due to effects like auroral emission, magnetic spots, gravitational waves, or temperature perturbations (Burgasser 2013, AN, 334, 32; Freytag et al. 2010, A&A, 513, A19; Robinson & Marley 2014, ApJ, 785, 158).

Marley et al. (2010, ApJL, 723, L117) and Burgasser (2013, AN, 334, 32) both suggest that multi-wavelength variability studies hold the most promise for confirming or refuting the patchy cloud or fragmentation model as the source of variability, but this data must be combined with advanced 3D atmosphere models to be interpreted properly. While these models do not exist yet, they should be developed in the near future, and the ability to obtain simultaneous multi-wavelength variability measurements of brown dwarfs is feasible with an instrument like OCTOCAM. With data in 8 bands, covering a wavelength range from 400 to 2350 nm, in just one night we can determine the level of variability for a given brown dwarf as a function of wavelength and determine whether the observed variability is in phase for each wavelength region. Variations in amplitude and phase can then be combined with current and future theoretical atmosphere models, to better probe and understand the source of brown dwarf variability and constrain theoretical models, especially those dealing with the evolution of objects across the L to T transition.

1.3.6. Low-Mass Binaries

Verify stellar evolution by accurately measuring the masses and radii of stars in eclipsing low-mass binary systems (Bayless, A. Kraus, Orosz)

Understanding the structure and evolution of stars is a basic goal of stellar astronomy, and is required in most other branches of astronomy, including the evolution of white dwarfs, neutron stars, and black holes. Accurate mass-radius relations for stars also affect the calculated mass and radius for transiting extra-solar planets (Southworth 2009, MNRAS, 394, 272; Quintana et al. 2014, Science, 344, 277). Low-mass stars (less massive than the Sun) are the most numerous stars in a galaxy for any galaxy classification: the characteristic mass of Milky Way stars in the disk is 0.1-0.2 solar masses (Chabrier 2003, PASP, 115, 763). However, low-mass stars have a discrepancy between stellar structure models (e.g. Baraffe et al. 2002, A&A, 382, 563) and observed masses and radii (Bayless & Orosz 2006, ApJ, 561, 1155), with the observed radii being up to 20% larger than predicted for the same mass (Torres & Ribas 2002, ApJ, 567, 1140).

The best opportunity for accurate measurements of the radii and masses of stars come from eclipsing binary stars (e.g., CM Dra with 0.001 solar mass accuracy; Metcalfe et al. 1996, ApJ, 456, 356). These measurements are essential to verify stellar evolution theory, and they rely on dynamical constraints from observed radial and rotational velocities, and geometric constraints from photometric time series observations. The mass-radius relation for solar-mass stars in binaries usually agrees well with stellar evolution models, but not at masses of ~0.75 solar masses or less. It is has been a long standing question whether the models are missing physics, or if there is an observational bias from the binaries, or both. Low-mass stars in binaries frequently have orbital periods of a few days, making the stars tidally locked with circular orbits. This gives a rotational velocity of ~100 km/s, or 50 times that of the Sun (Hilditch 2001, ISBN 0521241065). This rapid rotation could be inflating these binary stars (Kraus et al. 2011, ApJ, 728, 48). The inflation of stars due to rotation has been suggested by *Kepler* Telescope observations, but *Kepler* does not have multi-wavelength capabilities, with only one observing band in the visible, making this correlation inconclusive (Figure 7; Coughlin et al. 2011, AJ, 141, 78).

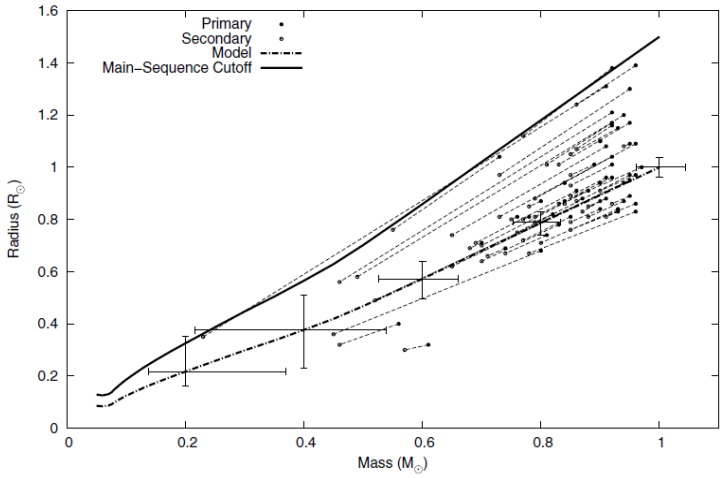

Figure 7 - Sample of low-mass eclipsing binaries with orbital periods between 1 and 10 days as observed with Kepler (Coughlin et al. 2011, AJ, 141, 78) compared to the stellar evolution model of Baraffe et al. 1998 (A&A, 337, 403) and Chabrier et al. 2000 (ApJ, 542, 464). There is a large number of stars that have radii much larger than predicted.

The rapid rotation of these stars can also produce significant magnetic activity, which will manifest as star spots. Observing these binaries in the optical-to-near-infrared bands, as proposed for OCTOCAM, gives a map of the eclipse geometry and the photosphere of these stars, including star spots (Zhang et al. 2014, MNRAS, 442, 2620).

The most precise measurement of the mass and radius of a binary requires measuring the radial velocity (RV) curve. With the RV curve, the mass, semi-major axis, and inclination are a function of only observable quantities, the amplitude of the velocity and the orbital period. In binaries, where the components are similar in mass, the spectrum of each star can be extracted. For low-mass stars, this requires high resolution, optical and near-infrared spectroscopy on 8-meter class telescopes since these stars are intrinsically faint and the peak of the emission in low-mass stars is redward of 600 nm. Measuring the Doppler shift of a single absorption line is not always possible if the star has a high level of activity, which will significantly change the observed spectrum (e.g., missing H-alpha stars, RS Can Ven, BY Dra, Fernandez-Figueroa et al. 1994, ApJS, 90, 433; J0516, Bayless & Orosz 2006, ApJ, 561, 1155). Therefore, the spectral range needs to cover ~1,500-2,000 nm in order to cross-correlate the

time-series spectra with an RV template spectrum. The spectral coverage proposed for OCTOCAM, in conjunction with its intermediate resolution, provides an ideal instrument for the measurement of binary RV curves.

1.3.7. Low-Metallicity Stars

Ascertain the nature of carbon-enhanced low-metallicity stars and their connection with the first stars in the Universe (Frebel)

A key question in the field of stellar archaeology concerns the nature of the carbon-enhanced metal-poor stars. These are old metal-poor stars ([Fe/H] < -2.5) in the halo of the Milky Way that show a relative enhancement in carbon compared to iron, usually defined to have [C/Fe] > +0.7. From an observational point of view, the frequency of occurrence of these stars has been well established (Placco et al. 2014, ApJ, 797, 21). As can be seen in Figure 8, particularly among stars with [Fe/H] < -3.5, carbon-enhanced metal-poor stars occur at a rate of 60%. Below Fe/H]<-4.0, 80% are carbon-enhanced metal-poor stars, and below [Fe/H]<-5.0 it is 100%. While this study is based on a fairly complete sample of all available literature high-resolution spectroscopic results, it should be noted that searches for metal-poor stars do not select for or against carbon-enhanced metal-poor stars as the primary selection feature is the Ca K line at 393 nm.

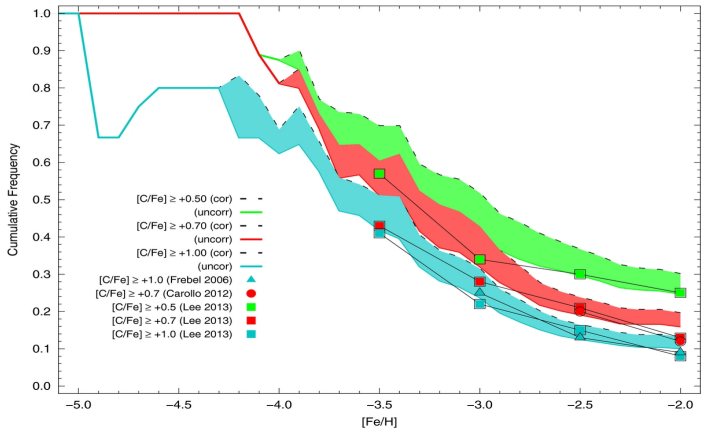

Figure 8 - The frequency of halo carbon-enhanced metal-poor stars steeply increases with decreasing metallicity (Placco et al. 2014, ApJ, 797, 21). The various data points are based on mid-resolution spectra, the shaded regions on high-resolution spectra. The dashed line of the red shaded area, corresponding to [C/Fe] > 0.7, is most relevant here.

The high frequency of carbon-enhanced metal-poor stars in the early universe reflects the nature of the PopIII progenitors believed to have been responsible for the metals observed in these stars. Carbon is produced and released into the interstellar medium through stellar winds (rotating massive stars; Meynet et al. 2006, ESO Astrophysics Symposia, 314) or supernovae (massive stars undergoing a mixing and fallback mechanisms; Umeda & Nomoto 2003, Nature, 422, 871). Observed carbon abundances together with other element abundances thus allow for a comparison with PopIII elemental yields to constrain PopIII properties such as mass, supernova explosion energy and mixing parameters.

Identifying more stars with low [Fe/H] is paramount to fully exploit this opportunity to study PopIII stars. A promising way forward are low- or medium-resolution surveys covering both the Ca K line and the CH G-band at 430 nm to identify more metal-poor stars but to simultaneously measure their carbon abundances as well. This can be done with medium-resolution spectra from an instrument like OCTOCAM. Previous surveys such as SDSS (Carollo et al 2012,

ApJ, 744, 195; Lee et al 2013, AJ, 146, 132) have done such work but found few stars in the [Fe/H] < -3.5 regime. Future efforts should concentrate on filling this gap as well as providing thousands of stars with [Fe/H] < -2.0 to finely map the carbon-enhanced metal-poor star frequency. Once identified, carbon-enhanced metal-poor star fractions can be established for different directions on the sky and separately within the inner and outer halo. This will not only unravel details about the structure of the Milky Way's older components but also about the formation and (continued) assembly history of the halo.

Similar as for metal-poor halo stars, iron and carbon abundance estimates are of great importance for stars in ultra-faint dwarf galaxies. They are ancient systems and allow for dwarf archaeology: using entire galaxies to study the early Universe. As new systems are discovered (such as the recent dwarfs found in Dark Energy Survey data; Bechtol et al. 2015, ApJ, 807, 50), follow-up observations are ongoing to characterize these systems. Medium-resolution [Fe/H] and [C/Fe] values for these generally faint stars (> 19 mag) can be used in the same way as for halo stars, i.e., to establish metallicity and carbon abundance spreads and frequencies. The results can be compared to simulation results of the first galaxies, as well as with the observational halo results. Only this way can the assembly of the stellar halo of the Milky Way through the accretion of small objects like the surviving ultra-faint dwarfs be constrained observationally.

1.3.8 Isolated Neutron Stars

Elucidate neutron star formation and evolution, and constrain the properties of their atmospheres and magnetospheres (Kaplan, Kargaltsev, Wachter)

Isolated (non-accreting) neutron stars have become one of the main focus areas in the present golden era of X-ray astronomy. This category includes neutron stars with very different properties: magnetars, radio-quiet isolated neutron stars, pulsars, rotating radio transients, and central compact objects in supernova remnants. We currently do not understand the underlying physical processes leading to such diversity of neutron stars. By probing neutron star spectra in very different frequency ranges, optical observations will allow us to better understand the neutron star formation and evolution. Optical spectra of neutron stars remain a poorly investigated territory because studying isolated neutron stars in the optical is very challenging. Even nearby isolated neutron stars are very faint (22–27 mag), and the major showstopper is the lack of high-throughput instruments (on an 8-meter class telescope) with high time-resolution capabilities.

High-resolution timing is very important because it allows disentangling the magnetospheric emission from other possible sources, such as thermal emission from the neutron star surface/atmosphere or a circumstellar (fall-back) disk, which could be left after the supernova explosion. The non-thermal emission is usually strongly pulsed and polarized while the other two mechanisms are expected to produce weakly pulsed or unpulsed emission.

Broadband coverage is also important. In middle-aged neutron stars, thermal radiation is expected to dominate over the magnetospheric component at shorter (ultra-violet) wavelengths, while the circumstellar disk emission (if present) and magnetospheric should dominate in the near-infrared. The former has been fairly well established in rotation-powered pulsars using *HST*

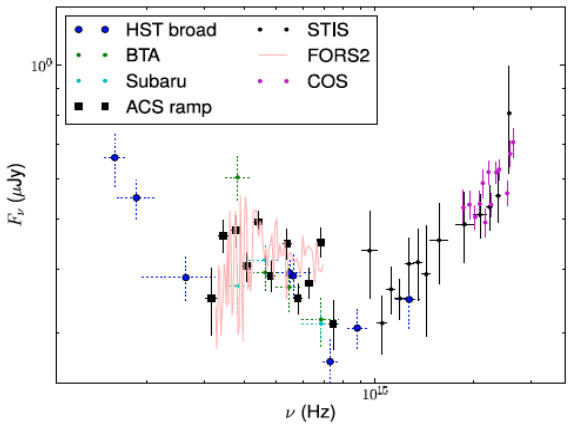

Figure 9 - Ultraviolet-to-near-infrared spectrum of pulsar B0656+14 (Durant et al. 2001, ApJ, 735, 33).

(Kargaltsev & Pavlov 2007, ApJ, 670, 655), while the latter could be an explanation for the complex spectrum of the nearby pulsar B0656+14 (see Figure 9). Sensitivity, high time resolution, and polarization measurement capabilities, can allow discrimination between various scenarios and advance our understanding of physics of matter in very strong magnetic fields. There is also some evidence for spectral features in pulsars (Durant et al. 2011, ApJ, 735, 33) and possibly in radio-quiet isolated neutron stars (Kaplan et al. 2011, ApJ, 736, 117), which can be studied with low-resolution spectroscopy (or even narrow-band photometry) provided high sensitivity of the instrument and telescope. Solidifying the so far tentative evidence for spectral features in isolated neutron stars is important, because it can provide direct measurements of the neutron star magnetic fields, and probe the state and composition of the neutron star surface layers and the full range of masses for neutron stars. The sensitivity and field of view of an instrument like OCTOCAM can also be used to detect diffuse emission from pulsar-wind nebulae, which are also, so far, primarily observed at X-ray and radio wavelengths. If available, Integral Field Spectroscopy can be used to detect binaries with non-accreting neutron stars and black holes, and to measure the 3-dimensional flow velocities in the H-alpha bow shocks around pulsars.

About 25 isolated neutron stars have been detected in the ultra-violet, optical or near-infrared. With an instrument like OCTOCAM it will be possible, for the first time, to perform phase-resolved photometry of these objects in the 400-2,350 nm range. This will allow us to study the connection between the optical/near-infrared and X-ray/gamma-ray emission, to shed light on the physical origin of optical-to-near-infrared emission, and to constrain properties of neutron star magnetospheres and atmospheres. For isolated neutron star studies, the critical parameters are time resolution (requiring ~10 milliseconds, but better resolution will allow us to study more pulsars), high sensitivity, and broad wavelength coverage. Having a high-throughput polarizer would be also very helpful for the isolated neutron star science, as long as it does not come at the price of one of the earlier mentioned instrument characteristics. Isolated neutron star studies with OCTOCAM will be complementary to those performed with *JWST* in the infrared, *Athena* in X-rays (highly prioritized ESA mission with a projected launch in 2028) and *WSO-UV* in the ultra-violet (joint Russian-Spanish telescope to be launched in 2017).

1.3.9. Magnetars

Determine the magnetar emission origin and mechanisms (de Ugarte Postigo, Kaplan, Kouveliotou, van der Horst, Wachter)

Magnetars are young, isolated, slowly rotating, neutron stars with extreme surface magnetic fields (dipole fields of 10^{13} –10^{15} G). Their X-ray luminosities by far exceed the rotational energy (spindown power), leading to the assumption that their bright X-ray emission is powered by their extreme field decay. Moreover, they are known to emit short X-ray bursts (of the order of 0.1 seconds) in random active episodes that may last up to ~100 days. Historically, two distinct types of neutron stars have been recognized as magnetars: Soft Gamma Repeaters (SGRs) and Anomalous X-ray Pulsars (AXPs); however, the class has increased to encompass dim isolated neutron stars, rotationally powered pulsars, and central compact objects. These sources are usually characterized by *(i)* relatively long spin periods clustered in a narrow range (2-12 s), *(ii)* large spin-down rates, *(iii)* bright persistent X-ray emission, and *(iv)* bursting behavior in hard X-rays/soft gamma-rays (for reviews, see Woods & Thompson 2006, ISBN 9780521826594; Mereghetti 2008, A&ARv, 15, 225).

The prevailing magnetar model postulates that they have super-strong surface magnetic fields (10^{13}-10^{15} G), and even stronger interior fields (up to 10^{16} G), whose decay powers both the persistent X-ray emission and their bursts (Duncan & Thompson 1992, ApJ 392, L9; Kouveliotou et al. 1998, Nature, 393, 235). These are mostly studied in the X-ray and soft gamma-ray regime, but they also emit radiation in other parts of the electromagnetic spectrum. Four out of the ~28 known magnetars have counterparts at radio wavelengths (Gaensler et al. 2005, Nature, 434, 1104; Camilo et al. 2006, Nature, 442, 892; Camilo et al. 2007 ApJ, 666, L93; Shannon & Johnston 2013, MNRAS, 435, L29), and a few more in near-infrared and/or optical bands (Wachter et al. 2007, Ap&SS, 308, 67). All magnetars in the Milky Way reside on the Galactic plane, in crowded regions with high extinction, which makes optical detections difficult and the near-infrared more suitable for observing them. Therefore, only three of them have been found in the optical (Hulleman et al. 2000, Nature, 408, 689; Durant & van Kerkwijk 2005, ApJ, 627, 376; Dhillon et al. 2011, MNRAS, 416, L16), but seven magnetars have near-infrared counterparts (e.g., Hulleman et al. 2001, ApJ, 563, L49; Wang & Chakrabarty 2002, ApJ, 597, L33; Hulleman et al. 2004, A&A, 416, 1037; Israel et al. 2004, ApJ, 603, L97; Israel et al. 2005, A&A, 438, L1). In four of these sources, near-infrared or optical pulsations have been found with the same period as measured in the X-rays (Kern & Martin 2002, Nature, 417, 527; Testa et al. 2008, A&A, 482, 607; Dhillon et al. 2009, MNRAS, 394, L112; Dhillon et al. 2011, MNRAS, 416, L16).

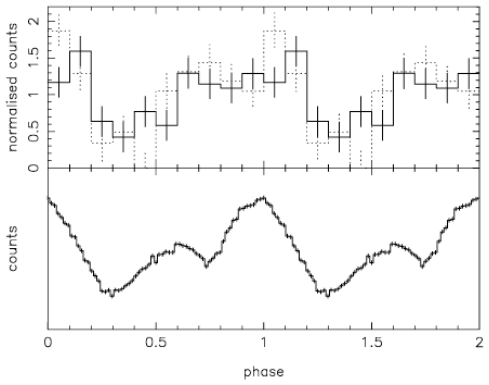

Figure 10 - Optical (top) and X-ray (bottom) pulse profile of a magnetar (Dhillon et al. 2005, MNRAS, 363, 609) with a typical spin frequency of ~0.1 Hz.

Optical or near-infrared spectroscopy of magnetar sources has not been systematically performed, and the study of possible lines is thus unexplored territory. Moreover, while there are many good quality data sets to study their emission mechanisms at X-ray energies, there are very few well-sampled spectral energy distributions in the optical-to-near-infrared regime to determine the origin of that emission. The high time

resolution capabilities of an instrument like OCTOCAM are crucial for studies of optical pulse profiles, pulsed fractions and optical-to-X-ray pulse lags. Unfortunately, the existing simultaneous optical/near-infrared and X-ray observations enabling such studies give varying results: in some cases the pulsed fraction is larger in the X-rays than in the optical and there is no significant lag, suggesting a magnetospheric origin of the optical/near-infrared emission (Figure 10; Kern & Martin 2002, Nature, 417, 527; Dhillon et al. 2005, MNRAS, 363, 609; Dhillon et al. 2011, MNRAS, 416, L16); in other cases the optical/near-infrared pulsed fraction is lower than the X-ray one and there is a lag, suggesting reprocessing, possibly in a disk (Dhillon et al. 2009, MNRAS, 394, L112). High time resolution observations would obtain a larger sample of high-quality broadband optical-to-near-infrared spectral energy distributions during magnetar outbursts, and constrain their emission origin and mechanisms.

1.3.10. Interacting Binaries

Study the physics of accretion streams and disks (Angeloni, Orosz)

Rapid photometric variability (hereafter simply flickering) as a result of accretion processes plays an important role in astrophysics at basically all spatial scales, from proto-planetary systems to binary stars, up to galaxy clusters. The associated phenomenology shows a wide range of time-dependent behavior, whose systematic investigation at the shortest time scales has so far been constrained predominantly by detector development and capabilities, more than by the underlying science. High time resolution astrophysics therefore represents an exciting research field for the next decade of fore-front science (see, e.g., Shearer et al. 2010, arXiv:1008.0605).

Generally speaking, we know that accretion processes are an expression of turbulence at work. In this sense, the fast variability arising from quite a heterogeneous group of astronomical systems (e.g., cataclysmic variables, X-ray binaries, young stellar objects, proto-planetary disks, etc.) can be seen as the result of turbulence in the accretion stream and/or disk. Even if flickering has no specific pattern, one expects the longer-lasting fluctuations to have larger amplitudes, simply because the turbulent motion in a larger eddy of the stream occurs on longer timescales, and thus emits more light. Flickering is a powerful diagnostic of nuclear burning processes, and the characterization of any coherent short periodicity in the light curve could bring valuable

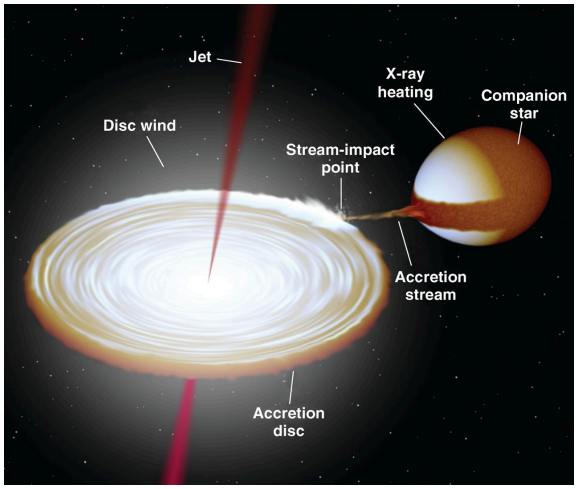

Figure 11 - An artist's impression (R. Hynes, Lousiana State University) of an interacting binary star: the hot spot, the accretion stream and the accretion disk, where the flickering likely arises from, are clearly recognizable.

information on a range of poorly studied magneto-hydrodynamic phenomena, for instance by uniquely constraining the modeling of gas/magnetic field interactions and the physics of accretion streams and disks (Figure 11).

We emphasize that even if flickering studies on a few bright objects date back to the 1990s (e.g., Bruch 1992, A&A, 266, 237), virtually no systematic study on the spectral energy distribution of this rapid photometric variability has been performed so far. Today, when multi-band information has to be gathered, the only solution is to observe the same target simultaneously with multiple telescopes. For instance, the cataclysmic variable AE Agr was monitored with 4 different telescopes to correlate the colors of the recorded flickering with the system physical parameters, e.g., the mass transfer rate and the size of the white dwarf magnetosphere (Zamanov et al. 2012, AN, 333, 736). It has also been suggested that simultaneous multi-wavelength observations would be fundamental in assessing the magnetic character of the accreting star (Zamanov et al. 1999, ASPC, 169, 337), opening a new research line where detailed theoretical modeling unfortunately does not have a parallel observational effort aimed at collecting systematic and comparable data sets.

An instrument like OCTOCAM, able to take eight simultaneous images at subsecond time intervals, when mounted on an 8-meter class telescope like Gemini, would open the way for a systematic panchromatic study of rapid variability phenomena at much faster and smaller (milli-magnitude level) scales than what is currently possible. It will allow astronomers not only to perform fast multi-band photometry on a much larger sample of objects, by monitoring very faint targets, but also to include in these investigation new classes of possible astrophysical flickerers, most notably novae and supernovae, usually not expected to show rapid flux variations (Schaefer, 2010, AAVSO Alert Notice #495), but also not studied in detail with a fast imaging instrument on short timescales.

1.3.11. Millisecond Pulsar Binaries

Constrain the equation of state of neutron stars by determining their maximum mass (Dhillon)

The primary motivation for studying neutron stars lies in their extreme physical conditions, since they possess densities equal to that found in atomic nuclei. One of the key outstanding questions is: what is the equation of state of neutron stars? The equation of state is the relationship between the density and pressure of the degenerate neutron gas and it determines the structure of the star. The equation of state of neutron stars is inaccessible to laboratory measurements and lies in a regime of great theoretical uncertainty. The best probe of the equation of state, and hence which flavor of exotic physics is correct, would be a simultaneous measurement of the mass and radius of a neutron star. Unfortunately, the prospect of making such a measurement is poor, and we must resort to other methods, one of which is to determine the maximum neutron star mass. Given that each equation of state predicts a different maximum neutron star mass, finding neutron stars with masses above these limits can rule out whole families of theoretical models, as well as delineating the lower mass limit of stellar mass black holes (currently believed to be around 3 solar masses).

To increase the chance of pinning down the equation of state, we have to find the most massive neutron stars. Evolution in a binary system offers the possibility to increase neutron star mass via accretion, in which case one would also expect the transferred angular momentum to spin up the neutron star to millisecond rotation periods. Hence the most massive neutron stars might be expected to reside in the binary millisecond pulsars, which are believed to be old pulsars, which were originally slowly rotating but have been spun up by mass transfer, typically from a low mass companion star.

The current record holder for the highest secure neutron star mass is indeed a binary millisecond pulsar: PSR J0348+0432 (Antoniadis et al. 2013, Science, 340, 448). Its mass, 2.01+/ 0.04 solar masses, was measured using a combination of pulsar radio timing and optical observations (photometry and spectrometry) of the companion star. This type of binary system is sometimes referred to as a black widow pulsar, since the neutron star is destroying its companion, offering a potential advantage for mass determination. Their optical light curves are often dominated by the low-mass companion star, and exhibit variability due to a combination of its ellipsoidal shape and irradiation of its inner hemisphere. By fitting multi-band light curves with a model, it is possible to determine the orbital inclination and the Roche-lobe filling factor. Combining this with the radial velocity curve of the companion and the pulsar timing orbit, it is then possible to reliably determine the neutron star mass (e.g. Figure 12; Romani et al. 2015, arXiv:1506.04332).

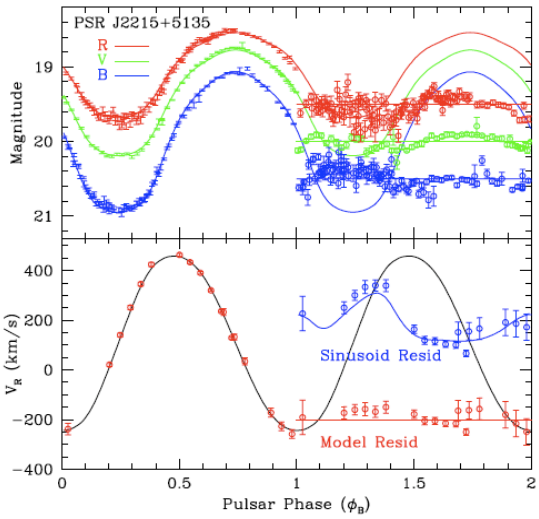

Figure 12 - Fast optical photometry (top) and radial velocity (bottom) of a millisecond pulsar system (Romani et al. 2015, arXiv:1506.04332). The first period shows the data and model; the second period the residuals after removing the best fit model that gives the neutron star mass.

This kind of work requires access to a high-speed, multi-band instrument on the world's largest telescopes, and many black widow pulsars need to be observed to reliably constrain the mass distribution. The availability of an instrument like OCTOCAM for Gemini would place us in a strong position to find the most massive neutron stars in our Galaxy.

1.3.12. X-Ray Binaries

Obtain new insights into accretion physics near the black hole event horizon and properties of jets (Bauer, Bayless, Corral-Santana, Curran, Hintz, Muñoz-Darias, Orosz, Wachter)

X-ray binaries are powered by accretion of matter onto a compact object such as a black hole or a neutron star. They allow us to study relativistic effects in strong gravity, particle acceleration at extreme velocities and, in the case of neutron stars, the structure and behavior of matter at the highest densities and strongest magnetic fields. They also provide dynamical determinations of compact objects masses and, in particular, the best evidences for the existence of stellar-mass

black holes. X-ray binaries are intrinsically broadband sources, and a broad optical-to-near-infrared coverage of these sources is of unique importance given the multiple sources of emission (relativistic jet, accretion disk and companion star) that can be simultaneously studied (e.g., Curran et al. 2012, A&A 547, 41; Russell et al. 2014, MNRAS 439, 1390; Figure 13). The science that can be done with an instrument like OCTOCAM will have a high impact on research lines related to *(i)* accretion physics *(ii)* mass measurements of compact objects, and *(iii)* characterization of new transient events.

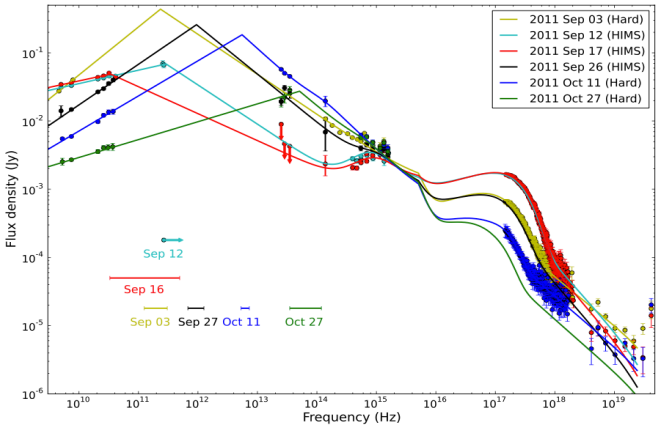

Figure 13 - This plot from Russell et al. (2014, MNRAS 439, 1390) demonstrates the importance of broadband observations when interpreting X-ray binaries. The near-infrared and optical regime is particularly important as it is here that we have multiple sources of emission (relativistic jet, accretion disk, companion star and reprocessing of X-rays) that need to be disentangled before the system is understood.

Emission from regions close to the compact object is highly (>30%) variable at minutes to sub-second timescales, and therefore simultaneous observations at multiple bands are required to produce constraining spectral energy distributions. Simultaneous observations with 100 millisecond temporal resolution will allow us to cross-correlate the optical/near-infrared data with itself and with simultaneous X-ray observations obtained from satellites, giving important information about the relationship between the inflow onto the compact object and the outflow of matter (see, e.g., Fender & Muñoz-Darias 2015, arXiv:1505.03526). Recent work has shown clear cross-correlations between the near-infrared and X-ray bands, probing the emission regions very close to the central black hole (Casella et al. 2010, MNRAS 404, L21). However, no current or planned instrument, except for OCTOCAM, allows a cross-correlation across the optical-to-near-infrared bands. Timing observations at X-ray frequencies forms much of the basis of our understanding of X-ray binaries (e.g., van der Klis 2003, in Compact Stellar X-ray Sources) and, when applied to the optical/near-infrared, may well revolutionize our understanding of the inflow-outflow relationship and of the level of X-ray reprocessing.

An instrument like OCTOCAM will also allow us to measure the mass of the central compact object through radial velocity and simultaneous multi-band optical-to-near-infrared studies. The latter capability, almost unique in an 8-meter class telescope, is fundamental, since it enables to unambiguously determine the accretion flow contribution to the companion star emission, which dominates the mass error budget through uncertainties in the orbital inclination (see Casares & Jonker 2014, in Space Science Reviews, arXiv:1311.5118). Broadband observations with an instrument like OCTOCAM will contribute to solve an open problem in the field: the tentative presence of a mass gap (3 to 5 solar masses) in the mass distribution of black holes and neutron stars, which

have strong implications for the supernova emission mechanisms (see Belczynski et al. 2012, ApJ, 757, 91).

Finally, in the next decade the number of transients, many of them powered by accretion, will increase significantly as more are detected by the upcoming LSST optical telescope, the *eROSITA* X-ray mission, and the Square Kilometer Array (SKA) radio telescope and its precursor instruments, ASKAP and MeerKAT. These new transients will require multi-wavelength follow-up to identify counterparts, measure distances and understand the possible new classes of objects. An instrument like OCTOCAM, using Gemini's target-of-opportunity capabilities, will be ideal due to simultaneous, multi-band observations over a field of view that will cover the error regions of most instruments. The proposed spectral capabilities of OCTOCAM and Gemini's light-gathering abilities will allow us to study the spectral features of dim sources, into the near-infrared, and hence directly measure properties of the accretion disk and the environment of the transients (e.g. Charles & Coe 2003, arXiv:8020, in Compact Stellar X-ray Sources), which is an important diagnostic to identify the progenitors.

1.3.13. Supernovae

Probe explosion physics and evolution of dust in the Universe; and further constrain cosmological parameters (Bauer, Bayless, Bauer, Bersten, Cenko, Folatelli, Fox, Galbany, Perley, Roming, Schmidt, Schulze, Thöne)

Despite significant progress in the supernova (SN) field over the past few years, near-infrared observations of SNe remain sparse. The lack of data is further perpetuated by the dearth of easy access to near-infrared instrumentation. Not only does Gemini allow for rapid-response, queue-based target-of-opportunity observations, but an instrument like OCTOCAM will offer simultaneous multi-wavelength observations that will coincide with other large missions, including LSST, *WFIRST* and *JWST*. Here we describe some of the key SN topics that will be probed by the next generation of optical-to-near-infrared observations of SNe, and the role Gemini can play.

Interacting SNe: In some cases, SNe may explode within a dense circumstellar medium. This pre-SN mass-loss history can serve as a direct probe of the late stages of the progenitor star's evolution and evidence of possible binarity (see Figure 14). Such interaction is also thought to power a portion of the new class of super-luminous supernovae. Early (<100 day) spectra of interacting SNe are dominated by emission lines and continuum generated by the interaction itself, so little is known about the underlying progenitor and explosion mechanism. As the interaction with the circumstellar medium subsides, the inner SN ejecta material is revealed, but by that point the radioactive ejecta have faded

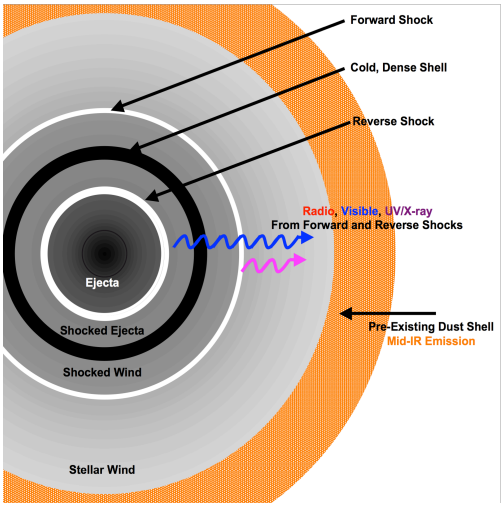

Figure 14 - Various electromagnetic emission sources in the circumstellar environment of SNe with dense pre-SN winds (adopted from Fox et al. 2010, ApJ, 725, 1768).

below the sensitivity thresholds of most telescopes. (Near-)infrared spectra are less susceptible to extinction by the dense circumstellar medium, particularly at late times (Fox et al. 2013, AJ, 146, 2; Fox et al. 2015, MNRAS, 447, 772). Low-resolution optical-to-near-infrared spectroscopy on big glass such as Gemini will build the sample size by pushing such late-time studies out to larger distances and later epochs.

Dust Characteristics: SN dust may be newly formed or pre-existing due to pre-SN mass loss and/or eruptions, which offers important clues regarding the SN progenitor and/or evolution of dust in the Universe. Dust is most commonly observed in Type IIn SNe (a subclass with narrow emission lines created by a slow-moving, dense circumstellar medium), but has also been found in other core-collapse SNe, and even in thermonuclear SNe Ia. The near-infrared is the most sensitive wavelength range to warm dust, but little is actually known about the dust composition and grain sizes. Only a single mid-infrared spectrum of a SN IIn exists to date (Fox et al. 2010, ApJ, 725, 1768), and the only direct quantization of SN dust grain size growth comes from simultaneous optical-to-near-infrared spectra obtained with VLT/X-shooter (Gall et al. 2014, Nature, 511, 326). An instrument like OCTOCAM will make more of these observations possible.

SN Hubble Diagram: Thermonuclear Type Ia SNe serve as a cornerstone for measurements of dark energy. Recent observations suggest that SNe Ia are likely superior distance indicators in the near-infrared since they are less affected by corrections for dimming by dust. A near-infrared Hubble diagram will offer the potential to constrain dark energy models. Efforts are already underway using observations with RATIR (Johansson et al., in prep.) and Gemini/NIRI (Barone-Nugent et al. 2012, MNRAS, 425, 1007; see Figure 15). With simultaneous imaging in multiple filters and state-of-the-art detectors, an instrument like OCTOCAM has a significant advantage over Gemini/NIRI and can push the redshift limit even further with more efficient integration times.

Furthermore, it has been proposed that differences in the host properties of SNe Ia, such as the mass, the age, the star formation rate, or the metallicity, could explain the observed second order heterogeneity in Type Ia light curves. With a spectral range of 370-2350 nm, OCTOCAM will be well suited to study many of these properties (e.g., oxygen abundance via emission line spectroscopy) over a wide range of redshifts. An image slicer as a mini-IFU would serve as a survey of SN host galaxies at high redshifts.

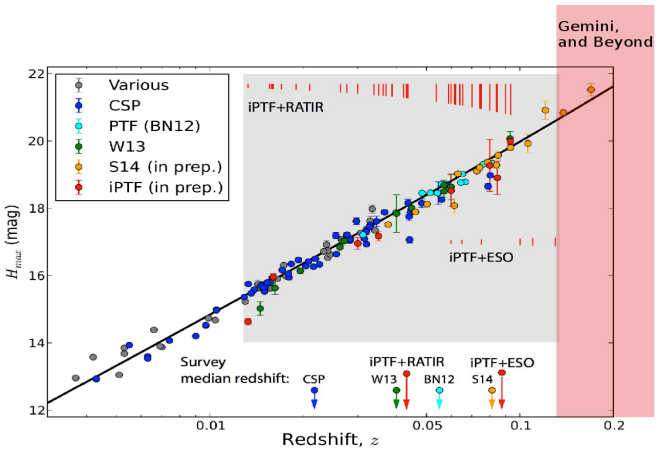

Figure 15 - State-of-the-art H-band near-infrared SN Ia Hubble diagram using a composite of data, including preliminary analysis of 35 SNe observed with RATIR (grey box) from 2013–2014 (Johansson et al., in prep.) and Gemini (light blue circles).

Along these lines, core-collapse Type II SNe show potential to be standardized in a similar manner as SNe Ia (Rodriguez et al. 2014, AJ, 148, 107). With well-sampled color curves, the corrected magnitudes (and hence distances) are comparable (1-3%) to current limitations of SN Ia cosmology. With simultaneous multi-band photometry, an instrument like OCTOCAM will allow us to build a uniform database of high-quality Type II SN light curves, thereby providing an independent method for measuring distances across a substantial portion of redshift space. Since this method has different systematics than SNe Ia, the resulting analysis will offer important constraints on achieving better than 1% accuracy on cosmological parameters by utilizing multiple methods.

Supernova shock-breakout detection: The first light from a SN emerges once the shock breaks out from the stellar surface and can offer important clues about the explosion physics (Soderberg et al. 2008, Nature, 453, 469). The breakout duration, however, is very short (less than 3 hours) and typically not detected by SN searches, which have cadences of a couple of days. The High-cadence Transient Survey (HiTS) is currently scanning 40 deg^2 in the g-band with the 4m Blanco Telescope/DECam instrument to search for very young SNe and to detect their shock breakouts. Fast data reduction allows the detection of such objects in real time (less than 3 minutes after the observation). When a good candidate is triggered by the software, a spectrum is needed to determine the type of the SN and, for very young events, to study the properties during the shock-breakout phase. Bersten et al. (2014 AJ, 148, 68) and Gal-Yam et al. (2014, Nature, 509, 471) have shown that spectra obtained hours after the explosion contain crucial information about the progenitor star and the mass-loss rate before the explosion. With Gemini's quick-response capabilities, an instrument like OCTOCAM would be ideal to follow up such early-time detections.

1.3.14. Supernova Remnants

Probe progenitors and dust evolution in supernova environs (Fesen, Pannuti, Lee)

The studies of extragalactic supernova remnants (SNRs) have entered an exciting new phase of study in modern astrophysics. SNRs are intimately associated with the evolution of the interstellar media of galaxies through the deposition of vast amounts of kinetic energy and chemically enriched material into the ambient medium. In addition, detailed observations of SNRs provide a path to investigate the final stages of massive stellar evolution, which remains a facet of stellar evolution that remains poorly explored by observations and poorly constrained by theoretical models. Finally, SNRs have emerged as the leading candidates for the accelerators of cosmic-ray particles to at least the so-called knee of the cosmic-ray energy spectrum. Taken together, a thorough understanding of the interstellar medium of galaxies cannot be realized without a complete and thorough understanding of the evolution of SNRs and related processes.

Observations of Galactic SNRs are hampered by such obstacles as considerable uncertainties in the distances to these sources, extinction along Galactic lines of sight, and the inability to survey effectively the whole Galactic disk for SNRs. Studies of extragalactic SNRs help address these difficulties through targeting of galaxies located at high Galactic latitude with nearly face-on orientations to minimize both Galactic and internal absorption effects. Furthermore, the whole disk of a galaxy may potentially be surveyed for SNRs rather than a small portion

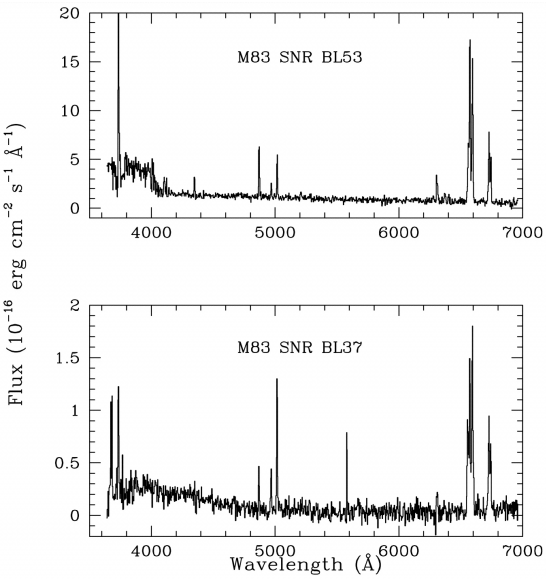

Figure 16 - One-dimensional optical spectra for two SNR candidates in the nearby face-on spiral galaxy M83 (Blair & Long 2004, ApJS, 155, 101). Notice the spectral lines at 6532 Å (corresponding to Hα), 6717 Å and 6731 Å (corresponding to the [SII] doublet).

(in the case of the Galaxy, only the immediate neighborhood around the Sun). Optical observations of extragalactic SNRs (imaging and spectroscopy) have typically led this particular field of study (see Matonick et al. 1997, ApJS, 113, 333; Matonick & Fesen 1997, ApJS, 112, 49), but tremendous advances in the sensitivity and angular resolution attained at complementary wavelengths at which searches for extragalactic SNRs are conducted, have permitted remarkable gains in our understandings of these sources in particular and SNRs in general. Specifically, the commissioning of X-ray observatories like *Chandra* and *XMM-Newton,* and radio observatories like the Jansky Very Large Array, have provided the right combination of sensitivity and angular resolution that may complement in a rigorous manner optical observations of extragalactic SNRs. Examples of nearby galaxies that have been the targets of deep imaging searches for SNRs (along with complementary spectroscopic observations of these sources) include M33 (Long et al. 2010, ApJS, 187, 495), M83 (Blair et al. 2012, ApJS, 203, 8) and M101 (Franchetti et al. 2012, AJ, 143, 85). As a result of these searches, the number of known extragalactic SNRs is approximately 800 (Pannuti et al. 2015, in prep.), nearly four times the number of known Galactic SNRs (Green 2014, BASI, 42, 47).

Spectroscopic observations of extragalactic SNRs with an instrument like OCTOCAM hold the potential to provide a large step forward in our understanding of properties of these sources. With high angular resolution that will be necessary for resolving confusing diffuse emission in the regions where extragalactic SNRs are often observed (such as the presence of adjacent HII regions), OCTOCAM observations will help to clearly detect spectral lines for which crucial density and velocity diagnostics that are important for probing the plasma conditions and the conditions of the ambient interstellar medium. For example, in the cases of particularly young SNRs (with ages ranging from approximately 200 to 500 years), spectroscopic observations made by an instrument like OCTOCAM will yield precise estimates of intermediate mass and iron peak elemental abundances. Furthermore, the sensitivity and spectral resolution capabilities at optical and infrared wavelengths of such an instrument will permit the extraction of spectra at multiple positions within targeted SNRs. This combination of spatial and spectral resolution will facilitate the study of 3-dimensional structures of SNRs, and the dynamics and chemistry of ejected and swept-up material. The study of these structures will help probe the conditions of the ambient interstellar medium prior to the supernova event (such as the amount of stellar mass loss and the role played by stellar winds), and the dynamics of dust evolution within the environments of SNRs; specifically, the

processes of dust grain formation and destruction within these environments, and important clues on whether SNRs are net creators or destructors of dust grains.

Prior optical spectroscopic observations of extragalactic SNRs have yielded crucial trends in the global properties of sources within a particular galaxy. For example, Blair et al. 2012 (ApJS, 203, 8) identified a total of 225 SNRs in M83 and noticed the large number of SNRs with associated strong [OIII]/Hβ emission, a ratio that is closely associated with high velocity shocks propagating through the insterstellar medium of a galaxy (see Figure 16). The detection of so many SNRs with such high-speed shocks has crucial bearings on our understanding of the interaction between populations of SNRs in a galaxy and cosmic-ray acceleration within the disk of the galaxy. To date, the typical spectral resolution attained by observations of extragalactic SNRs has been fairly modest. New spectroscopic observations of other extragalactic SNRs, which can be realized by observations with an instrument like OCTOCAM, will dramatically increase our ability to both obtain high-resolution spectra of large samples of extragalactic SNRs.

1.3.15. Gamma-Ray Bursts

Explore the Universe up to the very beginning of stellar formation, within the epoch of reionization (Butler, Cenko, de Ugarte Postigo, Fox, Kouveliotou, Perley, Roming, Schulze, Tanvir, Thöne, Vanden Berk, van der Horst)

Gamma-ray bursts (GRBs) are among the most powerful explosions in the Universe, and can be separated into two classes based on the duration and spectral properties of their gamma-ray emission. GRBs from the largest class, the so-called long GRB, are associated with core-collapse supernovae (e.g. Hjorth et al. 2003, Nature, 423, 847; Woosley & Bloom 2006, ARA&A, 44, 507) and found up to high redshifts (the most distant spectroscopically confirmed GRB has a redshift of 8.2; Figure 17; Tanvir et al. 2009, Nature, 461, 1254; Salvaterra et al. 2009, Nature, 461, 1258). The nature of the GRBs in the second class, the short GRBs, is less well known, but a binary merger of two compact objects is the most likely candidate. In the fireball model (e.g. Rees & Mészáros 1992, MNRAS, 258, 41P) the brief prompt gamma-ray emission is produced by shocks within the ultra-relativistically expanding outflow and the longer lasting multiwavelength GRB afterglow originates from the interaction between the ultra-relativistic ejecta and the surrounding medium. The resulting spectra of the prompt gamma-ray emission and the afterglow then decay on different time scales. An instrument like OCTOCAM for Gemini will contribute to a large range of GRB topics relating to the physics of

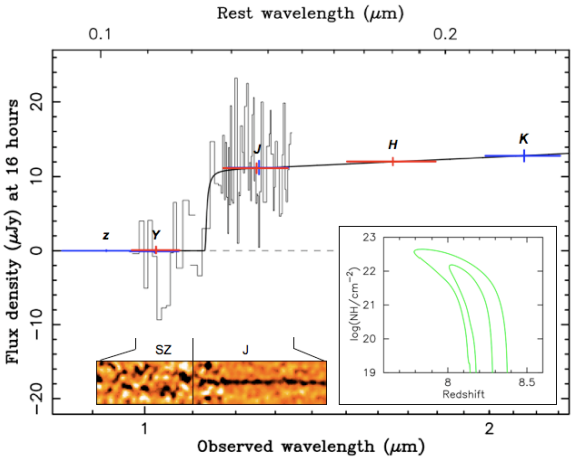

Figure 17 - Photometry and spectroscopy of the most distant spectroscopically confirmed GRB (Tanvir et al. 2009, Nature, 461, 1254). Besides the GRB redshift, the spectrum indicates there is little dust in the host galaxy, consistent with a low metal abundance.

GRB jets, their progenitors and their environments.

Gamma-ray burst follow-up: Gemini has the capability of rapid response observations for transient sources, which has led to some of the most high impact results from the Gemini observatory to date, also in the field of GRBs. Instrumentation-wise it has so far been limited compared to, e.g., the VLT, in terms of near-infrared spectroscopy and spectral resolution. An instrument like OCTOCAM will immediately solve this issue: simultaneous imaging in the optical and near-infrared allows us to efficiently identify and characterize the few high-redshift GRBs detected by gamma-ray satellites. Their detection is expected to increase in the early 2020s with the launch of the Chinese-French SVOM satellite with an onboard 45cm optical telescope sensitive to 950 nm. Any source not seen by this instrument will be a good candidate high-redshift event, and will require rapid ground follow-up with multi-band photometry (using the dropout technique) or spectroscopy into the near-infrared.

It has been calculated that the brightest GRBs and their afterglows should be visible at least to a redshift of 20 (e.g., Bloom et al. 2009, ApJ, 691, 723). The distribution of GRBs in redshift can be inverted to infer the high-redshift cosmic star formation rate density (assuming that at above a redshift of 4, GRBs are unbiased tracers of star formation; e.g., Robertson & Ellis 2012, ApJ, 744, 95). Deep searches for their host galaxies has already established that the majority of all star formation at redshifts above 6 is taking place in galaxies below the deepest *HST* limits (e.g. Tanvir et al. 2012, ApJ, 754, 46).

Short time-scale variability: Both the prompt gamma-ray and broadband afterglow emission can show variability. Due to the short duration, the variability in the prompt emission is mostly restricted to the gamma-ray regime. However, some exceptional bursts emit gamma-rays up to an hour or more (e.g., Campana et al. 2006, Nature, 442, 1008; Rossi et al. 2011, A&A, 529, A142; Thöne et al. 2011, Nature, 480, 72) and provide the unique opportunity to monitor the prompt emission at all wavelengths. On the other hand, afterglow variability (for an example, see de Cia et al. 2011, MNRAS, 412, 2229) can be caused by *(i)* ambient density fluctuations (Wang & Loeb 2000, ApJ, 535, 788), *(ii)* velocity substructures in the jet (Mészáros & Rees 1998, ApJ 405, 278), *(iii)* inhomogeneities on the emitting surface due to angular-dependent ejecta (patchy-shell, Kumar & Piran 2000, ApJ, 535, 152), *(iv)* refreshed shocks formed by the collision between slower shells and the leading decelerating blast-wave (Rees & Mészáros 1998, ApJ, 496, L1; Sari & Mészáros 2000, ApJ, 535, L33), or *(v)* late-time engine activity (Rees & Mészáros 2000, ApJ, 545, L73).

An instrument like OCTOCAM will allow to advance significantly in studying variability at all scales: photometry in 8 bands from the optical to the near-infrared with a high time resolution and the large aperture of Gemini, together with rapid response mode capabilities, enables us to explore this uncharted territory for a large number of GRBs and provide crucial constraints on prompt emission and afterglow models.

Gravitational wave sources: One of the forefront areas of astrophysics over the next decade will be multi-messenger transient searches: taking advantage of the recently enhanced sensitivity of the Advanced LIGO and Virgo instruments coupled with dedicated rapid follow-up, may finally allow detection and

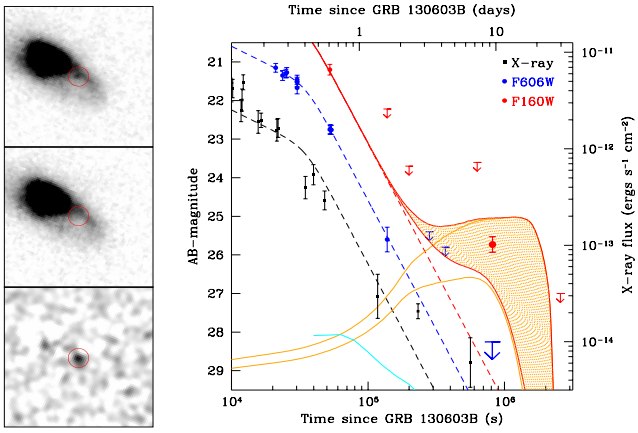

Figure 18 - Detection of near-infrared excess following a short GRB, consistent with expectations for a kilonova. The left panels show two epochs of HST imaging of the host (1 week and 1 month post burst) and the subtraction (bottom). The right panel shows the X-ray, optical and near-infrared photometry. The early light curve is dominated by the afterglow, but at late times the near-infrared (bold red point) is enhanced well above the afterglow extrapolation (hatched region shows a range of models from Barnes & Kasen 2013, ApJ, 775, 18).

characterization of astrophysical gravitational wave sources (see, e.g., Singer et al. 2014, ApJ, 795, 105). Such a multi-messenger detection would greatly enhance the scientific utility of such a discovery (e.g., Schutz 1986, Nature, 323, 310; Kochanek & Piran 1993, ApJ, 417, L17; Sylvestre 2003, ApJ, 591, 1152). The sources are expected to primarily be mergers of double neutron star binaries (although other systems are also possible), which will have a range of possible electromagnetic counterparts (Metzger & Berger 2012, ApJ, 746, 48). One of the most promising of these, and the only one to have been likely detected to date, is a so-called kilonova, arising from radioactive decay of highly neutron-rich ejecta (Li & Paczynski 1998, ApJ, 507, L59; Metzger et al. 2010, MNRAS, 406, 2650; Barnes & Kasen 2013, ApJ, 775, 18). One likely kilonova has been identified (Figure 18; Tangier et al. 2013, Nature, 500, 547), where a faint, red, transient source appeared 7 days after a short GRB. This near-infrared detection opens up a new electromagnetic window on this phenomenon, and does not rely on a preferred sightline, unlike the beamed gamma-ray emission from short GRBs. Therefore, kilonova signatures will be ideal for searches for electromagnetic counterparts to gravitational wave transients.

Follow-up of gravitational-wave events will present a number of challenges, related to the poor position localization and uncertainties in other parameters (e.g., Nissanke et al. 2013, ApJ, 767, 124). However, the ability of an instrument like OCTOCAM to rapidly assess the spectral energy distributions and time-domain evolution of possible optical/near-infrared transients, and to help figure out which (if any) is associated with a gravitational wave event, will be a significant advantage. For the initial science runs, sources are expected to be within 100 Mpc, which is considerably more nearby than most short GRBs. Therefore, we can expect an H-band magnitude of ~20, compared to H~25 mag for the only kilonova detected so far. Quickly distinguishing the red colors of kilonovae from other transients in the same large error region with the broad spectral response of an instrument like OCTOCAM, combined with its high throughput, makes it an ideal instrument for this purpose.

The interstellar medium at high-redshift: GRBs also serve to study the interstellar medium in their host galaxies at all redshifts by providing a background light source against which the absorbing gas and dust in the line-of-

sight can be observed. This allows us to study for instance abundances, kinematics, and ionization states. The shape of the continuum can also constrain the abundance and properties of dust along the line of sight. The availability of a flexible medium-resolution spectrograph is key to these studies. Accurate measurements of chemical abundances require a combination of wide wavelength coverage (to capture numerous transitions including Lyman-alpha) and a sufficiently high resolution to recognize saturated from unsaturated line profiles and investigate kinematics. The ability of an instrument like OCTOCAM to obtain the entire optical-to-near-infrared window at moderate resolution in a single observation is precisely what is needed for these types of studies. Particularly valuable are high redshift GRBs since they can probe the first galaxies and stars in the Universe, and also the end of the epoch of reionization. The huge demand for observations of this type with X-shooter on the VLT demonstrates the impact of such observations.

Characterization of high-redshift host galaxies: Long and short GRBs seem to be hosted in different types of galaxies, hence fully understanding their nature requires observations of their hosts when the afterglow has faded away. Host galaxy observations can provide clues on the stellar populations in long and short GRB host galaxies, provide evidence of kicks ejecting the progenitor from its birth site prior to explosion, enable searches for associations with globular clusters, determine if variables such as metallicity or stellar density affect the GRB cosmic rate, and if we can use long GRBs to constrain the global star formation rate density and population of star-forming galaxies in the early Universe, all the way into the epoch of reionization.

These investigations require observations of host galaxies in many different bands: the rest-frame ultra-violet to characterize the young stars, the rest-frame optical/near-infrared to measure the abundance of more mature stars and model the star-formation history; as well as spectroscopic observations to determine emission line based metal abundances (which cover a wide redshift range and, critically, shift into various near-infrared bands for redshifts above 0.5). Traditionally, this has been a highly time-consuming process. An instrument like OCTOCAM will change this situation completely as the entire optical-to-near-infrared spectral energy distribution can be obtained with one shot, and additional spectroscopy over the entire range also with one observation only. Such an instrument would therefore permit large and comprehensive surveys of the host galaxy population of a variety of transients in a manner that is not possible at present. A small Integral Field Unit would perform resolved studies of the host characteristics and compare them with the actual GRB site.

1.3.16. Active Galactic Nuclei

Acquire fundamental clues on the role of supermassive black holes and their formation in galaxy evolution (Bauer, Butler, Haggard, Treister, Vanden Berk)

A fundamental trait of active galactic nuclei (AGNs) is the broad wavelength range of their emission, which can span radio to gamma-ray wavelengths. Much of this emission comes from a relatively small region, which leads to another defining property of AGNs: their variability. The latter is particularly strong in the rest-frame optical and ultra-violet, where it can reach ~1 magnitude on timescales ranging from hours to months and years. Furthermore, because AGNs

are so luminous, they can be studied at essentially all observable redshifts (up to redshift ~8). Hence, having broad wavelength coverage is critical for AGN science. Despite the fact that AGNs have been studied for nearly a century now, there is still much we would like to know, such as: how does accretion work in detail? How do jets work in detail? What is the (range of) structure in AGNs? How do AGNs grow (in conjunction with their host galaxies)? Can AGNs be used as standard candles?

The proposed capabilities of OCTOCAM will help address many of these questions. The very broad optical-to-near-infrared simultaneous coverage will allow variability studies of AGN that probe a large fraction of the accretion disk emission at once, as well as emission lines from the broad and narrow line regions. This is especially important for reverberation mapping to constrain the physical size of particular emission regions, measuring super-massive black hole masses, and ultimately determining the fundamental physical properties of these systems. The wide wavelength coverage will also guarantee that these observations can be carried out for systems over a broad redshift range.

Furthermore, the combination of the efficient spectroscopic capabilities of an instrument like OCTOCAM and the flexible scheduling of Gemini, in concert with other space- and ground-based observatories, will be critical for placing new constraints on emission mechanisms and localizing where the emission occurs via the reverberation mapping technique. While wide-field imaging and massively multiplexed spectrographs will sample the most typical systems, they are poorly suited for probing the rare systems that extend parameter space and provide the strongest constraints on physical models. In particular, rare high luminosity AGNs can account for ~60% of the total black hole accretion, and these are the systems where the most important AGN feedback effects are expected to take place, probably setting up the black hole – galaxy co-evolution. The flexibility and efficiency of an instrument like OCTOCAM will fill this niche, allowing us to study the most extreme objects in more detail and at higher cadences. For instance, well-sampled spectroscopic monitoring campaigns of quasar variability across a wide wavelength range have the potential to reveal not only super-massive black hole masses and orbital radii of emission line gas (e.g., Woo et al. 2010, ApJ, 716, 269; Barth et al. 2013, ApJ, 769, 128), but also the geometric, temperature, and ionization structure of the accretion disk and broad emission line regions. In addition, variability monitoring of quasars with narrow absorption lines will identify the highest velocity gas intrinsic to the quasars, and provide limits on the sizes of intergalactic gas clouds, and clouds in the halos foreground galaxies.

With a ~3'x3' field of view for the proposed OCTOCAM instrument, and assuming an AGN source density of ~7,000 sources per square degree, about 15–20 sources can be observed simultaneously in a single observation. This is a more than adequate number, in particular if different observing strategies are considered. For example, it will be possible to carry out revolutionary studies of all the ~500 AGNs detected in the Chandra Deep Field South, which covers a total area of ~0.1 square degrees. The Chandra X-ray coverage of this field is currently being extended to 7 Ms, and a total of ~700 AGNs is expected to be detected. It will be possible to cover the whole field with ~40 OCTOCAM fields, which can be done in as little as one hour (depending on the chosen cadence and

required exposure times), thus providing very dense time coverage to carry out the largest variability study of moderate luminosity AGN up to significant redshifts (of ~2).

All these studies will be highly complementary with currently existing and planned space-based X-ray missions, such as *NuSTAR*, *astro-H,* and further in the future, *Athena*. The synergy between an instrument like OCTOCAM and these X-ray missions will allow the determinations of the most important AGN parameters such as size, black-hole mass, and bolometric luminosity for a large number, hundreds to thousands, of typical moderate luminosity systems up to cosmologically relevant distances. This will then be used to properly determine how and when the super-massive black holes that we know are getting their phenomenal amounts of material via accretion. In turn, this will provide fundamental clues to our understanding of the role of super-massive black holes and their formation in galaxy evolution. For this, the simultaneous optical to near/mid-IR coverage of the proposed OCTOCAM instrument is critical.

Finally, optical to near-infrared Integral Field Unit spectroscopy would be unique among planned instrumentation in the 2020 era, and will allow extremely powerful studies of nearby jet-dominated AGNs (e.g., Jorstad et al. 2001, ApJ, 556, 738) and distant multiply lensed quasars (e.g., Morgan et al. 2010, ApJ, 712, 1129), where simultaneous coverage of the moderately sized regions (e.g., along the axis of flaring jets or across multiple lenses spanning a few arcseconds) is critical. Note that the VLT/X-shooter's 4"x1.8" area is generally a factor of a few too small for such studies (see Figure 19). Multi-wavelength coverage will allow novel constraints on emission mechanisms via spatial and temporal decoupling of the spectral components.

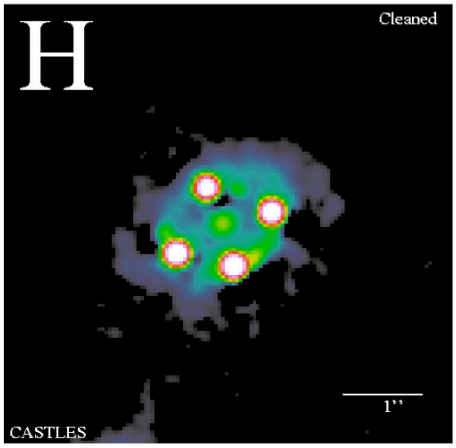

Figure 19 - HST image of a typical multi-lensed quasar (Claeskens et al. 2008, arXiv:0806.0567), which requires a large Integral Field Unit as proposed for OCTOCAM.

1.3.17. Tidal Disruption Events

Measure the mass and spin of supermassive black holes (Cenko, Tanvir, van Velzen)

One of the most recently discovered transient sources of emission are tidal disruption events (TDEs; Levan et al. 2011, Science, 333, 199; Bloom et al. 2011, Science, 333, 203), which occur when a star gets too close to a supermassive black hole and is pulled apart by the black hole's tidal forces (predicted by Rees 1988, Nature, 333, 523). Gemini's rapid target-of-opportunity follow-up capabilities will allow us to sample the early light curves, and provide unparalleled probes of the regions in close proximity to super-massive black holes, where general relativistic and black hole spin effects become dominant (Kesden 2011, Phys Rev. D., 85, 024037). TDEs will become commonplace in the era of LSST (Gezari 2009, ApJ, 698, 1367), and require dedicated observing programs with Gemini in order to extract maximal science from individual objects.

The spectroscopic features of TDE spectra are rich. So far, observations have shown that the luminosity, velocity and width of Hα, He, and coronal emission, all evolve with time (Komossa et al. 2008, ApJ, 678, L13; Arcavi et al. 2014, ApJ, 793, 38). Rapid spectroscopic follow-up of TDEs found by LSST (and near-future surveys such as the Zwicky Transient Factory) will enable us to probe the gas around quiescent supermassive black holes using reverberation techniques. Photometric sampling of the light curve by an instrument like OCTOCAM is important. First of all, the optical properties of TDEs form a unique locus: a blue and constant u-r color (van Velzen et al. 2011, ApJ, 741, 73, see Figure 20). Hence multi-epoch, multi-band photometric follow-up provides a means to discriminate TDEs found by single-band surveys from the much more frequent supernovae. Secondly, the rise time to peak is predicted to scale with the root of the black hole mass, hence well-sampled light curves may allow us to measure the mass of the black hole that disrupted the star. The properties of large TDE samples with deep, multi-band follow-up observations can be related to those of their host galaxies to address how super-massive black holes grow in relation to their hosts (Magorrian et al 1998, AJ, 115, 2285; Berti & Volonteri 2008, ApJ, 684, 822).

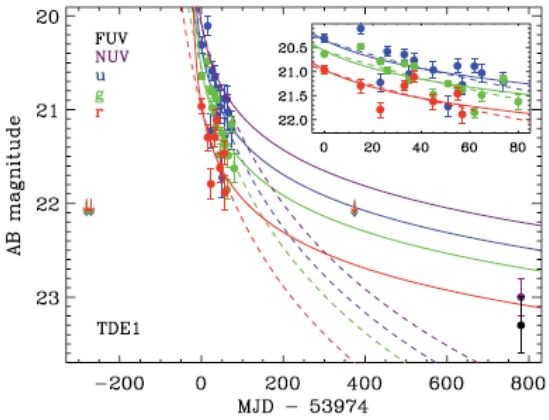

Figure 20 - TDE observations in several optical bands (van Velzen et al. 2011, ApJ, 741, 73) as a function of days after the observed peak.

Some tidal disruptions have been found by the bright non-thermal X-ray emission from a newly launched jet (Levan et al. 2011, Science, 333, 199; Bloom et al. 2011, Science, 333, 203). A big open question is why not every known TDE shows a similarly powerful jet (van Velzen et al. 2013, A&A, 552, 5); answering this question provides a fresh look at the old conundrum of quasar radio loudness (e.g., Kellerman et al. 1989, AJ, 98, 1195). Optical follow-up observations of jetted TDEs found by X-ray missions will be key to measure what fraction of the observed optical luminosity is due to the jet versus the thermal emission from the tidal debris. By measuring both the disk and jet component, one can estimate the fraction of accretion energy that is converted to jet power, which is a key parameter for models of black hole jets.

1.3.18. Galaxy Clusters

Shed light on the content of dark matter and the energy density of the Universe through lensing (Broadhurst)

The simultaneous multi-band imaging capability of an instrument like OCTOCAM will be of great support for using galaxy clusters to improve the precision of cosmological parameters. Lensing is achromatic, so optical-to-near-infrared photometry can provide the wide spectral range for securely identifying multiple images of a lensed object, and for assessing the richness of the lensing clusters from photometric membership. This will provide an essential complement to the limited imaging of *Euclid*, so that strong lensing can be properly examined with

the combination of high resolution monochrome *Euclid* images and deep broad color coverage.

We can envisage a substantial follow up of thousands of clusters in conjunction with *Euclid* and/or the LSST. The latter can provide limited color information and broadband imaging useful for weak lensing, and an instrument like OCTOCAM in combination with *Euclid* data provides optimized strong lensing; which when combined, gives the full radial mass profiles for a large survey of clusters selected with LSST/*Euclid*. This level of precision is not anticipated by any earlier survey, and can provide detailed lensing based cluster-mass profiles for thousands of clusters up to a relatively high redshift of 1.5.

The combination of strong and weak lensing provides the full logarithmic radial mass profiles (Broadhurst et al. 2008, ApJ, 685, L9) that has led to the successful CLASH program (Postman et al. 2010, ApJS, 199, 25), although limited to a few tens of clusters. It is clear that competitive constraints on cosmology are feasible with only a few hundred clusters (Mantz et al. 2015, MNRAS, 446, 2205). A current worry is the level of selection bias in these heterogeneously selected samples. X-ray selection is heavily relied on, and many of the clusters may be boosted in X-ray luminosity by ongoing mergers that compress and shock the cluster gas. The holy grail for this work is mass selection of clusters, by weak lensing surveys such as LSST or *Euclid*, where a few thousand massive clusters will bring a new level of precision for many important cosmological parameters.

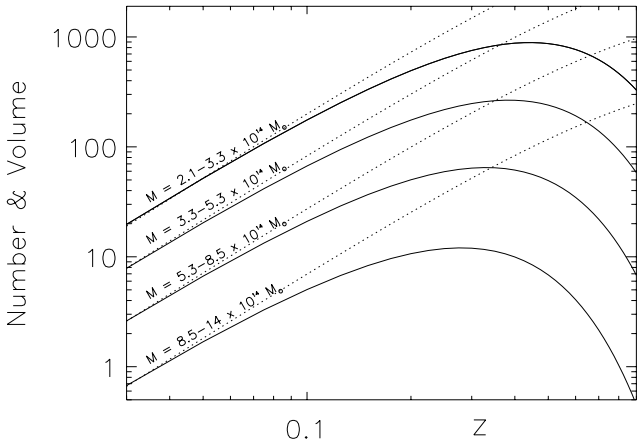

Figure 21 - Expected evolution of the number of clusters with redshift, compared to the volume, for a fixed area on the sky out to a redshift of 1. The rapid decline in the number density of clusters is greatest at higher mass and very sensitive to the growth rate of structure, which is not well constrained yet by current methods. This can be improved significantly by measuring lensing masses and multi-band photometry with an instrument like OCTOCAM.

Given the current lack of lensing selected samples, galaxy clusters still lag behind their potential to constrain cosmological parameters, dark matter components and testing General Relativity on large scales (Rapetti et al. 2011, PThPS, 190, 179). The number density of the most massive clusters of 10^{15} solar masses is expected to evolve by two orders of magnitude up to a redshift of 1 (Figure 21), providing a huge leverage on Ω_m and mass/richness bias estimation. The sensitivity of this growth rate to the relativistic neutrino density component may also be derived from the evolution of the cluster growth rate in this redshift interval, a parameter that has implications regarding the level of neutrino degeneracy and the general origin of matter/antimatter asymmetry (Huterer et al. 2015, APh, 23).

1.4. Science Requirements

Based on the science cases presented in the previous section, and the results of the science team surveys we have performed, we have established the science requirements for the different science cases. These requirements have resulted in technical requirements for OCTOCAM. Of course, not all the wishes of all the different scientists in the team could be met, especially given the large breadth of science topics and interests that our team is covering. Therefore, some trade-offs had to be made. In this process we have tried to accommodate as many different science cases as possible, but in some of the choices we have focused on those cases for which an instrument like OCTOCAM would be an extremely well suited instrument, i.e. those science cases that make optimal use of the unique combination of temporal resolution, spectral coverage for imaging and spectroscopy, and spectral resolution for spectroscopy.

Before discussing the prioritization we have done for the different capabilities of an instrument like OCTOCAM, we comment on two specific points that were part of our surveys: including the *u* band for imaging and spectroscopy, and the need for a fast response mode.

1.4.1. Including the *u*-Band

The original OCTOCAM proposal included *u*-band photometry, and spectroscopy down to 400 nm. However, the current coating of Gemini has a very low throughput in the blue wavelength range, which influences decisions on any kind of instrument designs. Given the science cases we cover, and possible future changes to the Gemini coating, we have asked our science team which particular science cases are mostly helped by including *u*-band photometry, and down to what wavelength spectroscopy should ideally be done. We have found that for the majority of science cases the *u*-band is not a necessity, although it could be useful. Most science team members preferred a good spectral resolution and continuous spectral coverage compared to including the *u*-band. Another consideration of a majority of the team members was that if a re-coating of Gemini harms the near-infrared portion of the spectral capabilities, they would prefer to have the current coating, because this is a unique feature of Gemini. However, we would like to point out the cases for which *u*-band photometry or pushing down the wavelength range for spectroscopy is relevant.

- Not directly related to any particular science case, but relevant for several of them, is the follow-up of transient sources discovered photometrically and/or spectroscopically with the LSST. For this one can argue that it is important to replicate as close as possible the specific photometric response of the LSST, which includes the *u*-band. The LSST is in fact one of the few large surveys to have a *u*-band filter. A characterization of certain transients in the *u*-band could therefore be particularly interesting for LSST science.
- The *u*-band is important for supernova dust extinction studies, since it is very much affected by dust extinction. Having the *u*-band together with the near-infrared bands can help studying extinction effects by comparing simultaneous photometric observations in all of these bands, but also by probing several lines in spectroscopy down to 370 nm.

- Tidal disruption events are very blue, and good photometric coverage in the blue bands, including the *u*-band, is useful for their characterization and distinguishing them from other transients, most notably supernovae.
- In the case of asteroseismology, the ultraviolet is useful for oscillation mode discrimination because of the behavior of the limb darkening coefficients. This requires photometry in the *u*-band, but not spectroscopy.
- Pushing down spectroscopy to short wavelengths is very useful for studying accretion in young stars, in particular for those that have complex and time-variable spectra across the optical and near-infrared. Simultaneous observations would allow for a calibration of different accretion indicators.
- For metal-poor stars the most relevant lines are situated below 400 nm, and spectroscopic coverage down to 370 nm would be crucial for this science topic.
- Fast variability in interacting binaries has much larger amplitudes in the near-ultraviolet than in the optical. As such, it is much more easily detectable in the *u*-band than in any other filter; the flickering amplitude reduces by an order of magnitude when moving from the *u*- to the *g*-band. At redder bands it becomes almost undetectable in most sources, also because other sources of emission become stronger than the compact star and/or the accretion disk, where the flickering most likely stems from.

1.4.2. Fast Response Mode

The science team has identified the timescales at which photometric and/or spectroscopic observations of transient sources should commence after the trigger provided by other facilities, at either optical or other wavelengths, to optimize the science output of an instrument like OCTOCAM. This can have implications for the operations of Gemini, in particular if a fast response mode would be required, either in an automated way or with a human in the loop.

The transient sources for which a response within one day would be sufficient are X-ray binaries and tidal disruption events. In both cases the outburst onset evolves over this timescale, and there is no large scientific gain by starting observations at an earlier time. This is also the case for most supernova science cases, although this has changed recently with the advent of *flash spectroscopy*. The latter captures the effects of the supernova shock breakout flash on material surrounding the star, in particular the stellar wind of the star that has just exploded. These kinds of observations enable unique studies of supernova progenitors. Another science topic that requires a response time within a few hours is magnetars, in which case the peak of the outbursts at X-ray/gamma-ray energies typically last a few hours, and capturing optical to near-infrared observations simultaneously could provide very valuable information on the mechanisms behind magnetar outbursts.

The shortest response times, at timescales of a few minutes, are preferred for gamma-ray bursts. For these timescales an automated fast response mode would be preferred. Observations within the first minutes would allow the study of several aspects in the early evolution of the gamma-ray burst jet, in particular pinning down the radiation processes that are also producing the prompt gamma-ray emission; the emission onset and dynamics of the shock at the head

of the jet; and the optical flash that is caused by the reverse shock traveling from the head back into the jet, enabling studies of the jet particle content and magnetic field structure.

1.4.3. Prioritizing Capabilities

Based on the two science team surveys, we have prioritized the core capabilities (multi-band imaging, multi-wavelength spectroscopy, time resolution) and added features (spectropolarimetry, Integral Field Unit spectroscopy) of the proposed OCTOCAM instrument. In Table 2 we give an overview of the importance of the different science capabilities, with scores from 1 (not important) to 5 (extremely important) per science topic. The motivations for the prioritization have been given in the discussions of the individual science cases. It is clear from the table that multi-band imaging and multi-wavelength spectroscopy are a high priority for almost all science topics. Time resolution is important for many of the science topics as well, in particular in the new era of time-domain astronomy. It can be seen from the table that adding spectropolarimetry and/or Integral Field Spectroscopy is very important for some of the science cases as well. Below we discuss some of the different capabilities or features in a bit more detail.

Science Topic	Multi-band Imaging	Time Resolu-tion	Multi-wavel. Spectr.	Spectro polari-metry	IFU Spectr.
Trans-Neptunian Objects	5	3	4	1	2
Extrasolar Planets	3	2	5	1	2
Asteroseismology	5	3	4	3	1
Massive Stars	5	3	5	3	5
Brown Dwarfs	5	5	4	1	1
Low-Mass Binaries	5	5	4	1	1
Low-Metallicity Stars	4	1	5	1	1
Isolated Neutron Stars	5	5	3	4	3
Magnetars	5	5	3	4	1
Interacting Binaries	5	5	4	3	2
Millisecond Pulsar Binaries	5	5	3	2	1
X-Ray Binaries	5	5	4	1	1
Supernovae	5	1	5	4	4
Supernova Remnants	5	1	5	2	3
Gamma-Ray Bursts	5	2	5	2	4
Active Galactic Nuclei	5	1	5	3	2
Tidal Disruption Events	5	3	5	2	1
Galaxy Clusters	5	2	4	1	4

Table 2 - Prioritization of capabilities and possible features of the OCTOCAM instrument, from 1 (not important) to 5 (extremely important).

Time Resolution

Having good temporal resolution is of course mostly relevant for transient sources. In Table 4 and Figure 22 we show the minimum temporal resolution that has been identified for the different science cases. The highest time resolution, ~0.01 seconds, is required for isolated neutron stars, and magnetars, to probe variability associated with their spin periods and/or bursting activity. Moderately high time resolution, ~0.1 seconds, is required for Trans-Neptunian

objects, asteroseismology, low-mass binaries, interacting binaries, and X-ray binaries. All the other science topics require a time resolution of a few Hz or less.

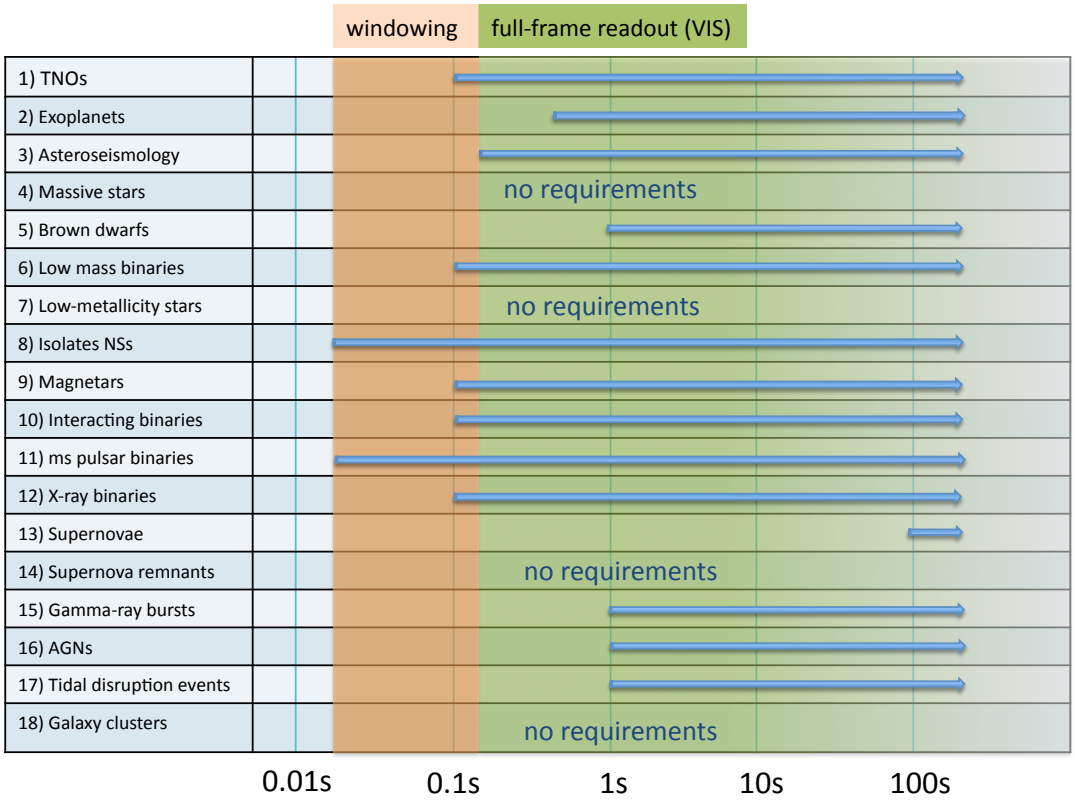

Figure 22 – Time resolution required for the different science cases, compared to the time resolution that can be obtained with OCTOCAM in windowing and full-frame readout modes.

Spectral coverage

The various science cases have different requirements when it comes to spectral coverage for imaging and spectroscopy. For imaging we have explored which bands are necessary or useful for each science case, ranging from *g*- to *K*-band and covering as many of the standard bands as possible (eight in total: *grizYJHK*). Figure 23 shows the bands that are absolutely necessary in dark green, and bands that are helpful but not necessary in light green. It is clear that there are a few science cases for which all the bands are absolutely necessary, and many of them for which all the bands would be useful to have. A few science cases just require a couple of bands on each side of the spectral extremes. In general, having all eight bands available at the same time is a very efficient way of using Gemini. In particular for transients, but also other objects that require high time-resolution observations, it is vital to have consistent data throughout all those bands at any time. For high-redshift transients, e.g. gamma-ray bursts, having simultaneous imaging in all those bands enables redshift determination using the drop-out method, for which a good coverage is necessary. The bottom line is that having the full coverage of all eight bands will enable a maximum scientific output. The vast majority has a minimum requirement of having the *g*-, *r*-, *i*- and *K*-bands, and the other four bands are in less demand. However, leaving out the latter four bands would seriously harm several of the science cases; hence an instrument like OCTOCAM would ideally cover all eight bands.

For spectroscopy we have explored the wavelength range equivalent to the eight bands mentioned before, with a maximum limit of 2350 nm and pushing down the lower limit to 370 nm. Figure 24 shows the wavelength ranges that are absolutely necessary for each science case in dark colored bars, and the ranges that are useful but not necessary in light colors. Also for spectroscopy there is not a homogeneous picture over all the science cases, as one would expect. And also for spectroscopy the bottom line is that a full coverage of this wavelength range from 370 to 2,350 nm will enable a maximum scientific output. Many of the arguments for a broad well-covered range in imaging also hold for spectroscopy.

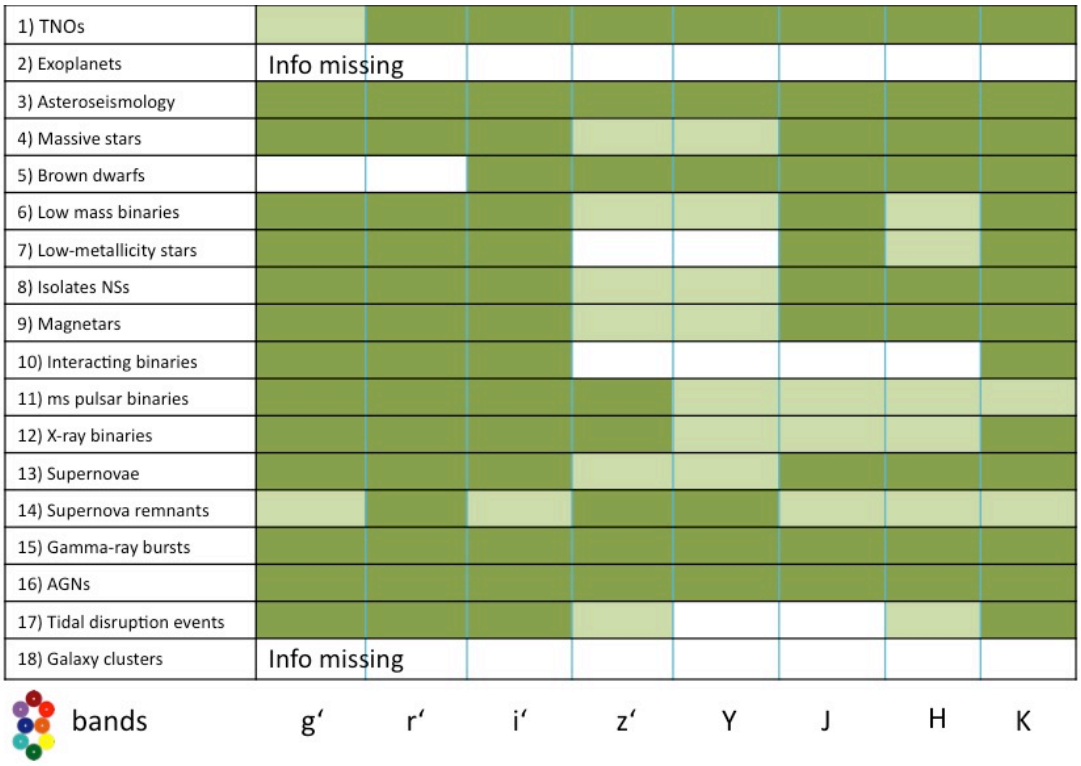

Figure 23 – Imaging bands required for the different science cases: dark green indicates bands that are absolutely necessary for each science case; light green indicates bands that are helpful but not absolutely necessary; and white bnds are those that are not necessary.

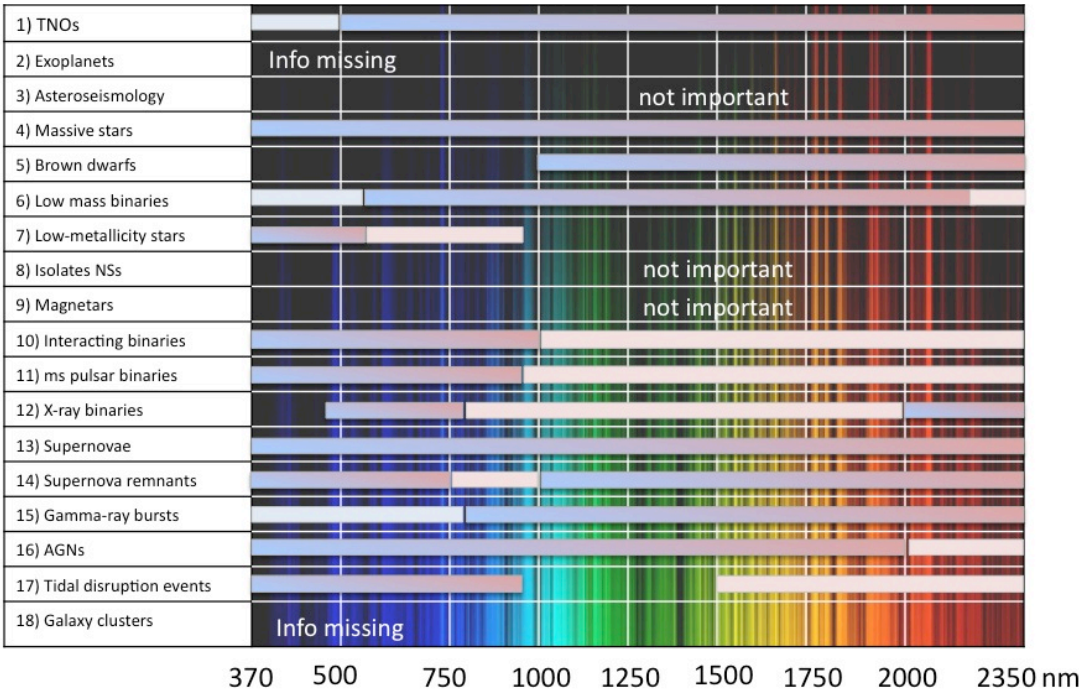

Figure 24 – Wavelength ranges required for spectroscopy, for the different science cases: dark colors indicate ranges that are absolutely necessary for each science case, and light colors indicate ranges that are helpful but not absolutely necessary.

Spectral resolution

Most science team members indicated that a spectral resolution of ~3,000-4,000 is optimal for carrying out their science. A few team members showed in interest in high-resolution (10,000-15,000) spectroscopy with echelle grisms. Even though they identified interesting science cases, the number of science topics that would rely on echelle spectroscopy is low, and the vast majority of the science team did not show a strong interest in echelle grisms as an added capability to an instrument like OCTOCAM. Most science team members indicated that they would worry about the efficiency and low number of targets that could benefit from this. Nonetheless, here we briefly highlight the science topics that would benefit from high-resolution spectroscopy.

Echelle spectroscopy would be useful to study the properties of absorptions due to gas in the surroundings of supernovae. Evolution of such absorptions can help to probe the evolution history of the progenitor and its mass-loss process, thus linking supernova types with their progenitor channels. High spectral resolution is also useful to study the interplay between pulsation and mass-loss events in stars, specifically by probing CO molecules in a band around 2,300 nm; and to study the circumstellar geometries and kinematics. For interacting binaries, high spectral resolution is essential for a detailed analysis of emission lines and their profiles, allowing models of the kinematics of the inter-binary region, constraints on the morphology of the mass flow (i.e., bipolarity), and to extract radial velocity curves and rotational broadening for determining the stellar masses. Finally, for metal-poor stars, high-resolution data is necessary for the lowest [Fe/H] candidates in the halo, to determine their full abundance pattern. Most of these stars are expected to be faint (i.e., >16 mag) so the traditional spectral resolution of 30,000 to 40,000 will become too time consuming. A mode with a

spectral resolution of 10,000 will allow some follow-up observations and provide at least a handful of elemental abundances needed for a PopIII yield comparison. This kind of mode would also allow for measurement of additional elements beyond iron and carbon, for a more complete characterization of the star formation and element enrichment history of these systems in dwarf galaxies.

Field of view

To determine the optimal field of view for an instrument like OCTOCAM, we have explored three different possibilities: field of view of 2'x2' with a plate scale of 0.12"/pixel; field of view of 3'x3' with a plate scale of 0.18"/pixel; and field of view of 4'x4' with a plate scale of 0.24"/pixel. The plate scales associated with the different fields of view are typical for the detectors used in the baseline design of OCTOCAM. Figure 25 shows the preferences for the various science cases, and it is clear that 3'x3' and 4'x4' are preferred over 2'x2'. We note that several science team members preferred 4'x4' over 3'x3' because of the larger number of possible calibration sources, not necessarily because their objects of interest are that much extended on the sky; and they have indicated that 3'x3' would also be sufficient. Some of the science team members who preferred 3'x3' have indicated that the larger plate scale for 4'x4' could negatively impact their science. Therefore we are adopting a 3'x3' field of view with a 0.18"/pixel plate scale for further considerations.

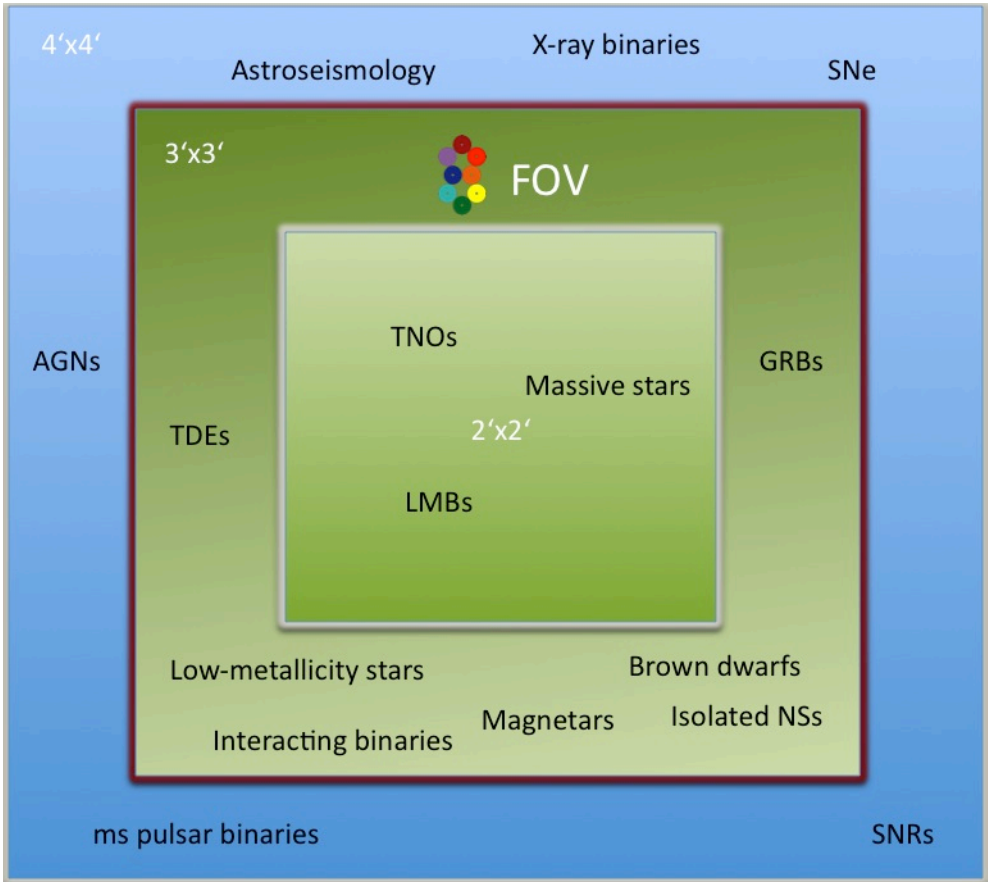

Figure 25 – Preferred field of view for the various science cases.

Spectropolarimetry

It is important to recognize that the radiation we see is not only described by its intensity as a function of wavelength and time. It is also important to know if the electromagnetic field associated with the radiation oscillates in a preferred direction, i.e., if the radiation is polarized. Polarization occurs whenever there is an asymmetry in the radiating source, or between the source and the observer, e.g., in the presence of a magnetic field or collimated beams of particles, or when the light is scattered by dust (e.g., the interstellar medium) or by a surface (e.g., that of an asteroid or of a planet). In all these situations we may benefit from the measurements of all Stokes parameters, i.e., not only Stokes I, which describes the intensity, but also Stokes Q and U, which describe the linear polarization, and Stokes V, which describes the circular polarization.

Indeed, many of our science team members have indicated that having spectropolarimetric capabilities on an instrument like OCTOCAM will be very exciting, complementing the information obtained through more traditional techniques. There are some research areas in which spectropolarimetry is by far the most important diagnostic technique, e.g., stellar magnetic fields, and other where spectropolarimetry is used frequently, e.g., studies of supernovae, solar system objects, circumstellar environments. High-impact science will come from exploiting the unique spectropolarimetric capabilities in the continuum, spanning the entire spectral range from the optical to the near-infrared. This capability would be unique in the world. In the following we highlight some of the most compelling science cases for spectropolarimetry.

A low- to mid-resolution spectropolarimeter attached to an 8-meter class telescope could be used for the detection and modelling of magnetic fields in faint objects, such as white dwarfs (e.g., Landstreet et al. 2012, A&A, 545, 30, and references therein) or massive stars in the Magellanic Clouds (e.g. Naze et al. 2015, A&A, 577, 107; Walborn et al 2015, arXiv:1507.02434). Low-resolution spectropolarimetry may be used for the study of magnetic fields in various regions of the H-R diagram (Bagnulo et al. 2015, submitted). In that respect, this science case is similar to those of programs carried out with FORS at the VLT, but with the added value that an instrument like OCTOCAM would extend the spectral range far into the near-infrared. In particular, polarimetric capabilities in the near-infrared will open the possibility to study magnetic fields in cool and ultra-cool M-type stars (for the interpretation of the polarization of molecular lines, see Afram & Berdyugina 2015, A&A, 576, 34). Given Gemini's sensitivity, OCTOCAM could play an important role for the study of the faintest of such objects. Note in particular that in brown dwarfs, studies of the polarization in the continuum may be uniquely interpreted in terms of cloud structure (patches, bands, etc.) and/or rotational flattening (Miles-Paez et al. 2013, A\&A 556, 125; Marley et al. 2011, MNRAS 417, 2876; Sengupta & Marley 2010, APJ 722, L143).

Spectropolarimetry is a powerful diagnostic tool to probe asphericity in unresolved sources such as SNe. The dominant agent producing the SN polarimetric continuum is thought to be Thompson photon scattering through an aspherical photospheric expansion (Hoflich 1991, A&A, 246, 481; Kasen et al. 2003, ApJ, 593, 788). Departures from asphericity can be visualized in the Stokes plane (Wang & Wheeler 2008, ARA&A, 46, 433). SN spectropolarimetry is

able to discriminate geometric and dynamical information for the different chemical constituents of the explosion. These observations can provide important clues about both the pre-SN mass-loss and the explosion physics (e.g., Mauerhan et al. 2015, arxiv:1506.08844; Mauerhan et al. 2014, MNRAS, 442, 1166). Spectropolarimetry with OCTOCAM will be an important addition to the field where current facilities are limited in availability and sensitivity.

Spectropolarimetric observations of comets can be modelled to understand the evolution of dust ejecta. In particular, it is now understood that the porosity of the monomer aggregates that compose comet eject may be estimated from the measurements of the polarimetric gradients in the optical and near-infrared. More compact aggregates means that the comet eject has been processed with the interaction of the solar wind, therefore polarimetry may bring constraints to the evolution of the comets (Kiselev et al. 2015, Polarimetry of Stars and Planetary Systems, 379, and references therein). Observations of asteroids and other atmosphereless objects of the solar system would be useful to characterize their surface structure and determine their albedo. It has been found, for instance, that some asteroids with marginally different reflectance spectra (in the optical) have totally different polarization spectra (Bagnulo et al., 2015, MNRAS, 446, L11). This suggests that asteroids with similar intensity spectra, at a microscopic level may have in fact a completely different structure. It is also known that the variation of linear polarization with wavelength and phase-angle (the angle between the Sun, the object and the observer) is correlated with the albedo and taxonomic class of the objects. This means that combined with photometry, a spectropolarimetric measurement may allow us to measure the size of an asteroid. Admittedly, the modelling of the observations is still in its infancy, but theoretical studies are rapidly progressing (e.g., Muinonen et al. 2015, Polarimetry of Stars and Planetary Systems, 114).

Spectropolarimetric techniques are also routinely employed for the studies of the interstellar medium, which so far has been limited to multi-band broadband polarimetric measurements, and of circumstellar environments. It is well known that imaging polarimetry gives information on dust grain alignment, hence on interstellar and circumstellar magnetic fields (e.g., Lazarian et al. 2015, Polarimetry of Stars and Planetary Systems, 81). Further constraints from spectropolarimetry will help us to better understand the phenomena of inner accretion in young stars (e.g. Oudmaijer & Drew 1999, MNRAS, 305, 166; Vink et al. 2003, A&A, 406, 703).

Spectropolarimetry of planet transit phenomena is a so far unexplored research area, but there are theoretical models that may use these observations for the characterization of the planet orbits (Carciofi & Magalhães 2005, ApJ, 635, 570). If this technique is successful, it will be incredibly useful for the studies of other solar systems. Characterization of extrasolar planet atmospheres (e.g., Stam 2008, A&A, 482, 989; Karalidi et al. 2013, A&A, 555, 127) is also a very exciting area, but might be at the limit of the instrument capabilities. Proof of concept experiments may be performed on Earth (e.g., Sterzik et al. 2012, Nature, 483, 64) and other planets and moons of our Solar System.

Finally, high-time resolution in astronomical polarimetry would mainly be at the level of discovery science. A potential interesting application is

spectropolarimetry of rapidly pulsating stars, or other pulsating stars that have a magnetic field, but this requires time-scales of several minutes at least. Therefore, there is probably no need for cycles shorter than a few seconds. Another possibility is to study pulsars, and although they are too faint for spectropolarimetry, interesting science could be done with imaging polarimetry. We note in this context that polarimetry requires a high signal-to-noise ratio, and thus high time resolution would make sense only if the observed phenomena are periodic, so that measurements can be folded, or if the targets are very bright.

Integral Field Unit

Within the science team, possible science applications for an additional Integral Field Unit for spectroscopy have been discussed. While it was not the highest priority for the majority of the science cases, it was deemed to be a nice addition for a few of them. In the case of Trans-Neptunian objects, it could be used to study some extended objects such as activated asteroids near their nucleus, and also low-activity or distant comets. For massive stars, Integral Field Unit spectroscopy could be useful to study the structure and kinematics of circumstellar material, disks, and possible jets. It could also be beneficial to construct 3-dimensional maps of giant extragalactic H II regions, or to explore a possible relationship between the star formation rate with the velocity dispersion or turbulence of star forming regions. The host galaxies of supernovae, gamma-ray bursts and active galactic nuclei could be studied better with such an added feature to an instrument like OCTOCAM. Also in the case of supernovae, it could be used to characterize the stellar populations around supernova sites. Finally, having an Integral Field Unit with a large field of view could be useful for follow-up observations of transients, since X-ray positions will perhaps only be known to several arcseconds precision in the early 2020s. This will be relevant for fast spectroscopy of sources, without performing imaging observations first.

1.4.4. Science-Driven Requirements

Based on the science cases and prioritization presented in this section, we have determined instrument requirements for OCTOCAM. These requirements are given in the Science Traceability Matrix (Table 4), which shows a flow-down from the general principles of the Gemini Science and Technology Advisory Committee (STAC) to the broad science goals of OCTOCAM, to the OCTOCAM science objectives, and finally the instrument requirements per science objective and for the whole instrument. In the Science Traceability Matrix we give the minimum instrument requirements per science topic, the expected performance of OCTOCAM for each topic (with the margin for reaching the minimum requirements), and the extra considerations or goals per science topic. The latter specifies which science goals would particularly benefit from the u band, high spectral resolution, high time resolution in windowed timing mode, echelle grisms, spectropolarimetry, and a large Integral Field Unit for spectroscopy. The last column of the Science Traceability Matrix shows the requirements that are input for the technical requirements that are discussed in the following sections.

1.4.5. Observing Time

To conclude this section, we provide estimates of the number of hours that would be required in the most optimal case to answer the main science

questions and/or carry out long-term investigations towards the science goals. The number of hours is given below per science topic. While for some science cases the total sample, and also the total number of hours, is clear, this is not the case for all of them, in particular for several of the science cases involving transients. In these cases the number of hours or nights per year is given. It is clear from all these numbers that an instrument like OCTOCAM would be at high demand for a lot of different science cases, resolving many big open questions in the larger community. Below we give a motivation per science topic for the number of observing hours, followed by Table 3 in which we give an overview of observing times together with the necessary observing conditions and seeing.

- *Trans-Neptunian objects:* 80-120 hours in total for simultaneous photometry, comprised of ~80 objects at 1-1.5 hour per object; ~100 hours of wide spectral range spectroscopy, about 100 objects with an average of 1 hour per object. The total amount is 200 hours.
- *Extrasolar planets:* 100-300 transiting gas giant planets, with 6 hours for each transit observation, and some objects require multiple observations to build up significant signal-to-noise. This leads to ~3000 hours in total.
- *Asteroseismology:* 10-15 hours per year per single short period object.
- *Massive stars:* 60-80 hours per years, as multiple observations are necessary for a sufficient sample of stars.
- *Brown dwarfs:* Observe 40-50 objects for a good sample of brown dwarfs at a range of wavelengths, with a minimum of one half night of observations per object (maybe returning to it again later in the semester), resulting in ~40-50 nights.
- *Low-mass binaries:* One week (half to full night) per binary system, targeting as many systems in the *Kepler* sample as possible (a few 100 in total). Required observation time is at least two times the orbital period of a binary system.
- *Low-metallicity stars:* 15 minutes per halo star for ~500 objects, resulting in 10-20 nights. For dwarf galaxy stars, 1 hour per star for spectroscopy, and with 10-20 stars per galaxy, this would take less than ~10 nights.
- *Isolated neutron stars:* 10-20 hours per object for spectroscopy and time-resolved photometry, for 2-3 systems per year, leading to 30-60 hours per year.
- *Magnetars:* ~10 hours for a source in outburst, with on average 1-2 sources in outburst per year.
- *Interacting binaries:* ~1000 hours in total for imaging and spectroscopy.
- *Millisecond pulsar binaries:* ~20 nights in total for imaging and spectroscopy.
- *X-ray binaries:* At most ~20 hours for a source in outburst, depending on the outburst magnitude and the system's orbital modulation. Furthermore, monitoring of these systems in quiescence to trace the orbital period and obtain the radio velocity of the secondary star, requires ~30 hours for photometry and spectroscopy, assuming a ~7 hour orbital period.
- *Supernovae:* One hour of exposure time per night allows for adequate photometry and/or spectroscopy of ~4 targets, assuming 15 minutes for acquisition and integration.

- *Supernova remnants:* ~120 hours of observing time per year for imaging and spectroscopy.
- *Gamma-ray bursts:* ~100 hours per year for photometry and spectroscopy of a large sample of gamma-ray bursts.
- *Active galactic nuclei:* Long-term reverberation mapping campaigns of tens to 100 hour per year for 5-10 years.
- *Tidal disruption events:* 2 hours of imaging and 1.5 hour of spectroscopy per source, with ~100 sources per year, leading to a total of 400 hours per year in total.
- *Galaxy clusters:* 10-100 hour per field for tens to hundreds of clusters, leading to 1000 hours for a deep field campaign. For an imaging study of 1000 nearby galaxies, ~1000 hours is required.

Science Topic	Observing time	Conditions	Seeing
Trans-Neptunian Objects	100h photom., 100h spectr. (100 obj.)	Grey/bright, photom./thin cl.	1”
Extrasolar Planets	3000h. (100-300 obj.)	Bright-dark, photom.	2”
Asteroseismology	10-15h per year per object	Bright-dark, photom.	2”
Massive Stars	60-80h per year	Dark-grey, photom.-clear	1”
Brown Dwarfs	40-50 nights (40-50 obj.)	Bright, clear	1-2”
Low-Mass Binaries	1 week per system	Dark-grey, photom.	2”
Low-Metallicity Stars	20-30 nights spectr.	Bright-grey, clear-thin clouds	1-2”
Isolated Neutron Stars	30-60h per year (2-3 obj.)	Dark	1”
Magnetars	10h per outburst (1-2 per year)	Dark	1”
Interacting Binaries	1000h photom.+spectr.	Grey, clear-thin clouds	1”
Millisecond Pulsar Binaries	20 nights photom.+spectr.	Bright-dark, non-photom.	1-2”
X-Ray Binaries	20h per outburst (a few per year), 30h per source	Dark-grey, photom.	1”
Supernovae	1h per night (4 obj.)	Bright, non-photom./photom.	1-2”
Supernova Remnants	120h per year photom.+spectr.	Dark-grey, non-photom.	1”
Gamma-Ray Bursts	100h per year photom.+spectr.	Bright, thin clouds	1-2”
Active Galactic Nuclei	tens-100h per year	Grey, non-photom.	1-2”
Tidal Disruption Events	400h per year photom.+spectr. (100 obj.)	Grey, photom.	1”
Galaxy Clusters	1000h (tens-hundreds obj.)	Grey-dark, photom.	1”

Table 3 – Observing time, observing conditions and seeing per science case.

Table 4 - Science traceability matrix.

OCTOCAM Science Traceability Matrix

STAC Principles	OCTOCAM Science Goals	OCTOCAM Science Objectives	Specific Science Objective Driven Instrument Requirements	Expected Performance (Margin)	Specific Science Objective Driven Instrument Considerations/Goals	General Instrument Requirements
1) The instrument should be a workhorse instrument, meaning that it has broad scientific appeal and enables a wide range of science cases. 2) The proposals should be science driven and include science cases. Science cases that provide synergies with new capabilities coming online (e.g. LSST, JWST, ALMA, etc.) are highly desirable, especially including capabilities needed to follow up survey discoveries. 3) The instrument should fit within the technical constraints of the Gemini telescopes as they now exist. 4) The expected cost of the instrument shall be capped at a cost that is to be determined as part of the process of defining the RfP. 5) The technical risk of the instrument should be modest, i.e. the success of the instrument should not depend upon some not-yet-proven technology. 6) The instrument should be highly efficient, maintaining the 8-m aperture advantage. 7) Although proposals for all instruments fitting these criteria will be fully considered, it is the majority opinion of the STAC that a wide-bandwidth moderate-resolution spectrograph is likely to prove most compelling.	1) Efficiently follow-up and characterize new and exciting phenomena discovered by the large surveys and giant telescopes of the 2020s, in the time domain window with simultaneous broad-wavelength coverage. 2) Create a workhorse instrument that optimizes the use of Gemini for broadband single-target observations both for imaging and spectroscopy. 3) Create a tool to study the origin and fate of our Universe by observing the first generation of stars and their environments through the first gamma-ray bursts; following the evolution of the Universe throughout cosmological times by observing galaxies at all redshifts; looking for the origin of our solar system in comets, asteroids, or transneptunian objects; and advancing the understanding of extreme phenomena physics such as magnetars, X-ray binaries, and neutron stars.	1) Multi-band occultations of Trans-Neptunian objects as probes of surface composition, potential companions and atmospheric traces.	PTR = 100 ms R_{Vis} = 3000 R_{IR} = 3000	PTR[1] = 33 ms (203%) R_{Vis} ≥ 3240 (≥ 8%) R_{IR} ≥ 3798 (≥ 27%)	Possible spectropolarimetry 10" x 10" IFU useful	Observing modes: Multichannel imaging and spectroscopy. Photometric Bandwidth: 370-2350nm (grziYJHK) Spectroscopic Bandwidth: 370-2350 nm Field-of-view: 3' x 3' Visible Resolution: R ≥ 3000 IR Resolution: R ≥ 3700 Entrance slits: 0.6", 0.8", 1.0", 1.2", 5" Image slicer: 3"x5" (5 slices of 0.6") Imaging Throughput: > 40% Spectroscopic Throughput: > 30% Imaging Detectors: > 1k x 1k Spectroscopic Detectors: > 2k x 1k Instrument Weight: < 2000 kg Spectropolarimetry: Full-Stokes
		2) Simultaneous multi-band imaging and spectroscopy to identify and characterize extra-solar planets and their atmospheres through transits.	PTR = 500 ms R_{Vis} = 3000 R_{IR} = 3700	PTR[1] = 33 ms (1415%) R_{Vis} ≥ 3240 (≥ 8%) R_{IR} ≥ 3798 (≥ 3%)	R_{IR} ≥ 4000	
		3) Asteroseismology to determine the internal structure of stars.	PTR = 100 ms R_{Vis} = 3000 R_{IR} = 3700 u-band limit ≥ 370 nm	PTR[1] = 33 ms (203%) R_{Vis} ≥ 3240 (≥ 8%) R_{IR} ≥ 3798 (≥ 3%) Complies	Photometric S/N = 100 High Dynamic Range R_{IR} ≥ 4000	
		4) Optical-to-near-infrared photometry and spectroscopy of massive stars to characterize their stellar winds in different phases of their evolution.	R_{Vis} = 3000 R_{IR} = 3700 u-band limit ≥ 370 nm	R_{Vis} ≥ 3240 (≥ 8%) R_{IR} ≥ 3798 (≥ 3%) Complies	Echelle grisms useful Possible spectropolarimetry 10" x 10" IFU useful R_{IR} ≥ 4000	
		5) Multi-band imaging of brown dwarfs to determine the composition of their atmospheres and the role of clouds on the opacity.	PTR = 1 s R_{Vis} = 3000 R_{IR} = 3000	PTR[1] = 33 ms (2930%) R_{Vis} ≥ 3240 (≥ 8%) R_{IR} ≥ 3798 (≥ 27%)		
		6) High resolution radial velocity curves of low-mass binaries to very stellar evolution by accurately measuring mass-radius relations.	PTR = 100 ms R_{Vis} = 3000 R_{IR} = 3000	PTR[1] = 33 ms (203%) R_{Vis} ≥ 3240 (≥ 8%) R_{IR} ≥ 3798 (≥ 27%)		
		7) Determine the nature of carbon-enhanced low-metallicity stars and their connection with the first stars.	R_{Vis} = 3000 R_{IR} = 3700	R_{Vis} ≥ 3240 (≥ 8%) R_{IR} ≥ 3798 (≥ 3%)	Echelle grisms useful u-band important R_{IR} ≥ 4000	
		8) Perform phase-resolved photometry of isolated neutron stars to study the connection between the optical and X-ray/gamma-ray emission, shed light on the physical origin of the optical-to-near-infrared emission, and constrain properties of their atmospheres and magnetospheres.	PTR = 15 ms R_{Vis} = 3000 R_{IR} = 3000 u-band limit ≥ 370 nm	PTR[2] = 12 ms (25%) R_{Vis} ≥ 3240 (≥ 8%) R_{IR} ≥ 3798 (≥ 27%) Complies	PTR = 10 ms Spectropolarimetry interesting 10" x 10" IFU useful	
		9) Well-sampled spectral energy distributions in the optical-to-near-infrared regime to constrain the emission origin and mechanisms of magnetars.	PTR = 100 ms R_{Vis} = 3000 R_{IR} = 3000	PTR[1] = 33 ms (203%) R_{Vis} ≥ 3240 (≥ 8%) R_{IR} ≥ 3798 (≥ 27%)	PTR = 10 ms Spectropolarimetry interesting	
		10) Study the physics of accretion streams and disks in interacting binary systems.	PTR = 100 ms R_{Vis} = 3000 R_{IR} = 3000	PTR[1] = 33 ms (203%) R_{Vis} ≥ 3240 (≥ 8%) R_{IR} ≥ 3798 (≥ 27%)	Echelle grisms useful Possible spectropolarimetry 10" x 10" IFU possibly useful u-band important	
		11) Multi-band imaging of binary millisecond pulsars to constrain the equation of state of neutron stars.	PTR = 15 ms R_{Vis} = 3000 R_{IR} = 3000	PTR[2] = 12 ms (25%) R_{Vis} ≥ 3240 (≥ 8%) R_{IR} ≥ 3798 (≥ 27%)	PTR = 10 ms	
		12) Complement X-ray/gamma-ray observations to extend our understanding of accretion and jet physics in X-ray binaries.	PTR = 100 ms R_{Vis} = 3000 R_{IR} = 3700	PTR[1] = 33 ms (203%) R_{Vis} ≥ 3240 (≥ 8%) R_{IR} ≥ 3798 (≥ 3%)	Spectropolarimetry interesting R_{IR} ≥ 4000	
		13) Optical-to-near-infrared measurements of supernovae to probe interactions with a dense circumstellar medium, shock-break outs, dust and geometric and dynamical configurations; and to push the current redshift limits and constraints on the cosmological parameters.	PTR = 100 s R_{Vis} = 3000 R_{IR} = 3700	PTR[3] = 5.25 s (90%) R_{Vis} ≥ 3240 (≥ 8%) R_{IR} ≥ 3798 (≥ 3%)	Echelle grisms useful Spectropolarimetry useful 10" x 10" IFU useful u-band limit as low as possible R_{IR} ≥ 4000	
		14) Probe supernova progenitors and their surroundings with supernova remnant photometry and spectroscopy.	R_{Vis} = 3000 R_{IR} = 3700 u-band limit ≥ 370 nm	R_{Vis} ≥ 3240 (≥ 8%) R_{IR} ≥ 3798 (≥ 3%) Complies	10" x 10" IFU possibly useful R_{IR} ≥ 4000	
		15) Multi-band imaging and spectroscopy to observe gamma-ray bursts to probe the beginnings of stellar formation and the epoch of reionization.	PTR = 1 s R_{Vis} = 3000 R_{IR} = 3700	PTR[1] = 33 ms (2930%) R_{Vis} ≥ 3240 (≥ 8%) R_{IR} ≥ 3798 (≥ 3%)	Spectropolarimetry useful 10" x 10" IFU useful R_{IR} ≥ 4000	
		16) Wide spectral range observations of active galactic nuclei to determine their fundamental physical properties, also providing fundamental clues in understanding galaxy evolution, in particular the role of supermassive black holes and their formation.	PTR = 1 s R_{Vis} = 3000 R_{IR} = 3700	PTR[1] = 33 ms (2930%) R_{Vis} ≥ 3240 (≥ 8%) R_{IR} ≥ 3798 (≥ 3%)	Largest field-of-view possible Possible spectropolarimetry 10" x 10" IFU possibly useful R_{IR} ≥ 4000	
		17) Complement X-ray/gamma-ray observations of tidal disruption events to measure the mass and spin of supermassive black holes.	PTR = 1 s R_{Vis} = 3000 R_{IR} = 3700	PTR[1] = 33 ms (2930%) R_{Vis} ≥ 3240 (≥ 8%) R_{IR} ≥ 3798 (≥ 3%)	u-band important R_{IR} ≥ 4000	
		18) Imaging lensing clusters of galaxies to determine the content of the dark matter and the energy density in the Universe.	R_{Vis} = 3000 R_{IR} = 3700	R_{Vis} ≥ 3240 (≥ 8%) R_{IR} ≥ 3798 (≥ 3%)	R_{IR} ≥ 4000	

Notes: PTR = photometric time resolution; R = spectral resolution; [1]Assuming a readout of a 30x30 pixel window at 50 kHz and 2 e^- read noise; [2]Assuming a readout of a 30x30 pixel window at 3 MHz and 8 e^- read noise; [3]Assuming a full-frame readout at 50 kHz and 2 e^- read noise.

1.5. Concept of operations

In this section we describe a typical observing night with OCTOCAM. We present observations that use the different observing modes (multiband imaging, spectroscopy, high-time resolution imaging, high-time resolution spectroscopy, integral field spectroscopy and spectropolarimetry) and show how the observations are performed, including the required calibrations. OCTOCAM is thought as an instrument that is easy to operate, with a limited amount of observing modes, which limits the number and length of calibrations. The night astronomer operates the instrument by executing the observing blocks and calibration scripts. In the current design, the guiding of the instrument relies on the telescope's wavefront sensor. A slit-viewing camera could be added if flexures between the sensor and the instrument port were found to be too large. OCTOCAM will not require specialized training of the night astronomer for its use. Further details, based on the proposed instrument design, including the performance, overheads, and calibration plan are given in Section 3. Instrument performance and operations.

The user interface:

First we will present an example of a possible graphical user interface (GUI) that the astronomer would be using while operating the instrument. There would be three main user interface windows:

1. *Imaging GUI:* Will show the last 8 individual images acquired by the different bands of OCTOCAM. The exposure times of each band will be introduced automatically when selecting an observing block or modified manually by the night astronomer (the exposures can be adjusted proportionally, so that the user does not need to introduce 8 values). There will also be a main window with one image at full resolution. Clicking on the different images the user can select the image displayed on the main window. Selecting several images the user can see a deeper image combining the different bands or a color image formed by several bands.

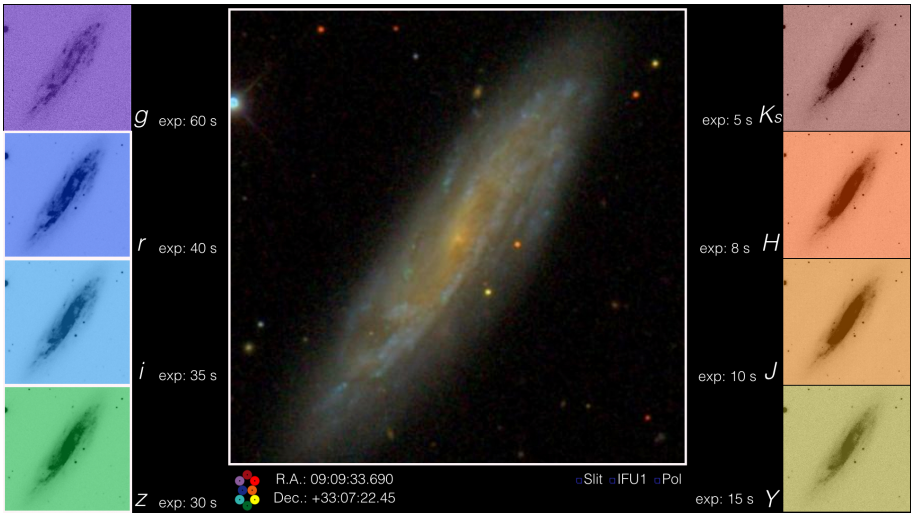

Figure 26 - Example of the imaging graphical user interface. The central image shows a color combination using 3 selected channels.

2. *Spectroscopy GUI:* For spectroscopy the user will first use the imaging GUI to perform the acquisition. In this case it will show the location of the slit, IFU or spectropolarimetry apertures to help with the object acquisition. To optimize the acquisition time there will be an automatic mode, the system will perform real time astrometry and center the slit/aperture in the exact coordinates (for ToO observations the system can be set up to select the brightest object within a specific error-box). In the manual mode, the user will click on the desired object and it will be centered on the required aperture. A though-slit image will be only shown in the manual mode, whereas the automatic mode would directly proceed to spectroscopy. Next, the spectroscopy GUI will appear showing the 2D spectral images as they come along. As the instrument has only one spectral setup, the image will be easily able to show the wavelength of each pixel. The user will also have the option to display the sky corrected spectrum with one click.

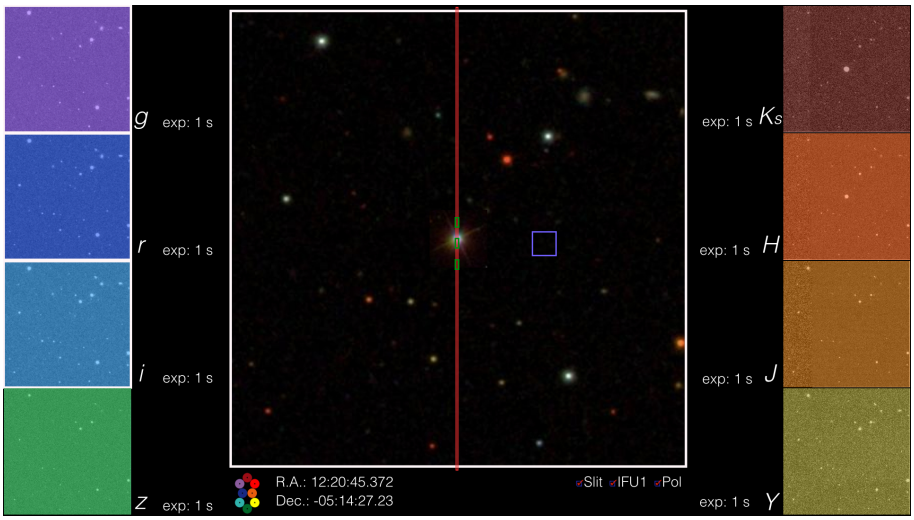

Figure 27 - Graphical user interface showing the acquisition for the spectroscopic mode. The long slit, IFU (the IFU acquisition is offset from the long slit position) and polarimetric apertures are shown in red, blue and green, respectively.

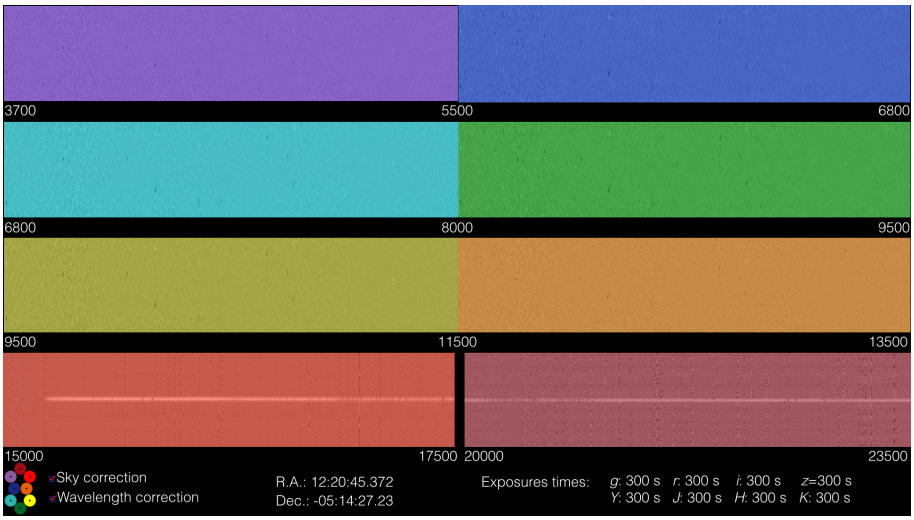

Figure 28 - Spectroscopy graphical user interface, showing the complete wavelength coverage. The sky contribution has been removed to improve the visibility of the science object.

3. *Pipeline GUI:* Finally, there will be a third user interface that will show the result of the pipeline reduction. There the user will be able to review the 1D extraction of the different objects in the slit, the reduced images, or the reconstructed IFU data-cube.

A night of science observations:

- ***Daytime calibrations:*** As described in the calibration plan, including biases, arcs, flats, etc.). Daytime calibrations are performed automatically by executing an observing script by the daytime astronomer. All the arms will perform the calibrations simultaneously, with exposure times adapted for each arm, making daytime calibrations short and efficient.
- ***Twilight calibrations***: As the observations are performed in all bands simultaneously (no need to change filters), the setup changes are very fast (<5 seconds) and the readout is very fast, the full instrument calibrations require very little time. The observing script will adapt the exposures of each of the arms so that observations can be performed simultaneously. Thanks to the use of optimized observing scripts, we will be able to calibrate all the observing modes of the instrument within a fraction of the twilight.
  - Blank field: Once the telescope is pointed to a blank field, a script is run to perform the observations, adjusting the exposure times of the different bands and changing the mode as required.
    - IFU flats.
    - Spectroscopy flats.
    - Spectropolarimetry flats.
    - Imaging flats.
  - Standard star observations: A single spectrophotometric star can serve to obtain the instrument calibration, going automatically through the different modes indicated below. As the observation is performed simultaneously in all bands, calibration is very fast, which allows observing several stars at different elevations to obtain an even better flux calibration. Although we expect the instrument to be stable from night to night, a focus check will be performed during the observation of the sandards.
    - Photometric standards (either with a spectrophotometric standard or with a photometric field).
    - Spectrophotometric standard (5” slit)
    - Spectrophotometric standard (IFU)
  - Polarization standards: If the spectropolarimeter is going to be used during the night, the calibrations will include the following:
    - Zero polarization standard
    - High-polarization standard
  - Telluric standards: If requested by the user, telluric standards will be observed during the night, using the same slit setup as the science observations and at a similar airmass.

- ***Night time observations:***
  - *Multiband imaging: Observation of a sample of faint objects (e.g. galaxies) to obtain spectral energy distributions:* Imaging programs with OCTOCAM are very easy and straightforward to execute. The coordinates are parsed to the telescope and while slewing, the instrument is set up (the instrument is ready to observe in just a few seconds).
    With 8 simultaneous imaging bands, the observing efficiency of Gemini is multiplied by eight. Thanks to the fast readout, the effective time-on-target, as compared to other instruments, is even higher. Within the first hour of the night, OCTOCAM can obtain what would currently be a nights-worth of Gemini observing.
    If the goal of the observing program is to cover a large field of view with multiple filters OCTOCAM is more efficient than any other instrument available in Gemini. With its 3'x3' field of view simultaneously observed in 8 bands, OCTOCAM has an effective coverage of 72 square arcminutes per exposure.
  - *A rapid response observation: Immediate spectroscopy of a high-redshift gamma-ray burst:* For this observation, we envision the existence of a rapid response mode. During the execution of a running observation, an alert arrives at the telescope. If the priority of the program producing the alert is high enough, it will interrupt the ongoing exposures. The data will be immediately readout, so that no information is lost, and the instrument will set up for the urgent observations, while the telescope is automatically slewing. The object acquisition will be done either by the automatic acquisition system as standard procedure, or by the telescope operator, if the automatic system fails. To optimize reaction times, through-slit images will not be performed in the rapid response mode unless explicitly requested by the user. The acquisition for spectroscopy observing blocks (OBs) in OCTOCAM is produced in the 8 bands simultaneously, providing the astronomer with a full spectral energy distribution of the object that is going to be observed. This can be crucial for objects like GRBs: a GRB at redshift > 9 would only be observable in the near-infrared bands, and the characteristic dropout would already give the astronomer an idea of the redshift, before starting the spectroscopy. Furthermore, OCTOCAM will have the advantage of being able to acquire in any of its 8 bands (or a combination of several, to increase the depth of the image), increasing the efficiency of the acquisition. A fast observation of such a high-redshift GRB would not be possible with instruments like X-shooter, as there is no near-infrared acquisition. Furthermore, the 8 acquisition images allow an extremely reliable flux calibration: each arm can be corrected independently.
    An even faster observation could be performed by blindly responding to the alert by using the IFU, without the need of an acquisition image, and even without waiting for the telescope optics to close the loop. With the field of view of the IFU unit, we would be able to observe the science object absorbing the pointing uncertainty of the telescope.

- *Spectropolarimetric observation: The geometry of a supernova explosion:* The spectropolarimetry OB is executed in a similar way as the spectroscopy one. When doing the acquisition, the apertures of the spectropolarimetry mode are shown. They consist of 3 apertures of 2 arcseconds separated by 6 arcseconds, in the direction of the slit (see Figure 27). The central aperture will collect the light from the science object, whereas the other two apertures will be use to observe clean sky areas for subtraction of the sky contribution in the science spectrum.
  The output of the spectropolarimetric observation will consist of 6 traces, a pair for each of the apertures. Each pair of spectra will have perpendicular polarization. To obtain full Stokes polarimetry of the object, the observation will consist of 6 different exposures between which the modulator is rotated.
  There is, however, an alternative way to use the polarimeter to obtain linear polarization of the continuum with low-resolution spectroscopy in a single exposure. This method allows us to obtain high time resolution observations of bright, rapidly varying objects (e.g. the recent outburst of the black hole x-ray binary V404 Cyg, or the early moments of a bright GRB). For more details on the spectropolarimeter and its operation alternatives, see Section 2.11. Spectropolarimeter. The only peculiarity of the spectropolarimetric observations is the need to obtain observations of spctropolarimetric standards (high- and zero-polarization stars).
- *High time-resolution imaging: Observing an occultation of a Trans-Neptunian object:* High time-resolution imaging of stellar occultations by dwarf planets is a very powerful technique to study the planets' atmospheres and rings. With OCTOCAM, mounted on an 8-meter telescope, this tool becomes even more powerful due to the simultaneous observation in 8 different bands and the fact that fainter stars can be used with this technique. Once more, the usage of OCTOCAM for this purpose would be straightforward. The user would have selected the exposure time of the different arms either to obtain simultaneous observations with the same exposure times in each of the 8 arms, or with different exposure times to obtain a fixed signal-to-noise ratio in the observations of the different arms. Once this is done, the support astronomer would just have to execute the OB. By selecting the desired object within the pipeline environment, the user would use the pipeline functions to obtain a real-time light curve of that object as the observations are progressing.
- *High time resolution spectroscopy: Continuous spectroscopy during the outburst of an accreting black hole:* Some sources are bright enough and so rapidly variable that obtaining high time resolution spectroscopy is feasible and would produce a very valuable insight of extreme physical processes. The operation of OCTOCAM in the high time resolution spectroscopy mode, is as simple as the long slit spectroscopy. The user would use an acquisition sequence to place the object in the slit and the observations would start straight away. To increase the time sampling of the observations, the user can choose to read only a fraction of the slit, in which the object(s) of interest is(are) located. Data reduction is equivalent to the one of

traditional observations, although much more demanding if performed in real time.

- *IFU observation: Host galaxies of supernovae explosions:* The Integral Field Unit of OCTOCAM will be a unique feature, as it will be the only one able to cover such a broad spectral range simultaneously. It benefits from the 3' slit length of the instrument to provide sky coverage of 63 square arcseconds (9.7"x6.8"), or a total of 884 spaxels with a size of 0.18"x0.4". As seen in Figure 27, the acquisition of the IFU unit is slightly displaced from the center of the field. This is due to the optical arrangement of the mirrors, which refocus the object light onto a pseudo slit that is placed along the same position as the instrument slits, in the center of the field.
  The IFU mode will benefit from the automatic acquisition sequence: Astrometry will be performed in the acquisition data to ensure that the object is automatically placed on the IFU within a fraction of an IFU slice size. Apart from the acquisition sequence, the observations are equivalent to the long slit observation, with the only difference in the pipeline execution, that requires additional tasks to reconstruct the data-cube.
  An alternative use of the IFU is to obtain spectroscopy of point-like objects at the highest possible resolution without having slit losses due to bad seeing. During bad seeing conditions, the science object will be placed in the IFU area. The spectrum would be then reconstructed and the light of the object combined to obtain a single observation with the highest possible signal. As the pseudoslit of the IFU has a width of 0.4", the instrument would work at its maximum resolution. The large area of the IFU ensures that there will be enough sky coverage to perform a good subtraction, even in the worst seeing conditions. For extended objects covering the whole IFU, a separate sky image could be necessary. An alternative design would be to have the edge slices further away from the centre of the IFU for sky subtraction.

2. Technical requirements and instrument design

2.1. Top level requirements and flow-down

The sources for the OCTOCAM instrument requirements are (1) *General Instrument Requirements* from the STM described above and (2) *Key Gemini interface requirements*. Figure 29 illustrates the flow-down of requirements from Science through OCTOCAM subassembly requirements. The flow-down figure is marked to show who is responsible for generating these requirements.

During the feasibility study, the OCTOCAM team generated the science requirements shown in section 1.4 of this document as requested by the Gemini Science and Technology Advisory Committee (STAC). Once the OCTOCAM science team received input from the Gemini community, they evaluated the *Specific Science Objective Driven Instrument Requirements* to determine the best design of the OCTOCAM instrument. The PI then flowed the *Specific Science Objective Driven Instrument Requirements* to the instrument Systems Engineering team as *General Instrument Requirements*. The expected performance margin for these requirements is shown in the Science Traceability Matrix and Section 2.1.3 of this document.

The *Key Gemini interface requirements* are shown in Figure 29. Note that there are more requirements that were evaluated and are implemented in the OCTOCAM design. Only the key requirements are shown in this figure.

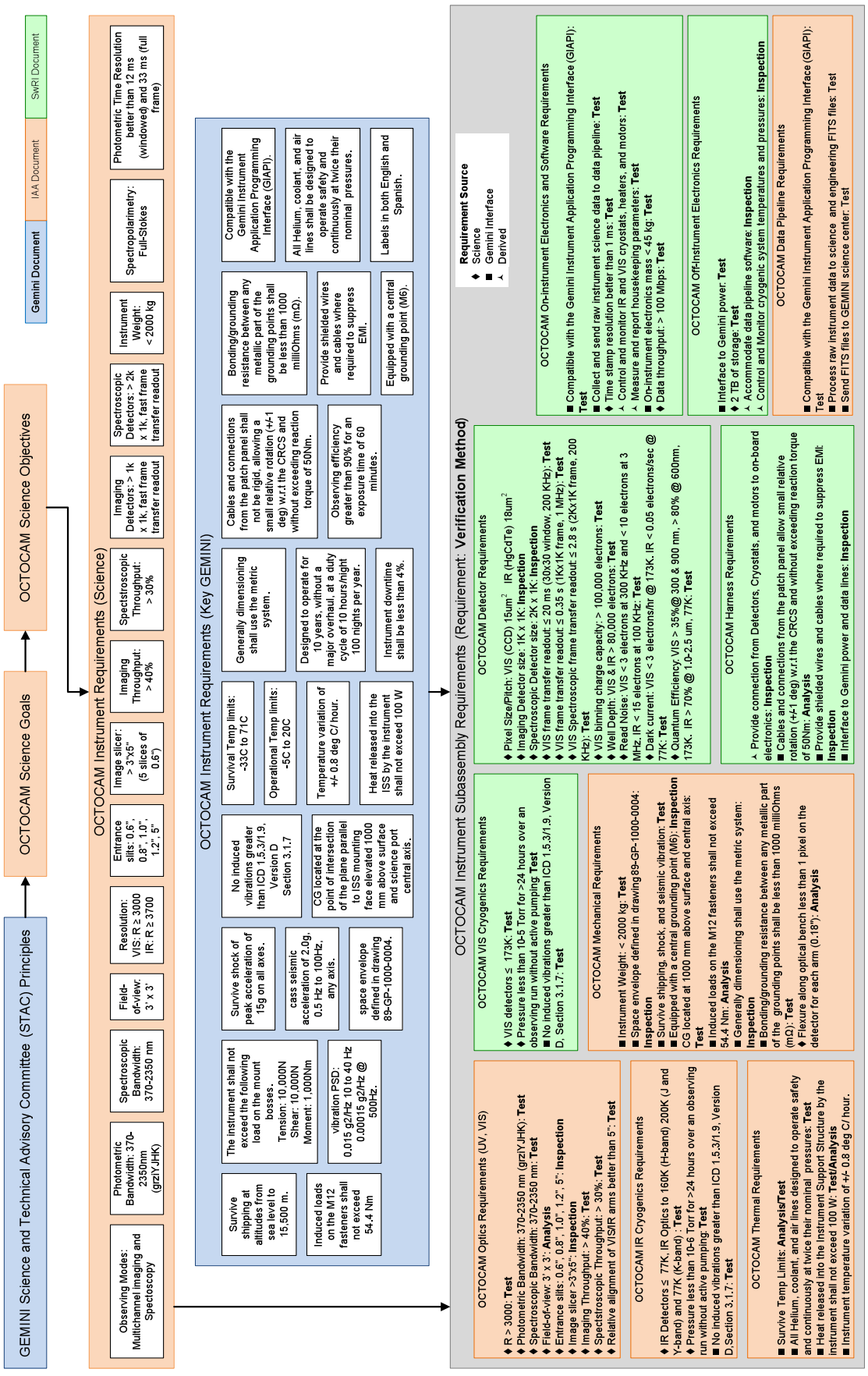

Figure 29 - OCTOCAM requirements flow-down.

2.1.1. Requirements generation and verification process

The next phase of the OCTOCAM instrument project includes the development of an instrument requirements document and subsystem specifications as shown in Figure 30. Initial versions of these specifications will be developed before the instrument Systems Requirements Review. These specifications include design and interface requirements.

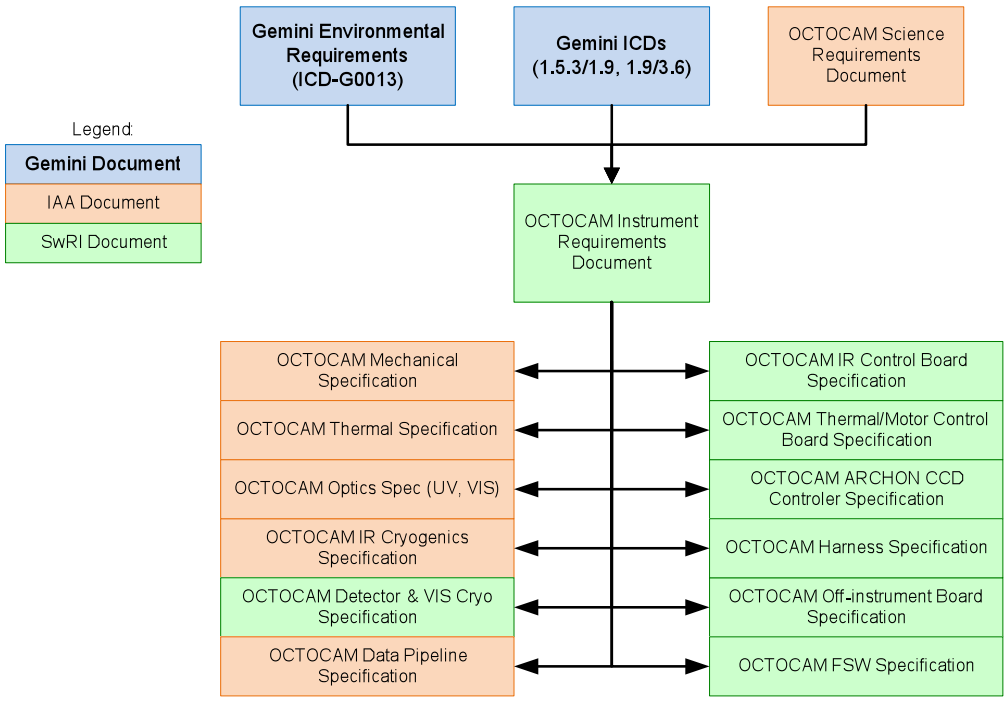

Figure 30 - Specification tree of OCTOCAM.

During the development of these requirements documents, the OCTOCAM Systems Engineering team implements a top-down requirement decomposition (performance, function, and interface), followed by a bottom-up analysis of the design implementation and verification (See Figure 31). The requirements decomposition process includes an evaluation of the top level requirement and decisions on implementation of that requirement into the design of the instrument subsystem.

Requirements are verified at the lowest level possible (i.e. circuit board) to uncover issues as early as possible and repeated at higher levels as needed to show compliance with interface and higher level requirements. Following initial development of the OCTOCAM instrument requirements, the OCTOCAM Systems Engineering team works with the Science and Subassembly teams to generate verification methods and plans for all requirements. Verification methods include Analysis, Inspection, Test, and Demonstration. Verification planning is a statement of the specific analysis, inspection, or test that will be used to verify that requirement. This verification planning strategy ensures that the team fully understands requirements and also their verification mechanism. The outputs of this planning are cross-referenced matrices that are incorporated into all verification paperwork (e.g., test procedures, design review reports, etc.). By completing this process early, the Systems and I&T teams can be sure that test procedures are written in a manner that not only completely validates their hardware and software, but also fully verifies all requirements.

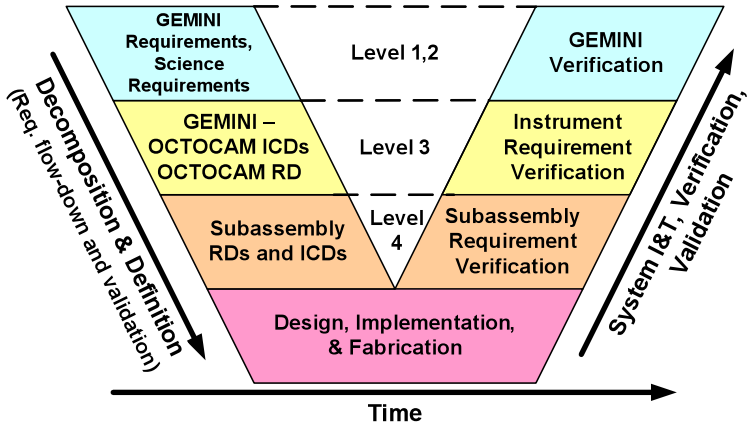

Figure 31 - Top-down requirements decomposition.

2.1.2. Requirements flow-down

As mentioned earlier, the OCTOCAM technical requirements were generated based on the top-level science requirements as well as the Gemini interface requirements. The initial OCTOCAM requirements flow-down is shown in Figure 29. This figure is a summary of the requirements. More detail will be added to the OCTOCAM Subassembly Requirements during the next phase of the project to fully define all of the Subassemblies in the OCTOCAM instrument. The requirements are split out by Subassembly and the planned verification method is in bold text. Each requirement has an indication of whether its source is from science, Gemini interfaces, or whether the requirement was internally derived (see top right hand corner of bottom box of requirements for legend).

2.1.3. Top level requirements compliance

The expected performance margin for the *Science Objective Driven Instrument Requirements* are in the Science Traceability Matrix and Section 1.4 of this document. The table below shows the Instrument science requirements compared to the current instrument capability.

Science Requirement	Capability
Observing Modes: Multichannel imaging and Spectroscopy	Compliant
Photometric Bandwidth: 400-2350nm	Compliant: *grziYJHK$_S$*
Spectroscopic Bandwidth: 370-2350 nm	Compliant: 370-2350 nm
Field-of-view: 3’ x 3’	Compliant: 3.07’x3.07’
Resolution: R > 1500 for g-band, R > 3000	Compliant: R = 3000 to 4000
Entrance slits: 0.6”, 0.8”, 1.0”, 1.2”, 5”	Compliant
Image slicer: > 3“x5“	Compliant: 9.7” x 6.8”
Imaging Throughput: > 40%	Compliant: 41%
Spectroscopic Throughput: > 30%	Compliant: 33%
Imaging Detectors: > 1k x 1k, fast frame transfer readout	Compliant
Spectroscopic Detectors: > 2k x 1k, fast frame transfer readout	Compliant
Instrument Weight: < 2000 kg	Compliant: 1854 kg
Spectropolarimetry: Full-Stokes	Compliant
Photometric Time Resolution better than 100 ms	Compliant: ~ 100 ms 1kx1k full frame ~ 10 ms 30x30 window

Table 5 - Requirements and capabilities of the instrument.

2.2. Instrument design

2.2.1. Design summary

Based on the input from the science team and the evaluation of some technical trades (as detailed in the following section) we flow-down the requirements of OCTOCAM to satisfy the largest possible scientific interests that we found within the Gemini community. Using these requirements we define the characteristics of the instrument that can be summarized as follows:

- OCTOCAM will have both imaging and spectroscopic capabilities.
- It will use high-efficiency dichroics to split the wavelength coverage into windows that cover standard filters such as the visible Sloan *g*, *r*, *i* and *z*, and the NIR *Y*, *J*, *H* and K_S.
- Imaging will be seeing limited with appropriate sampling for the typical conditions of Gemini and a field of view of 3'x3'.
- Spectroscopy will be performed with a single long slit of 3' and a spectral resolution of the instrument should be R > 3000. This is especially relevant in the NIR, where the sky emission of OH molecules dominates the background. These features begin to be resolved at R~1000, but a resolution beyond 3000 is desirable to efficiently observe faint continua between the emission lines.
- Detector technology will be chosen to allow high time-resolution observations, both in the optical and NIR without compromising traditional observations.
- OCTOCAM will have an atmospheric dispersion corrector to allow corrected observation at different sky elevations.
- We propose the addition of an integral field unit allowing performing spectroscopy of the largest possible sky coverage.
- We propose to add a spectropolarimetry unit.

The following figure schematically shows the design of OCTOCAM. The light arriving from the telescope first goes through the atmospheric dispersion corrector, immediately after which light enters into the cryogenic chamber. 150 mm after passing through the entrance window, the light is focused on the focal plane. There, a carriage can select the different focal plane elements: The different slits, an integral field unit, the polarizing optics or just a clear opening to perform imaging. After the focal plane light encounters the first dichroic, which splits the optical and the nIR light. The nIR light is transmitted and continues its path within the cryostat, whereas the reflected optical light exits the cryostat through a second window.

At this point further dichroics split the light into 4 optical and 4 nIR arms. The optical designs of both optical and nIR arms are similar: A collimator produces a parallel beam that is refocused into each of the eight detectors by cameras that will be optimized for each wavelength range. Within the collimated beam we can either place a VPH grism to perform spectroscopy or just leave it clear to perform imaging. In the case of the g-band, where the spectral coverage is larger than the one of the standard filter, we include a filter to obtain a standard transmission.

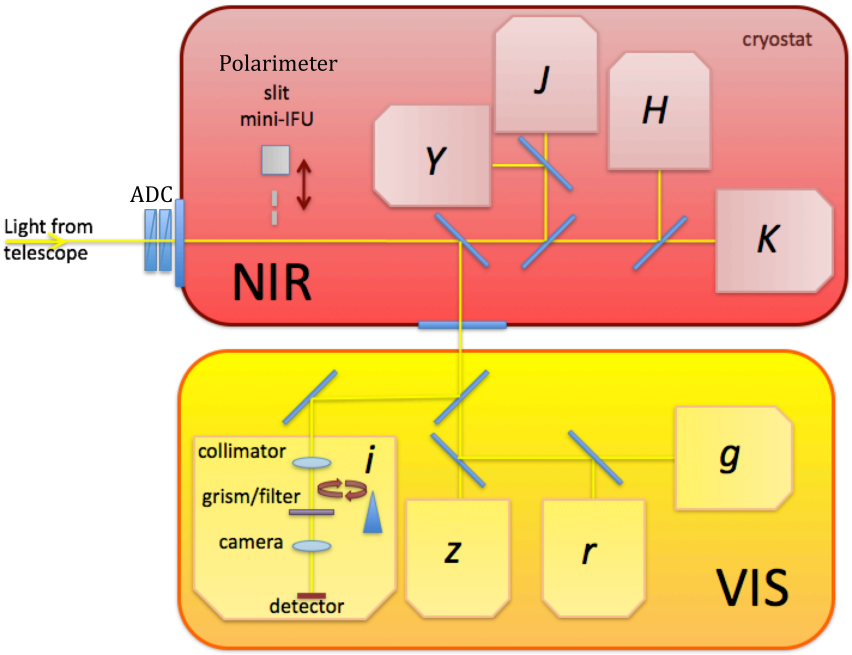

Figure 32 - OCTOCAM schematic layout. The optical arms (*g*, *r*, *i*, *z*) are located outside of the cryostat, reserved for the near-infrared channels (*Y*, *J*, *H*, K_S).

Thanks to the usage of state of the art detectors, OCTOCAM can also perform at high time-resolution without losing performance in more classical long exposure operation. In the optical we plan to use 2kx2k frame transfer e2v detectors and in the NIR 2kx2k Hawaii 2RG detectors. These detectors allow subsecond readout times in full frame, and even shorter with windowed modes.

The central 1kx1k of each detector will be used for imaging, where we will cover a sky area of 3'x3'. For spectroscopy OCTOCAM will a 2kx1k area, so that the light is dispersed in twice the amount of pixels. This allows us to reach higher spectral resolutions, while still using the full 3' long slit. The following figure shows the detector layout for both imaging and spectroscopy. In the case of the g-band channel, and given that the relative spectral coverage is larger, we use a 4kx1k detector area to provide a similar resolution to the one achieved in other arms.

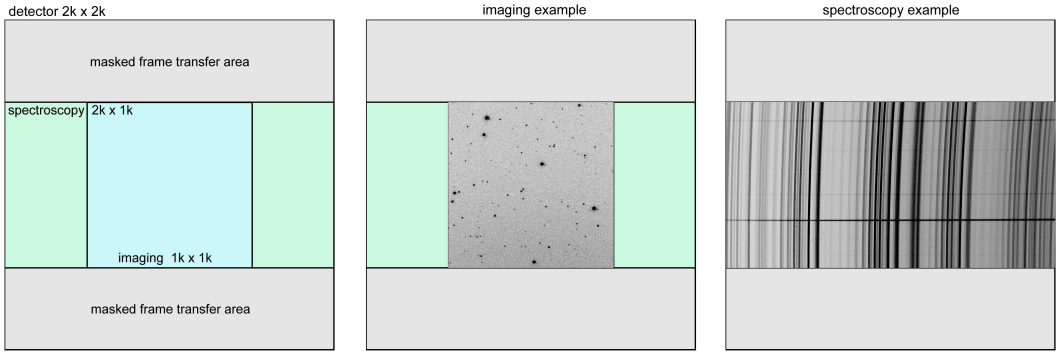

Figure 33 - Detector layout of OCTOCAM in the r, i and z visible arms. The NIR arms have a similar layout, whereas the g-band arm uses a detector of 4kx4k, in which 4kx1k are used for spectroscopy and 1kx1k for imaging.

2.2.2. Trade study

Increasing the resolution from the 3000 of the proposal to 4000-5000

In the instrument proposal we presented an instrument that would obtain spectroscopy between 4000 to 24000 Å at an average resolution of around 3000. During the proposal evaluation the committee requested a trade study to see if the spectral resolution could be increased to the range between 4000 and 5000. There are several factors that need to be taken into account when determining the spectral resolution of the instrument:

- Spectral resolution due to the optics: Spectral resolution compromised by instrument geometry and size. OCTOCAM is a multiplexed instrument. The geometry should be kept as simple as possible, thus straight imaging/spectroscopic beam was preferred over ruled reflective gratings. Angular dispersion is limited by the prism size required to obtain the angle of incidence on the grating. Getting higher linear dispersion can be improved by using longer camera focal lengths, but for a fixed resolution size means bigger pupil. As a summary, we can say that 50mm is a pupil that meets current requirements at the smallest size.
- Number of pixels in the dispersion direction: In the original design we had detectors of 2kx2k, for which 1kx1k were used for imaging and 2kx1k were used for spectroscopy.
- Slit width: The numbers that we are considering are assuming a slit that covers 3 dispersing elements (0.54" as projected in the sky). Thus, signal is correctly sampled over Nyquist.

In our case we intend to build an instrument that is as compact as possible, given the limited space and mass that we can mount on the instrument ports. With this purpose, we have limited the pupil size to 50 mm. This by itself can limit the resolution of classical VPH grisms. However, the most relevant limiting factor in our design is the amount of pixels that we have in the detector. To increase the resolution, the original design already included the use of extended detector area for spectroscopy, using 2kx1k pixels, as compared to the 1kx1k used for imaging.

To obtain a higher and more uniform spectroscopic evolution we propose to increase the number of spectroscopic channels, including Y-band. In the case of the g-band arm, and due to the larger relative wavelength coverage in this arm, we are including a detector area of 4kx1k for spectroscopy. Increased detector area allows for higher spectral resolution, but requires larger, more complex optics.

With the proposed setup, the average resolution is increased from 3150 to 3921 and made much more uniform. A further increase in resolution, maintaining the instrument design concept, would require increasing the detector area in all the arms. This would complicate the optical design and significantly increase the required investment in detectors. We understand that the proposed design represents a good compromise.

In the following tables, we show the spectral coverage and resolution of the arms of OCTOCAM in the proposal design and in the final one. To calculate the resolution we have assumed 3 pixel resolution elements corresponding to a slit

width on sky of 0.54". With the IFU, the sampling is smaller than 3 pixels, and the resolution higher than reported here. In the final design some overlap between the different optical arms will be included, depending on the final performance of the dichroics.

Band	Minimum wavelength	Central wavelength	Maximum wavelength	Spectral coverage	Spectral resolution
u	330	365	400	70	---
g	400	480	560	160	2000
r	560	620	680	120	3440
i	680	745	810	130	3820
z	810	905	1010	190	3170
J	1010	1200	1350	400	2350
H	1500	1650	1800	300	3660
K	2000	2150	2400	400	3580

Table 6 - Spectral coverage and resolution of the different arms in the proposal design of OCTOCAM.

Band	Minimum wavelength	Central wavelength	Maximum wavelength	Spectral coverage	Spectral resolution
g	370	460	550	180	3489
r	550	615	680	130	3229
i	680	745	800	130	3820
z	800	875	950	150	3885
Y	950	1035	1120	170	4156
J	1150	1250	1350	200	4267
H	1500	1630	1760	260	4280
K	2000	2175	2350	350	4242

Table 7 - Spectral coverage and resolution of the different arms in the final design of OCTOCAM.

Extending the spectral coverage towards the ultraviolet

The original design of OCTOCAM included 8 bands in imaging (*ugirzJHK*) and coverage from 4000 to 24000 Å in spectroscopy. We were requested to study the extension of the spectral coverage towards the u-band. To do this we have to consider the parameters that limit the *u*-band coverage:

- Atmospheric transmission.
- Telescope mirror coating. Gemini currently has what is probably the most efficient coatings of the 8m class telescopes. However, the reflectivity of these mirrors falls sharply below 4000 Å.
- Optics transmission within the instrument. Producing an instrument with broad wavelength coverage requires a very careful selection of materials and coatings. When increasing the wavelength coverage the overall efficiency of the instrument can also drop.

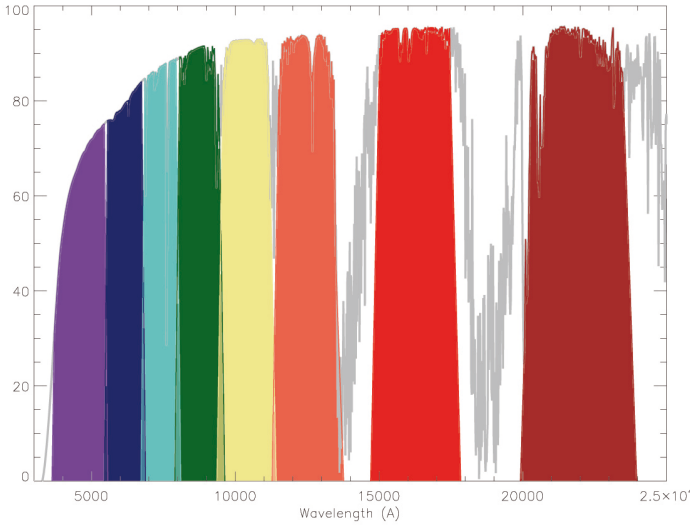

Figure 34 - Transmission of atmosphere and telescope before entering the instrument. The colors indicate the different observing bands of OCTOCAM.

We have chosen to extend the spectral coverage down to the wavelength where the transmission of atmosphere and telescope were larger than 25%. In the case of Gemini this happens at around 3700 Å. Figure 34 shows the transmission of atmosphere plus telescope mirrors before entering the instrument. To extend this spectral coverage we have increased the lower range of the g-band. This extended coverage would have implied a lower resolution in this arm. As explained before this problem has already been addressed by doubling the detector area of this arm.

Adding an Atmospheric Dispersion Corrector

We have also studied the benefits and drawbacks of including an atmospheric dispersion corrector for the instrument. The design originally proposed for OCTOCAM did not include such an element. However, this meant that whenever using the instrument at large zenithal distances, the slit would need to be placed at a parallactic angle to avoid slit losses due to atmospheric refraction. Adding an ADC solves this problem and allows us to make full use of the capabilities of the instrument independently of the area of the sky that we are observing. However, the broad spectral coverage requires a careful selection of materials and coatings, as it is very difficult to make an efficient ADC that works across the entire range.

Our design efforts have shown that we can build an ADC that works with efficiencies of ~90% across the complete wavelength range, with a slightly larger loss at the very extreme wavelengths both at the red and blue ends. We consider that the benefits of having an ADC compensate the efficiency loss.

We have considered the possibility of making the ADC deployable, so that it could be inserted and extracted from the optical path, so that the user could choose if they wanted to use it. This idea is not implemented in the baseline design, but could be developed in the future.

2.2.3. Systems engineering and interface requirements

The OCTOCAM Systems Engineering team performs the following tasks during OCTOCAM development, design, assembly, testing, and installation onto the Gemini Observatory:

1) Identify and track verification of technical requirements through a comprehensive test program
2) Control system interfaces
3) Manage technical resources
4) Ensure technical coordination of the instrument team
5) Assist the PM with management of the risk reduction program.

Gemini interface requirements are shown in the requirements flow-down (Figure 29). The OCTOCAM Systems Engineering team evaluated the Gemini-provided Interface Control Drawings and other supporting information to determine what instrument requirements would need to be included in order to interface with Gemini. The OCTOCAM instrument is compliant with these interface requirements.

Instrument Subassemblies

A top-level block diagram of the OCTOCAM instrument is shown in Figure 35. The main subassemblies are noted below. More detail on each subsystem is included in the sections referenced below.

1) Optical Design – Section 2.3
2) Mechanical Design – Section 2.4
3) Infrared Cryostat – Section 2.5
4) Detectors – Section 2.6
5) On-Instrument and Off-Instrument Electronics – Section 2.7
6) On-Instrument Control Software – 2.8
7) Data Reduction Pipeline – 2.9

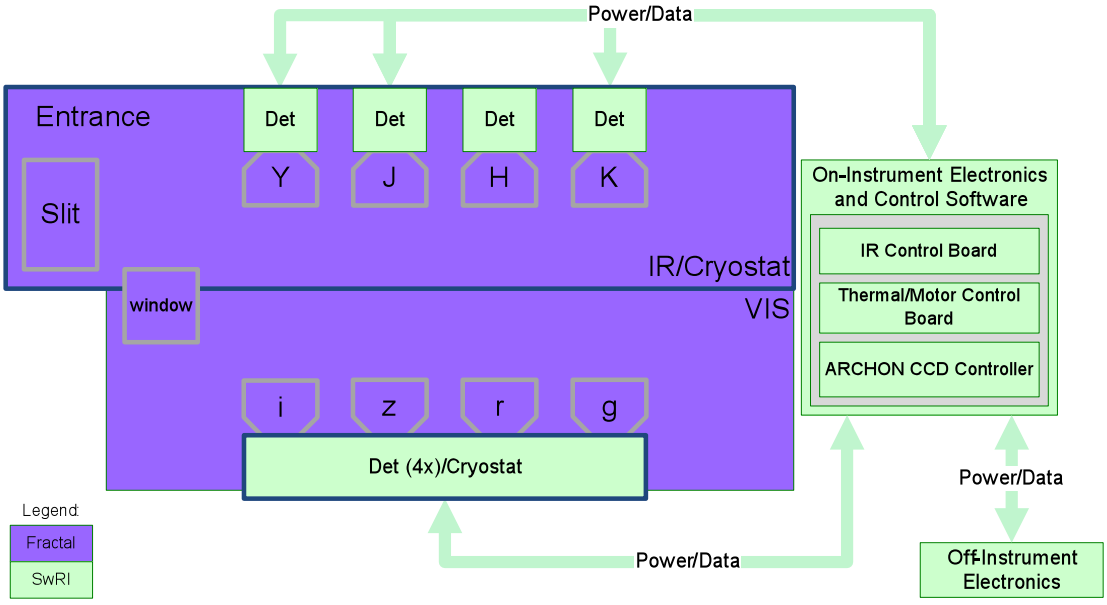

Figure 35 - Block diagram of the OCTOCAM instrument.

Feasibility of Concept

The science and interface requirements were used by the OCTOCAM team to design the instrument's subassemblies. The designs presented in the latter sections of this document were evaluated for feasibility and compliance with the science and interface requirements.

Observatory interface compliance

The OCTOCAM team has reviewed the Gemini interface requirements and has taken them into account during our design process. The key requirements from Gemini are included in the requirements flow-down shown in Section 2.1.2 (Requirements flow-down). OCTOCAM will be compliant with all requirements. Specific details on requirements compliance is included in the subassembly sections.

Mass budget estimation

With the present configuration, we have roughly estimated the mass budget of the complete instrument. With the contingency margin of 20% that has been considered, OCTOCAM is still comfortably within the mass limit of the focal port (2000 kg).

Element	Weight (kg)
Optics	40
Space frame	245
Cryostat (top)	83
Optical bench	220
Cover	67
Opto-mechanics	90
Electronics boxes	458
VIS arm cooling system (SwRI)	44
Cold bench	156
CCD controllers	24
Cryocoolers (2x)	45.2
Radiation shield and supports	40
Glass-epoxy supports (x6)	6
ADC mount – rotator	10
VPH stages (4x)	24
TOTAL	**1545 kg**
Contingency (20%)	**309 kg**
TOTAL with Contingency	**1854 kg**

Table 8 - Mass budget.

2.3. Optical design

2.3.1. General Layout

OCTOCAM is an eight arm imaging spectrograph as seen in Figure 36 and Figure 37. All arms share common pre-optics and focal plane where the focal plane carriage positions slits, IFU and polarimeter optics.

After a careful analysis we chose a design with a single slit, which ensures that all the spectrographs are fed by light from the same sky position and guarantees a better data calibration. A single slit eliminates the need of adding active optics to compensate flexure and obtain an alignment between slits that would be never perfect. Finally, a single focal plane also allows the installation of an integral field unit and a spectropolarimeter.

The light from telescope crosses the ADC for chromatic atmospheric correction. The NIR arms (Y, J, H and K_S) and the slit are enclosed inside a cryostat whose entrance is CW1 (Cryostat Window 1). This window is made in IR fused silica and has a size of 180mm x 30mm. A dichroic reflects VIS light (g, r, i and z bands) to an exit cryostat window, CW2. This window is made of BK7 and has dimensions of 180mm x 30mm. Thus, the VIS arm is at environment observatory conditions (hereafter called "warm").

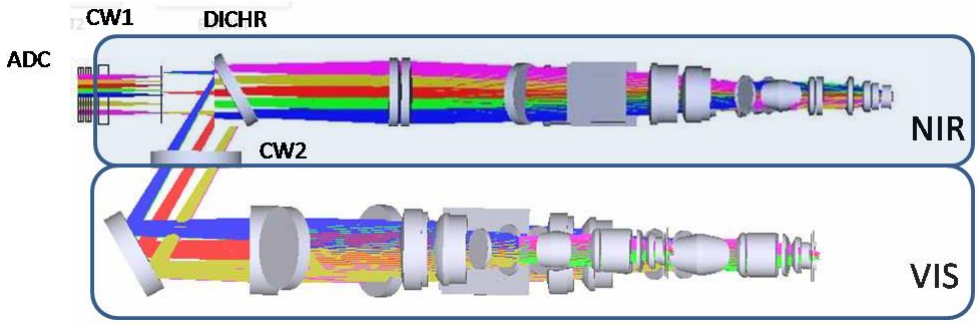

Figure 36 – Layout. Side view.

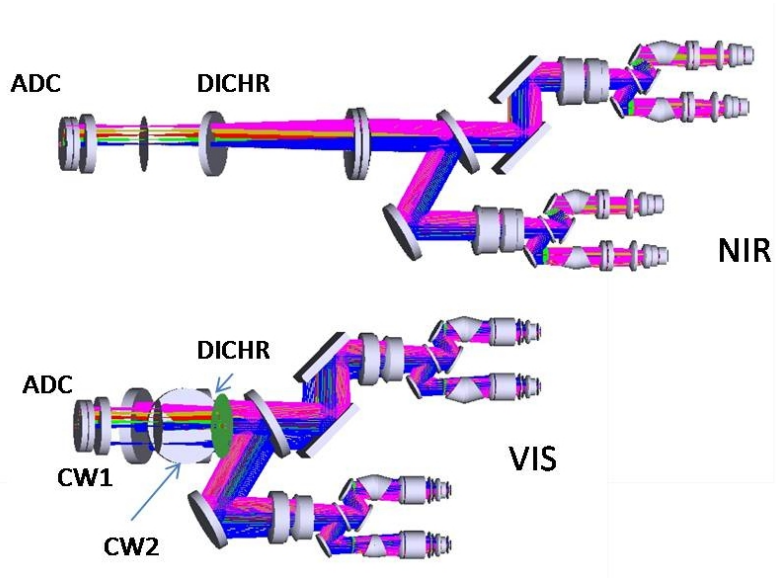

Figure 37 - Layout. Top view. The four VIS arms and the four NIR arms are shown.

Being thermally stable, the focus of all NIR arms will be stable and provided by the telescope optics. The VIS arms will have individual focusing mechanisms within the camera optics.

2.3.2. Atmospheric dispersion corrector

The Atmospheric Dispersion Corrector, ADC, is based in a double Amici prism set. Prisms are circular and have 170mm in diameter to provide full, unvignetted correction (for both imaging and spectroscopic modes).

The corrected wavelength range expands from 0.37 μm - 2.35 μm and is designed to work for zenithal distances of up to 50 deg. At lower elevations there is some chromatic degradation that could derive in slit losses in the bluest part of the spectrum (60 deg from zenith within 1"). Below these elevations, the use of parallactic angle is recommended for spectroscopic observations. Prisms have been designed to provide an un-deviated beam (if ADC is removed) at 550 nm. In future stages of the design we will consider the possibility of allowing an ADC that would go in and out of the optical path to increase the efficiency of observations (by ~11%) when the ADC is not needed.

Building an ADC capable of working at larger zenithal angles is possible, but with the penalization of thicker prisms and consequently lower transmission. This design has been chosen as a compromise of transmission and efficiency of scientific operations.

Figure 38 shows the ADC layout. Prisms materials are S-FTM16 and S-FPM2 from Schott.

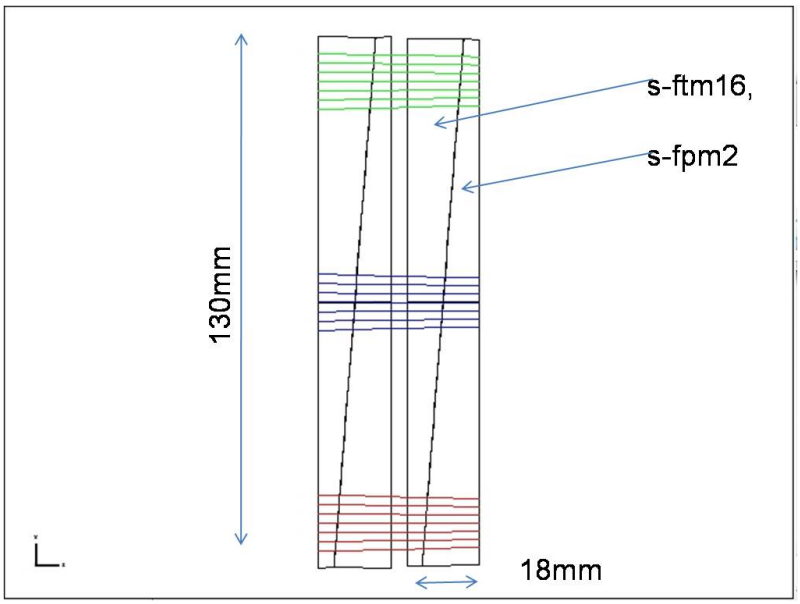

Figure 38 - Layout and aperture if only used for spectroscopy.

Figure 39 shows how the ADC corrects the atmospheric dispersion at an elevation of 45 deg. Figure 40 shows the efficiency of the current ADC design. In the design phase of the instrument we will work on improving the selection of coatings and materials to enhance the overall efficiency as we believe that there is still space for improvement.

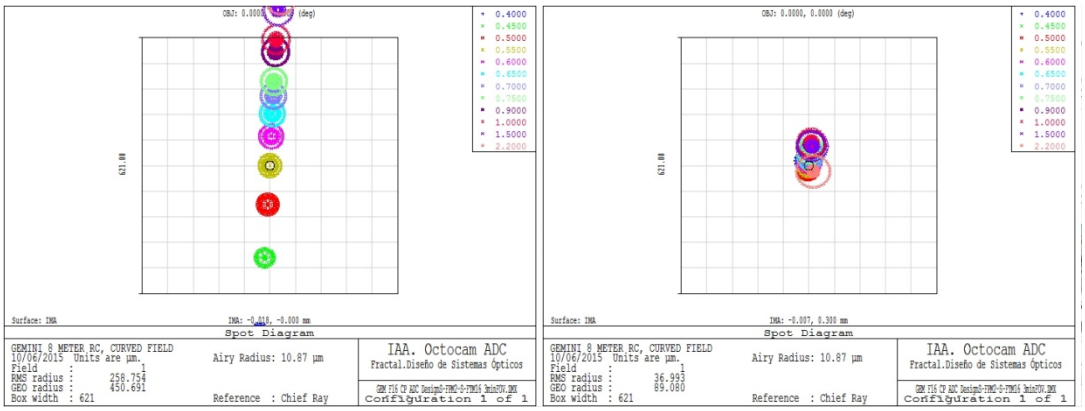

Figure 39 – Behavior of the light without (left) and with (right) ADC. Elevation is 45 degrees. Box size matches the slit width at Gemini (0.54").

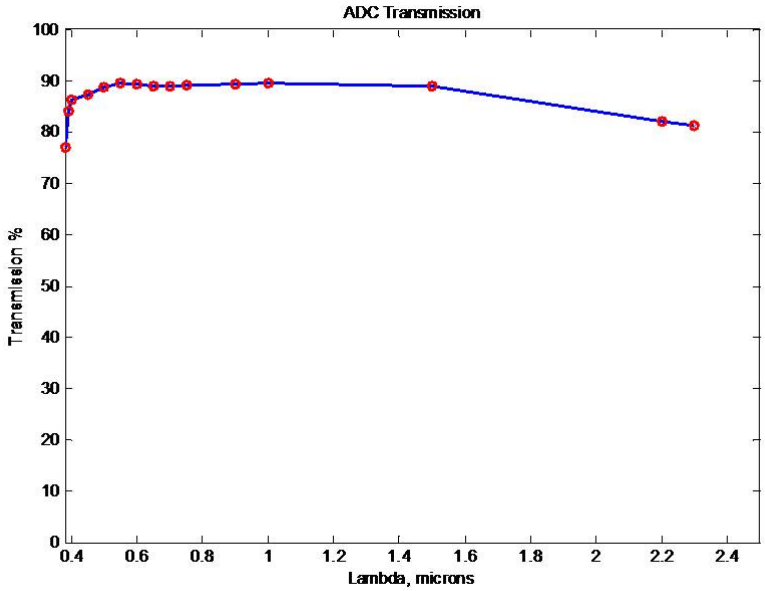

Figure 40 – Transmission of the ADC, including coatings, glass absorption ,and Fresnell losses.

Figure 41 shows the degradation out of the designed range (0 deg – 50 deg), even beyond the typical limit of operation of the Gemini telescopes (60 deg). All boxes in the figure have a 1-arcsec side. In the particular case of the IFU, the observations are tolerant of imperfect atmospheric dispersion correction, being able to work out of the ADC design range. The field of view with the full wavelength range is however slightly smaller in the direction of the atmospheric dispersion after correcting for this dispersion via software.

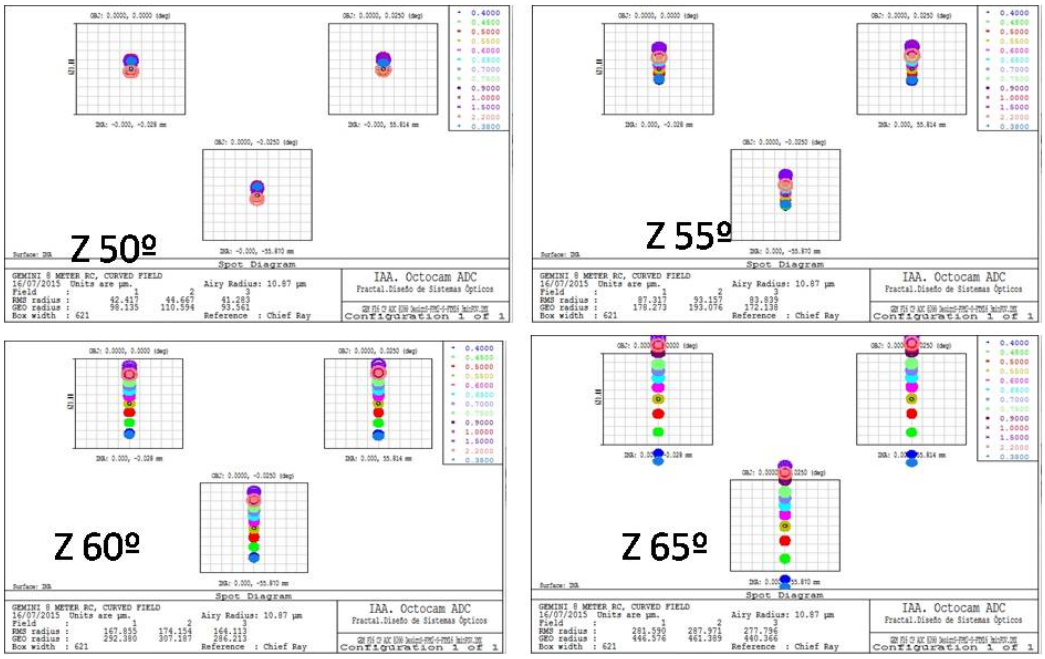

Figure 41 - Degradation out of designed range (nominal from 0 deg to 50 deg). 1" boxes.

2.3.3. Cryostat windows and dichroic

The cryostat windows (CW1 and CW2) are flat. The main difficulty is the AR coatings due to the broadband range. Figure 42 and Figure 43 show predicted curves from a manufacturer (Tafelmaier) on feasible coatings. These values will be the ones used for throughput error budget.

The dichroic for the NIR arm and CW2 for the VIS arm will be used tilted 30 deg. This tilt introduces a dominant astigmatism at all the focal planes. Dichroic thickness will be minimized to lower the effect (20mm in current design) but CW2 is limited by the pressure safety factor.

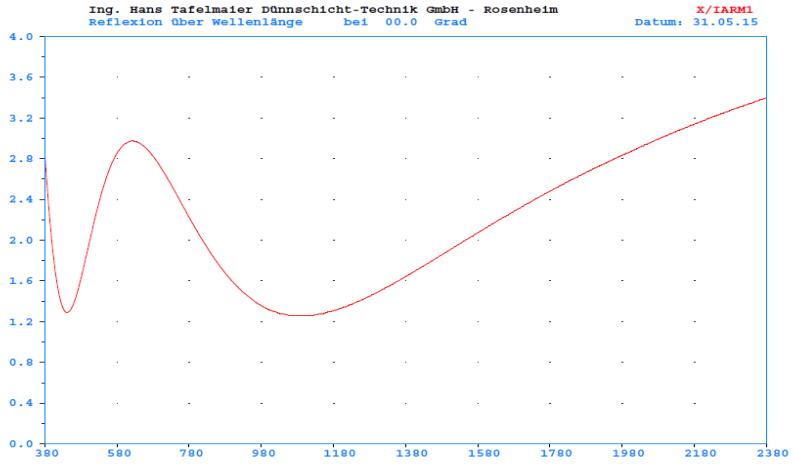

Figure 42 - Broadband AR coating. This will be used for ADC, CW1 and CW2. The mean loss is 2.3%.

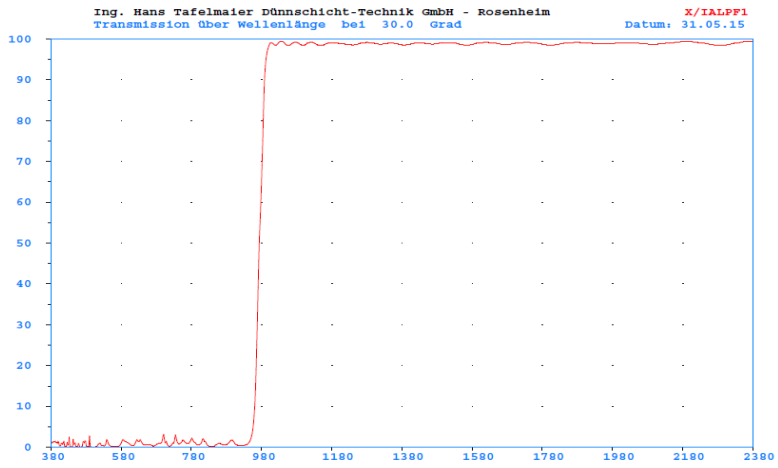

Figure 43 - Dichroic transmission for an AOI of 30 deg. T > 97%.

The CW2 window is not only the exit of the VIS channel, but will also have to prevent the IR thermal photons to get a path to the NIR cryostat. Thus a dichroic coating shall be also applied on this window to reject incoming NIR photons. Additionally, specific baffling shall be addressed during the stray light analysis, in the next phase. We note that there is not direct optical view from the NIR detectors to this window.

2.3.4. NIR arm

The design follows a classical collimator-grating-camera layout, being all refractive elements. To provide the required scale from the telescope focal plane (621 micron/") to the detector (0.18"/pixel or 100 micron/"), the ratio effl cam/effl coll is 6.21.

A 50 mm pupil was selected because this is the minimum size that can provide camera focal length and dispersion elements for the required resolution for the required slit size.

All the four arms are identical and there are not aspheric lenses in the current design. All selected glasses are well known IR candidates. Index n(T) models are available.

We extract an arm and remove the folders and dichroics for clarity leaving only the powered elements. The collimator layout is shown in Figure 44. This subsystem is made of 6 decoupled singlets. The design could eventually be simplified in the next phase at least by removing one lens.

NIR COLLIMATOR	
Effective focal length	**810 mm**
Full FOV (deg)	10.7 deg
Pupil size	50 mm
F#	F 16.2

Table 9 - NIR Collimator main parameters.

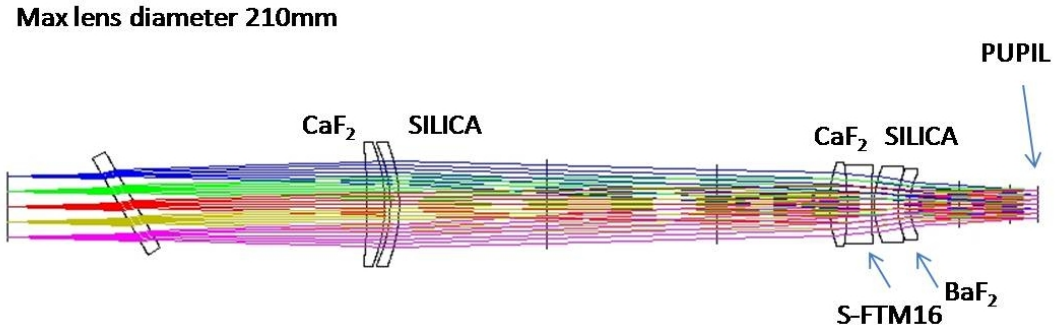

Figure 44 - NIR Collimator layout.

Using a perfect camera after the collimator, we can see the residual aberrations of the collimator. These aberrations are introduced by the dichroic. Lateral color and astigmatism are shown in the spot diagram of Figure 45.

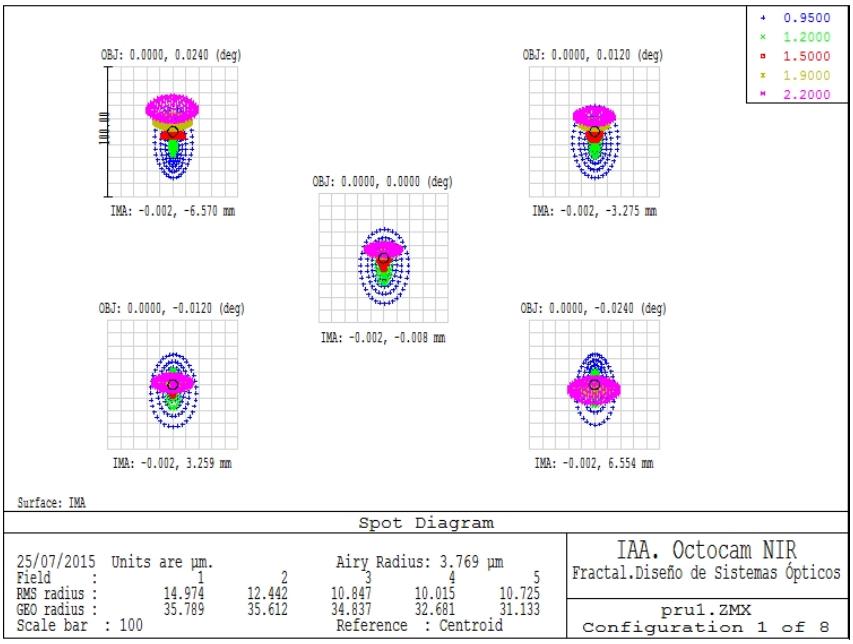

Figure 45 - NIR Collimator performance. Full wavelength range.

The collimator provides a 50mm pupil. Some lateral color from the ADC is seen at different elevations. As bands are narrow the effect is not large, although the final pupil position shall be adjusted to the mean position of the elevation range (see VIS arm for more detail). The optical design has been made so that cold Lyot stops can be placed in each of the NIR arms, although they are not shown in the mechanical design in this phase. The IFU (see Section 2.10) has its own high-quality Lyot Stops.

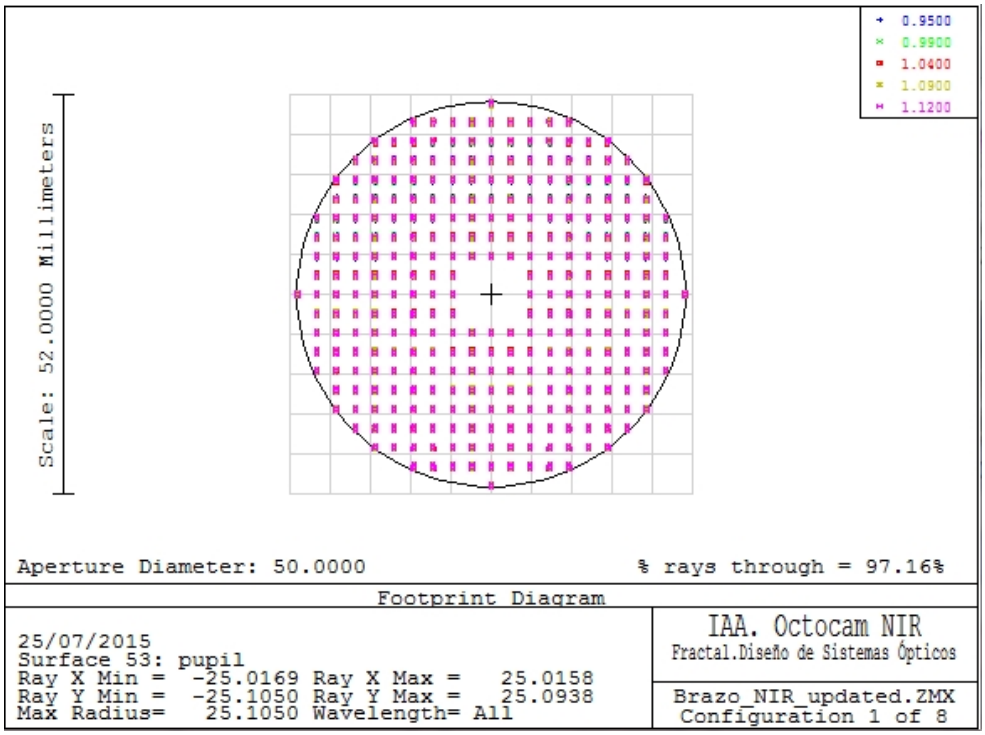

Figure 46 - Pupil position at *Y* band (maximum chromatic aberration in the NIR arms).

The camera layout is shown in Figure 47. This subsystem contains 6 singlets. The camera main parameters are shown in Table 10 .

NIR CAMERAS	
Effective focal length	130 mm
Full FOV (deg)	18 deg
Pupil size	50 mm
F#	F 2.6

Table 10 - NIR Camera main parameters

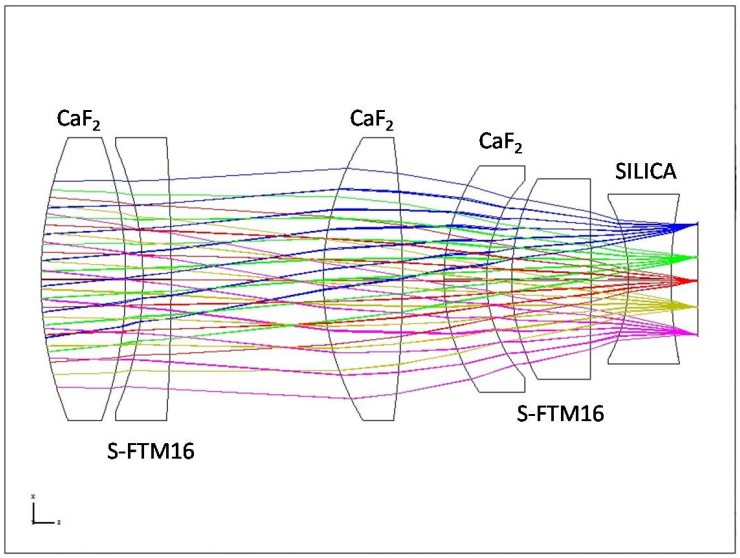

Figure 47 - NIR Camera layout.

The camera alone, being illuminated by a 50mm collimated beam in an 18º FOV provides a good image quality performance at focal plane, as shown in Figure 48.

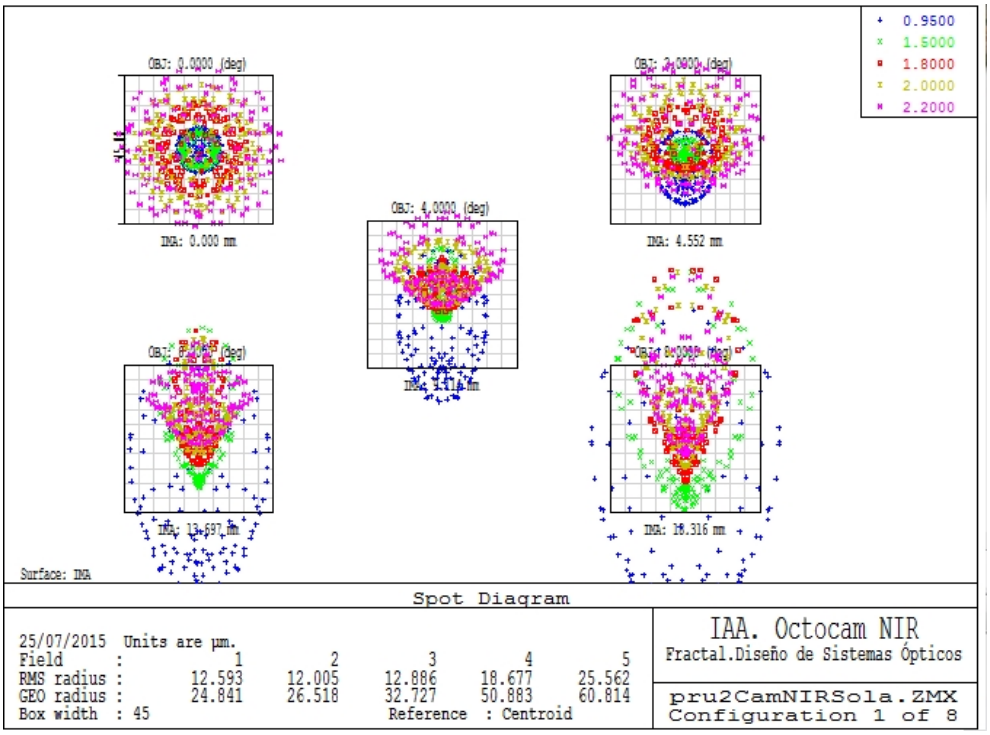

Figure 48 - NIR Camera image quality in the NIR full wavelength range.

To assemble the four arms into a compact volume, a number of folder mirrors and dichroic uses are needed. These are summarized in Table 11.

	Dichroic in reflection	Dichroic in transmission	Folder mirrors
ARM 1	1	2	2
ARM 2	2	1	3
ARM 3	2	1	3
ARM 4	3	0	4

Table 11 - NIR arm. Flat elements required.

In the NIR arm mirrors will be gold coated.

The thermal stray light budget is an important issue to be considered.

There are two main apertures CW1 and CW2 where undesired light can enter the cryostat. The exit dichroic and window, CW2, which is always open (for both imaging and spectroscopy modes). An absorption cold filter right before leaving CW2 could be required to control high AOI photons from the VIS chamber.

An entrance field stop at the nominal focal plane shall be available to block stray light.

Finally, a fixed pupil stops will be introduced in the NIR bands, especially in the K_S band for thermal emission control.

2.3.5. VIS arm

The VIS design also follows a classical collimator-grating-camera made of all refractive elements. To provide the required scale from the telescope focal plane

(621 micron/") to the detector (0.18"/pixel or 83.3 micron/"), the ratio effl cam/effl coll is 7.45.

A 50 mm pupil was selected because it is about the minimum size that can provide camera focal length and dispersion elements for the required resolution for the required slit size.

Three arms are identical except for the *g*-band, where a bigger camera covering a 4Kx1K detector area (in the spectral mode) has been designed.

We extract an arm and remove the folders and dichroics for clarity, leaving only the powered elements. The collimator layout is shown in Figure 49. The main parameters are summarized in Table 12. This subsystem is made of three doublets. It is possible to simplify the design in a future optimization by removing one of the lenses.

VIS COLLIMATOR	
Effective focal length	**810 mm**
Full FOV (deg)	10.7 deg
Pupil size	50 mm
F#	F 16.2

Table 12 - VIS Collimator. Main parameters.

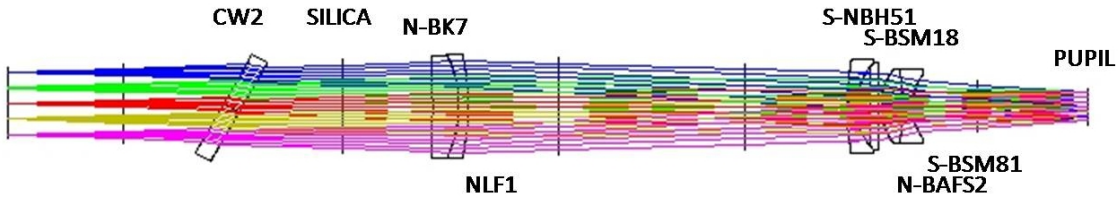

Figure 49 - VIS Collimator layout.

Using a perfect camera after the collimator, we can see the residual aberrations of the collimator. The current lateral color is introduced by the collimator and balanced at the camera. Some astigmatism due to CW2 is seen in the spot diagram Figure 50.

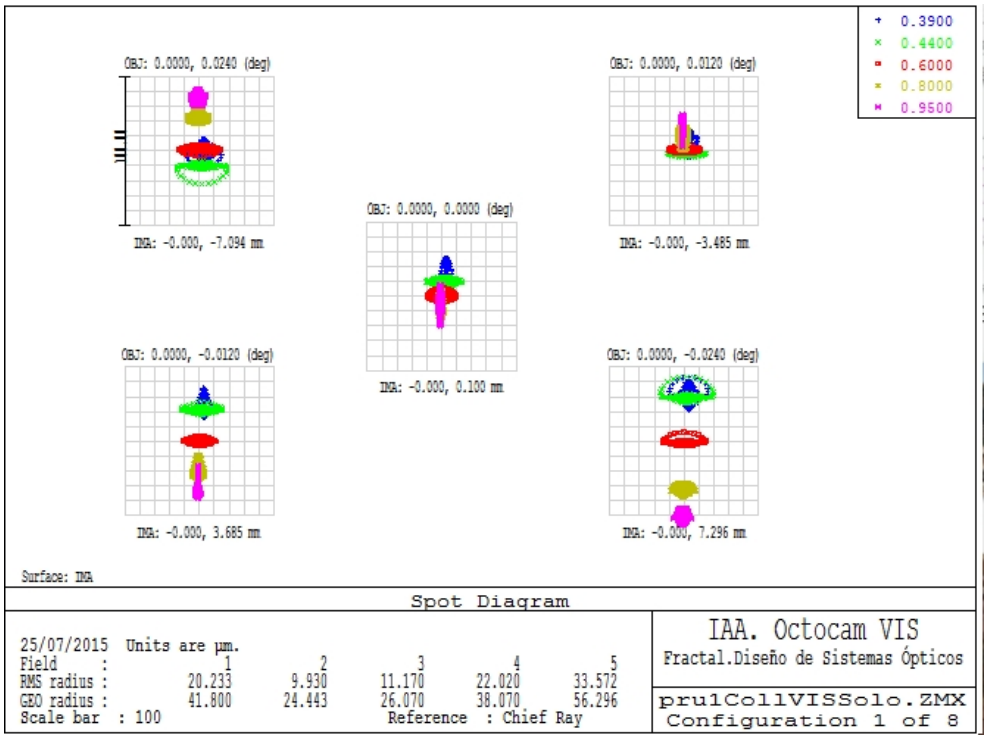

Figure 50 - VIS Collimator performance. Full wavelength range.

The collimator provides a 50 mm pupil with some minimum residual aberration from the ADC and the collimator. It has no effect in the performance, and is slightly oversized.

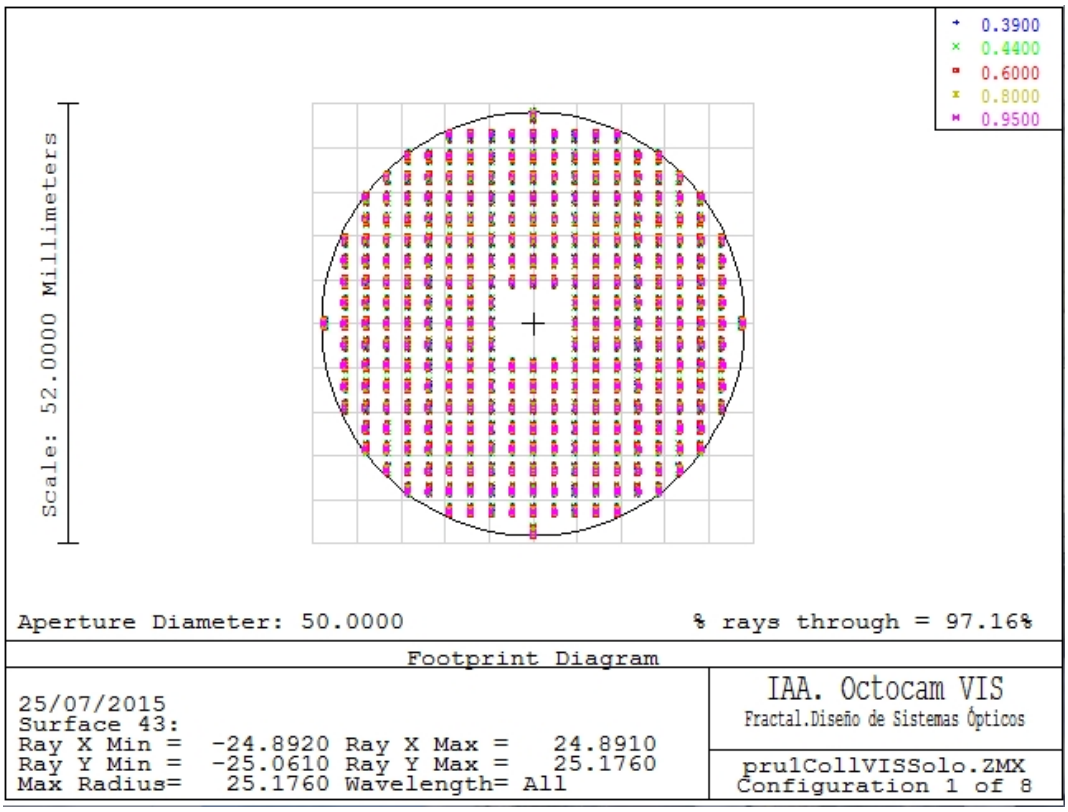

Figure 51 - Pupil footprint in the whole VIS wavelength range.

An ADC not placed in a pupil position (as it is the case) corrects chromatic aberrations at the focal plane, but introduces chromatic aberrations in the pupil images. There are no effects in having an oversized pupil in the VIS channel, but an increase of thermal noise should happen if all flux is to be used at NIR. As each of the band passes of each arm has a small wavelength range, a fixed decentering of the pupil stop should allow centering the pupil with minimum losses (increasing the aperture to 51mm to accept 50mm pupil for *Y* band). At the K_S band the errors are lower because of the smaller dispersion.

Figure 52 shows four plots: The plots on the top of the figure are given at Zenith (as in Figure 51) while the plots in the bottom are for a zenith angle of 50 deg. The pupil shift can be clearly seen in the lower plots. For each set, we have plotted all the wavelengths on the right panel and a selected wavelength on the left. We note that, as the spectral ranges will be separated into the different channels, the actual effect within each channel will be much lower.

In NIR the effect is lower also since we will shift the cold stop as required for the channels *H* and K_S to get a good thermal suppression.

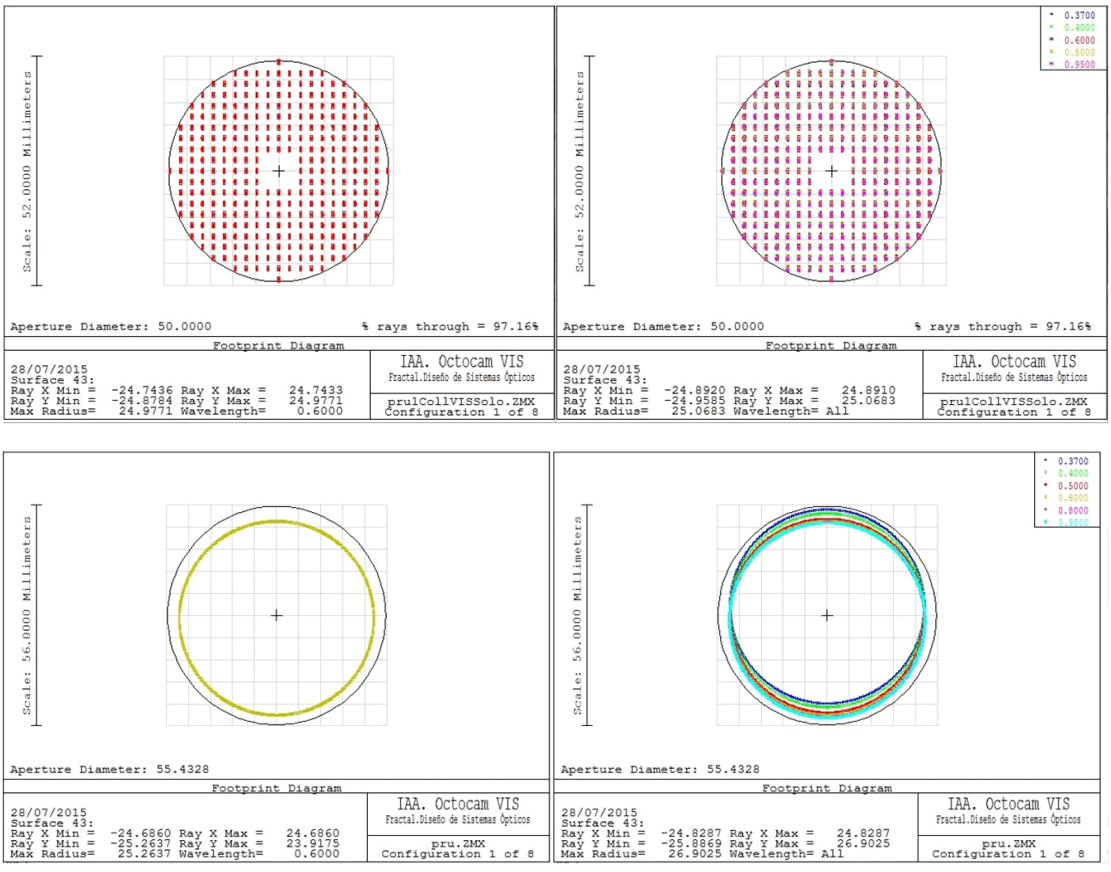

Figure 52 - Pupil footprint when pointing at Zenith (top) and at 50 deg (bottom). In each case pupils are plotted at a selected wavelength (monochromatic) at 600nm (left) and the whole wavelength range (right). Diameters at Zenith are 49.8 mm for monochromatic and 50.01 mm for the whole range. Diameters at 50 deg are 49.16 mm for monochromatic and 52.70 mm for the whole range.

There are two VIS camera designs:

The first camera design is made for the *r*, *i* and *z* arms (can also be used for *g* if a 1kx2k detector was chosen). The main VIS camera parameters are shown in Table 13.

VIS CAMERAS (*r*, *i*, *z*)	
Effective focal length	108.5 mm
Full FOV (deg)	18 deg (corner)
Pupil size	50 mm
Detector coverage	30.72 mm x 15.36 mm
F#	F 2.17

Table 13 - VIS 2Kx1K camera. Main parameters.

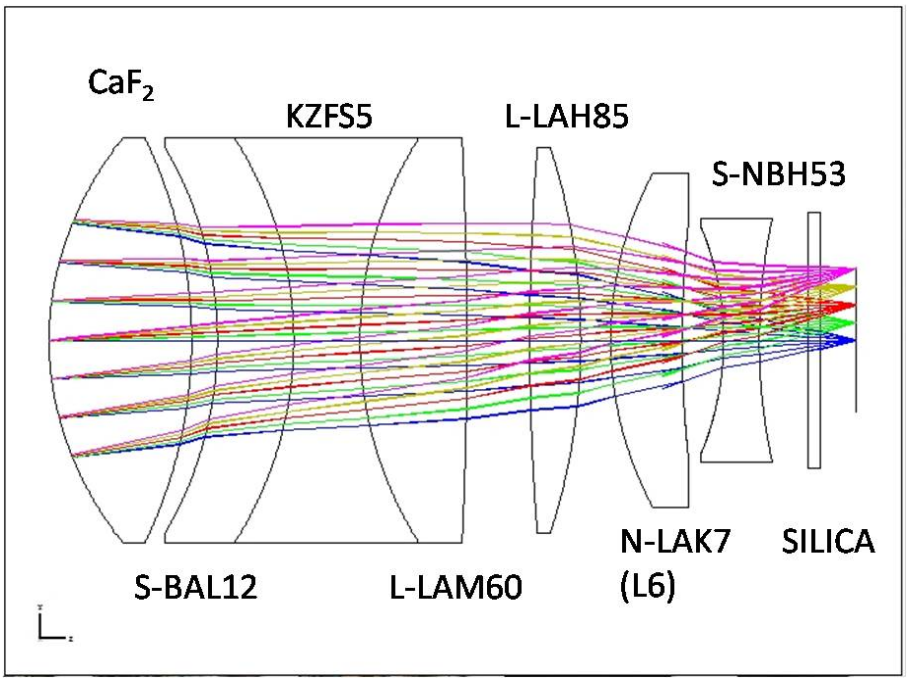

Figure 53 - VIS Camera layout.

The camera alone, being illuminated by a 50 mm collimated beam in an 18 deg FoV is shown in Figure 54. The maximum lens diameter is 90 mm with one aspherical surface (first surface on CaF_2). Active focus is foreseen at L6 to optimize image quality. After a trade-off study we find this lens to be the most adequate for focusing, and feasible in spite of the limited space. This is preferable to other possibilities such as moving detectors or other optics.

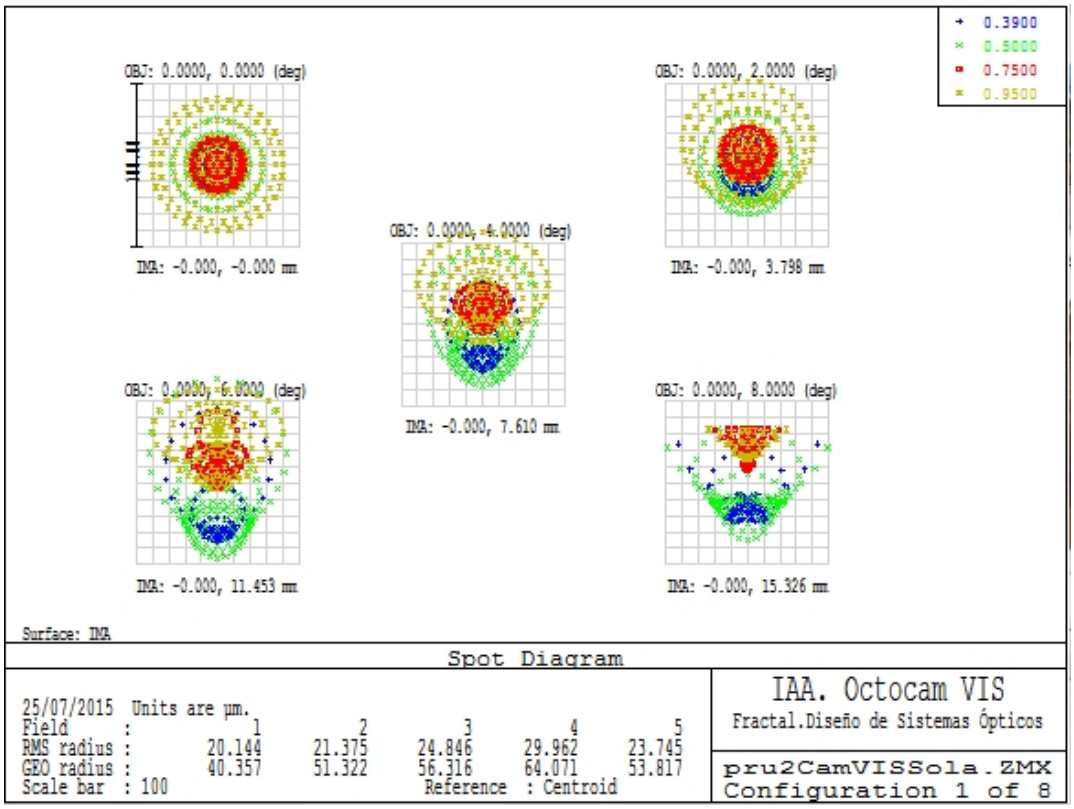

Figure 54 - VIS Camera image quality in the VIS full wavelength range.

There is a second camera design to cover the *g*-band at the required resolution.

This camera (see layout in Figure 55) uses the same collimator as the previous one. The design is made to cover 4 kpx in the spectral direction and 1 kpx in the spatial direction.

The VIS 4k x 1k camera main parameters are shown in Table 14.

***g*-BAND CAMERA**	
Effective focal length	**108.5 mm**
Full FOV (deg)	32.5 deg (corner)
Pupil size	50 mm
Detector coverage	61.44 x 15.36 mm
F#	F 2.17

Table 14 - VIS 4Kx1K Camera. Main parameters.

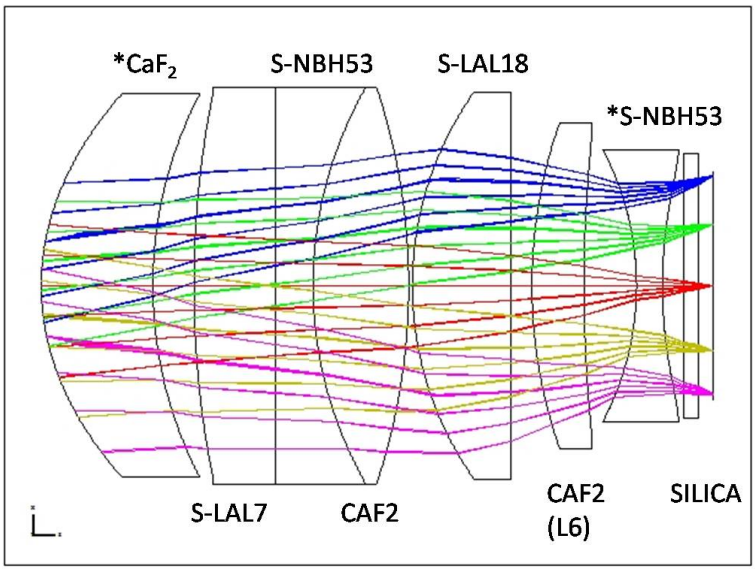

Figure 55 - VIS 4K x 1K Camera layout. Aspheric surfaces are shown with *.

The camera performance alone, being illuminated by a 50 mm collimated beam in a 32 deg FoV is shown in Figure 56. The maximum lens diameter is 90 mm with two aspherical surfaces (first surface on CaF_2 and L7 on S-NBH53). Active focus is foreseen at L6 to optimize image quality. Lateral chromatism is balanced with the collimator.

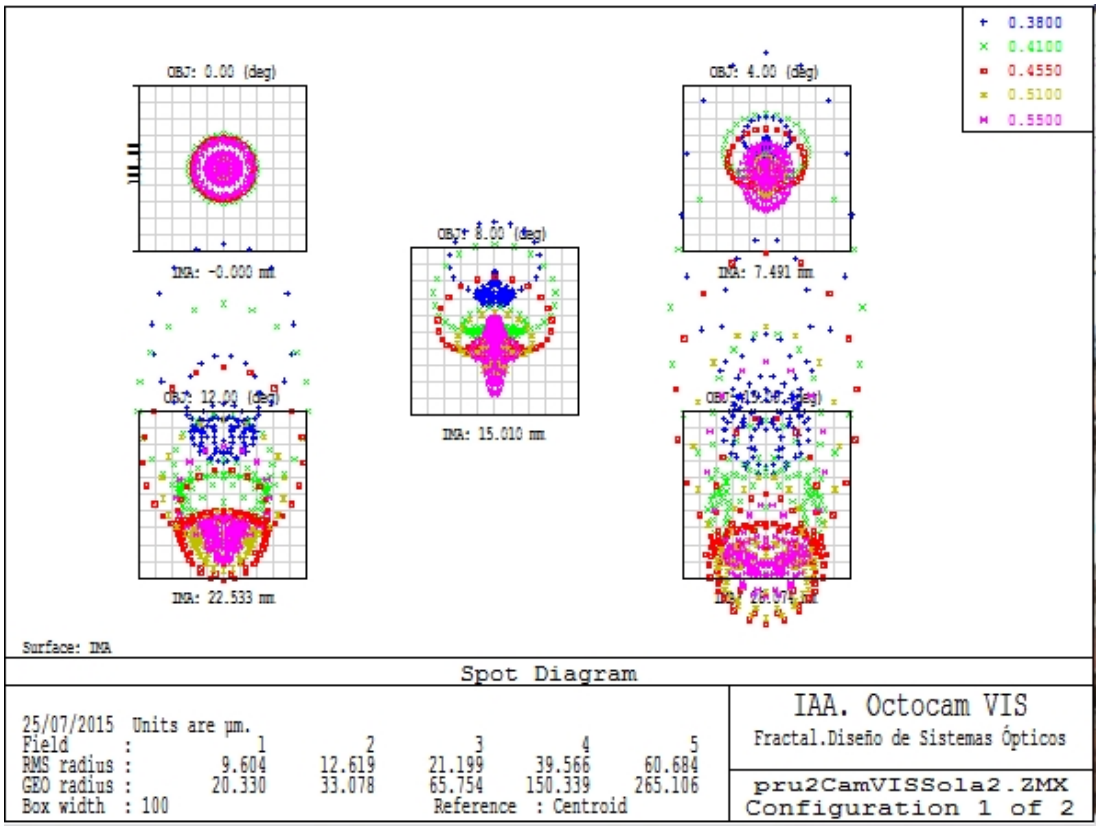

Figure 56 - 4k x 1k Camera image quality in the VIS full wavelength range.

Aspherical manufacturability requires further work for specification and contact with manufacturers.

In order to assemble the four arms in a compact space, a number of folder mirrors and dichroic uses are used. These are summarized in Table 15.

	Dichroic in reflection	Dichroic in transmission	Folder mirrors
ARM 1	1	2	2
ARM 2	2	1	3
ARM 3	2	1	3
ARM 4	3	0	4

Table 15 - Flat elements required.

Coatings for the mirrors in the VIS arm will be made on protected silver (*r*, *i*, *z*-bands) and aluminum (*g*-band) although coating details will be studied in more detail after consultancy with providers in a future phase.

2.3.6. Performance analysis

We have shown the individual performances of collimator and camera. Aberrations (such as lateral color) are balanced, thus the full unit performs better than the individual subsystems. In the performance analysis we show the full system. In a later phase the system will be analyzed and optimized to minimize the presence of ghosts.

Imaging mode. NIR arms:

There is one channel for each band, *Y*, *J*, *H* and K_S bands. The imaging FoV covers 1K x 1K pixels on the detector (3.07' x 3.07' on sky), with 18 µm/pix (see Figure 57).

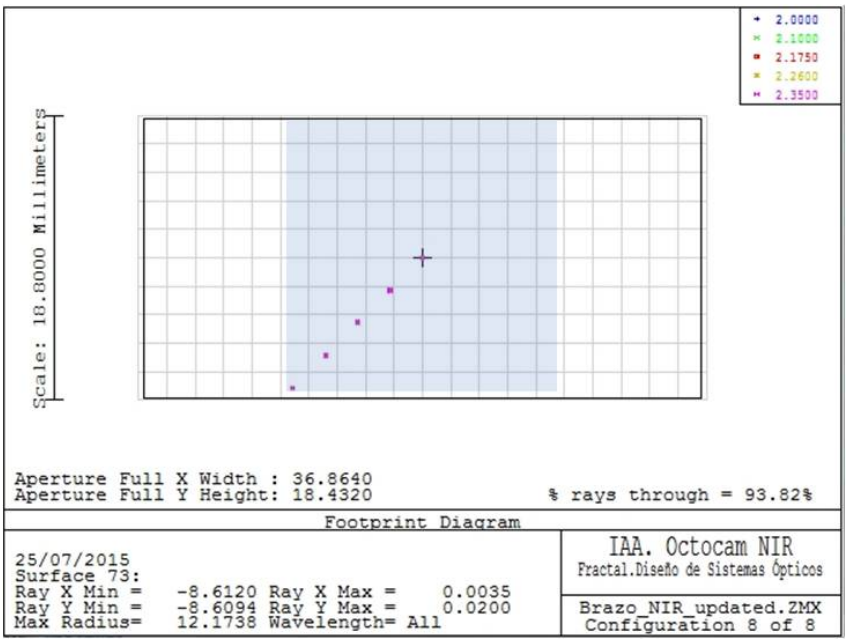

Figure 57 - NIR Detector view with the imaging area in blue. It is the same plot for the other channels.

The current image quality is providing 80% EED in less than 0.54".

	Y	*H*	*J*	K_S
EED at 80%(in pixels)	1.8	1.1	1.2	1.5

Table 16 - Image quality. The EED shown contain the worst case fields.

As a reference we show the spot diagram for each channel. See Figure 58.

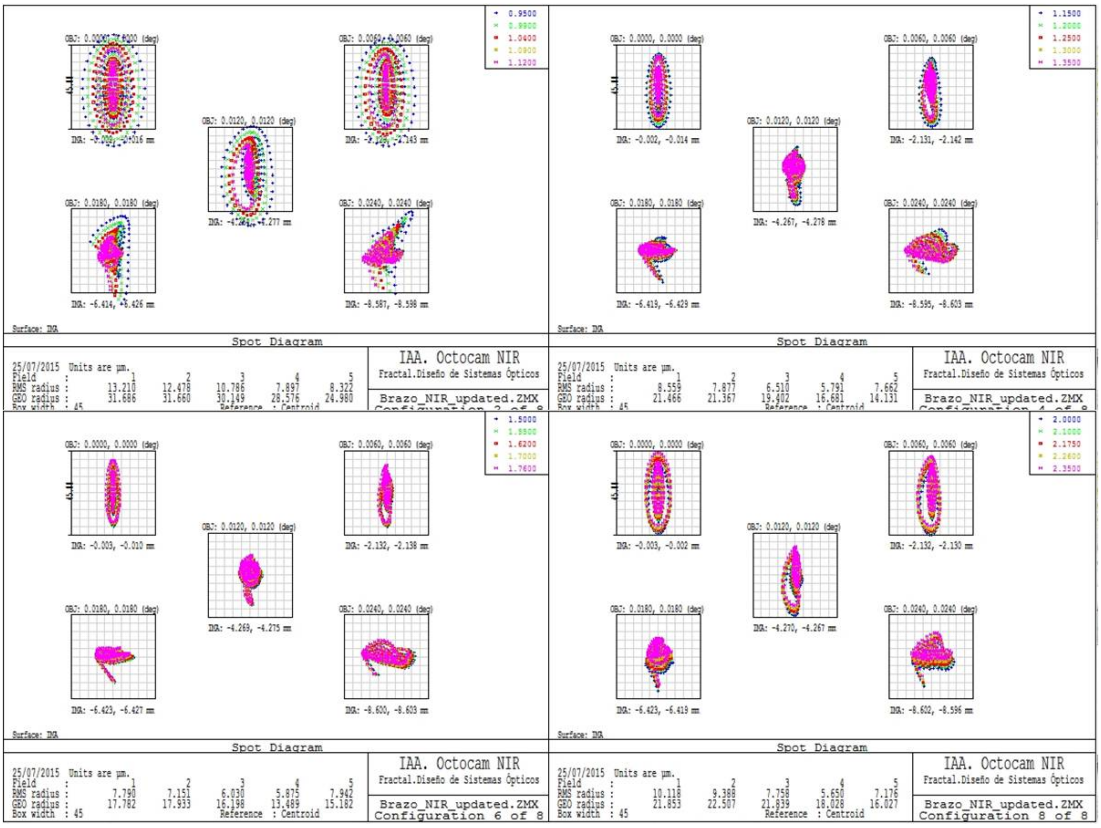

Figure 58 - Spot diagram for *Y*, *J*, *H* and K_S. Imaging Mode. Boxes are 45 microns wide (< 3 pixels).

The selected wavelengths are those used in the spectroscopy mode.

Distortion

The distortion has been plotted in Figure 59, which shows the results for *Y*, *J*, *H* and K_S bands. The maximum distortion level found is 1.2%. It is fully feasible to reach the level of 0.5% without further problems in the next optimization. A requirement should be given to be able to introduce this restriction in the merit figure. The merit figure used for optimization in Zemax during this phase has been the image quality requirement only.

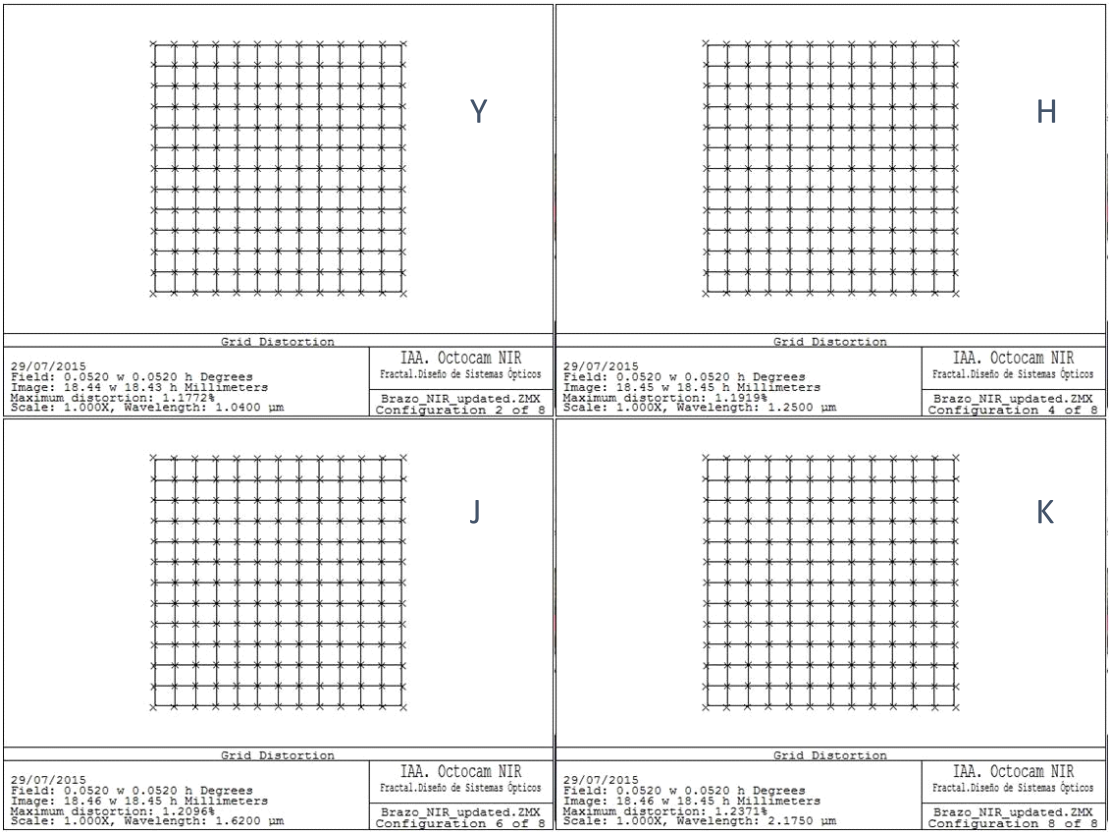

Figure 59 - Field Distortion. Imaging mode. Plots for Y, H, J and K bands.

Spectroscopy mode. NIR arms:

The main grating parameters and measured resolution in Spectroscopy mode are shown in Table 17.

BAND	Lin/mm	CWL (µm)	R at CWL	Spectral coverage (µm)
Y	1270	1.040	3886	0.95-1.12
J	1090	1.250	4016	1.15-1.35
H	810	1.620	3798	1.5-1.76
K	639	2.175	4068	2.0-2.35

Table 17 - NIR Spectroscopy Mode. Main spectral characteristics. A slit width of 0.54" on sky and 3 pixel resolution elements have been considered to compute the resolution.

The dispersive elements are shown in Figure 60. These can be inserted in the beam to provide the spectral dispersion. They consist of a VPH hologram sandwiched between two FS windows.

Two identical Cleartran prisms are used to obtain the desired AOI into the VPH. The maximum thickness has been limited under 50mm as this is a manufacturer limit in the CVD process to grow the blank. In the current design prisms are glued to the FS. It is to be analyzed the real coupling in cryogenic temperature of these elements (with different CTE).

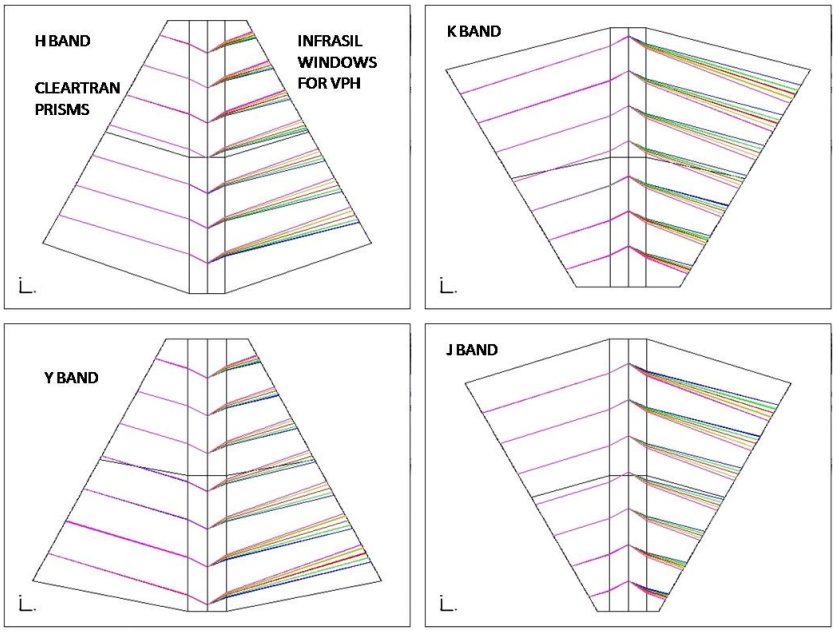

Figure 60 - Dispersive elements layout for H, Y, J and K band.

Figure 61 and Figure 62, the spot for image quality on detector in use is shown.

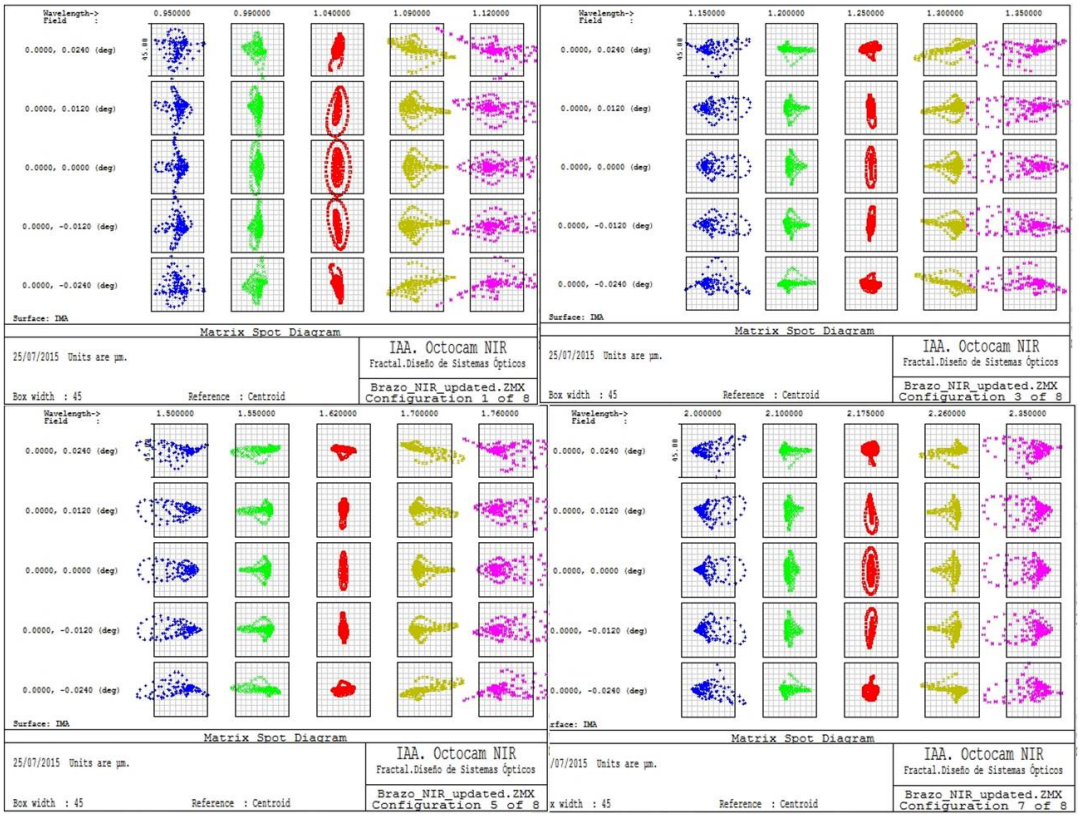

Figure 61 - Image quality (spot diagram) for each band, including all the optics and VPH. Each figure corresponds to the the fields shown in Figure 62. Box size is 2.5 pix.

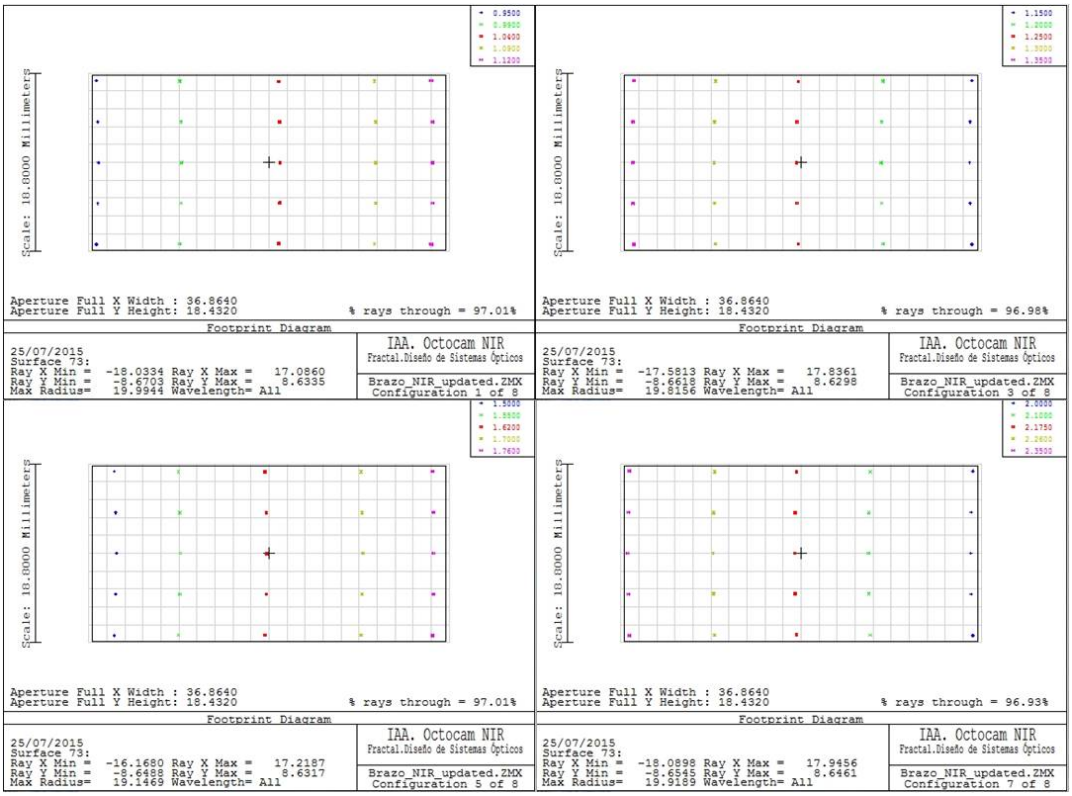

Figure 62 - Detector footprint showing the different wavelengths in each channel. The slit is centred in the middle of the image (from top to bottom). Spectral dispersion is from left to right. Zoom image to see wavelengths (band).

The average EED 80% is shown in Table 18. These numbers have been computed from all the spots shown in Figure 62.

	Y	*J*	*H*	*K*
EED at 80% (in pixels)	1.8	1.7	1.7	1.4

Table 18 - Image quality summary for the different bands.

NIR arms. Throughput

The following considerations have been taken into account.

- ADC. Internal absorption and 2.5% loss per air/glass surface (x 4)
- CW1. Average coating. Mean loss 2.3% (x 2). Negligible absorption
- Collimator. Internal absorption and 1.5% per air/glass (x 6)
- VPH. Hologram central efficiency of 0.85. Loss prisms (1.5%/surface (x2)
- Camera. Internal absorption and 1.5% per air/glass (x 12).
- Dichroics - T in transmission > 0.985 per surface. Negligible absorption
- Dichroics - R in reflection. 0.98.
- Folders. Gold. (0.99)

	Y	*J*	*H*	K_S
Wavelength (microns)	1.04	1.25	1.62	2.175
ADC	0.895	0.895	0.890	0.830
CW1	0.954	0.954	0.954	0.954
DICHR-R	0.960	0.960	0.960	0.960
COLLIMATOR	0.830	0.830	0.810	0.710
VPH	0.820	0.820	0.820	0.820
CAMERA	0.830	0.830	0.821	0.760
DICHR-T	0.940 (2)	0.970	0.970 (1)	-
DICHR-R	0.980 (1)	0.960 (2)	0.960 (2)	0.940 (3)
FOLDERS	0.980 (2)	0.970 (3)	0.970 (3)	0.960(4)
TOTAL	**0.42**	**0.42**	**0.40**	**0.30**

Table 19 – *Y*, *J*, *H* and K_S band transmission.

Imaging Mode. VIS arms

The three *r*, *i* and *z* band cameras use 1kx1k detector area providing 3.07' x 3.07' FOV in the sky.

	g	r	i	z
EED at 80%(in pixels)	2.3	1.6	1.6	1.6

Table 20 - Image quality summary for the different bands. Worst case.

In Figure 63 the footprint for the *z* band camera is shown.

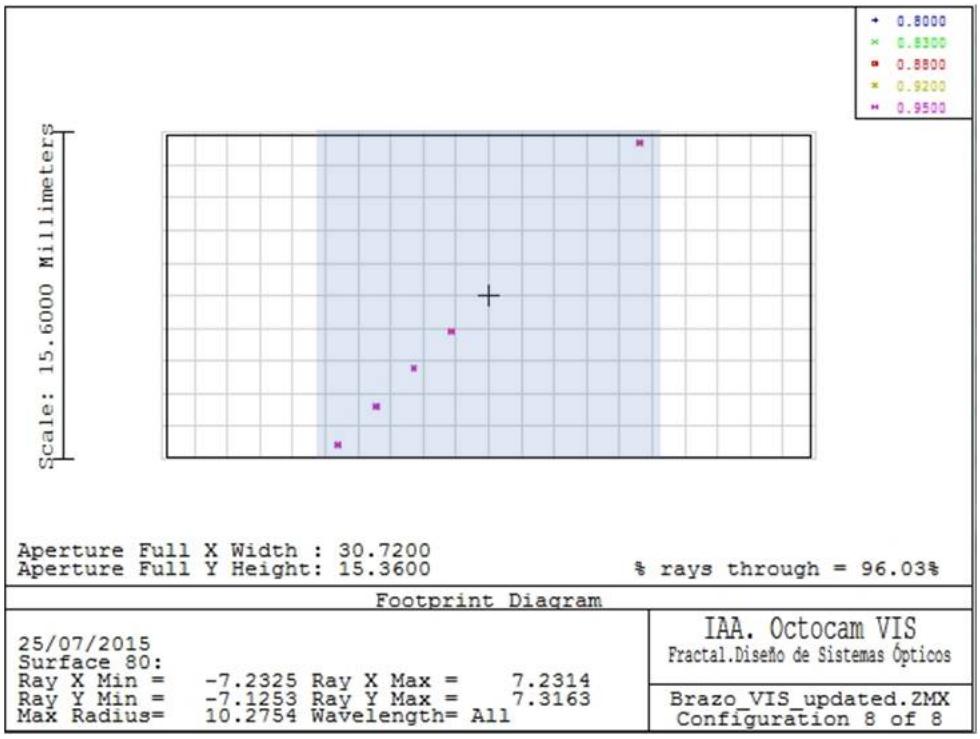

Figure 63 - VIS arms. Image Quality. Footprint for the z band. Zoom to see wavelengths.

Image quality is better than 80% EED in 25 microns (1.6 pixels) for *r*, *i* and *z* bands. Spot diagrams are shown in Figure 64.

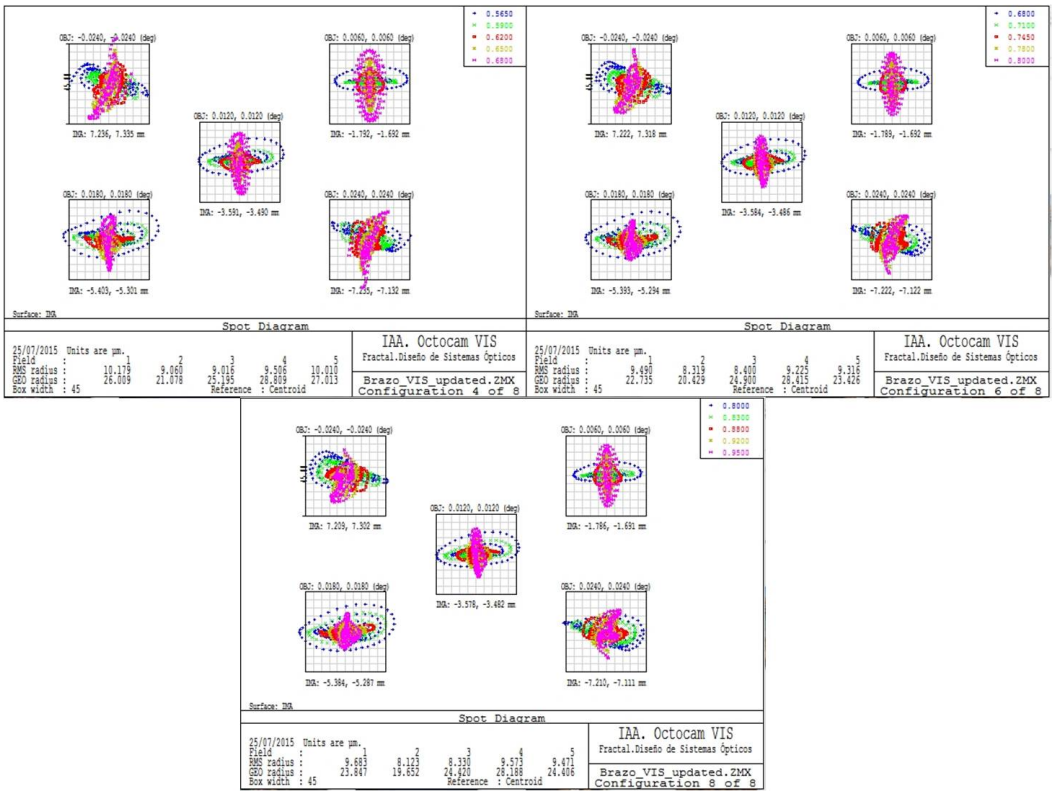

Figure 64 - VIS arms. Image Quality. Spot diagrams for *r*, *z* and *i* bands. Boxes are 3 pixels wide.

The *g*-band camera provides a 1kx1k imaging area, the same as for the previous cameras. Footprint and spot diagram are shown in Figure 65. 80% EED is within 34 microns (2.3 pixels) for g band.

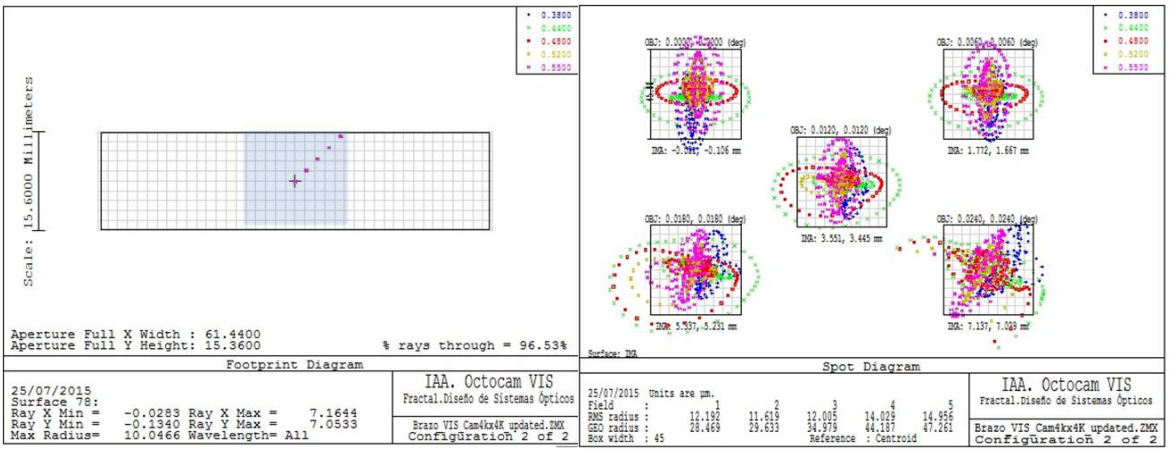

Figure 65 – *g*-band camera performance. On the left the imaging area coverage. On the right the spot diagrams. Zoom to see wavelengths.

Distortion

The distortion has been plotted in Figure 66, which shows the results for *g*, *r*, *i* and *z* bands. The maximum distortion level found is 1.2%. It is fully feasible to reach the level of 0.5% without further problems in the next optimization. A requirement should be given to be able to introduce this restriction in the merit

figure. The merit figure used for optimization in Zemax during this phase has been the image quality requirement only.

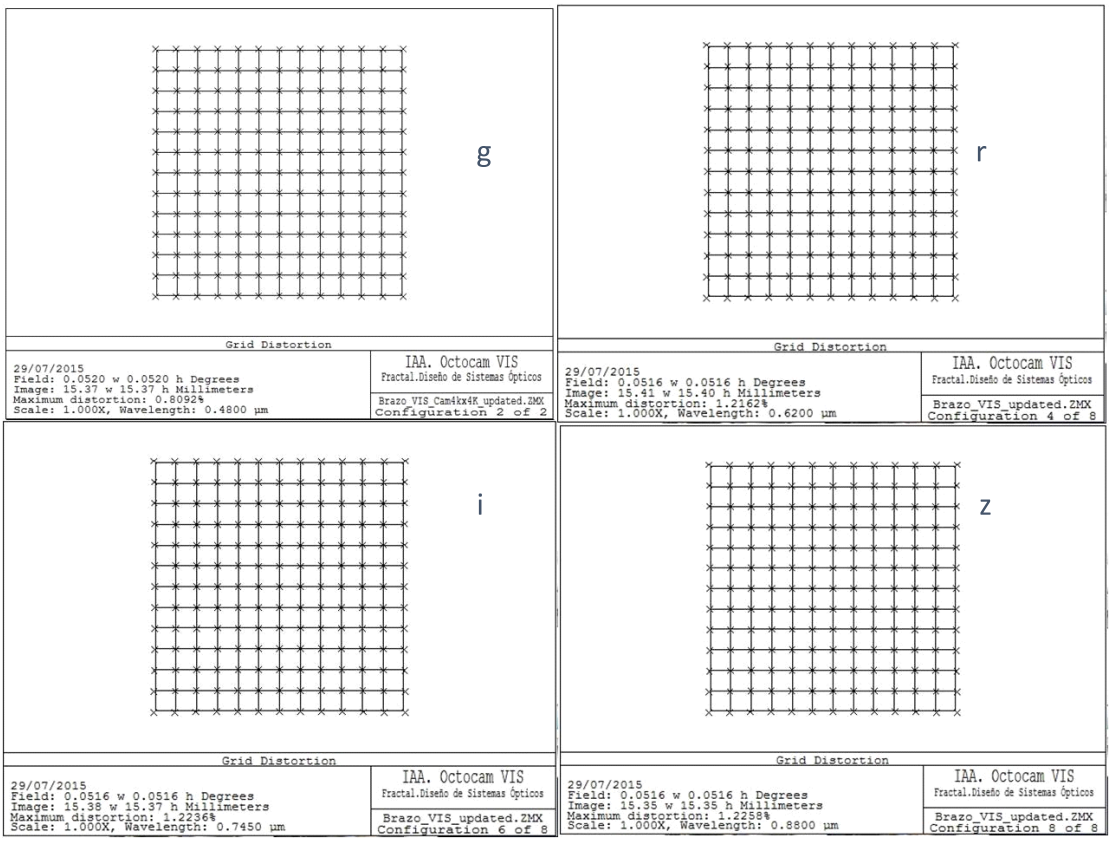

Figure 66 - Field Distortion. Imaging mode. Plots for g (on 4k x 1k camera), *r*, *i* and *z* bands.

Spectroscopy mode. VIS arms

Two camera types fixed to the mode will be used. A FOV 4k x 1k camera for the *g* band, and a FOV 2k x 2k camera for *i*, *r* and *z* bands.

The dispersive elements are shown in Figure 60. These can be inserted in the beam to provide the spectral dispersion. They consist in a VPH hologram sandwiched between FS windows.

Two identical SF6 prisms (<50mm in maximum thickness) are used to obtain the desired AOI into the VPH, see Figure 67. In the current design prisms coupled to the FS.

The main grating parameters and obtained resolution are shown

BAND	Lines/mm	CWL (nm)	R at CWL	Spectral coverage
g	2200	455	3369	380-550
r	1640	620	3240	565-680
i	1425	745	3352	680-800
z	1200	880	3273	800-950

Table 21 - Main spectral characteristics. A slit width of 0.54" on sky and 3 pixel resolution elements have been considered to compute the resolution.

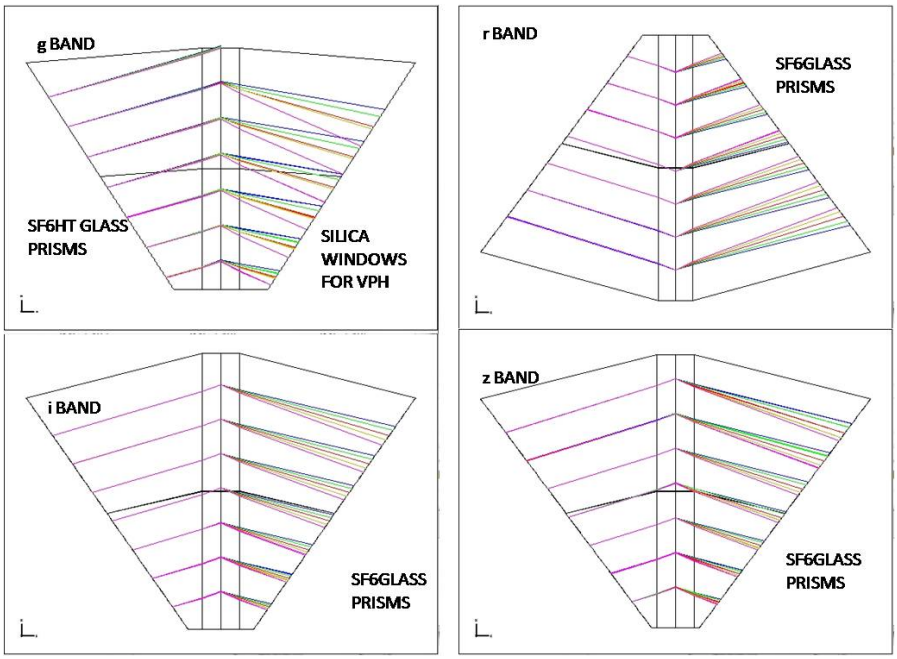

Figure 67 - Dispersive elements layout.

Spot diagrams and field position on the detector are shown in Figure 68 and Figure 69 for the *r*, *i* and *z* cameras. Some adjustments can be done in the dispersive power to increase marginally resolution.

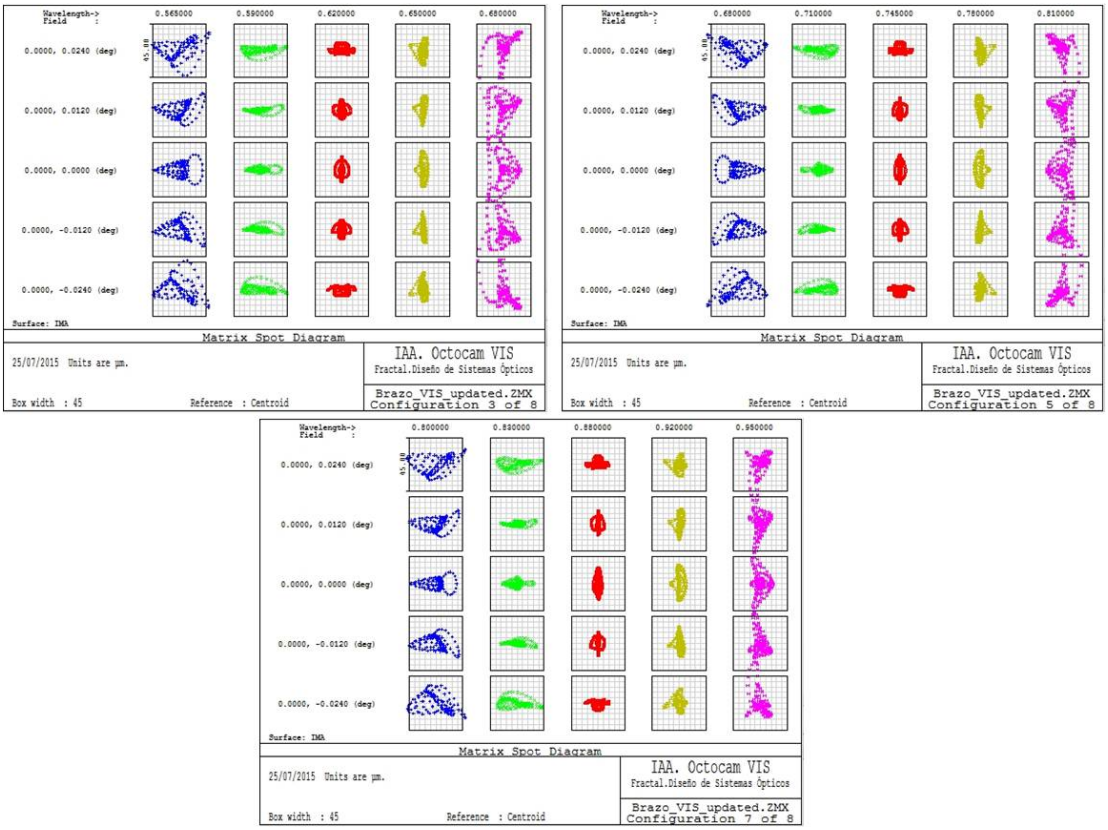

Figure 68 - Image quality (spot diagram) for *r*, *i* and *z* bands, including all the optics and VPH. Each figure correspond to the fields shown in Figure 61. Box size 3 pixels.

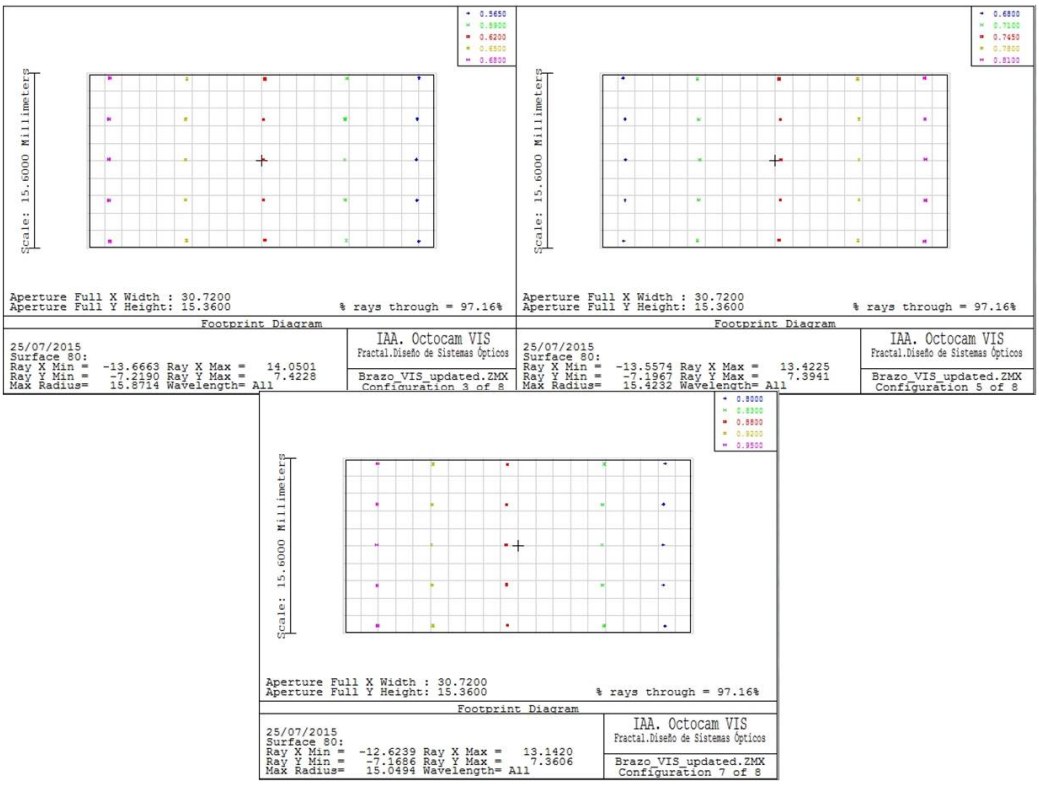

Figure 69 - Detector footprint showing the different wavelengths in each channel. The slit is centred in the middle of the image (from top to bottom). Spectral dispersion is from left to right. Zoom image to see wavelengths (band).

The *g* band camera with the 4k side view provides the spectral performance shown in Figure 70.

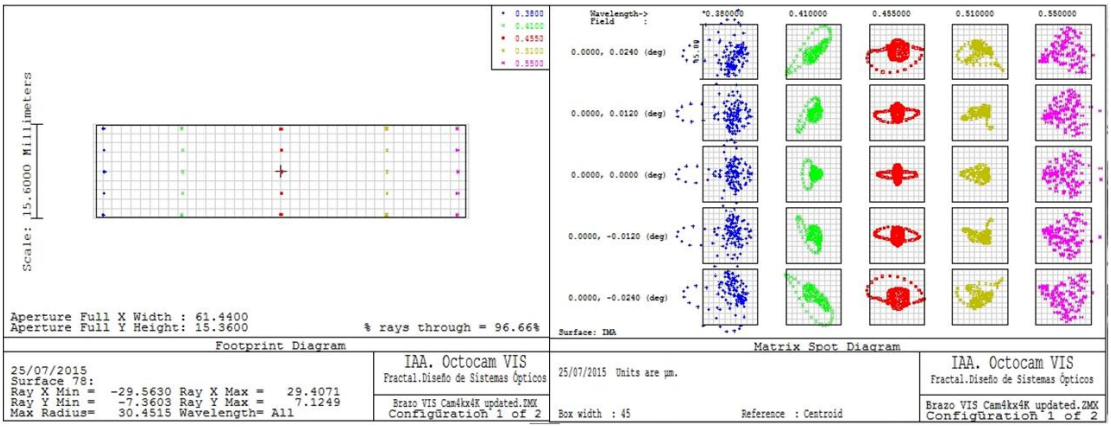

Figure 70 - *g*-band performance with the 4K FOV camera. On the left the detector footprint. On the right the psf of each field. Boxes are 3 pixels wide.

The average EED 80% is shown in Table 22. These are computed from all the spots shown in Figure 69 and Figure 70.

	g	r	i	z
EED at 80%(in pixels)	1.7	1.7	1.6	1.6

Table 22 - Image quality summary for the different bands. Averaging worst fields.

VIS arms. Throughput

The following considerations were taken into account:

- ADC. Internal absorption and 2.5% loss per air/glass surface (4)
- CW1. Average coating. Mean loss 2.3% (2). Negligible absorption
- CW2. Average coating VIS Loss 1.5%.
- Collimator. Internal absorption and 1.5% per air/glass (6)
- VPH. Hologram central efficiency of 0.85. Loss prisms (1.5%/surface (2))
- Camera. Internal absorption and 1% per air/glass (12).
- Dichroics-T in transmission >0.985 per surface. Negligible absorption
- Dichroics-R in reflection. 0.98.
- Folders. Aluminum g band, silver r,i,z. (0.98)

	g	*r*	*i*	*z*
Wavelength (nm)	455	620	745	880
ADC	0.873	0.890	0.891	0.891
CW1	0.954	0.954	0.954	0.954
DICHR-R	0.980	0.980	0.980	0.980
CW2	0.970	0.970	0.970	0.970
COLLIMATOR	0.817	0.870	0.880	0.879
VPH	0.820	0.820	0.820	0.820
CAMERA	0.860	0.863	0.867	0.866
DICHR-T	0.940(2)	0.970	0.970 (1)	-
DICHR-R	0.980 (1)	0.960 (2)	0.960 (2)	0.940 (3)
FOLDERS	0.920 (2)	0.940 (3)	0.940 (3)	0.920 (4)
TOTAL	**0.39**	**0.43**	**0.44**	**0.43**

Table 23 – *g*, *r*, *i* and *z*-band transmission.

The g-band efficiency shown here uses an improvement to the design by changing materials to Y-type (Ohara) or similar. A deep discussion with the VPH provider (e.g. Wasatch Photonics) and also looking for Y-type materials for prisms is needed to study the options to improve VPH unit transmission.

Error Budget. Tolerances

The instrument provides two main operation modes; spectroscopy and imaging.

The as-built unit has to provide the required science performance.

Spectroscopy mode:

The resolution element shall provided in three pixels. Thus the FWHM of the slit will be three pixels. We will model the light distribution as gaussians.

For practical purposes (optical analysis) the evaluation of the EB will not be made in terms of FWHM, but in terms of RMS spot radius, and considering 1D Gaussian profile in the spectral direction. Thus, in order to compute the EB, we will translate the FWHM and EE_{80} to the σ of a Gaussian. The 80% of the energy under a 1D Gaussian is contained below ±1.28 σ.

The following relations are maintained:

$$rms\ spot\ radius = \left(\frac{2\sigma^2}{2}\right)^{1/2} = \sigma \quad (1)$$

$$FWHM = 2.35 * \sigma \quad (2)$$

$$EER80 = 1.28 * \sigma \quad \text{(1D gaussian)} \quad (3)$$

From FWHM=3 pix, we have total budget of σ = 1.27 pix

The slit contains 80% of the energy in 2.4 pix (EER80=1.2), thus σ=0.94 pix (using 3)

Thus the complete budget is $\sigma^2 = 1.27^2 - 0.94^2 = 0.85^2$, σ = 0.85 pix

Imaging mode:

According to the previous requirement, the psf FWHM will be 0.35" (using 2 pixels). Thus a natural seeing of 0.5" FWHM can be degraded to 0.61".

$$psf^2 = seeing^2 + psf^2 = 0.5^2 + 0.35^2 = 0.61^2 \quad (4)$$

The σ=0.85 pix is the complete instrument budget, that shall allocate the following errors.

$$\sigma^2_{instrument} = \sigma^2_{\substack{nominal \\ design}} + \sigma^2_{\substack{optical \\ manufacture}} + \sigma^2_{\substack{integration/ \\ assembly}} + \sigma^2_{uncompensated} + \sigma^2_{thermal} \quad (5)$$

Our most demanding unit due to the fast F# and wider FOV is the VIS arm with the 4k x 1k camera in the *g* band. We will show a preliminary EB to meet the 0.85 pix (12.75 microns) criterion for this configuration.

The nominal error (design baseline) is obtained using the fields and wavelengths shown in Figure 71 by computing the spot RMS radius. Notice we have not taken all wavelengths to the absolute edge, but the ones in the figure.

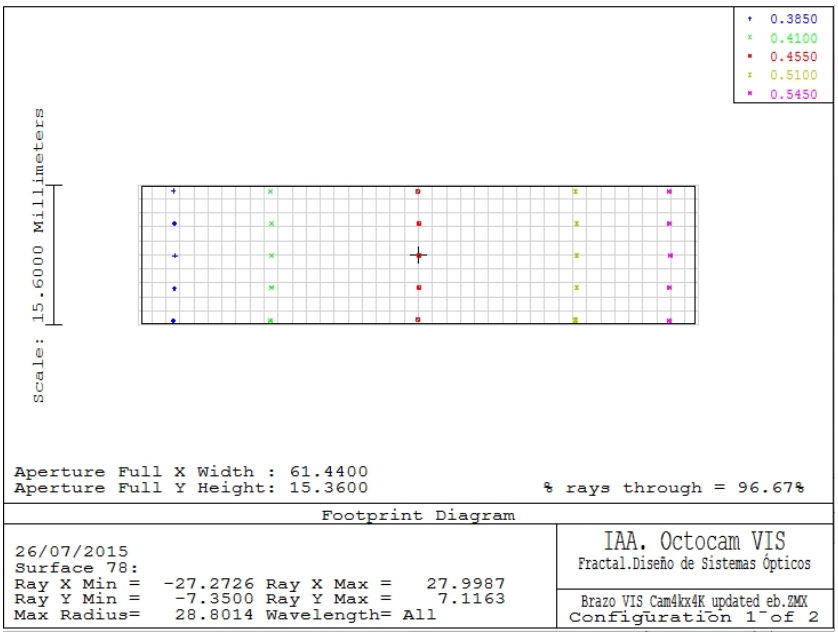

Figure 71 - fields and wavelengths to compute the spot radius rms for the EB.

The RMS spot radius computed by the software is 9.7 microns. The preliminary EB is shown in Table 24. The most difficult unit is related to the camera, which has been analyzed in more detail, as it will take the largest contribution of the budget.

ITEM	σ (μm)	Verification
Nominal design error:	9.7	Nominal design (full system cam 4kx4k)
Collimator fabrication and alignment	3.7	Low F# collimator. Easy to obtain.
Camera fabrication and alignment	5.6	***As per Monte Carlo simulation with the tolerances given in*** Table 25 ***and*** Table 26
Pupil element and ADC	2.0	
Glass inhomogeneity	2.5	Blank specification
Assembly and integration	3.0	At the subsystem level.
Folders, Dichroics	2.0	Small cross section apertures. Will perform difracction limited
Thermal	0.5	Focus compensation allowed
Total	**12.7**	Maximum: 12.75 μm

Table 24 - Error budget structure for the spectroscopic *g* band mode.

In order to confirm the EB assignment, a Monte Carlo analysis for the camera was done with the tolerances shown in Table 25 and Table 26.

ITEM	R1 (mm)	R2 (mm)	Surfaces irregularity (fringes @632.8 nm)	Thickness (μm)	Wedge (arc min/ μm)	Flatness. Power (fringes @632.8 nm)
CAM1	64 ± 0.08	111 ± 0.1	0.5 – 0.5	± 50	± 1.0’	--
CAM2	264 ± 0.2	flat	0.5 – 0.5	± 50	± 1.0’	1
CAM3	flat	107 ± 0.1	0.5 – 0.5	± 50	± 1.0’	--
CAM4	107 ± 0.1	-169 ± 0.1	0.5 – 0.5	± 50	± 1.0’	--
CAM5	89.9 ± 0.1	flat	0.5 – 0.5	± 50	± 1.0’	1
CAM6	132.8 ± 0.1	386.6 ±0.2	0.5 – 0.5	± 50	± 1.0’	
CAM7	-78.5 ± 0.1	133 ± 0.1	0.5 – 0.5	± 50	± 1.0’	
Detector window	--	--	0.5 – 0.5	± 100	± 2.0’	1 - 1

Table 25 - Manufacturing tolerances for the individual elements of the refractive camera.

Element	Position X (mm)	Position Y (mm)	Position Z (mm)	Tilt X (arc min)	Tilt Y (arc min)	Tilt Z (arc min)
CAM1	Compensator	Compensator	± 0.05	3	3	-
CAM2	± 0.1	± 0.1	± 0.1	2	2	-
CAM3						-
CAM4						-
CAM5	± 0.07	± 0.07	± 0.05	3	3	-
CAM6	± 0.1	± 0.1	± 0.05	2	2	-
CAM7	± 0.05	± 0.05	± 0.05	3	3	-

Table 26 - Integration tolerances within the Refractive Camera.

The tolerances of the camera used two compensators: a decentering lens (CAM1) to correct for non-symmetrical aberrations, as well as back focal length. Aspherical parameters were not included. Q type asphere model and tolerances will be used upon manufacturer feedback. Current design is with "even asphere polynomials".

These preliminary tolerances show that the worst subsystem is within reasonable manufacturability parameters. Further iteration during next phases would be required for a complete EB and optical specification.

2.3.7. Alternative optical design

As part of the feasibility study, we explored another, less conventional design alternative. As in the baseline design, a flat dichroic divides the light beam into the VIS and NIR arm after the focal plane. This dichroic is placed inside the cryogenic chamber that contains the NIR arm. The light goes out from the chamber to the VIS arm through a flat window.

The design is then similar for both VIS and NIR arms: After going through the collimator the beam goes through two dichroic beamsplitter cubes. The first dichroic cube divides the light into three different wavelength ranges, bending two of these branches towards their respective cameras (defining two channels) and letting the rest of the light pass in the straight direction to the second cube. This second cube divides the remaining light into two channels that exit in opposite directions. See the 3D layout in Figure 72. Two of the channels are folded by mirrors into the cameras.

In the imaging mode, the cameras are directly illuminated by the beams that exit from the cubes. This is translated into a much more compact and cheaper instrument. Figure 72 shows 4 working modes: 2 spectral and 2 imaging modes.

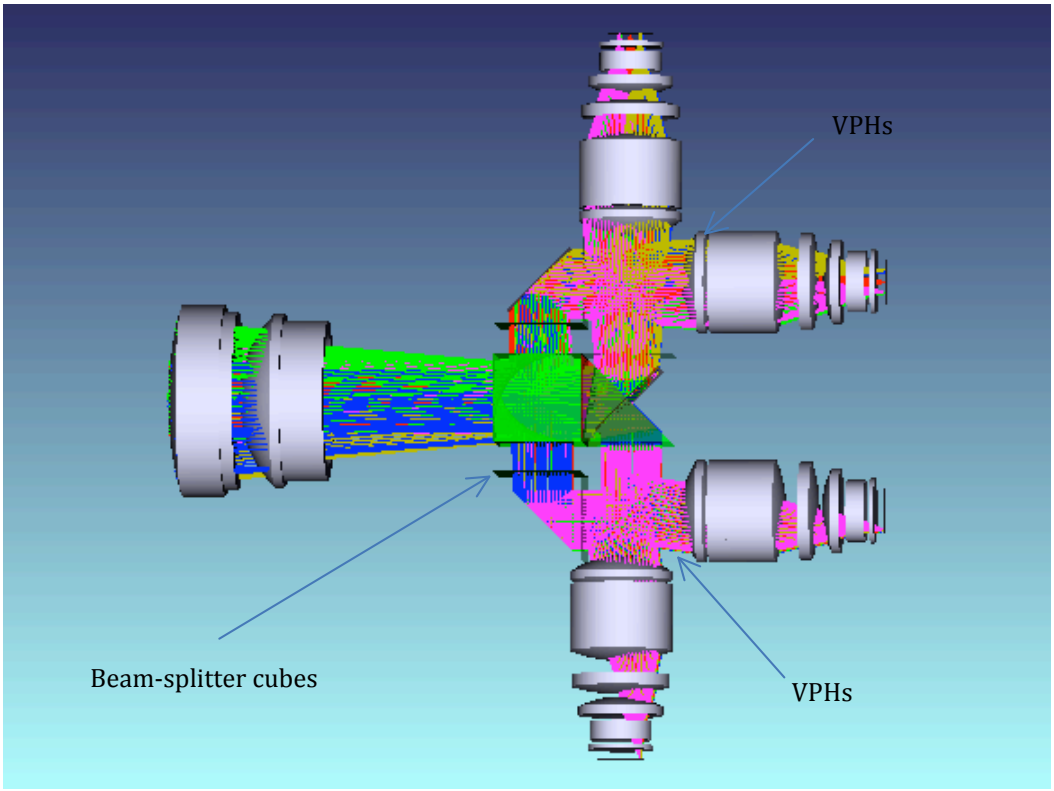

Figure 72 - Design #2: Overall layout.

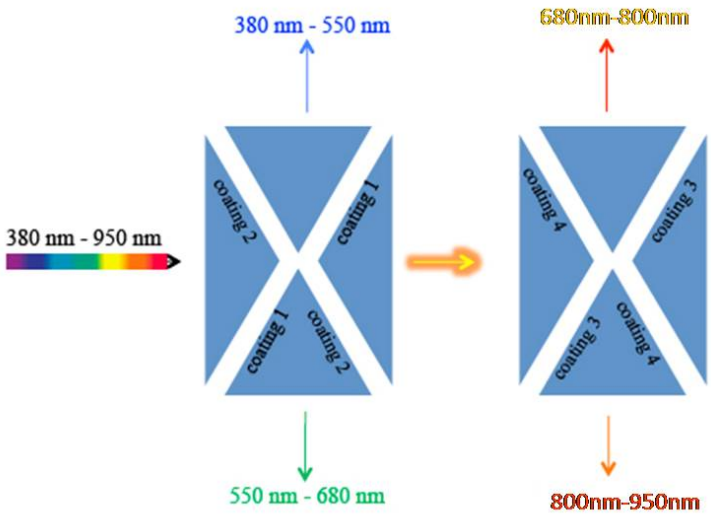

Figure 73 - Graph showing how the two beam splitter cubes work for splitting the light into different channels for the VIS arm.

The spectroscopy works by inserting a double grating into the optical path, where the light beams cross. The channels that were going in the imaging mode to each pair of cameras are switched, as shown in Figure 75.

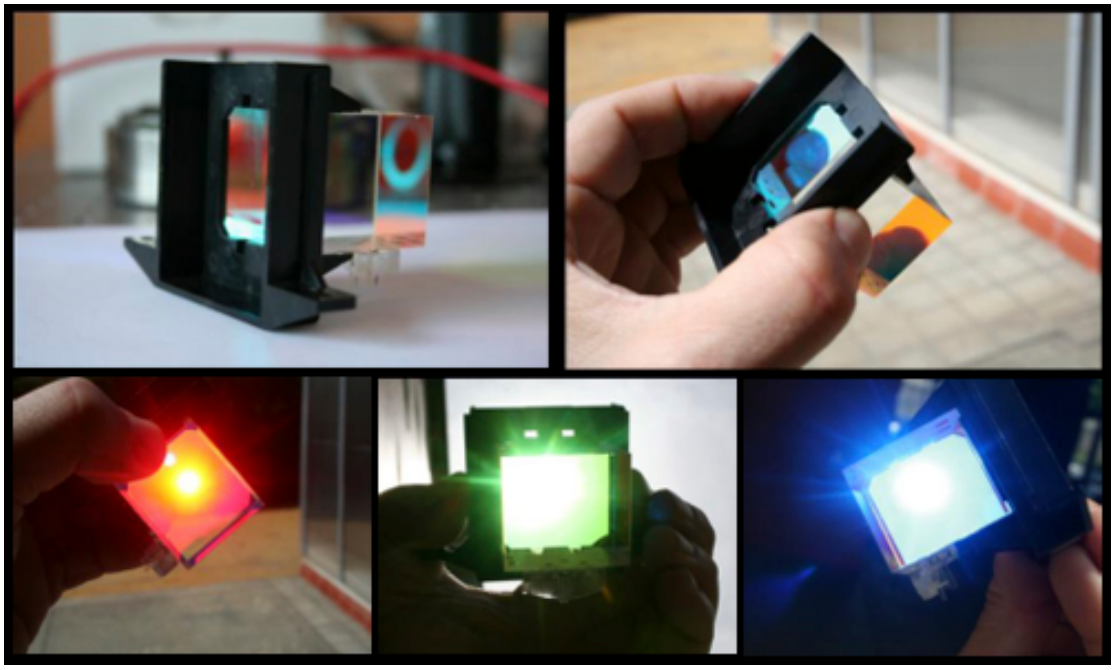

Figure 74 - Example of a dichroic cube being manipulated by our Optical Engineer. The three bottom figures show the R reflectance, the G transmission, and B reflectance respectively.

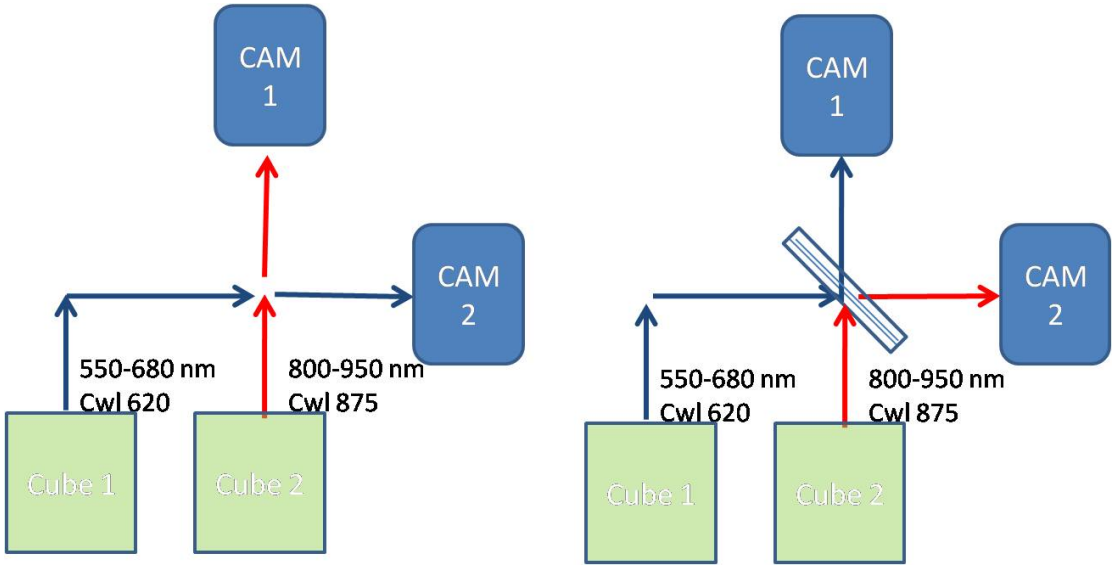

Figure 75 - On the left, the imaging mode. On the right, the spectral mode. Notice that r and z channels are crossed in the cameras 1 and 2.

The spectroscopy mode makes use of 2 VPH gratings, see a schematic overview in Figure 76, where we can see the grating for *g* – *i* channels (left) and the grating for *r* – *z* channels (right) behavior.

Each dispersion unit contains two gratings. The rationale behind the concept is that while one grating will be very efficient diffracting the required wavelength range, it should be "inexistent" in the remaining range. That non-diffracted range will hit the second grating and then diffract. We can check the transmission efficiency curves for both multiplexed gratings in Figure 81. Those figures show that transmission out of the wavelength range that delimits each channel is

always below 10% (and in some cases nearly zero). A summary of the grating's main parameters can be found in Table 27.

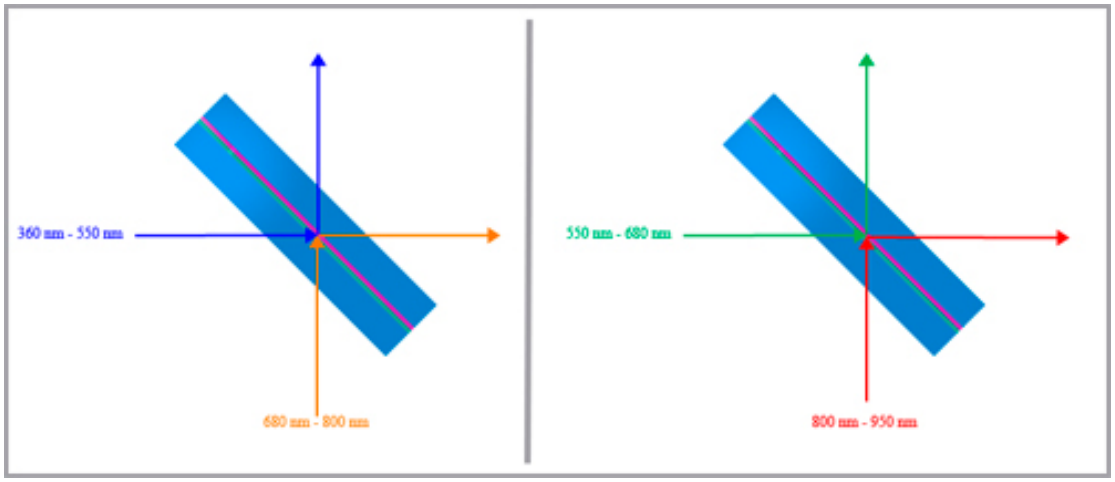

Figure 76 - Multiplexed gratings used in Design#2 for the channels g - i and r - z respectively.

Channel	Spectral Range (nm)	λ_{Bragg}(nm)	VPH lin/mm	R	AOI	Peak Eff
g	360 – 550	455	3107	3906	45°	< 80%
r	560 – 680	620	2280	3894	45°	~80%
i	680 – 800	745	1898	3890	45°	> 80%
z	800 – 950	875	1616	3900	45°	~85%

Table 27 - Desing#2 VIS arm grating information.

Channel	Spectral Range (μm)	lines/mm	R	AOI
Y	0.95 – 1.12	1350	3880	45°
H	1.5 – 1.76	860	3730	45°
J	1.12 – 1.32	1150	3650	45°
K	1.97 – 2.34	645	3670	45°

Table 28 - Design#2 NIR arm gratings information.

Table 28 gives us a summary of the power resolution using 3 pixels and the line density of each grating in the NIR arm. It is to be noticed, that due to the selected geometry, a high AOI (45 deg) is obtained as a baseline. This means higher dispersive power, so we can use a smaller pupil and camera focal length to obtain the resolution.

The way in which the multiplexed VPH are designed is optimized to avoid contamination originated from other diffracting orders, especially the zero order is by using a prism, as shown in Figure 77. In this case, gratings will be slanted to provide the required Littrow geometry. No further checking was done with the company to this final design, but we do not foresee problems regarding tilting the lines.

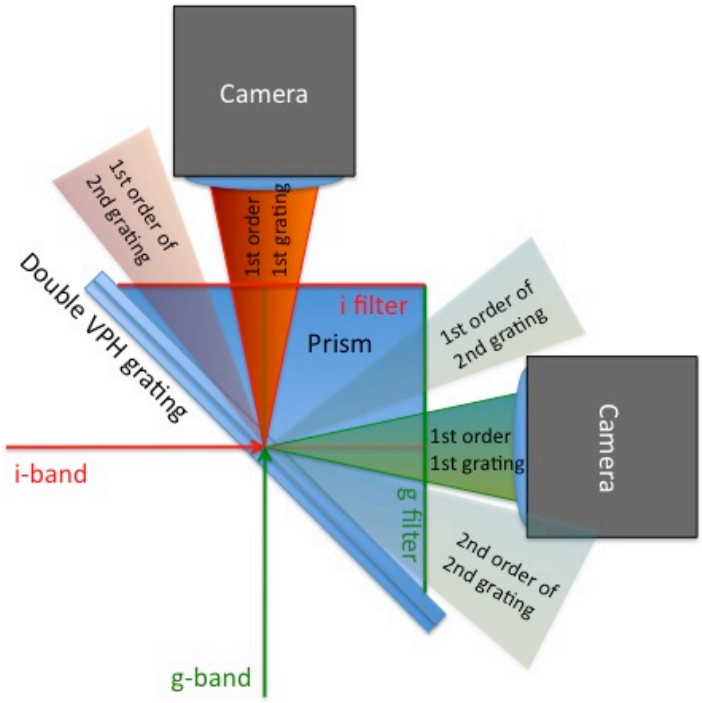

Figure 77 - Layout about how the to prevent contamination from other diffracting orders.

A detailed Non Sequential Model was implemented in both double gratings to explore possible contaminations between orders and gratings. The analysis covered all order combinations between -2 and 2 for both gratings. In Figure 78 the nominal paths for the *r-z* grating is shown.

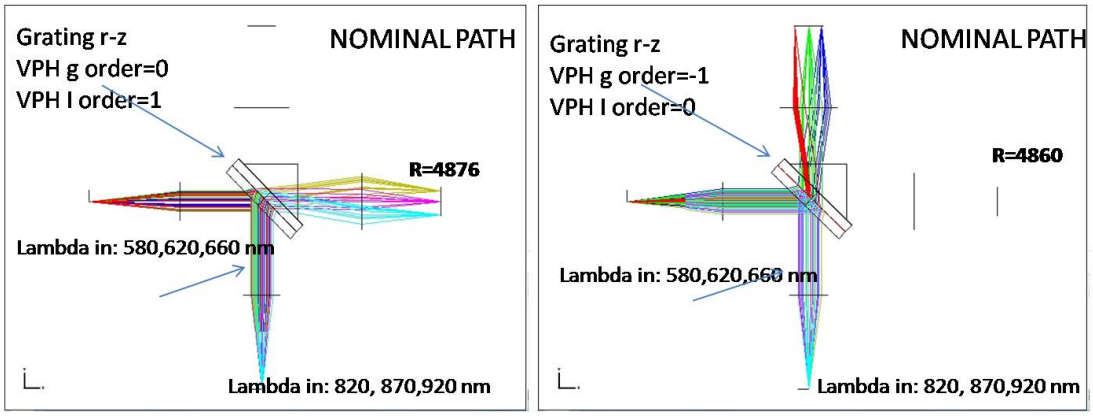

Figure 78 - Nominal paths for the *r - z* grating in their respective wavelength ranges. Cameras are represented by fake paraxial lenses.

The analysis shows no cross contamination for any grating. Some examples of the undesired geometries are shown in Figure 79 and Figure 80 for both assemblies.

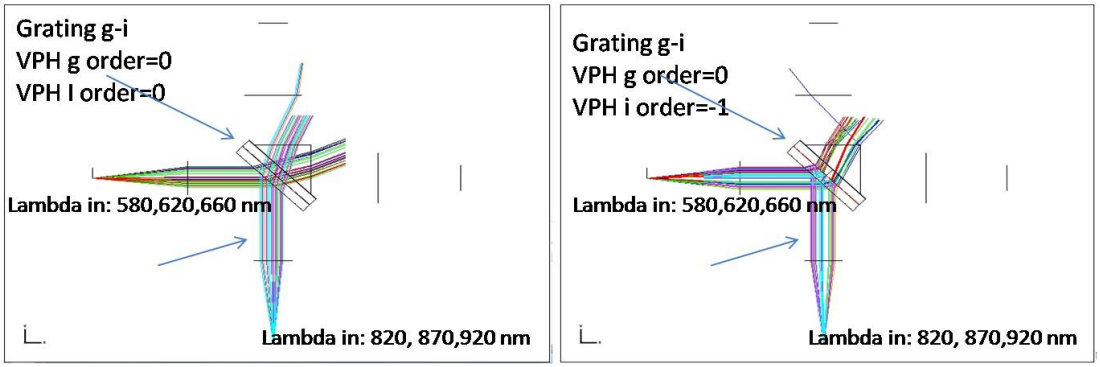

Figure 79 - Some undesired paths, not reaching the detector for the g - i grating.

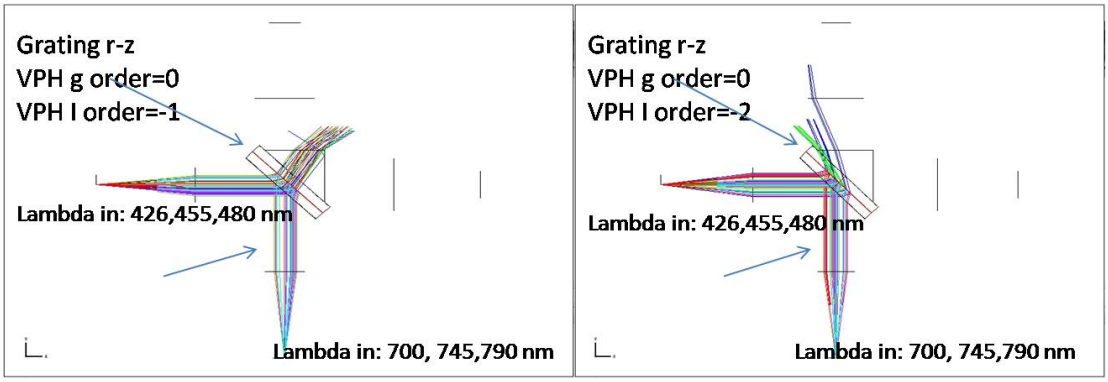

Figure 80 - Some undesired paths, not reaching the detector for the r - z grating.

In Figure 81 we show the answer to a request to Wasatch Photonics, on the specific gratings for the VIS channel. Each grating has to provide a good performance in two wavelength ranges. One range with very high diffraction efficiency while the other has no iteration with the grating (very low diffraction efficiency).

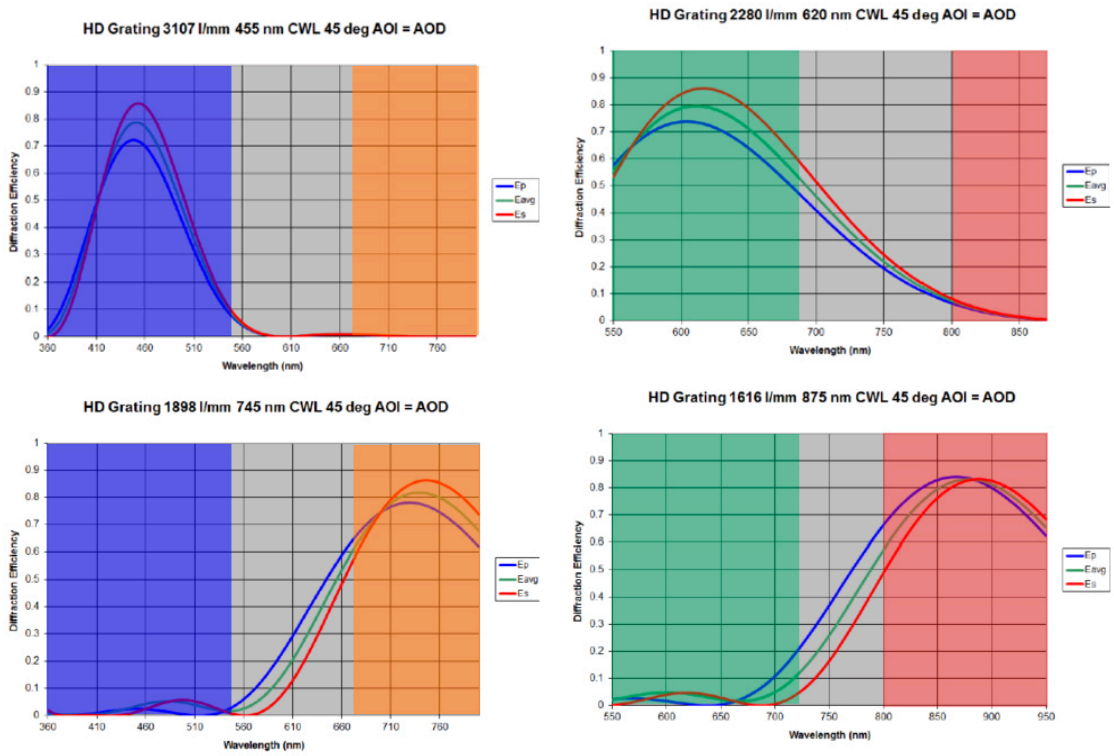

Figure 81 – Left: Efficiency curves for *g – i* channels. The blue and orange shadowed areas match the spectral ranges covered by channels g and i respectively. Right: Efficiency curves for *r – z* channels. The green and red shadowed areas match the spectral ranges covered by channels r and z respectively.

NIR arms:

Figure 82 shows an optical layout if the NIR arm for the second design, where the collimator is compound by 3 doublet lenses (Figure 83) with a focal of 648 mm and a pupil diameter D = 40 mm. The camera (Figure 84) is composed by a set of two doublets and two singlet lenses with an effective focal length of 87 mm. It is worth mentioning that with this design, a smaller pupil and a shorter focal length is needed to obtain the required resolution as compared to the baseline design.

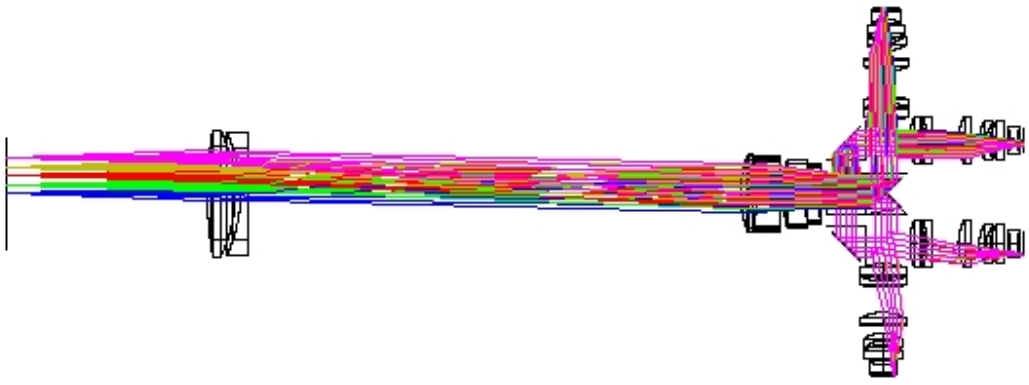

Figure 82 - Optical layout of the NIR arm.

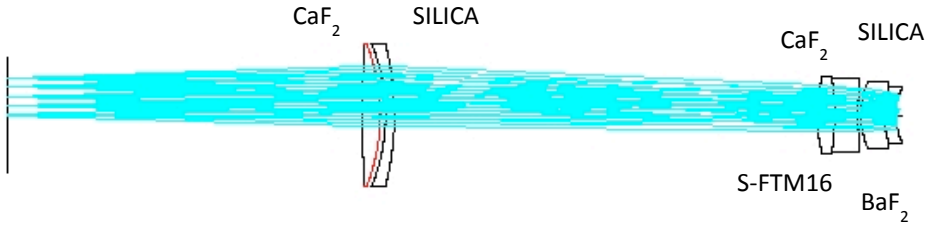

Figure 83 - Collimator of the NIR arm.

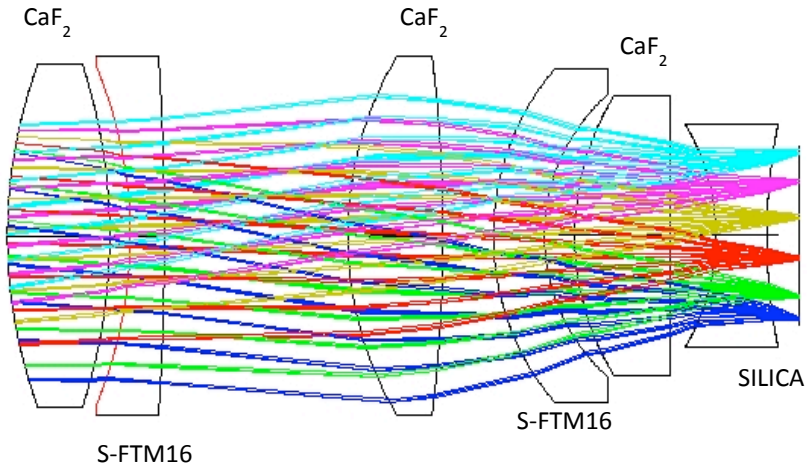

Figure 84 - Camera of the NIR arm.

The full optical performance of this design is not presented here due to space limitation. However, it is available upon request from the project documentation.

VIS arms:

As described previously, the light that comes into the VIS arm has been reflected from the first dichroic and left the cryogenic chamber through a window. After passing the collimator, the system is similar to that for NIR arm.

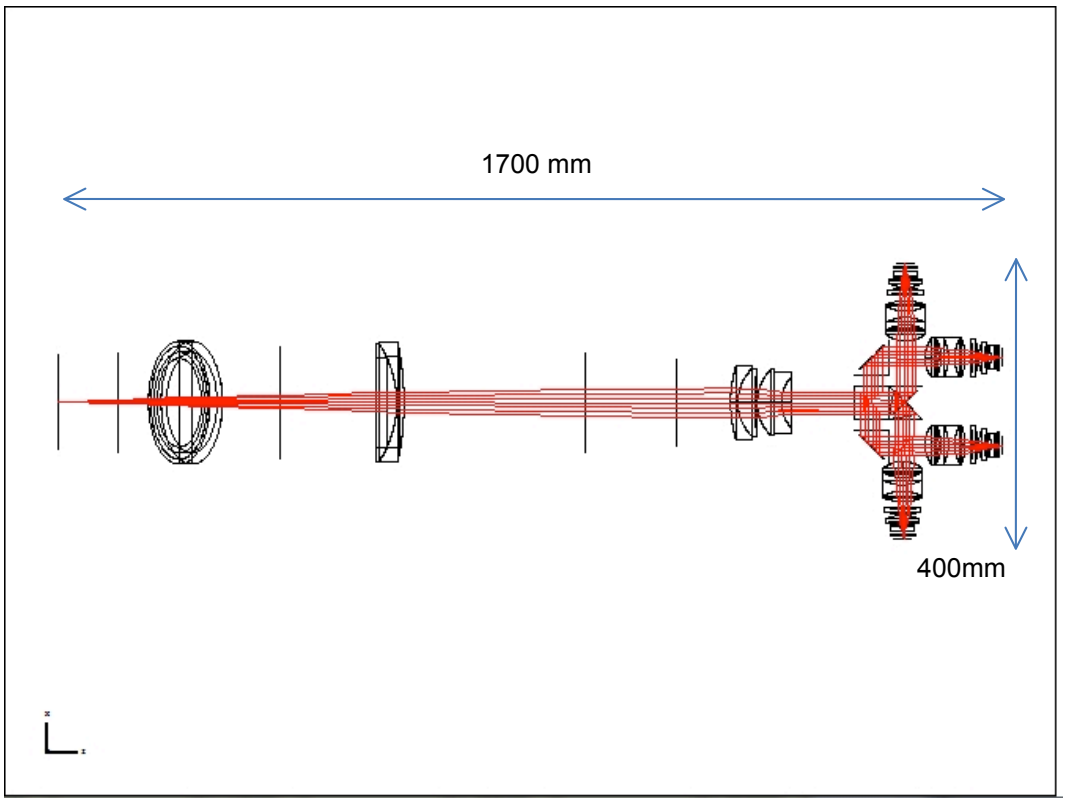

Figure 85 - VIS unit optical layout.

The collimator (Figure 86) is designed with 3 doublets establishing a focal length of 680 mm, maintaining the same F-number as in the baseline design (i.e., F16.2) with a reduction of the pupil size (D = 40 mm).

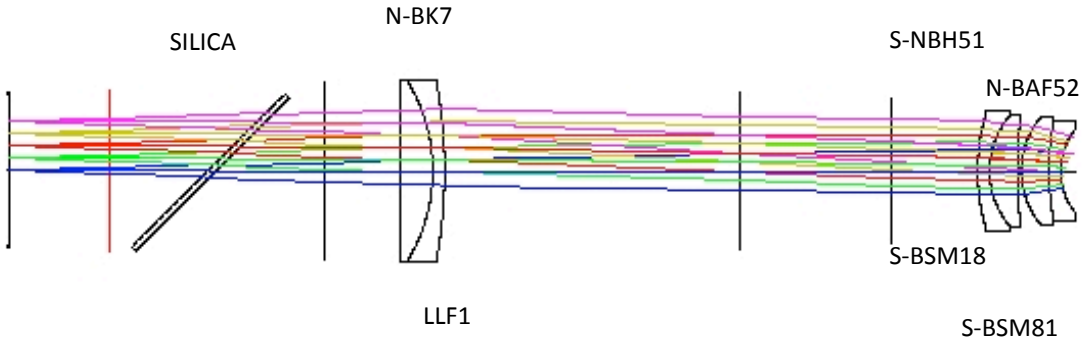

Figure 86 - VIS Collimator layout.

The camera of each channel is compounded by: 1 triplet,4 singlet lenses. It gives an effective focal length of 87 mm, obtaining the same F-number (F2.17) than the previous design. The instrument scale obtained for the VIS arm is 0.18″ pixel^{-1} (pixel size 15 μm).

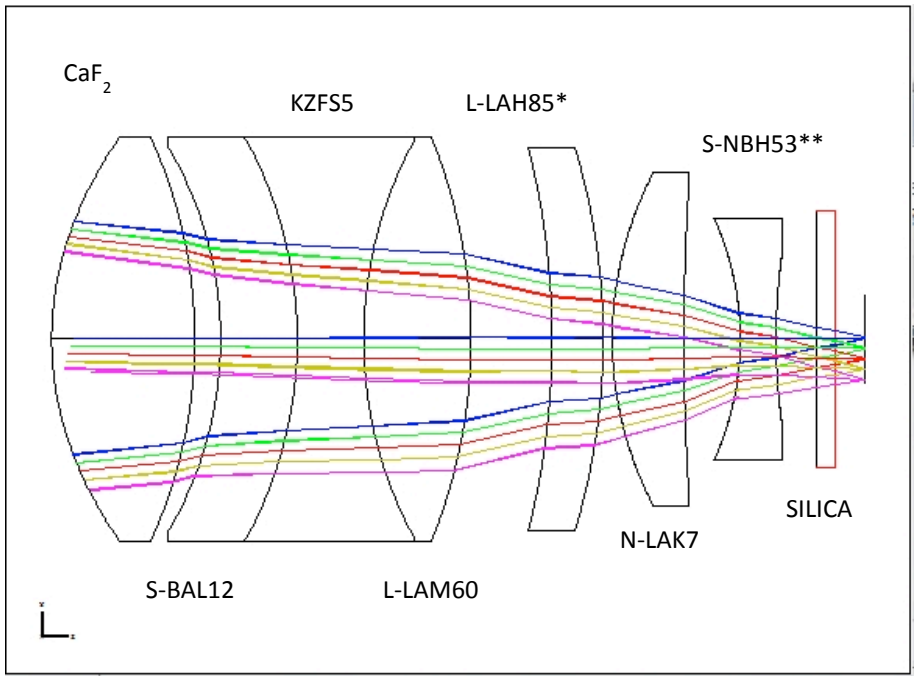

Figure 87 - Camera optical layout. (*) Active focusing in this lens ± 0.15 mm. (**) Shutter between this lens and silica window (more details on these mechanisms are given in Section 2.4.4).

The full optical performance, of this design is not presented here due to space limitation, but is available in the project documents.

Conclusions:

This innovative concept has a certain number of attractive features, much less optics (1/3rd optical mass), delivers higher resolution for the same pupil and is more compact than the "traditional one".

The core concept is based in two nonstandard ideas in astronomy: multiplexed gratings and beam splitter cubes. We found manufacturing unresolved uncertainties with the companies we contacted.

These are basically related to efficiencies of coatings performance that cannot guarantee full success at this moment. Preliminary contact with the coatings manufacturers showed rejection to quote on 45 deg cube dichroics with high efficiencies and sharp slopes. The feedback provided poorer performances from the ones we would have expected. Thus it seems that the new concept would require a feasibility demonstration program and extra work in these two ideas before a design can be safely offered to the astronomical community.

Based on the extent of our inquiries, readily available manufactured coatings could not be sources and therefore we could not proceed with this alternative design. Consequently, we keep the original design as baseline concept, although the alternative one could be recovered if we manage to obtain reliable and efficient coatings. We foresee the possibility of developing this design by prototyping during the design phase.

2.4. Mechanical design

The objective of this phase is to give a conceptual mechanical design fitting both the proposed optical configuration and the Gemini available envelope. This can give an initial feel of size, weight, and general view of the instrument.

The following figures show the general view of the proposed mechanical concept of the instrument. In Figure 88 we show the Gemini instrument support structure (ISS) of the Cassegrain focus of the telescope. Attached to it there will be a truss-like space frame structure that will support the instrument as well as the electronic boxes and any other required equipment that will rotate with OCTOCAM. The complete system must fit within the available envelope (described on Gemini drawing 89-GOP-1000-004 rev E, see Figure 89, Figure 90, Figure 91, and Figure 92). The size of the Electronics boxes shown in the figures is 600 x 600 x 850 mm.

The structural design of OCTOCAM is based on a single focal plane for all arms and a very symmetric structure. Both camera groups are attached to the same optical bench. Its performance is very predictable and, unlike other more complicated structural designs, it is easily tunable to control the deflection to desirable values at certain locations. This can be done with passive means that should be designed placing control nodes during a detailed finite element analysis of the structure. In this way, we would avoid the need for additional active elements to compensate for flexure.

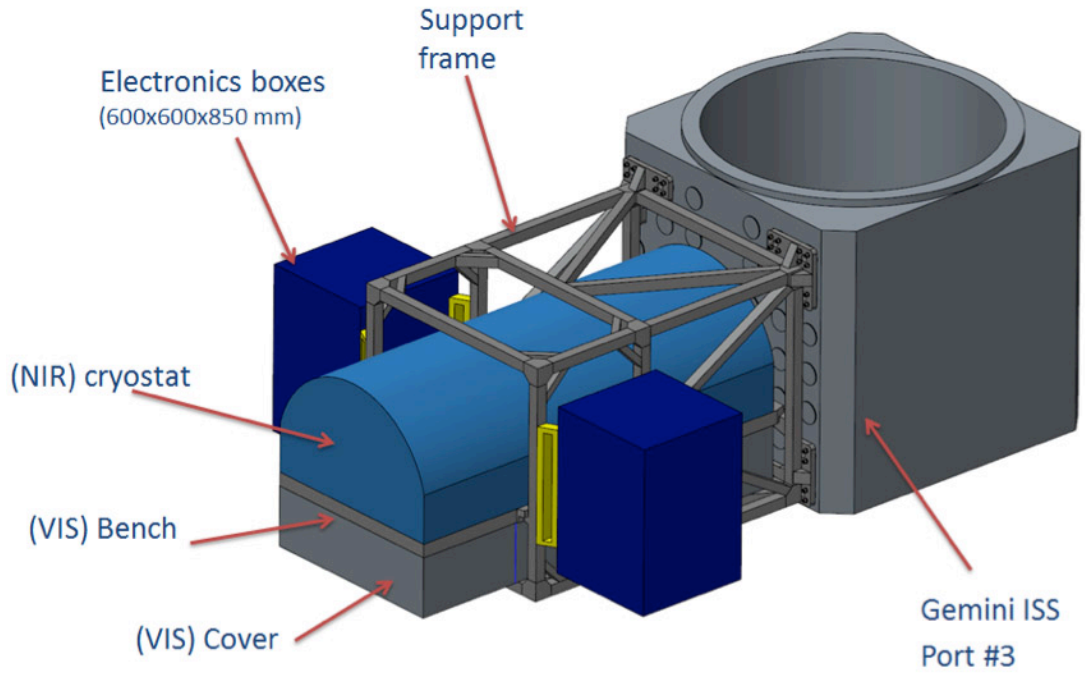

Figure 88 - General view of OCTOCAM .

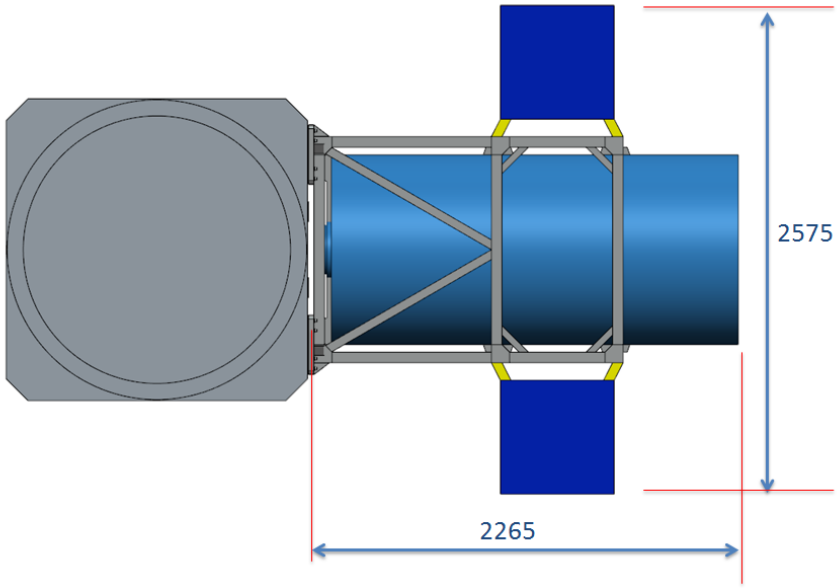

Figure 89 - Top view.

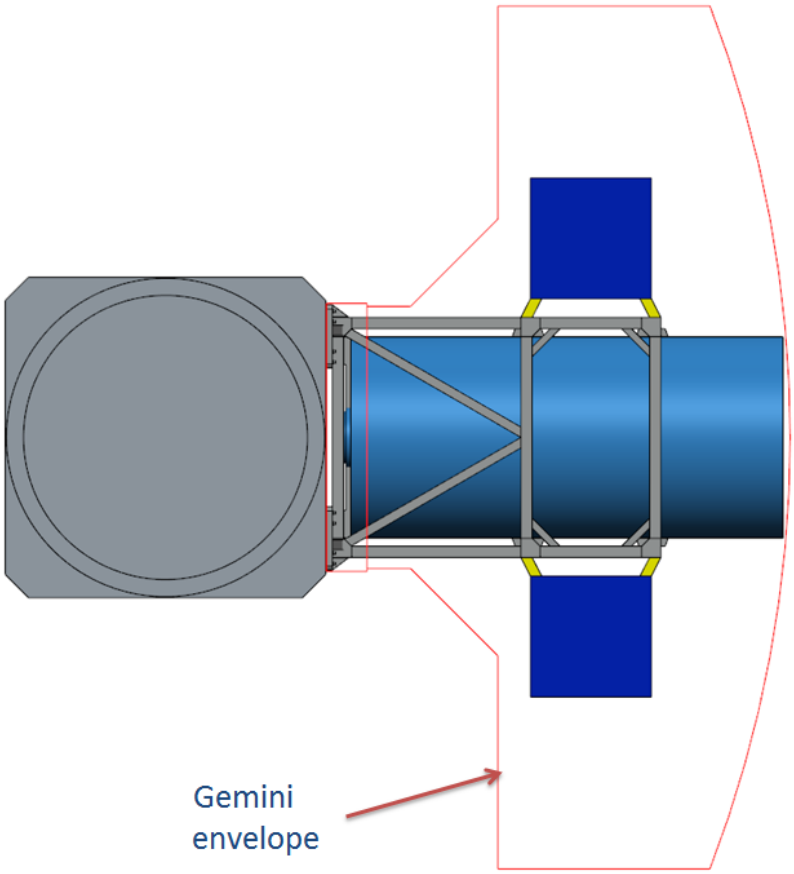

Figure 90 - Top view of OCTOCAM with Gemini envelope.

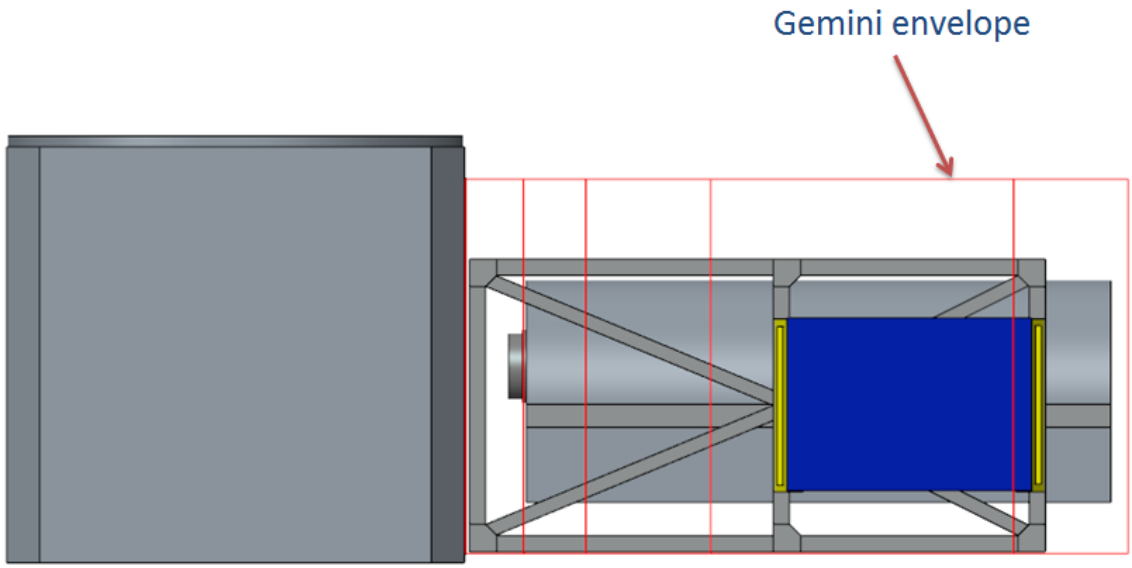

Figure 91 - Lateral view of OCTOCAM with Gemini envelope.

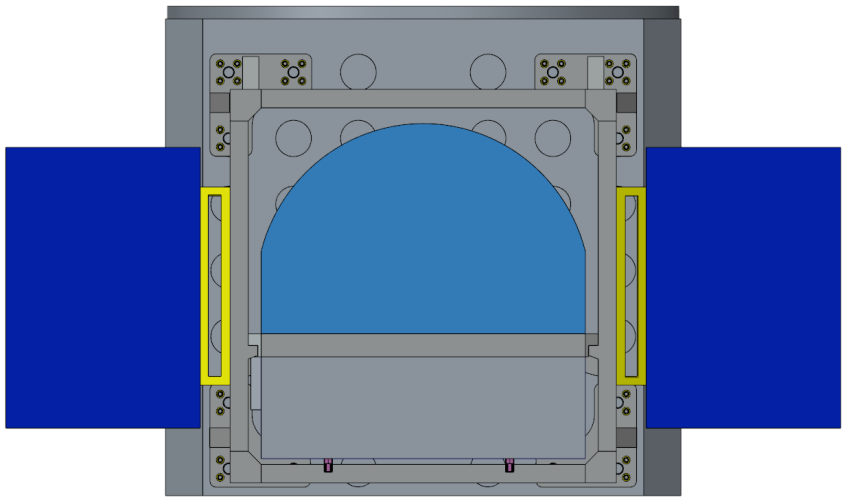

Figure 92 - Back view of OCTOCAM.

2.4.1. Space frame

Figure 93 shows the space frame that is attached to Gemini ISS. The electronic boxes are attached symmetrically to the frame. Counterweights can be inserted on the frame to locate the center of gravity at an adequate position. It should be made out of hollow steel tubes with the ISS I/F plates and stiffeners welded to it. Its size is 1190 x 1190 x 1660 mm. The yellow elements are the supports for the electronic boxes.

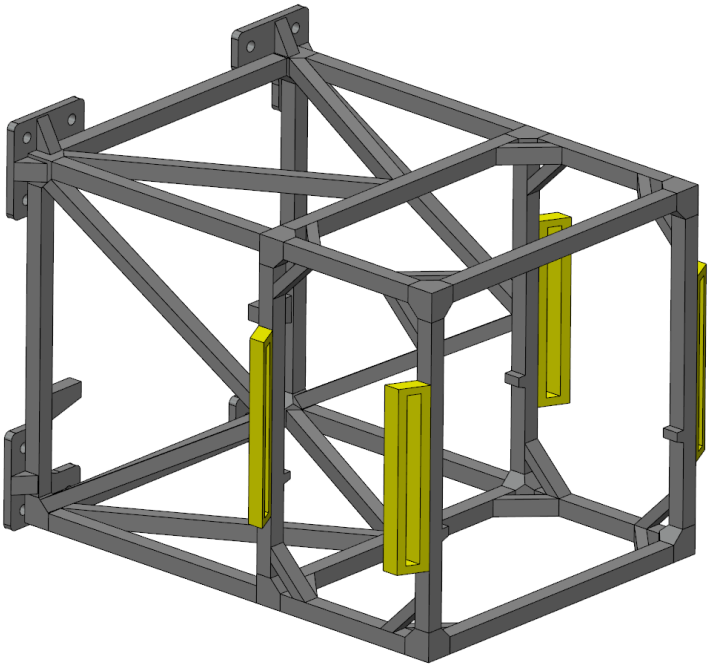

Figure 93 - Space frame.

The optical bench is attached to the space frame at 3 locations one either side, one near the center of gravity of the assembly and also on two other positions to relieve weight (Figure 94 and Figure 95). This will be calculated in detail on a later stage of the instrument design, and its behavior during the instrument rotations should be evaluated.

The design is based on a two-bay approach with a first load-carrying section with a Serrurier configuration and a second bay with a central aperture to provide easy access to the VIS channel on the optical table. The electronic boxes should also be attached to this second bay.

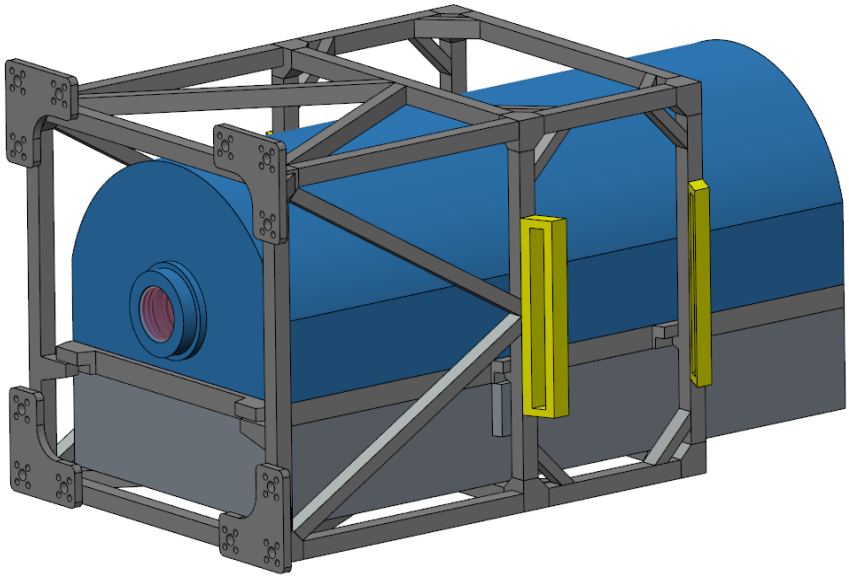

Figure 94 - The central bench is attached to the space frame at 3 locations on either side.

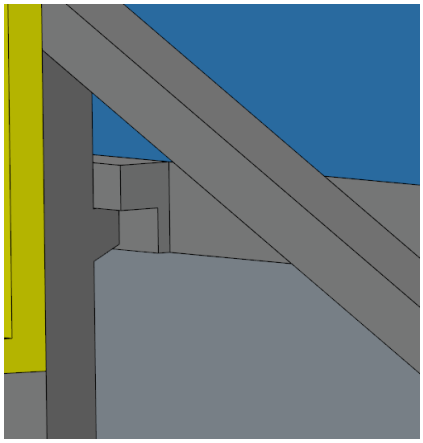

Figure 95 - Detail of the support of the bench on the space frame

2.4.2. Cryostat and NIR bench configuration

Like any other infrared instrument, the NIR channel of OCTOCAM shall be enclosed in a vacuum container where it is cooled down to cryogenic operational temperature. Inside the cryostat, the NIR detectors should be cooled to their operational temperature, which will be maintained with precision. In addition, all optical elements and their optomechanical mounts must also be cooled. To maintain the system cool, the elements will be properly isolated from the outer elements, which are at room temperature. Radiation shields, passive or active-cooled, are widely used for this purpose.

In the configuration that what we present here, the base of a D-shape cryostat serves as an optical bench for the VIS channel optomechanical mounts (Figure 96). Even though they are not widely seen on IR instrumentation, D-shape vacuum chambers are standard for several vendors (see Figure 97).

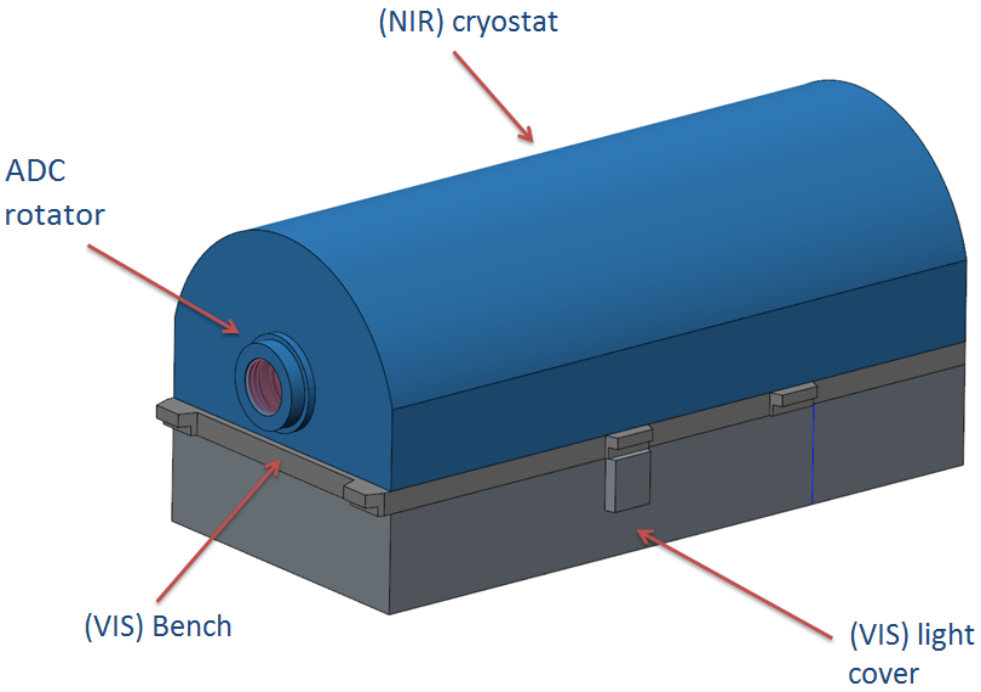

Figure 96 - Cryostat and optical bench.

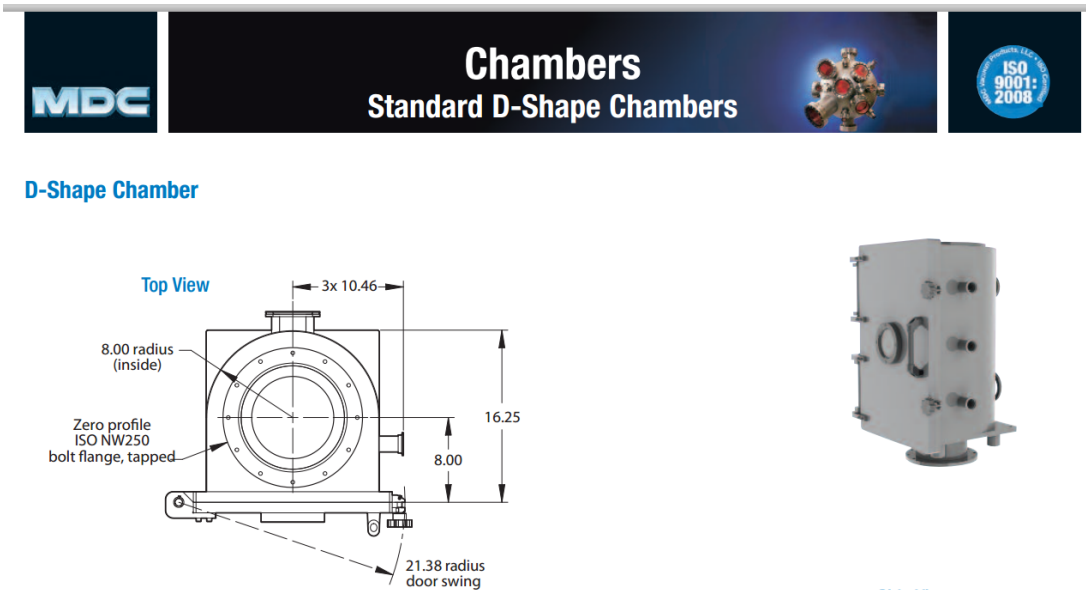

Figure 97 - Example of commercially available standard D-shape vacuum chamber.

The cryostat should have both an entrance and an exit window, with high optical transmission and able to withstand the pressure differential.

The VIS optical bench, which is also the bottom plate of the cryostat, should be stiff, but as light as possible. We propose an aluminum alloy honeycomb sandwiched structure. On top of it, several opto-mechanical mounts will hold the optical elements with precision, and maintain its shape and position:

- On the VIS channel, during night-day and summer-winter temperature variations
- On the NIR channel, from the room temperature alignment to the cooled operational environment.

The ADC prisms rotator should be located in front of the entrance window of the cryostat. The system is composed of two independent rotations: one rotation of one prism with respect to the other and other rotation of the overall ADC with the telescope rotation. The VIS channel will be enclosed with a light cover (made out from thin aluminum panels with an inner support structure). Figure 98 shows the interior of the cryostat.

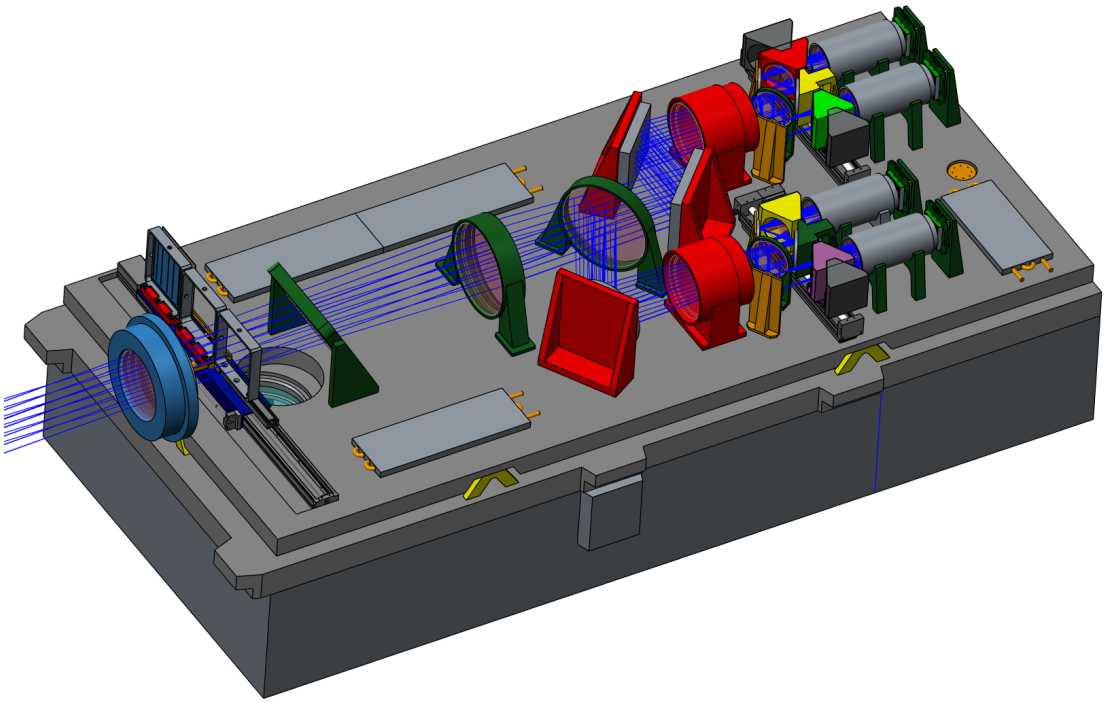

Figure 98 - NIR channel optical bench.

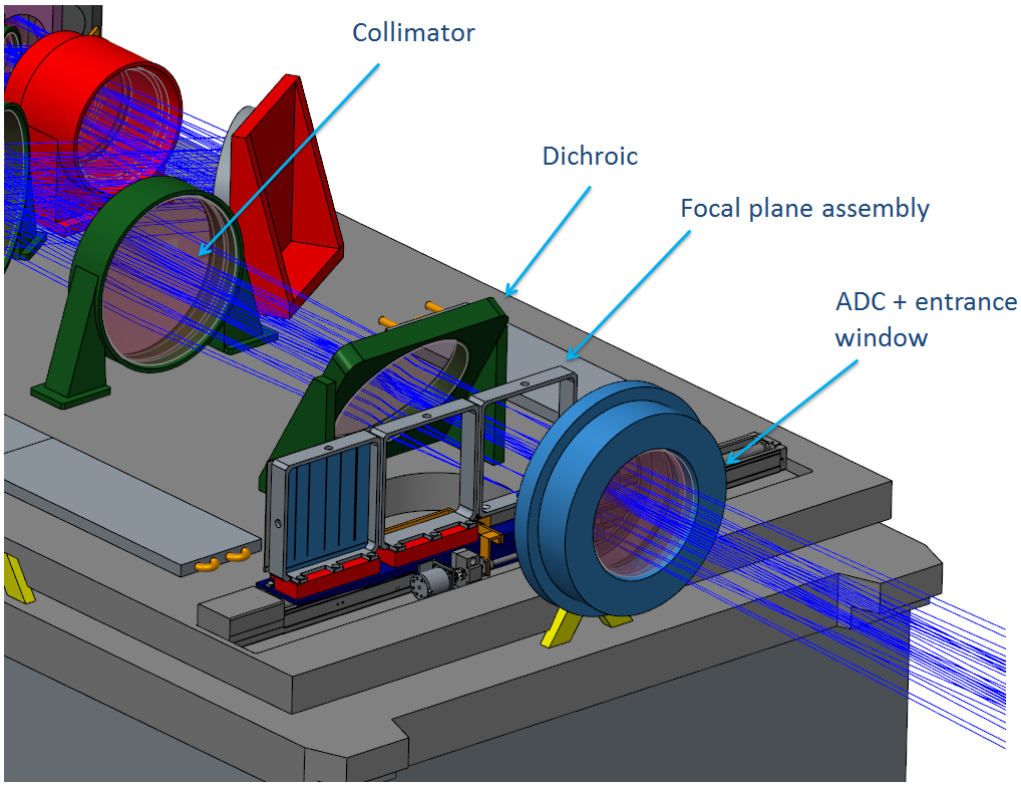

Figure 99 - NIR channel optical bench. Entrance of light.

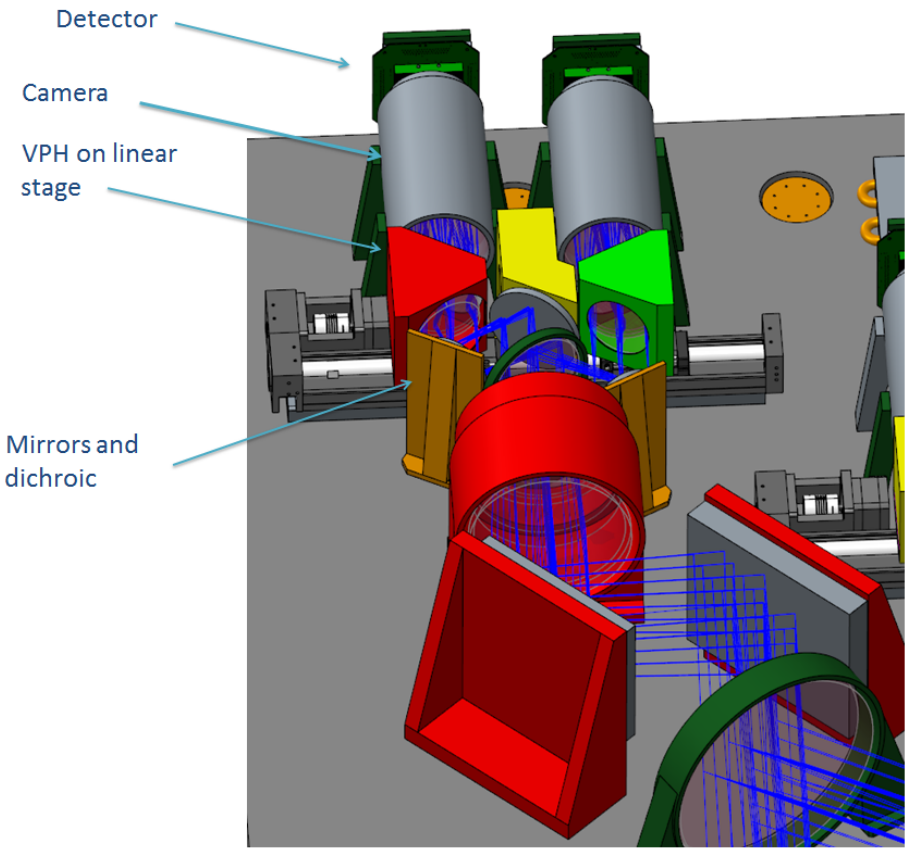

Figure 100 - NIR channel optical bench. End of travel.

The free space in front of the telescope focal plane dedicated to the slit assembly is 155 mm, with a height (up to the radiation shield) of 251 mm. The focal plane carriage that positions the slits, IFU, and spectropolarimeter occupies this space.

All the optomechanical mounts are located on another bench, the “cold bench” that must be cooled down to the operational temperatures. This bench should also be stiff but light. We propose an aluminum alloy structure with a large number of back pockets to make it lightweight.

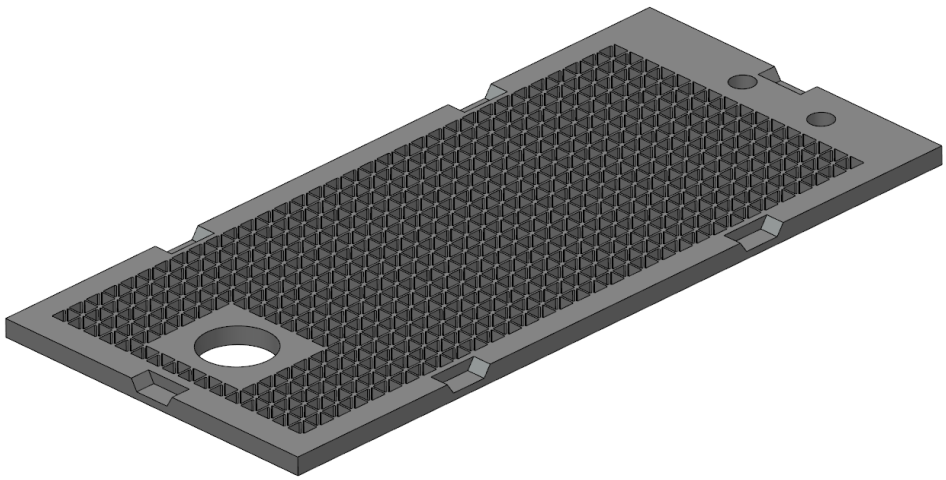

Figure 101 - Cold bench.

The cold bench is isolated from the bottom of the cryostat with a set of fiberglass-epoxy (G-11 for example) supports, which offer very low thermal conductivity and high stiffness and strength. A V-shape can be useful to allow certain differential thermal dilatation between the cold bench and the cryostat bottom.

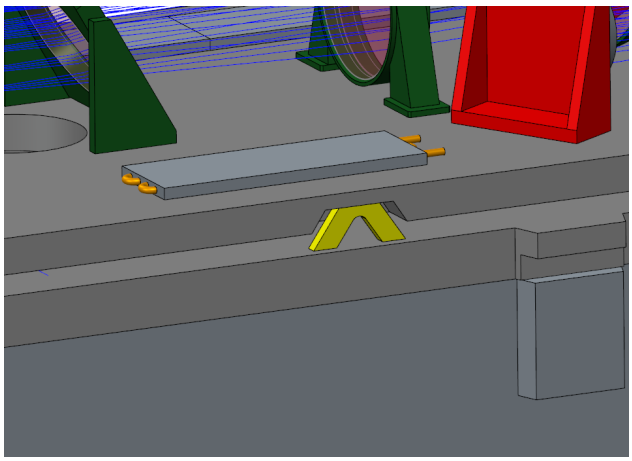

Figure 102 - Detail of one of the isolating supports of the cold bench.

The cold bench is enclosed within a radiation shield to maintain temperature control. The radiation shield, made out of highly polished aluminum sheets, must be attached to the cold bench, to prevent direct conductive heat transfer from the bottom of the cryostat.

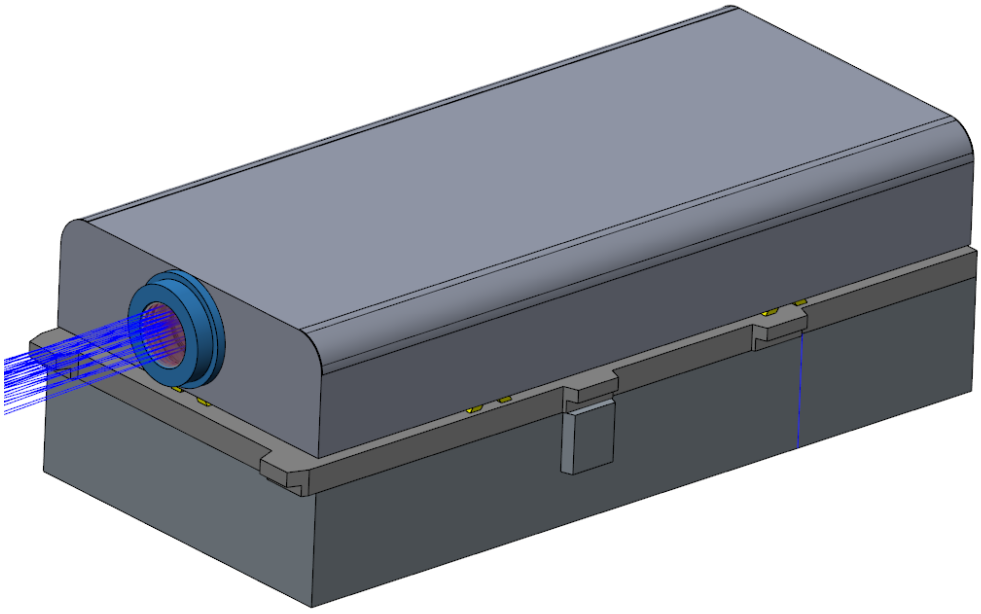

Figure 103 - Radiation shield.

Due to the size of the optical bench, it could be useful to have a pre-cooling system. This will be a circuit of liquid nitrogen that cools the bench at several locations with heat exchangers. Once the bench is cold, the LN2 flow is removed

and the remaining gas exhausted. On Figure 102 one of the heat exchangers is shown, just above the fiberglass V support.

The cryogenic temperature is maintained with two helium closed-cycle cryocoolers. The coolers are located on a common support at the end of the VIS side of the optical bench. The cold finger of both cryocoolers will be located at the surface of the cold bench. To this point, several high-purity copper thermal links must be routed to the different elements.

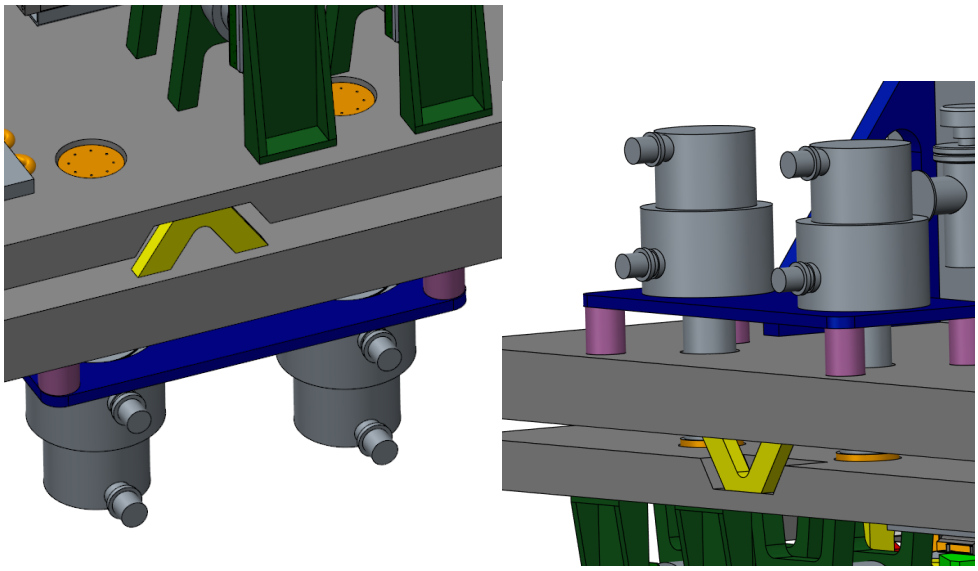

Figure 104 - The coolers are located on a common support and the end of the VIS side of the optical bench. The 4K cold fingers reach the surface of the cold bench.

2.4.3. Visible channel

The light from the entrance dichroic is deviated to the VIS channel through a hole in the cold bench and another one in the main bench. Vacuum seal is ensured at the window located within the main bench hole, equipped with the appropriate O-rings (the same way as in the main entrance window).

The optomechanical mounts for dichroics, mirrors and lenses follow the same design approach as those in the NIR channel. The VPHs are also mounted on translation stages. At the end of the bench there is the system dedicated to cool the VIS detectors. This is to be designed by SwRI. At present, it incorporates one cryocooler. Figure 105, Figure 106, and Figure 107 describe the VIS channel.

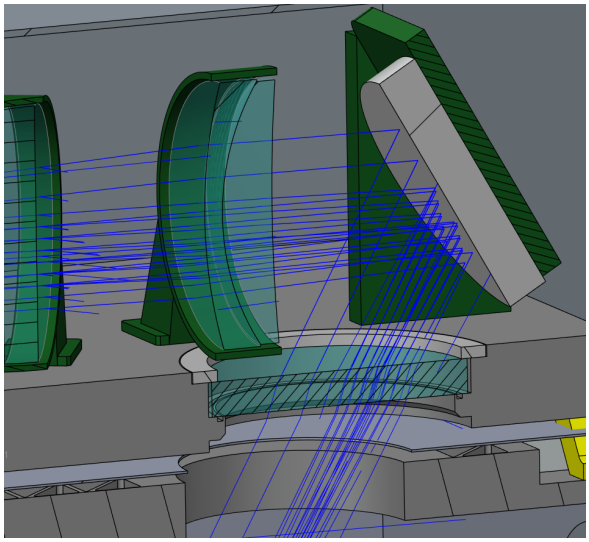

Figure 105 - The light from the entrance dichroic is deviated to the VIS channel.

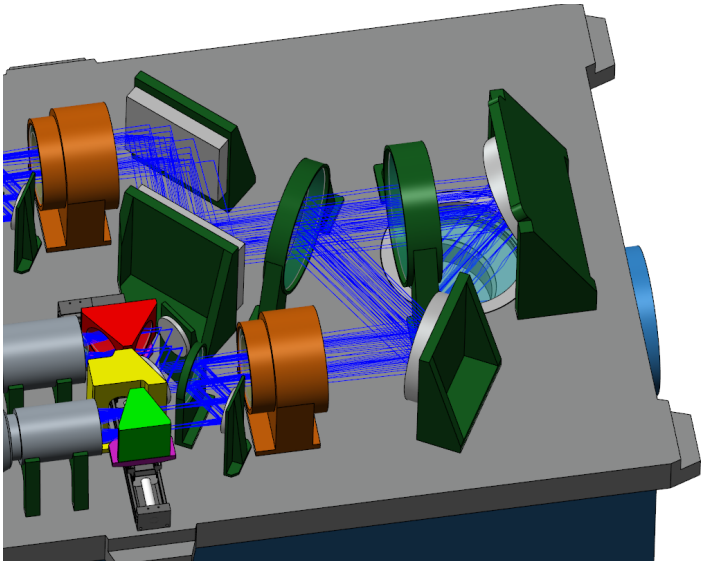

Figure 106 - First elements of the VIS channel.

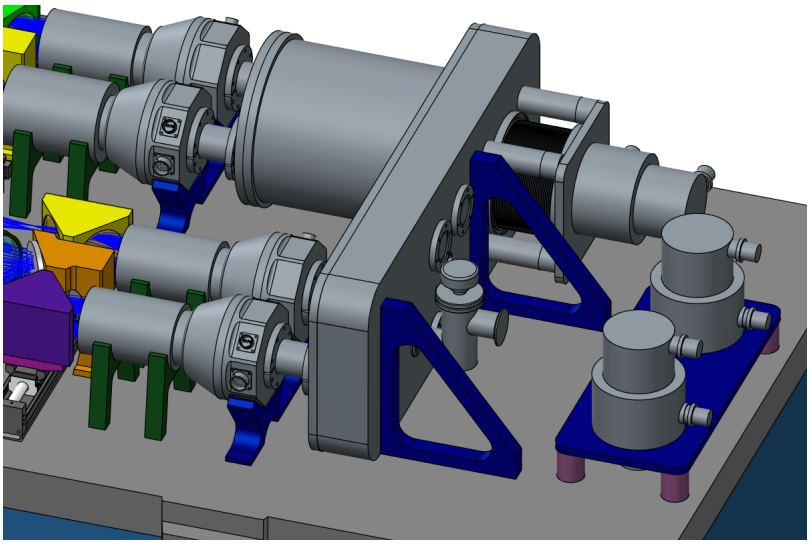

Figure 107 - Last elements of the VIS channel.

2.4.4. Mechanisms

In addition to the ADC rotators mentioned before, there will be several mechanisms:

- A lens within the camera that shall move to adjust the focus variation with temperature.
- A shutter inside the camera. The shutter can be inserted after the last camera lens and before the cryostat window. A commercial iris shutter of 34 mm aperture can be inserted here and actuated from the exterior of the camera with a bistable actuator.
- A mechanism at the focal plane to position slits, IFU and polarimeter.
- Translation stages for inserting the VPHs and filters (where needed).

Translation of VPHs

The proposed mechanism incorporates two sliders driven by a single right and left-hand threaded standard accuracy lead screw. When the crank is turned, the sliders simultaneously move towards or away from each other. So with a single motor, both VPHs are introduced or extracted from the optical train.

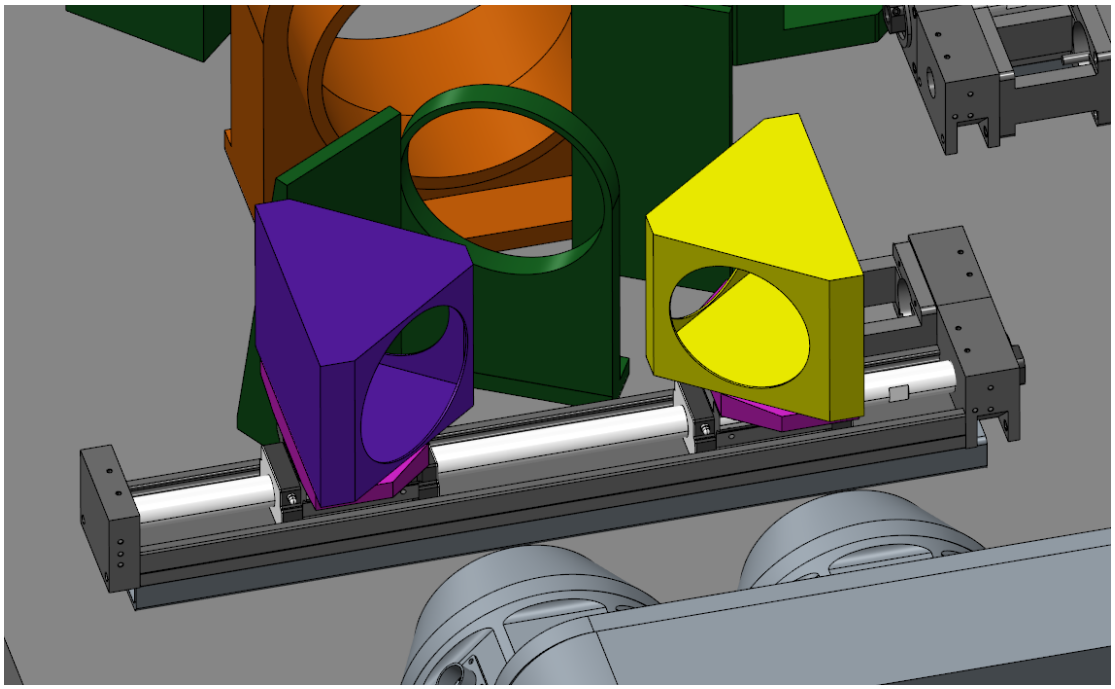

Figure 108 - Translation stage for the VPH gratings mounts. IN.

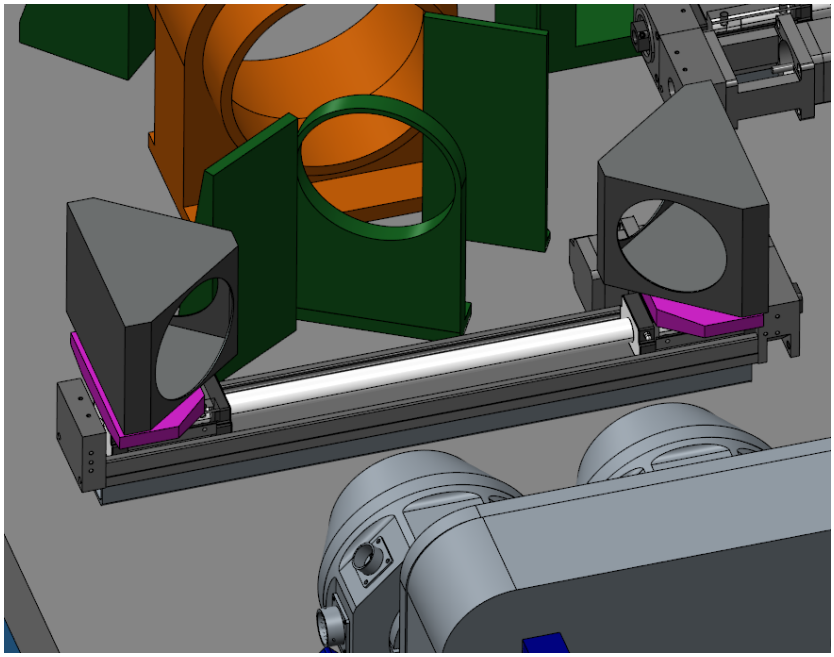

Figure 109 - Translation stage for the VPH gratings mounts. OUT.

In the case of the NIR, the mechanisms are to operate in vacuum and must be kept cold. Probably the same stage can be used, but removing the grease and replacing it with dry lubrication. The motor must be cryogenic compatible. Means of cooling the stages must be incorporated.

In front of the *g*-band camera there is one filter that is placed on the same sliding platform as the VPH. When the grating is extracted from the beam, the filter is inserted. When the VPH enters, the filter is hidden below the folder mirror "arched" mount.

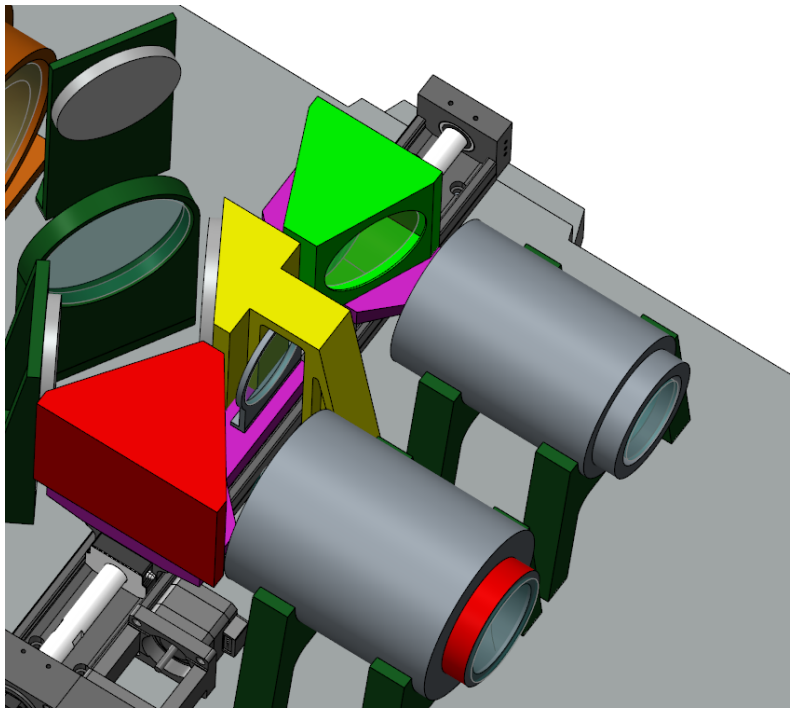

Figure 110 - When the VPH is at the beam, the filter is hidden below the mirror mount.

Translation of a camera lens for focus adjustment

The 6th lens of the camera can be displaced for adjusting the image quality in several bands. One possible (non unique) solution is to place the lens in a subcell that, even though is fitted within the common barrel, can be displaced along the optical axis. Placing three grooves at the outer border of the barrel, and attaching a flat thin plate to the lens cell, it can be displaced with 3 motorized miniature actuators. Within the barrel, the lens cell must be working against a flexure to come back to its position and preload the movement.

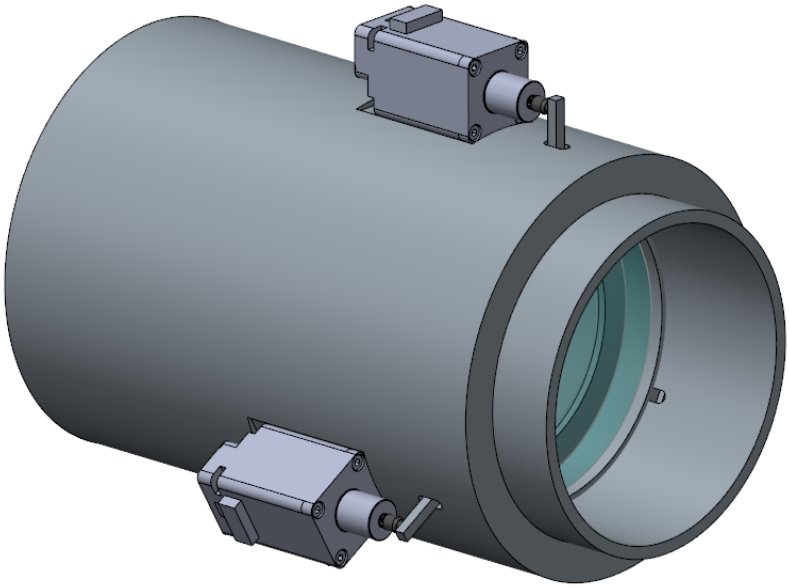

Figure 111 - Configuration of the moving lens subcell within the camera.

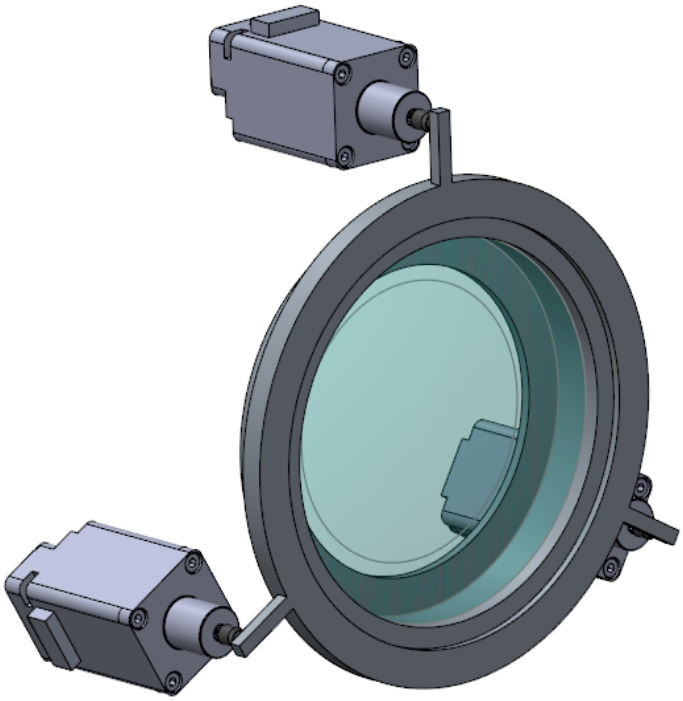

Figure 112- Configuration of the moving lens subcell with 3 actuators.

Focal plane mechanism

At the focal plane there is another cryogenic translation stage that exchanges the slits, the IFU unit and the polarimeter.

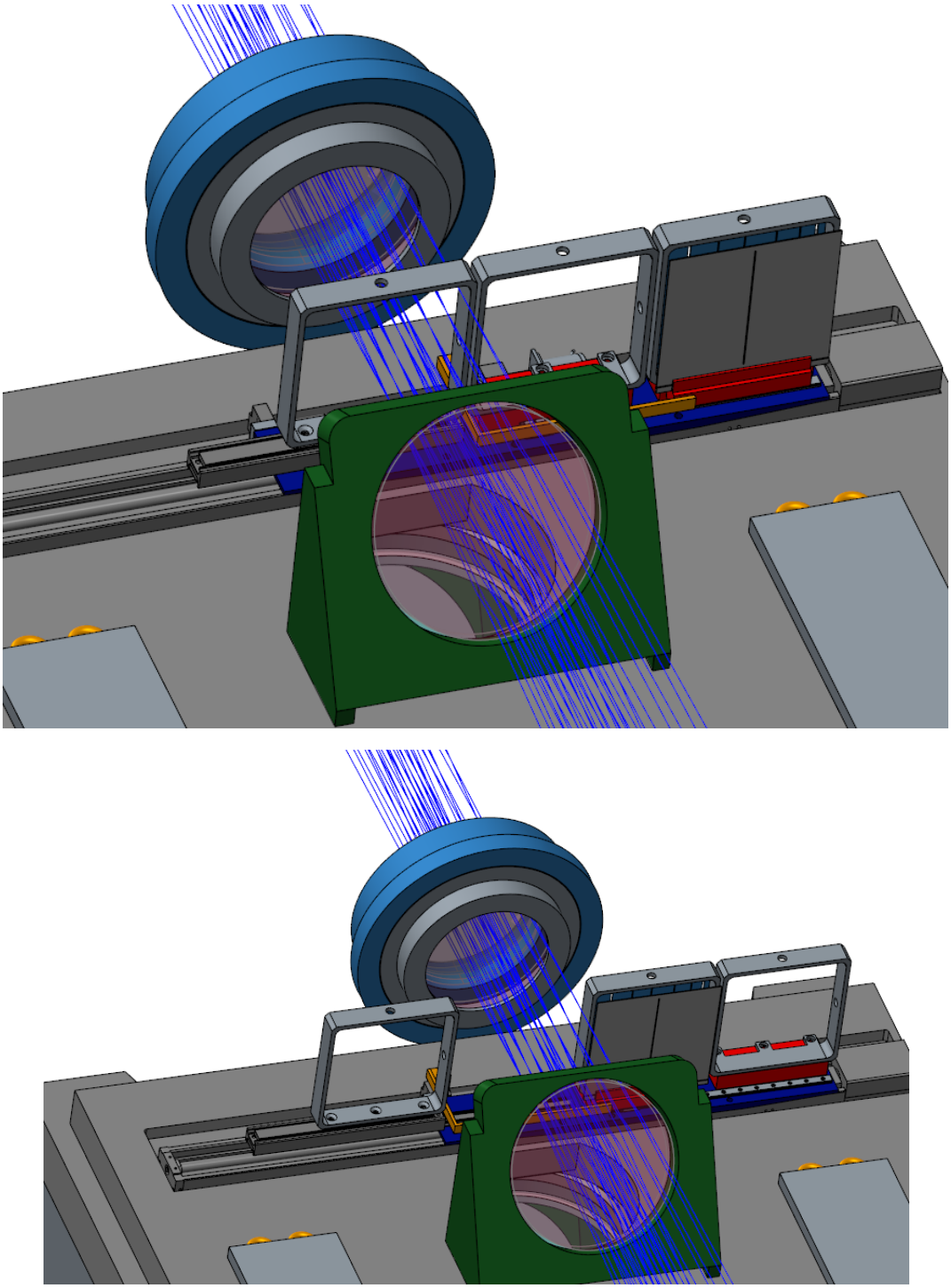

Figure 113 - Configuration of the focal plane location.

As it is seen in Figure 113, there are 3 frames on which those subsystems are placed. On the central one, there is a sheet with several slits that can be changed by moving the stage. At the same position there is another sheet with a central aperture (a mask). A second motor moves this mask, keeping it centered while

the frame with the slits is displaced. This allows us to have a large number of slits within a limited space. This 2nd motor also moves the rightmost frame to leave the OPEN position for imaging mode. The mask moves together the frame. The size of the frame is 150 x 150 mm.

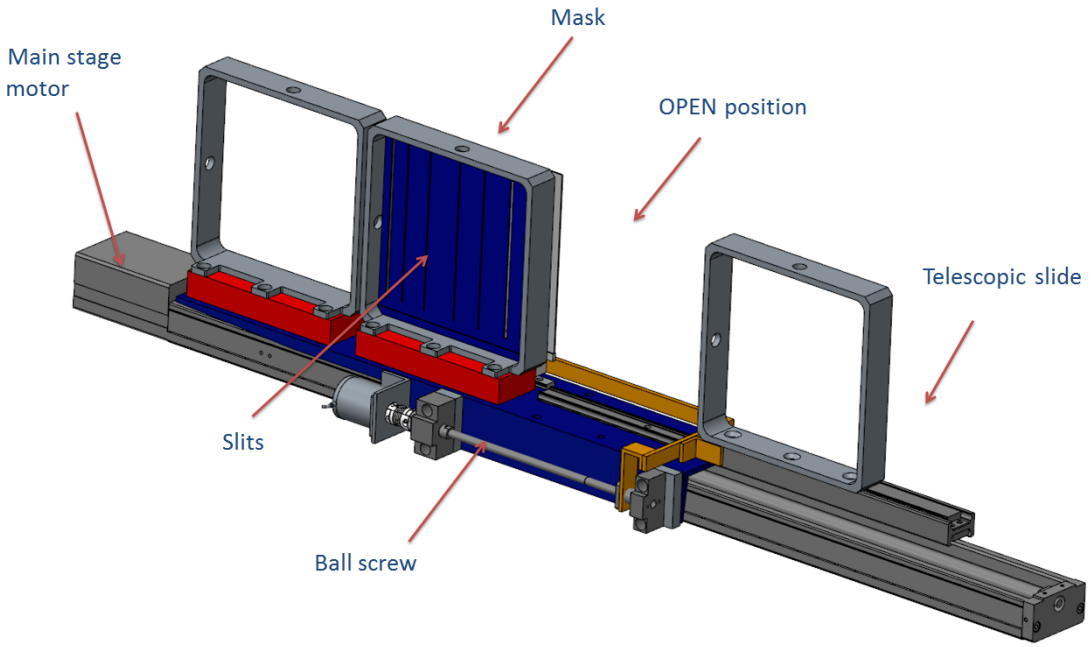

Figure 114 - Elements of the focal plane assembly.

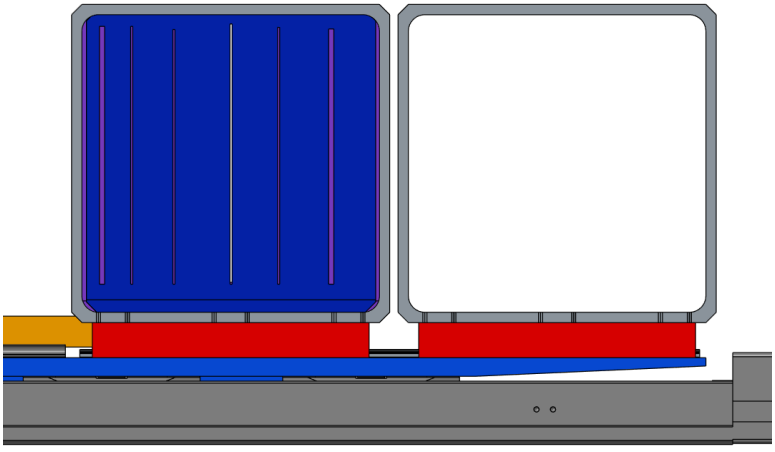

Figure 115 - Slits on a thin metal sheet.

2.4.5. Accessibility

The design of the space frame was done with accessibility in mind. In the case of the cryostat, the instrument must be removed from the frame (which can be kept at telescope) and taken to the lab, where the cryostat can be safely opened.

On the VIS channel, access to the elements that are susceptible to maintenance or inspection is done with apertures located on the cover. There is one aperture in

the middle part of the bench, and the last part of the cover can be completely removed to access the cryocoolers. Other elements can be reached by removing other smaller panels on the cover.

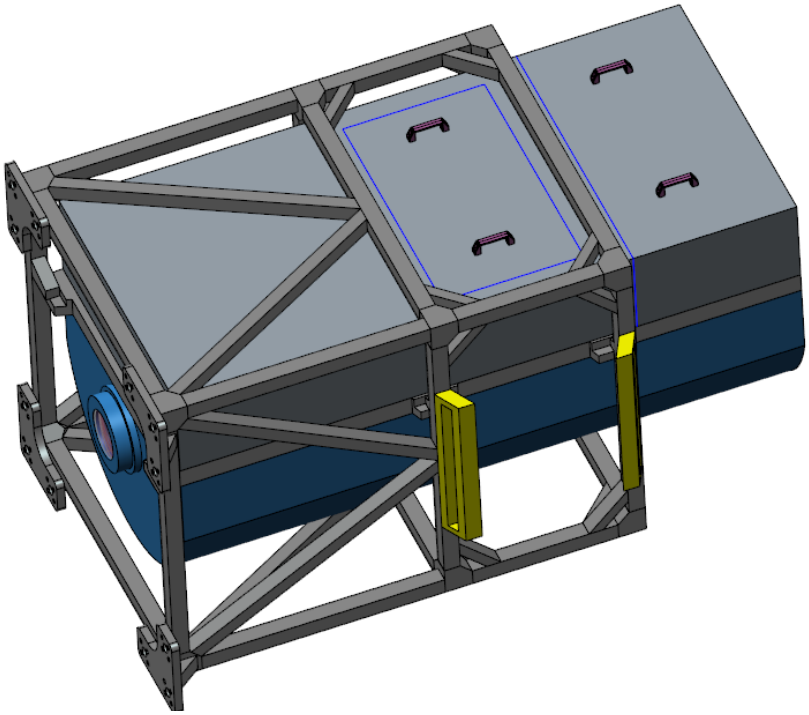

Figure 116 - View of the openings location on the VIS cover.

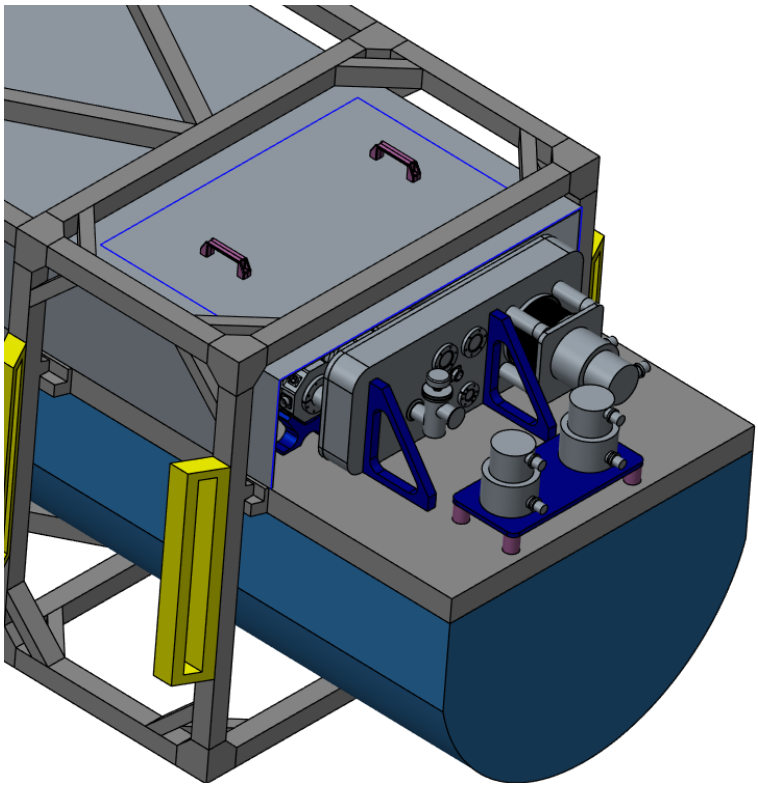

Figure 117 - Rear part of the cover removed to access the cryocoolers.

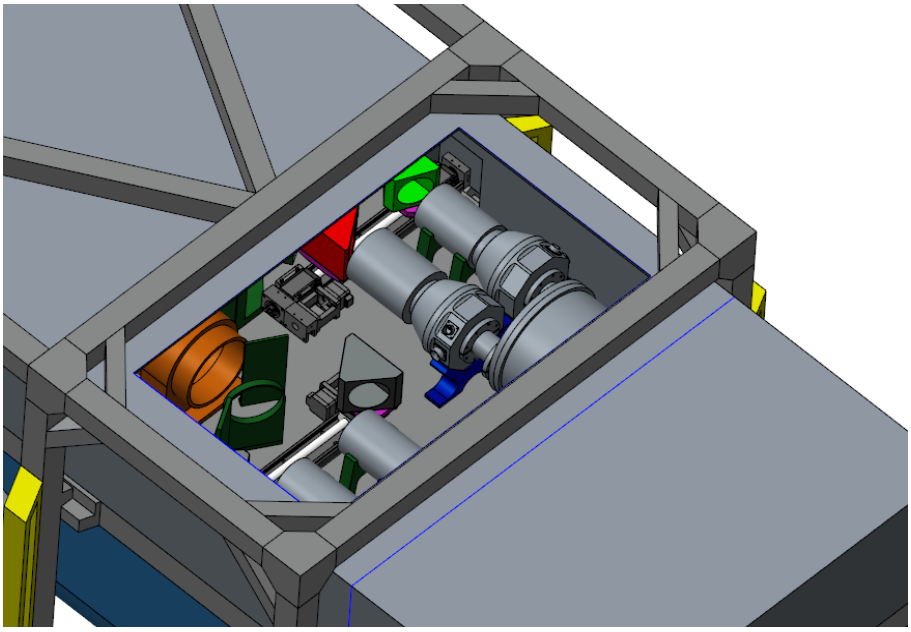

Figure 118 - Large panel removed to access the CCD heads and VPH slides.

2.4.6. Installation of the instrument

The procedure of assembly and installation of the instrument can be understood from the Figures throughout this section. The space frame is a stiff unit that will not be disassembled.

The assembled cryostat, with the VIS channel elements underneath and its cover, is mounted on the I/F locations on the space frame. At these locations there should be locating pins and screwed joints to:

- Make the assembly repeatable.
- Make the junction stiff, to allow the rotation of the instrument on all axes.

To mount the instrument on the frame, it must be slightly raised above the pins and the inserted on them.

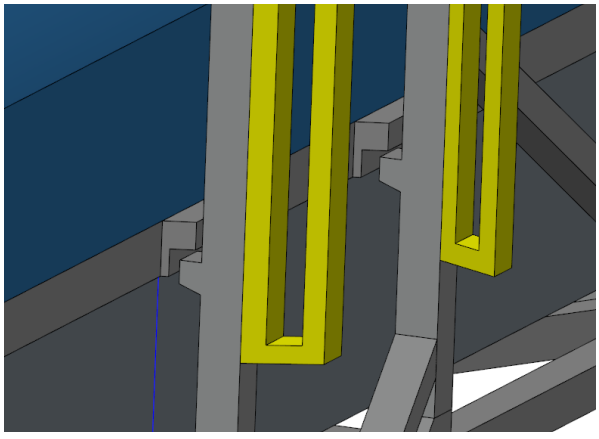

Figure 119 - The instrument is slightly raised to be inserted or removed from the space frame.

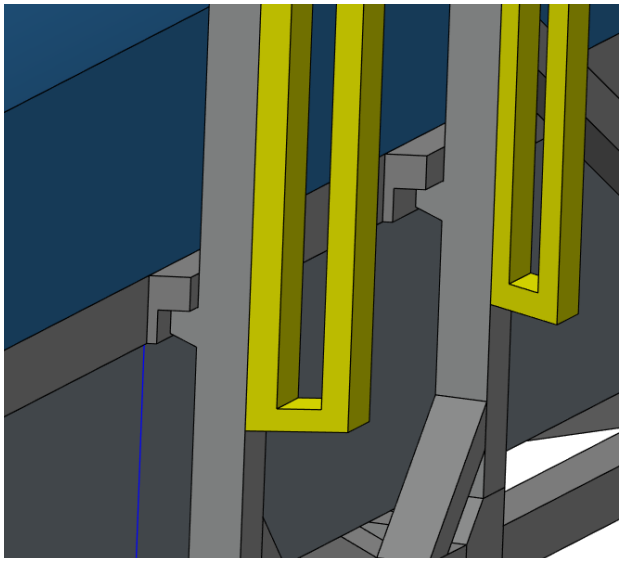

Figure 120 - The optical bench now is resting on the I/F plates of the frame.

Once the cryostat is attached to the space frame, the assembly can be installed on the Gemini ISS with the interface plates. M12 screws are used to attach it. On this design, the space frame is screwed to the ISS with up to 24 screws.

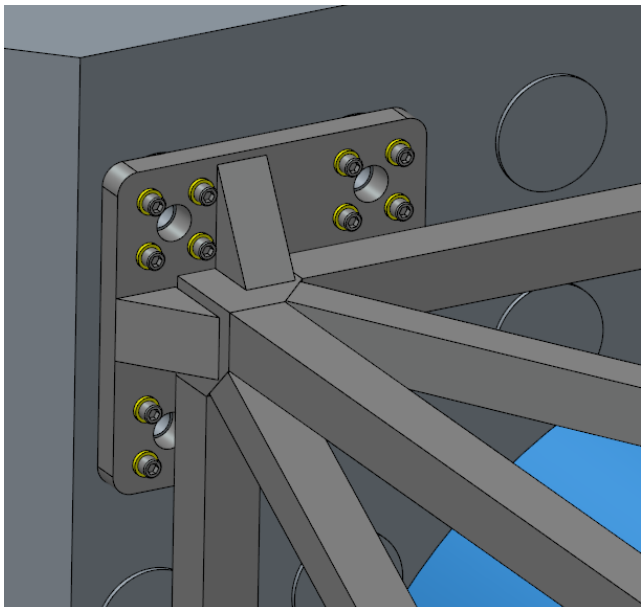

Figure 121 - The space is attached to the ISS with M12 screws.

2.4.7. Conclusions

- **Problems or show-stoppers**

At this moment, we do not identify any meaningful problem regarding the mechanical feasibility of the proposed design.

- **Main mechanical external interfaces: envelope and mass**

It is feasible to fit the instrument within the available envelope at Gemini, as shown in the Figures presented in this section.

The estimation of the instrument weight shows that we are well below the 2000 kg limit for the Gemini ISS (Section 2.2.3). This approach to the mechanical solution confirms that the instrument will be able to fit Gemini mass limit.

- **Integration, handling and accessibility**

We don't identify any problem with the integration of the instrument, and there is room for good access to the maintenance elements. More openings could be made in the cover to access other specific elements, if required.

- **Flexures and vibration**

The main sources of internal vibration on the instruments are the cryocoolers (3 units) and the motors. Mounting these elements on vibration-isolation systems will help to isolate these vibrations.

Regarding the flexures, the structural design of OCTOCAM is based on a very symmetric structure. The space frame supports the central bench, on which all the weight is located. Its performance is very predictable and, unlike other more complicated structural designs, it is easily tunable to control the deflection to desirable values at certain locations.

One critical issue regarding instruments flexure is the relative deflection between the slits and the optical elements and the detector. Since all of these are resting on the same bench, this is very controllable.

We do not foresee problems with flexures that cannot be successfully managed with a detailed structural design.

2.5. Cryogenics

In this section we provide an initial estimation of the power needed for the cryogenic system of OCTOCAM's infrared stage.

First we present an estimation of the thermal balance. We consider a nominal mean temperature of 281K at the Gemini Telescope. Three different temperatures levels must be reached and maintained inside the cryostat:

- 77K in the cold bench.
- 65-70 K in the detectors.
- ~40K in a cold getter.

We have five main thermal inputs:

- Radiation from the warm exterior walls of the cryostat.
- Conduction trough the cold bench supports.
- Conduction trough electrical cables entering the cryostat.
- Conduction through LN2 piping of the precooling system.
- Radiation from entrance and exit windows.

For the radiation from the exterior walls, if we assume a standard aluminum emissivity ε=0.04, we get 10 W/m^2 for the more than 7.2 m^2 of external wall surface.

With a single passive radiation shield we can achieve half of this input. Cooling the shield or using MLI, this value can be further reduced. We consider a cooled shield, giving one quarter of the load, which can lead to 18 W. The heat flow through the G11 support legs is estimated in 10W. Conduction trough the piping of LN2 pre-cool can be estimated to be 3W.

The conduction through the electrical wire can only be roughly estimated, since the cables are not yet defined. We have 4 cryogenic motors, with 4 cables each (copper, 0.5 mm^2), temperature sensors, heater resistors for the detectors, etc. If we estimate a total cable length of 2,5 m the corresponding thermal input is about 10 W.

The entrance and exit windows have a maximum radiative input if of the order of 1.5W each, 3W for both.

With the above rough computation we can estimate an input of **41-45W**. We can safely assume a conservative estimate of 50 W, including the losses on thermal links and interfaces.

Cooling hardware

Concerning the pre-cooling system, it should be capable of cooling down a mass of ~270 kg (the cold bench with the optomechanics on it) to 77 K. Since the latent heat of LN2 is 160 KJ/l, at least 270 liters of LN2 shall be required to cool the NIR arm.

The temperature is then maintained by using cryocoolers. Following the previous estimate, the cooling power must balance 50 W of heat load.

The cryocoolers must also provide a load near 4W at 65K-70K for each detector.

Several differences exist between Pulse Tube (PT) cryocoolers and Gifford-McMahon (GM) cryocoolers. One that is decisive for our case is that the performance of PT cryocoolers is orientation-dependent. PT cryocoolers only work properly when they are operated in a purely vertical orientation with the 2nd stage pointing down. GM cryocoolers will lose some cooling power when the cold head is not operated vertically, but the base temperature will not be affected. GM cryocoolers can operate in any orientation.

On a very interesting testing campaign performed in ESO on 2010, they did a survey reviewing commercially available state-of-the-art high-cooling power 2-stage cryocooler systems for a potential use in powerful scientific instruments for ground-based astronomy[1]. They presented the development of a dedicated test-bed as well as vibration and performance measurements on different 2-stage refrigerator systems:

[1] Low-vibration high-cooling power 2-stage cryocoolers for ground-based astronomical instrumentation (Gerd Jakob, Jean-Louis Lizon, 2010)

- Oerlikon Leybold COOLPOWER 10MD.
- Sumitomo (SHI) SRDK-408D2 and -408D.
- Brooks (CTI) Cryodyne M-1050.
- Oxford Instruments, Austin Scientific 1050 CS.
- Oerlikon Leybold COOLPOWER 4.2K.

As a conclusion of the testing, they selected Oerlikon Leybold COOLPOWER 10MD, which offered substantial advantages in flexibility (variable motor frequency) and orientation insensitivity along with best compromise for a low vibration device combined with high cooling power.

The Leybold Coolpower 10MD has a quite pure sine spectrum with a moderate peak at the 1st frequency and low amplitudes at the harmonics. Operated at 60 r.p.m., this cooler has the lowest amplitude at the 1st frequency peak of all investigated 20 K coolers. At the nominal motor speed of 120 r.p.m. the 1st frequency peak amplitude is competitive with respect to the other coolers, but is offering almost twice as much cooling power. The 1st frequency can be shifted within a range from 0.33Hz to 2.67 Hz depending on the selected motor speed. Operated at 120 r.p.m., the 1st frequency is 2 Hz with harmonics at 4 Hz, 6 Hz, 8 Hz, etc.

The Leybold 10MD is selected because it has an especially low vibration cold head. The vibration isolation support for the cryocoolers is not yet designed. It can be a simple elastomeric support or more complicated, similar to ESO's HAWK-I and CRIRES configuration, with several bellows. Combining these supports with a careful selection of the operating frequencies will minimize vibrations.

The refrigeration capacity is 110W at 80K (first stage) and 18W at 20 K (second stage). The 2nd stage would be dedicated to the detectors and getter, and the first stage to the rest of the elements. The cold head has a mass of 22.6 Kg.

At first sight, a single 10 MD Cryocooler could be sufficient to cool the NIR arm of OCTOCAM. In any case, we propose including 2 of these coolers to be safe and handle the uncertainties of the rough estimations.

During the final phases of the study we have already been in contact with the sales representative that will be providing the 10MD Cryocoolers, with whom we are working towards a better understanding of the vibration parameters.

2.6. Detectors

OCTOCAM uses 8 separate focal plane arrays: 4 e2v CCDs and 4 Teledyne Imaging Sensors (TIS) HgCdTe hybrid CMOS detectors. These will provide the instrument with spectral coverage from approximately 370nm through 2,350 nm (*g* through K_S bands).

The selected VIS CCDs are e2v CCD231-42 devices. They are 4-output, 2048 x 2064 back-illuminated scientific CCDs with 15um^2 pixels. These devices offer a very low dark current (~3 e^-/hour) and low read noise (~3 e^- rms @ 200 KHz readout rate) @ 173K. Our CCD's will be custom ordered/processed as frame transfer devices, with the top/ bottom 520 x 2048 areas optically blocked via an aluminum mask. This results in a CCD with a 2048 (H) x 1024 (V) active optical area.

The near-infrared detectors are Teledyne H2RG focal plane arrays in the ground-based astronomy package. These are 2048 x 2048 pixel (2040 x 2040 sensitive) HgCdTe devices with 18um^2 pixels. The H2RG HgCdTe devices typically have a dark current of approximately 0.01 e^-/sec and a read noise of less than 15 electrons @ 100 KHz/output readout rate (i.e."slow mode") at 77K. For our *H* and K_S band channels, 2.5 µm material-cutoff devices will be used. For our *Y* and *J* band channels we will consider using substrate-removed, 1.7 µm cutoff devices, although the final choice will also depend on factors such as the detector noise (which is generally higher in the 1.7 µm devices).

Each Teledyne H2RG focal plane array will be controlled and readout by an accompanying Teledyne "SIDECAR" (System for Image Digitization Enhancement Control And Retrieval) ASIC. Each SIDECAR will in turn be interfaced to a (dewar-external) Teledyne SIDECAR Acquisition Module (i.e. "SAM', the successor to the Teledyne JADE-2 card). This SAM can control up to 4 SIDECAR ASICs, and also provides USB 2.0 (Windows OS), Camera Link, and Gigabit Ethernet (Windows, UNIX, Linux, and OS-10) communication interfaces.

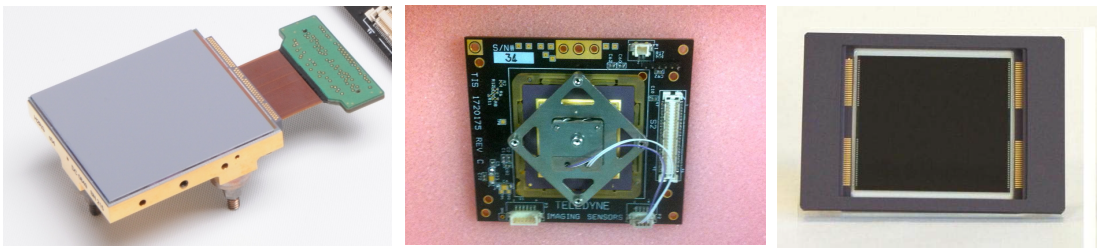

Figure 122 - Teledyne H2RG (GBA), Teledyne SIDECAR (Cryo) ASIC, and e2V CCD231-42 CCD.

2.6.1. e2v CCD Description and Performance

The e2V CCD231-42 selected for the OCTOCAM visible camera has an image area of 2048 x 2064 pixels and split readout registers at both top and bottom with charge detection amplifiers at both ends. A gate-controlled drain is also provided to allow fast dumping of unwanted data.

The output amplifier is a two-stage type designed to give minimum noise at pixel rates of up to 3 MHz, and has an output impedance of 400 Ω. Dummy outputs are also available, to reduce common mode noise rejection (differential signal

sensing). Figure 123 shows the basic CCD architecture. Table 29 lists CCD performance specifications.

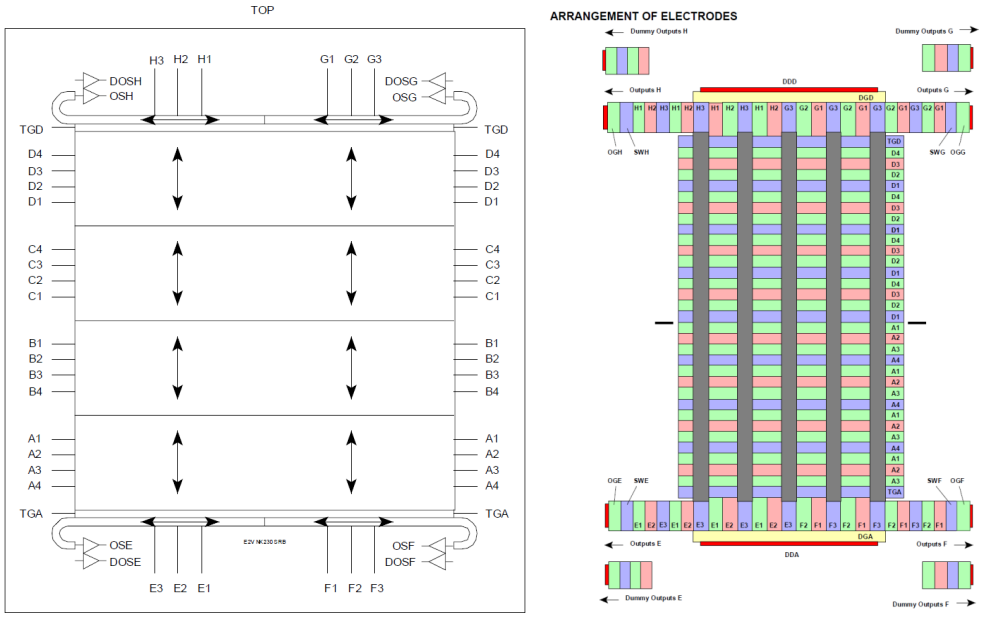

Figure 123 - e2v CCD231-42 Sensor Architecture. Sections B & C have 512 rows each. Sections A & D have 520 rows each. Each row has 2048 image pixels.

	Min	Typical	Max	Units
Peak charge storage (image)	275,000	350,000	-	e^-/pixel
Peak charge storage (register/SW): OG low (mode 1) OG high (mode 2)	 - -	 300,000 350,000	-	 e^-/pixel e^-/pixel
Output node capacity: OG low (mode 1) OG high (mode 2)	 - -	 200,000 600,000	 - -	 e^- e^-
Output amplifier responsivity: mode 1 mode 2	 5.0 -	 7.0 2.5	 - -	 $\mu V/e^-$ $\mu V/e^-$
Readout noise	-	2	3	e^- rms
Maximum readout frequency	-	1000	3000	kHz
Dark signal: at 173 K at 153 K	 - -	 3 0.02	 - 2.0	 e^-/pixel/hr e^-/pixel/hr
Charge transfer efficiency: parallel serial	 99.9990 99.9990	 99.9995 99.9995	 100 100	 % %
Spectral range	300	-	1060	nm
Peak quantum efficiency	-	90	-	%

Table 29 - e2v CCD231-42 Performance Chart. Unless otherwise stated, specifications are for operation at 173K. Read noise is for a pixel clock of 50KHz, correlated double sampling. NOTE: Mode 1 is using registers for summing (binning) operation.

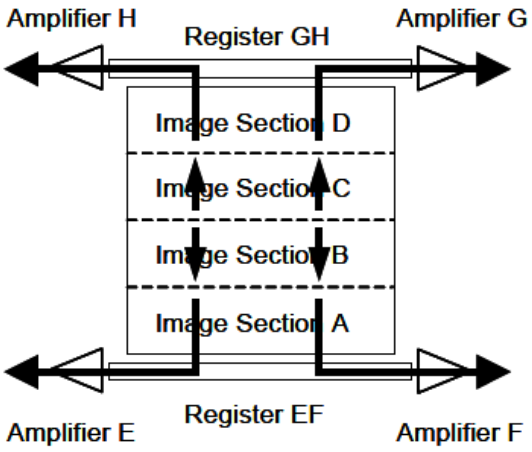

Figure 124 - e2v CCD231-42 Split Frame Transfer Operation. Sections A & D are optically masked.

e2v CCD Quantum Efficiency, Coatings, and Silicon

The 231-42 CCDs have several coating options offered, and are also available as standard or deep depletion silicon devices (for enhanced red response), see Figure 125 and Table 30. Table 31 lists preliminary coating selections for the four VIS channels of OCTOCAM.

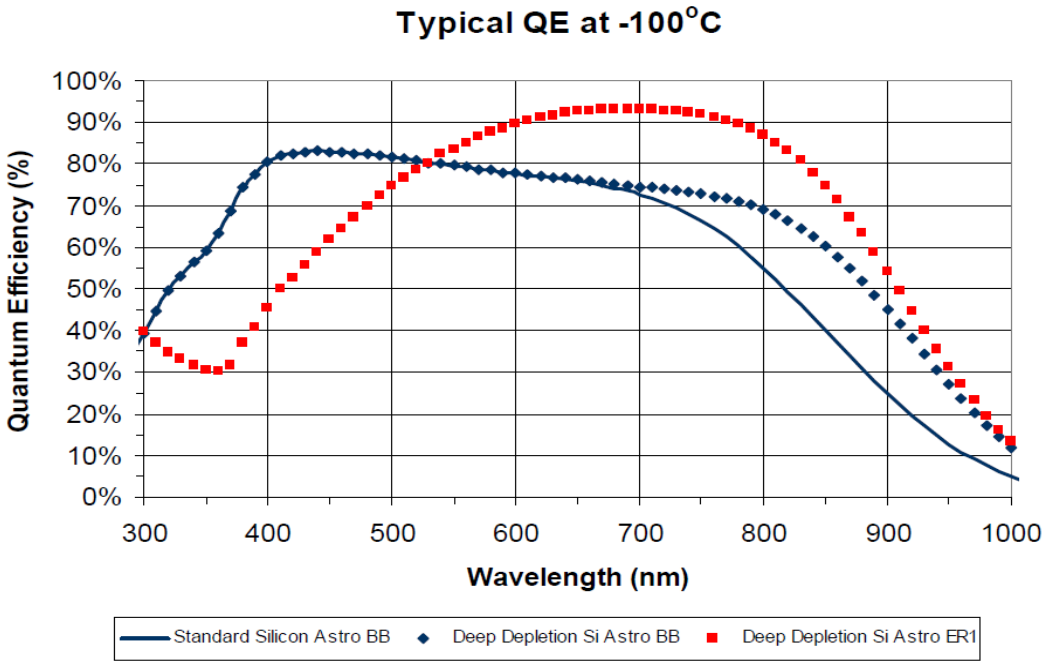

Figure 125 – e2v CCD231-42 QE/AR Coatings.

	Standard silicon Astro Broadband	Deep depletion silicon Astro Broadband	Deep depletion silicon Astro ER1 response	Maximum Pixel Response Non-Uniformity PRNU (1 σ) (%)
Wavelength (nm)	Minimum QE (%)	Minimum QE (%)	Minimum QE (%)	
350	40	40	20	-
400	70	70	35	3
500	80	75	65	-
650	75	70	80	3
900	25	40	45	5

Table 30 - e2v CCD231-42 AR Coating QE Minimums.

Initial OCTOCAM Device Type/Coatings	
BAND	COATING
g	Deep Depletion Silicon Astronomy Broadband (BB)
r	Deep Depletion Silicon Astronomy ER1
i	Deep Depletion Silicon Astronomy ER1
z	Deep Depletion Silicon Astronomy ER1

Table 31 - Recommended e2v AR coatings for OCTOCAM.

e2v CCD Readout Rate Performance

For our normal imaging mode operation, the central 1024 x 1024 area will be used. For spectroscopy, the full 2048 x 1024 area is typically used. Deep depletion-type silicon devices have been selected for all four bands. Summary estimated frame rate/data acquisition data tables at slow (i.e. low CCD read noise) and maximum (3 MHz) pixel clocking speeds and various imaging and spectral operational (i.e. normal, binning, window) modes are provided below. Figure 126 provides read-noise vs. pixel readout rate data.

A larger device, an e2v CCD231-84 configured for split 4096 x 1024 frame transfer mode operation, is being considered as a possible device for *g*-band spectroscopy therefore frame rate data for it has been included.

Binning	50KHz	1MHz	3MHz
1 x 1 (i.e. none)	0.19Hz (5.25s)	1.87Hz (535ms)	10.8Hz (93ms)
2 x 2	0.76Hz (1.32s)	14.1Hz (71ms)	37Hz (27ms)

Table 32 - CCD 231-42 Imaging Mode Readout Performance (Central 1K x 1K).

Window	50KHz	1MHz	3MHz
30x30 (x,y=100,100)	32 Hz (30.8ms)	79 Hz (12.6ms)	83 Hz (12ms)

Table 33 - CCD231-42 Imaging Mode Readout Performance 30 x 30 Window (with 15MHz Charge Dump Clock).

Binning	50KHz	1MHz	3MHz
1 x 1 (i.e. none)	0.1Hz (10.5s)	1.9Hz (530ms)	5.6Hz (180ms)
2 x 1 (vertical bin)	0.19Hz (5.25s)	3.74Hz(270ms)	10.81Hz (93ms)
2 x 2	0.38Hz (2.7s)	7.34Hz (136ms)	20.5Hz (49ms)

Table 34 - CCD 231-42 Long Slit Spectroscopy Mode Performance (2k Spectral x 1k Spacial).

Binning	50KHz	1MHz	3MHz
1 x 1 (i.e. none)	0.045Hz (22s)	0.83Hz (1.2s)	2Hz (500ms)
2 x 1 (vertical bin)	0.093Hz (10.8s)	1.5Hz (0.66s)	3.2Hz (312ms)
2 x 2	0.18Hz (5.56s)	2.3Hz (0.43s)	4.0Hz (0.25s)

Table 35 - CCD 231-84 Long Slit Spectroscopy Mode Performance (4k Spectral x 1k Spacial).

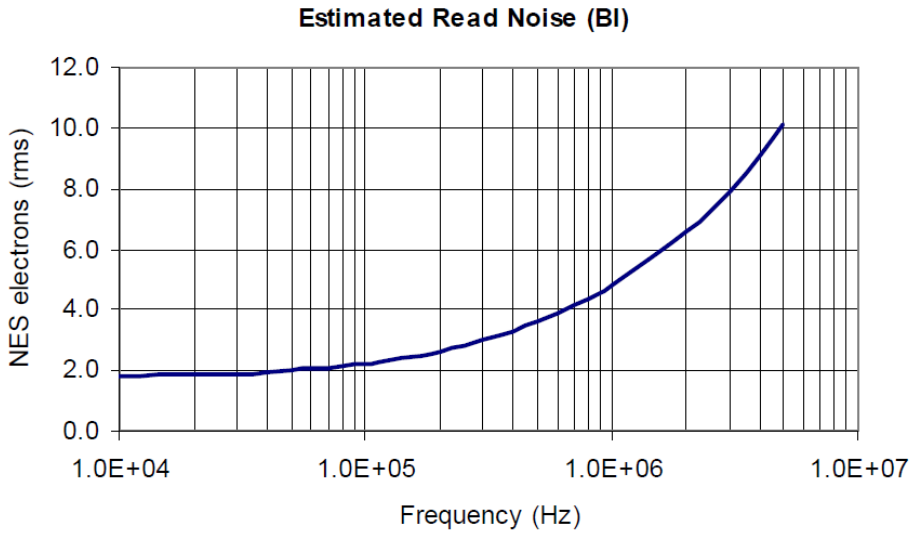

Figure 126 - e2v CCD231-42 Typical Output Amplifier (Read) Noise Performance vs Readout Clock Frequency. Measured using correlated double sampling, and in charge summing mode (mode 1) @ 173K.

2.6.2. Teledyne H2RG Near Infrared Focal Plane Array Description and Performance

The near-infrared detectors selected are Teledyne H2RG focal plane arrays in the standard ground-based astronomy package.

As previously mentioned, 2.5 µm material-cutoff devices will be used our *H* and K_S band channels. The OCTOCAM *Y* and *J* band channels may use substrate-removed, 1.7 µm cutoff devices. These cutoff wavelengths match the atmospheric transmission windows and *H* and K_S filter bands. Figure 127 shows the H2RG device and its overall architecture.

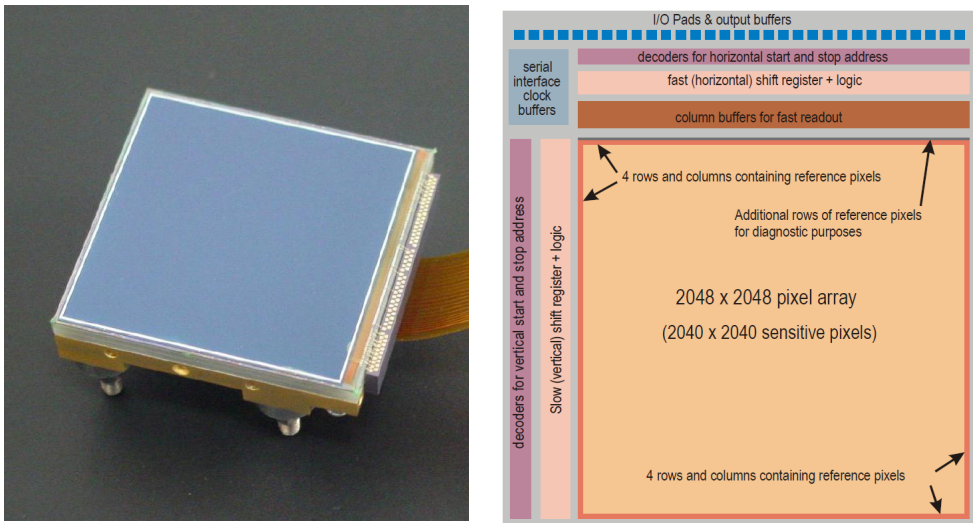

Figure 127 -Teledyne H2RG Device and Configuration.

This ground based astronomy package has three copper-tungsten (CuW) feet, which provide a 3-point pseudo-kinematic mount for the device. They also serve as the primary thermal conduction link to the cold H2RG mount. A 92-pin Hirose flex cable connector is used to connect to a nearby SIDECAR ASIC board, and connects all 32 outputs of the H2RG. Figure 128 shows the Teledyne SIDECAR ASIC block diagram and details.

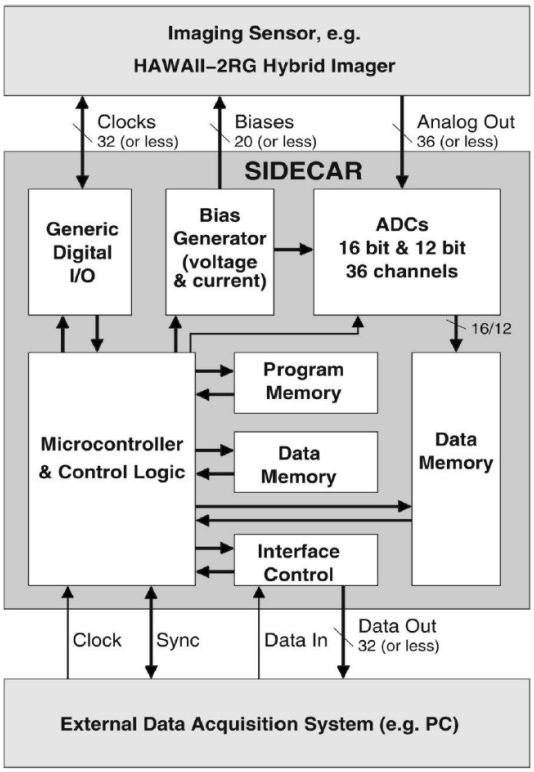

Figure 128 - Teledyne SIDECAR ASIC Block Diagram.

Die Dimension	22 x 14.5 mm²
Technology	0.25 µm CMOS
Analog Input	36 independent channels, fully differential
Preamplifiers	Programmable gain (-3 to 27 dB) and bandwidth
16 bit ADCs	Up to 500 kHz sample rate (1 mW / channel at 100 kHz)
12 bit ADCs	Up to 10 MHz sample rate (10 mW / channel at 5 MHz)
Bias Outputs	20 output channels, selectable voltage or current DACs
Digital I/O	24 channels (CMOS), 16 channels (LVDS) fully programmable
Micro-controller	16 bit RISC, low power, excellent arithmetic capabilities
Program Memory	16 kwords (16 bit / word)
Data Memory (µC)	8 kwords (16 bit / word)
Data Memory (ADC)	36 kwords (24 bit / word)
Array-processor	Adding & multiplying and DMA control per ADC channel
Digital Interface	LVDS or CMOS, custom serial protocol, up to 32 parallel lines
Operating Temperature range	30 K – 300 K
Radiation	Complete design is single event upset protected

Table 36 - Teledyne SIDECAR ASIC General Information.

H2RG / SIDECAR Readout Rate & Performance

The H2RG is structured as 32 adjacent 2048 x 64 pixel blocks or vertical bars, which compose the 2048 x 2048 focal plane array. Each of these 32 blocks has their own output circuit/amplifier, and can also be user-programmed to internally connect to either 4 or 1 H2RG output amplifiers (for low power applications). For OCTOCAM, we will generally operate in the full output configuration, using 16 outputs for central 1k imaging mode, and all 32 outputs for the full 2048 K wide spectral mode. However, it should be noted that if the H2RG is configured in window mode, only 1 output amplifier is used.

The SIDECAR ASIC has two general modes of data acquisition: a 500KHz (max) "slow" mode, and a 10MHz (max) "fast" mode. The tradeoff for increased readout speed higher power consumption and read noise, and lower signal digitization resolution (12 bit vs. 16 bit in slow mode).

All timing and frame rate/read times are calculated with the H2RG operated to provide a 1024 x 2048 pixel frame size. With full 32-output operation, there is no difference in image readout times between a 1K-wide and a 2K-wide image, since the 2K-wide image has 2X the quantity of output amplifiers as the central 1K-wide image section does.

Parameter	Unit	Specification	Goal	Measured
Power Dissipation	mW	≤ 1.0	≤ 0.5	0.297
Cutoff wavelength @ 120 K (50% of peak QE)	µm	1.65 - 1.80	1.70 - 1.75	1.72
Quantum Efficiency (QE) at 800 nm	%	≥ 50	≥ 70	58
Quantum Efficiency (QE) at 1000 nm	%	≥ 50	≥ 70	57
Quantum Efficiency (QE) at 1230 nm	%	≥ 70	≥ 80	73
Quantum Efficiency (QE) at 1500 nm	%	≥ 70	≥ 80	86
Median Dark current @ 0.25 V bias and 120 K	e-/s	≤ 0.05	≤ 0.01	0.001
Median Read Noise (single CDS)	e-	≤ 30	≤ 15	18.92
Well Capacity at 0.25 V bias	e-	≥ 80,000	≥ 100,000	95,563
Crosstalk	%	≤ 2	≤ 1	0.9
Operability	%	≥ 95	≥ 99	98.32
Cluster: 50 or more contiguous inoperable pixel	%	≤ 1% of array	≤ 0.5% of array	0.01

Table 37 - Typical Teledyne Science-Grade H2RG Performance Data, 1.7um device. Data taken with a 100 KHz pixel clock, unbuffered 4-output mode.

Parameter	Unit	Specification	Goal	Measured
Power Dissipation	mW	≤ 1.0	≤ 0.5	0.426
Cutoff wavelength @ 77 K (50% of peak QE)	µm	2.45 - 2.65	2.50 - 2.55	2.53
Quantum Efficiency (QE) at 800 nm	%	≥ 55	≥ 70	83
Quantum Efficiency (QE) at 1000 nm	%	≥ 55	≥ 70	88
Quantum Efficiency (QE) at 1230 nm	%	≥ 55	≥ 70	83
Quantum Efficiency (QE) at 2000 nm	%	≥ 70	≥ 80	83
Median Dark current @ 0.175 V bias and 37 K	e-/s	≤ 0.1	≤ 0.01	0.005
Median Read Noise (single CDS)	e-	≤ 18	≤ 12	9.43
Well Capacity at 0.250 V bias	e-	≥ 65,000	≥ 100,000	120300
Crosstalk	%	≤ 5	≤ 2	0.9
Operability	%	≥ 95	≥ 99	99.58
Cluster: 50 or more contiguous inoperable pixel	%	≤ 1% of array	≤ 0.5% of array	0.00

Table 38 -Typical Teledyne Science-Grade H2RG Performance Data, 2.5um device. Data taken with a 100 KHz pixel clock, unbuffered 4-output mode.

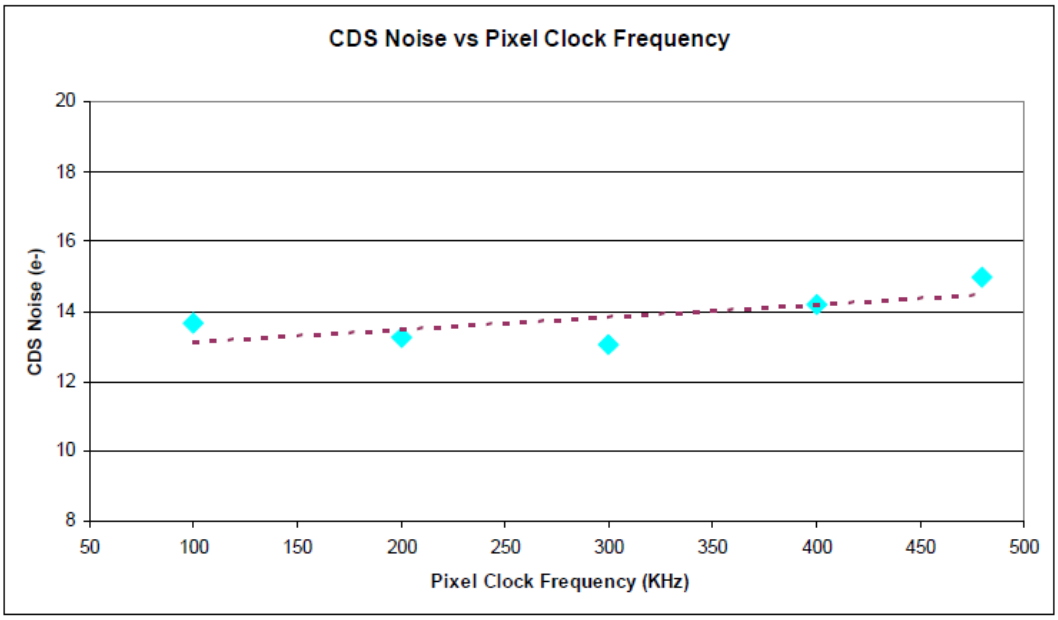

Figure 129 -Teledyne H2RG "Slow" Mode Read Noise vs Pixel Clock Frequency. Data taken @ 77K, 250mv bias.

SIDECAR MODE	Full (1Kx2K) Max Frame Rate	Sampling Mode	Estimated Read Noise
500KHz (slow, 16bit)	3.8Hz (262 ms)	CDS	10-15 e^-
10MHz (fast, 12 bit)	76Hz (13.2 ms)	CDS	65-75 e^-
500KHz (slow, 16bit)	0.12Hz (8.4 s)	Fowler-32	3-4 e^-

Table 39 - H2RG/Sidecar Maximum Frame Rates for Slow and Fast Modes. Given for a single fame, i.e. read-read time after pixels have been reset (i.e. minimum exposure times).

SIDECAR MODE	Ramp-Frame Rate	Estimated Read Noise
500KHz (slow, 16bit)	7.6Hz (131 ms)	15-21 e^-
10MHz (fast, 12 bit)	152Hz (6.6 ms)	90-105 e^-

Table 40 - H2RG/Sidecar Maximum Frame Rates for a Single Frame (Sample-up-the Ramp)

2.6.3. e2v CCD Cooling and Packaging, Baseline Concept

The baseline CCD packaging and cooling concept is shown in Figure 130. This concept uses a Sumitomo Heavy Industries CH-104 77K Gifford McMahon cryocooler to cool all 4 CCDs. This unit is rated at 42W cooling power @ 77K. Cooling power is not position sensitive, so our dewar will not be sensitive to telescope orientation. This approach ensures that we will have ample cooling power to be able to operate the CCDs at 173K.

Temperature control is done both locally in each camera head, and on the main cold sink/cooler head. Under-temp (143K for the CCD231-42) cooler shutoff will also be implemented. Each CCD will be mounted on a combination cold-sink/preamp board, which is also cooled. Electrical interfacing to each CCD is performed at the camera head level. The vacuum cylinder connecting each camera head to the main dewar/vacuum case will have a vacuum flex bellows joint that will allow each camera head to be individually optically aligned and secured as needed. Additional concept detail is shown in Figure 131.

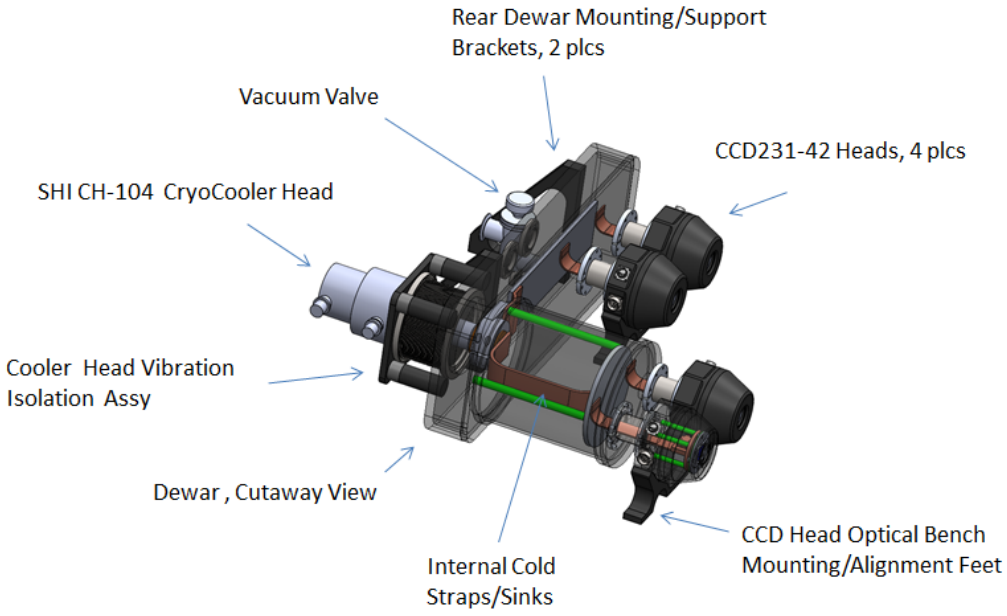

Figure 130 - OCTOCAM CCD Dewar Concept.

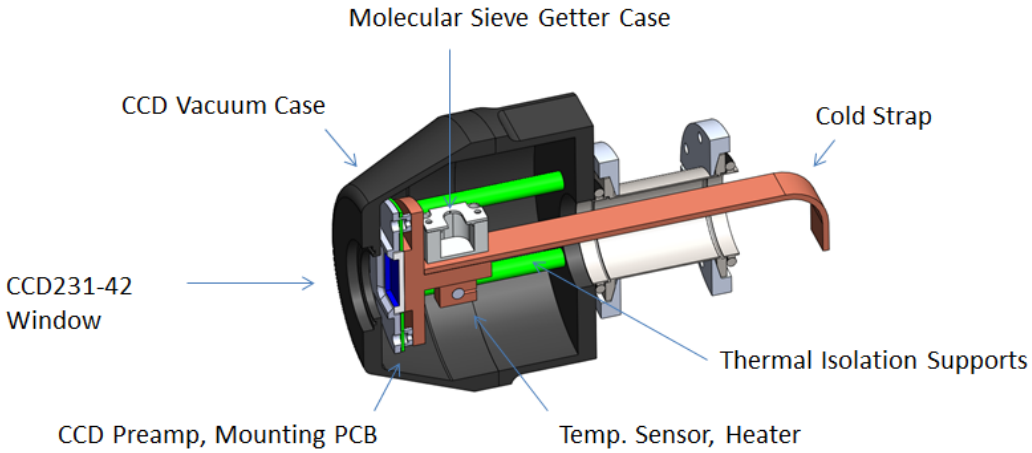

Figure 131 - OCTOCAM CCD Head Concept Detail, Cutaway View.

2.6.4. e2v CCD Cooling and Packaging, Developmental TEC-version Concept

In addition the baseline GM cooled CCD Camera head/dewar assembly, a thermoelectric (TEC)/Peltier-cooled CCD housing concept is also being pursued. Chilled coolant (0C-10C) flowing through each head would provide the heat sink/heat removal for the TEC. This concept/approach, if adequate cooling power can be achieved has the obvious advantages of a self-contained standalone CCD package, along with lower cooling system complexity/mass, and no/very low mechanical vibration.

The use of this concept would only be possible with some advances among cryogenic detector/optical packaging companies, but currently there is some ongoing engineering/technology development activity among some of these organizations. Therefore this concept may be a future option if a TEC approach allows cooling the OCTOCAM CCDs down to the 170K-180K range.

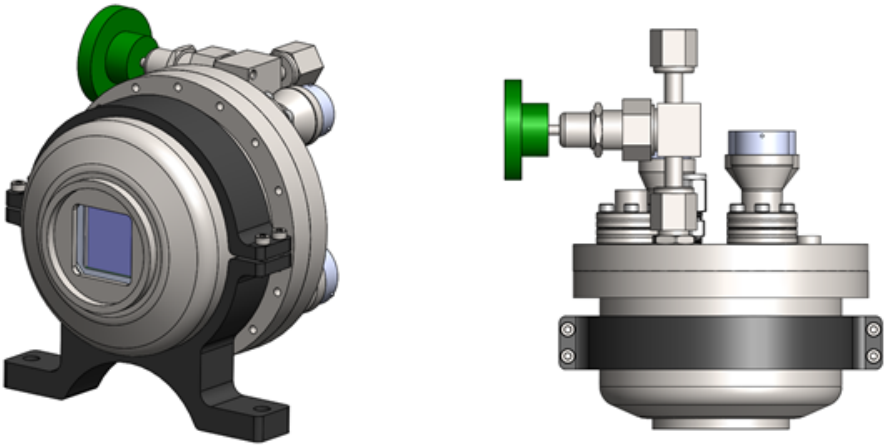

Figure 132 - Developmental TEC Cooled CCD Concept.

2.7. Electrical Design

The OCTOCAM instrument electronics package consists of a local instrument PC (LPC) and three controller setups. These allow for remote control of the following items.

- Four visual detectors.
- Four IR detectors.
- Cryo-coolers.
- Motors.
- Shutters.
- Monitoring of the on-instrument temperature sensors, currents and voltages.

Each controller assembly consists of multiple printed circuit boards (PCB). See Figure 133. To simplify the overall design and ease of assembly the three electronics assemblies communicate with the LPC via 1 gigabit Ethernet (1GE).

Each controller is assembled in a custom chassis with adapters for connecting to the local liquid cooling loop.

In addition to the local instrument electronics, the OCTOCAM electronics include an external PC (EPC). This is a much more powerful rack mount server style PC, which receives and processes all the data from the on-telescope instrument. This data is processed and stored as described in section 2.9. Data reduction pipeline. The EPC is also responsible for controlling and monitoring the external portions of the cryogenic system (valve status, temperatures, pressure).

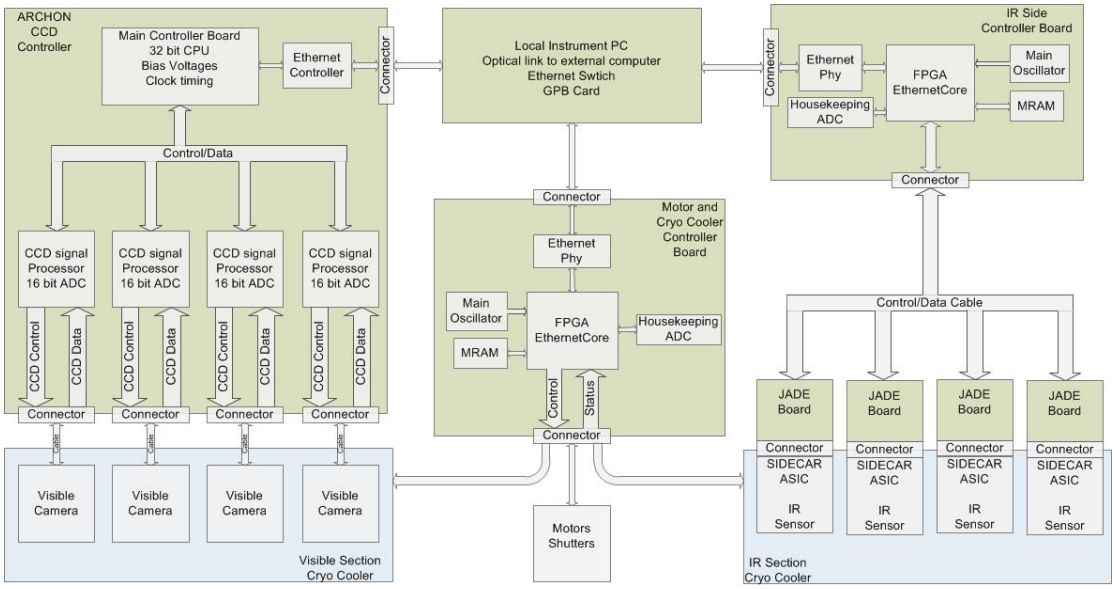

Figure 133 - Diagram of OCTOCAM's electronic system.

2.7.1. Local PC

The local instrument PC consists of a small off the shelf PC with an Ethernet switch and a GPS time card. The LPC will have custom designed software allowing for either local or remote control (via the external computer) of the various detector

assemblies. Data will be received from the detector assemblies, re-packetized and forwarded, via optical link, to the off instrument rack mount computers.

The LPC setup also includes the various power supplies needed to power the detector assemblies. These are all simple off the shelf power supplies controlled by the LPC via USB.

2.7.2. IR Controller Board

The custom IR controller board (IRCB) is located at the IR sensor heads together with the four JADE boards. The IRCB provides setup and control for all four IR detectors and their respective local JADE boards and SIDECAR ASICS. To minimize NRE the design will implement a SwRI FPGA HDL core for controlling the SIDECAR ASIC's , this already existing core will be instantiated four times in the IR controller FPGA allowing for complete individual control of each ASIC and detector. The board also includes a basic housekeeping analog to digital controllers allowing for monitoring of local voltages and currents as well as multiple temperature sensors located at various points in the IR detector assembly. Once an acquisition has been started, the FPGA will receive the raw digitized data from the active sensor(s), packetize it and forward it to the LPC via the Ethernet link.

2.7.3. ARCHON CCD Controller

The ARCHON modular CCD controller from Semiconductor Technology Associates (STA) has been selected as the visual detector side controller.

The ARCHON computer board consists of a FPGA with an instantiated 32 bit CPU, supporting memory and an Ethernet controller. This highly modular system incorporates 16-bit four-channel analog to digital controllers modules, four such modules will be utilized -one per detector. To minimize noise insertion the ARCHON system will be located immediately on top of the CCD's giving the minimal possible cabling from the raw analog CCD data output to the input preamps on the analog to digital controller modules. As with the IR system the raw analog to digital controller data will be received by the FPGA/CPU, packetized and forwarded to the LPC via Ethernet.

The ARCHON chassis will be redesigned by SwRI to not rely on passive or forced air cooling, the electronics will be housed in a custom aluminum chassis allowing for connection to the local liquid cooling loop.

2.7.4. Motor and Cryocooler Controller (MCC)

The MCC is a custom electronics board with a SwRI designed FPGA allowing for remote control of the instrument motors, shutters (see Table 41) and cryocoolers. All motors and shutters have individual control circuits allowing for maximum configurability. The MCC also houses the electronics used for overall instrument housekeeping, all external voltage, current, temperature and status signals are measured by the MCC and then forwarded to the LPC via Ethernet.

Unit	Function	Type	#
ADC	Operation	Rotation	2
Focal Plane	Placement	Linear/rot.	2/3
NIR	Grism/filter	Linear/rot.	2
NIR	Dither	Push/pull	2
NIR	Shutters	Open/close	4
VIS	Grism/filter	Linear/rot.	2
VIS	Focusing	Linear/rot.	4
VIS	Shutters	Open/close	4
Spectropol	Operation	Rotation	1

Table 41 – Moving elements foreseen for OCTOCAM.

2.8. Instrument software

The OCTOCAM Instrument Software is defined as the software that:

1. Provides the command and status interface between the Gemini Observatory and the OCTOCAM instrument electronics, and
2. Acquires and routes science data from the instrument to the OCTOCAM Data Pipeline software.

The following subsections outline the basic requirements and design of the Instrument Software.

2.8.1. Software Requirements

The following list represents the fundamental software requirements that were identified during the feasibility study effort. This list will serve as a high-level baseline from which a detailed set of instrument software requirements will be derived during the development effort.

- The Instrument Software shall provide a command interface to the OCTOCAM motors and cryo controllers.
- The Instrument Software shall provide a command interface to configure the OCTOCAM visible and IR detector controllers and data acquisition modes.
- The Instrument Software shall collect and report status and housekeeping data from the detector and motor controllers and the cyro subsystem.
- The Instrument Software shall be capable of acquiring data from the detector controllers at a rate of 100 Mbps.
- The Instrument Software shall be capable of time-stamping acquired data at a minimum accuracy of 1 millisecond.
- The Instrument Software shall be controlled by and report status and faults to the Gemini Observatory via the Gemini Instrument Application Programmer Interface (GIAPI).
- The Instrument Software shall route instrument science data and associated engineering data to the Data Pipeline Software.

2.8.2. Software Design and Interfaces

The Instrument Software is comprised of two Computer Software Configuration Items (CSCIs) as defined in Table 42.

CSCI	Description
Local Instrument PC Software	Implements the direct interface to the motor, cryo, and detector control electronics. Configures the instrument for science observations per commands from the Control Room PC Software. Acquires and timestamps science data and routes it to the Data Pipeline Software. Collects and reports the health and status of the Instrument to the Control Room PC Software.
Control Room PC Software	Implements the interface to the Gemini Observatory via the GIAPI programming interface. Translates and routes commands from the GIAPI interface to the Local Instrument PC Software. Receives status and housekeeping data from the Instrument PC Software and translates and routes it via the GIAPI interface. Translates and routes commands and status between the cryo compressors and the GIAPI interface. Provides a GUI that enables local (i.e. non-GIAPI) configuration and limited operation of the instrument for test purposes.

Table 42 - Instrument Software Configuration Items.

In addition to these two development items, the interface to the visible detector is planned to be a commercial off-the-shelf (COTS) controller. As such, while COTS controller will not require any software development per se, the controller will have to be setup and configured to tailor its functionality to the needs of OCTOCAM.

The following block diagram illustrates the design of the Instrument Software, as well as the interface to the Data Pipeline Software. The top half of the diagram illustrates the design of the Local Instrument PC Software; the bottom half of the diagram illustrates the design of the Control Room PC Software. Note that the Data Pipeline Software, which also executes on the Control Room PC, is described in the following section.

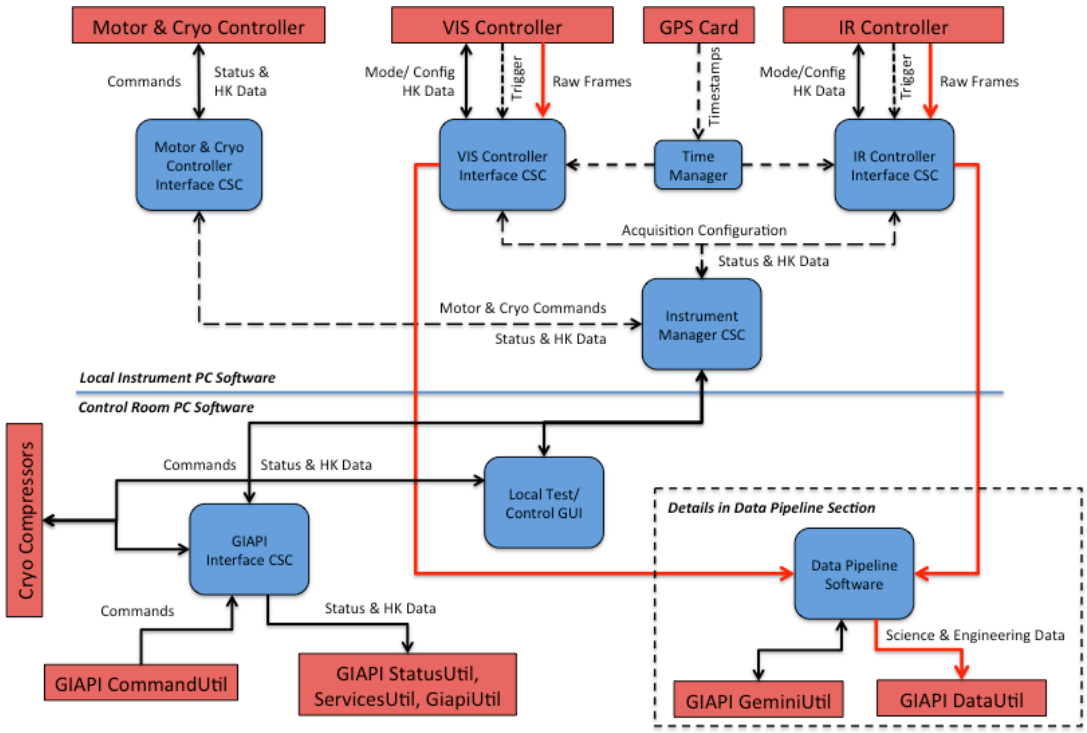

Figure 134 - Instrument Software Block Diagram.

2.8.3. Software Development Environment

Both the Local Instrument PC Software and the Control Room PC Software will be hosted on Linux PCs. The software will be developed in the C++ Programming Language using standard open source tools and compilers. Since commencement of development is yet in the future, the specific Linux distribution and compiler versions will be determined as one of the initial planning tasks in the development phase.

The Subversion revision control software will be used for software configuration management. The SwRI Project Information Management System (PIMS) will be used to capture and track software Problem Reports and Change Requests (PRs/CRs).

The Local Instrument PC and the Control Room PC will be acquired as a project cost. However, the necessary development tools will be provided by SwRI and will not be a project cost. The Control Room PC will be a standard rack-mount PC; refer to Section 2.8.2 for additional details on the Control Room PC and special mechanical packaging that will be needed for thermal dissipation.

2.9. Data reduction pipeline

The OCTOCAM data pipeline software resides on the Control Room PC (described in the Instrument Software section) where it interfaces with the instrument software to receive the science and engineering data and interfaces with the Gemini system to process to FITS files and provide those files to the Gemini Data Storage Network (GDSN).

The OCTOCAM Data Reduction Pipeline is defined as the system that:

1. Obtains the raw instrument science and engineering data from the OCTOCAM instrument software system,
2. Processes the OCTOCAM raw data into calibrated and science units in FITS files with standard headers, and
3. Provides the FITS files to the Gemini Data Storage Network (GDSN).

2.9.1. Requirements

The following are the fundamental data pipeline requirements identified during the feasibility study effort. This list serves as a high-level baseline from which a detailed set of data pipeline requirements will be derived during the development effort.

- Understand and integrate with the Gemini system
- Compatible with the Gemini Instrument Application Programmer Interface (GIAPI)
- Process raw data to science and engineering FITS files
- Associate additional files with datasets where appropriate
- Forward well-formed, easily viewable datasets to Gemini through GIAPI data protocols (REQ-GIAPI-INS-07)
- Provide FITS files to the GDSN

2.9.2. Design and interfaces

The OCTOCAM data pipeline interfaces with the OCTOCAM instrument software to obtain the raw data, processes it for science analysis, and interfaces with the Gemini System for public access of the data.

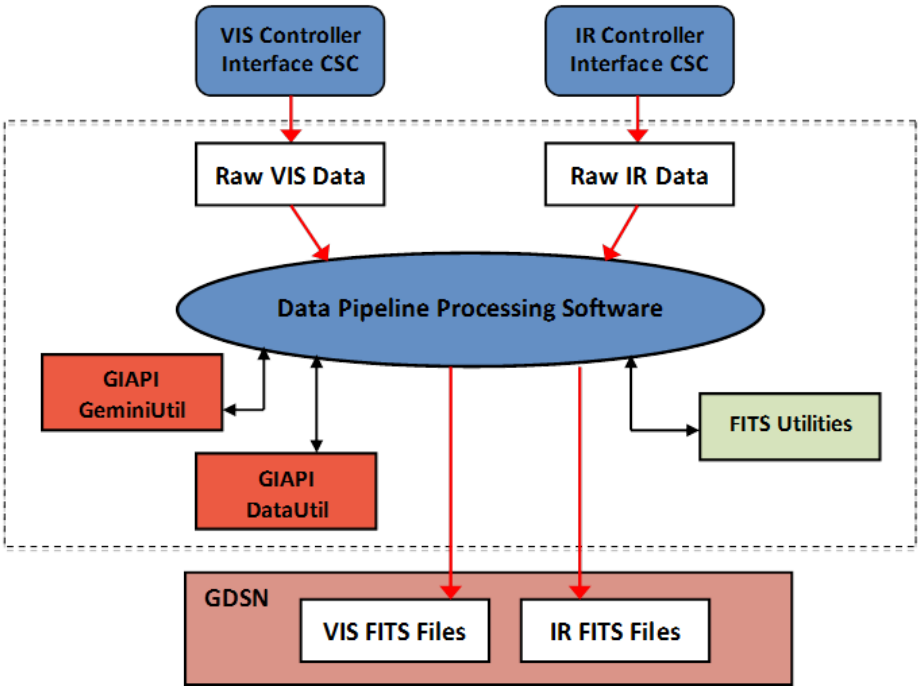

Figure 135 - Data flow for the instrument pipeline.

The OCTOCAM data pipeline interfaces directly with the OCTOCAM instrument software on the Control Room PC to obtain the time-stamped science and engineering data in its raw form. This includes any ancillary data (housekeeping,

etc.) necessary for generating well-formed, easily viewable FITS headers for science analysis.

Once the OCTOCAM data has been reduced and processed for science analysis, the data in the form of FITS files are put into the Gemini System using the GIAPI data protocols (DataUtil). To generate well-formed, easily viewable datasets in FITS format, proper headers need to be provided. The GeminiUtil GIAPI interface is used to access the World Coordinate System (WCS) as well as other utilities necessary to provide the header information.

2.9.3. Pipeline Software Environment

The Data Pipeline Software will reside on the Control Room PC, which is hosted on a Linux PC. The software will be developed in the C++ programming language using standard open source tools and compilers. The specifics will be determined as one of the initial planning tasks in the development phase. The Subversion revision control system will be used for software configuration management and the SwRI Project Information Management System (PIMS) will be used to capture and track software Problem Reports and Change Requests (PRs/CRs).

2.9.4. Pipeline tasks

The pipeline will be run in real time at the observatory and it should also be available for the users to use if they need to tune some parameters to optimize the reduction for their science.

The following codes mark when each task should be performed, for the real time operation as follows:

· During twilight, as soon as the corresponding calibration frames are obtained

- Just after the standard stars have been observed (often at the end of twilight).

* During night, as soon as science observations are made

Imaging in the VIS arms

· Create a bias frame for each of the channels: by average combining the bias images that are daily obtained according to the calibration plan.

· Create a flat field image for each of the channels: (a) Subtract the corresponding bias frame to each of the flat field images obtained during twilight (or dome flats, although twilight flats are normally preferred). (b) Normalize each corrected flat field image. (c) Detect and mask the stars in the twilight flats that may affect the frames (d) Combine the normalized image to a single normalized flat field for each of the arms.

- Correct standard star images: (a) Subtract bias. (b) Divide by flat field.

- Astrometric calibration of the standard star images.

- Detect standard stars and obtain photometry. Aperture photometry of the standard stars in the field.

- Calculate the photometric conversion from counts to flux for each band. This will allow to evaluate if the night is photometric (comparing with historical values) and have the photometric calibration ready to perform real time estimation of object magnitudes.

* Correct science images: (a) Subtract bias. (b) Divide by flat field.

* Astrometric calibration of the science images (may not always be possible).

* Combine images (if required)

Imaging in the NIR arms

· Create bad pixel masks

· Create flat fields, either from sky flats or from dome flats (flats-on - flats-off).

· Create dark frames, although these will not often be used for the scientific calibration

- Correct standard star images: (a) Divide by flat field. (b) Create a sky frame. (c) Subtract sky frame from science images.

- Astrometric calibration of the standard star images.

- Detect standard stars and obtain photometry. Aperture photometry of the standard stars in the field.

- Calculate the photometric conversion from counts to flux for each band. This will allow to evaluate if the night is photometric (comparing with historical values) and have the photometric calibration ready to perform real time estimation of object magnitudes.

* Correct science images: (a) Divide by flat field. (b) Create a sky frame. (c) Subtract sky frame from science images.

* Astrometric calibration of the science images (may not always be possible).

* Combine images (if required)

Spectroscopy in the VIS arms

· Create a bias frame for each of the channels: by average combining the 10 bias images that are daily obtained according to the calibration plan.

· Create a response image for each of the channels: (a) Subtract the corresponding bias frame to each of the flat field images obtained during twilight (or dome flats, although twilight flats are normally preferred). (b) Normalize each corrected flat field image. (c) Combine the normalized 2D spectra (d) Fit a function to the continuum and subtract that function from the flat field to create the response curve.

· Create wavelength correction from arc images: (a) Subtract the bias from the arc images and divide them by the response curves. Combine arcs of different

lamps and exposures to create the master arc. Identify the emission lines with catalogued emissions and calculate the wavelength solution for each arm.

- Correct standard star images: (a) subtract bias, (b) divide by response, (c) apply wavelength calibration.

- Extract standard star.

- Calculate the flux calibration for each standard star in each arm.

- Subtract the sky contribution (either by fitting the background or by performing nodding along the slit.)

* Correct the science spectra: (a) subtract bias, (b) divide by response, (c) apply wavelength calibration.

* Flux calibrate the 2D spectra.

* Extract the science objects.

Spectroscopy in the NIR arms

· Create a response image for each of the channels: (a) Subtract the corresponding bias frame to each of the flat field images obtained during twilight (or dome flats, although twilight flats are normally preferred). (b) Normalize each corrected flat field image. (c) Combine the normalized 2D spectra (d) Fit a function to the continuum and subtract that function from the flat field to create the response curve.

· Create wavelength correction from arc images: (a) Subtract the bias from the arc images and divide them by the response curves. Combine arcs of different lamps and exposures to create the master arc. Identify the emission lines with catalogued emissions and calculate the wavelength solution for each arm.

- Correct standard star images: (a) subtract bias, (b) divide by response, (c) apply wavelength calibration.

- Extract standard star.

- Calculate the flux calibration for each standard star in each arm.

- Subtract the sky contribution (either by fitting the background or by performing nodding along the slit.)

* Correct the science spectra: (a) subtract bias, (b) divide by response, (c) apply wavelength calibration.

* Flux calibrate the 2D spectra.

* Extract the science objects.

Integral Field Unit spectroscopy

Similar to the spectroscopic reduction, but each slice should be corrected independently and at the end we need to reconstruct the spectra into a data-cube.

Spectropolarimetry

Similar to the spectroscopic reduction, it additionally requires to combine the various spectra according to some well know procedures. Calibrations and routine checks will be performed by observing standard stars, both strong-polarized and non-polarized. These data will be used both for calibration and for housekeeping of the instrument and pipeline.

2.10. Integral Field Unit

Integral Field Units (IFUs) have been in use on telescopes in the past 20 years with great success. Gemini has the GMOS IFUs North and South, which are fiber-lenslets IFUs, and the NIFS spectrograph, which has an Advanced Image Slicer (AIS) in front of the spectrograph. An IFU on OCTOCAM would not only give the full spectrum from 0.37 μm to 2.35 μm in one observation but also give a larger field of view than the existing IFUs and a much lower detector noise due to the larger pixel solid angle in square arcseconds. All of this together would considerably increase the throughput and scientific applications of OCTOCAM.

OCTOCAM covers both the VIS and the NIR so this put new conditions on an IFU. In term of transmission, fiber systems are difficult to use in the NIR, in particular because of the low transmission of standard fibers in the K band. Slicers on the other hand use mirrors so would need a good reflective coating for the whole of the VIS and NIR. Fortunately, coatings as Enhanced Silver now give an average reflectivity over the full VIS+NIR bandwidth of >98%. Combined with the higher performances of slicers compared to fiber systems with or without microlenses and the success of slicers on telescopes, a slicer system is the obvious choice (Content et al. 1998, SPIE, 3354, 187).

The AIS has now been universally adopted and IFUs using this concept are on telescopes all over the world. Among them, KMOS and MUSE, both on the VLT, contain 24 AIS, which are made of a total of more than 3300 mirrors. The Keck telescope has the ESI-IFU AIS, and the JWST will contain 5 slicers all using the basic design of the AIS or a simpler modified design but with lower performances. The very first AIS was however the GNIRS slicer which was accidentally destroyed with the first GNIRS. It worked perfectly well before the accident even giving a higher transmission than a slit of similar resolution over the wavelength range of 2 to 5 μm due to losses from slit diffraction and the particularities of the slicer design. Most of these slicers are for the NIR but ESI and MUSE are for the VIS. The advantages of the AIS and the fact that it is a proven technology many times over - especially on Gemini which saw the first of them - for both the VIS and the NIR made it the chosen concept for the OCTOCAM IFU.

An important fact for an OCTOCAM slicer is that the ESI and MUSE slicers are in the VIS because the tolerances for the VIS are much tighter than for the NIR so the technology for the VIS should be the one used. The only additional challenge is that the IFU will be at much lower temperature than in ESI and MUSE because

of its use in the NIR but this is not a critical mechanical problem for a system with no moving parts. Also, a cryogenic test was made on ESI-IFU by putting it in liquid nitrogen, which it successfully passed (Sheinis et al. 2003, SPIE, 4841, 1078S).

2.10.1. Requirements

The field of view should be larger than the existing fields of view of IFUs on Gemini instruments. NIFS has a field of 3" x 3" and the GMOS IFUs have fields of 7" x 5" in their largest configuration with 2 slits. The field of view of the OCTOCAM IFU is 9.7" x 6.8".

Spatial resolution should be at least better than the seeing, preferably not far from half the seeing, to get a good sampling while maintaining a proper spectral sampling. The slice width is 0.4" while the pixel size is 0.18" so a spatial element is 0.18" x 0.4" which is not far from half the typical seeing in the largest direction. The slice width gives a spectral element 2.3 pixel wide which is larger than the minimum sampling of 2 pixel. This gives a resolution 1.3 times larger than the standard of 3 pixel, including tolerances.

The transmission should be at least 80% on average and at least 50% at all wavelengths. There are 6 reflections in the IFU. Enhanced Silver coatings give an average reflectivity >98% over the whole range so the average transmission should be >89%. The minimum reflectivity is at 370 nm but should be >92% so the transmission should be >60% at that wavelength. The GMOS IFUs have a transmission of about 63% while the NIFS IFU has a transmission around 95% (including fore-optics) so the OCTOCAM slicer will have a transmission higher than the average of the 2 instruments, which is 79%.

This however does not tell the whole story about the signal-to-noise ratio because both instruments are affected by the detector noise due to the small pixel sizes of these instruments. NIFS has pixels of 0.045" x 0.05" while the GMOS IFU has pixels of 0.041". With pixels of 0.18" OCTOCAM will have 14 times less pixels than NIFS and 19 times less than the GMOS IFUs per square arcsecond on the sky. This will considerably reduce the detector noise.

The image quality, defined as the 50% EED, must be better than 0.15" on average with a goal of 0.1". The present design gives an average of 0.04" to which the effect of the tolerances will be added. The tolerances will be adjusted accordingly.

2.10.2. Basic design

The AIS is made of fore-optics and 3 mirror arrays which are called the slicing mirror array, the pupil mirror array and the slit mirror array. The AIS slices the focal plane into many long and thin images that are reimaged side-by-side at the slit of the spectrograph (Figure 136). The width of the slice images then becomes the width of the slit.

The first part of the AIS is the fore-optics which reimages the focal plane of the spectrograph on the slicing array. This is done with the proper magnification. In previous AIS, the magnification was made larger in the spectral direction than in the spatial (anamorphic magnification) so that a square spatial element on the

sky (a spaxel) is imaged on the detector on one pixel in the spatial direction but 2 pixels in the spectral to get the proper sampling of the spectral element. This however comes with a reduction in the size of the field of view. It is not necessary with OCTOCAM because the seeing is typically many pixels wide so a slit of half the typical seeing is already more than 2 pixel wide.

The slicing mirror array is made of many long thin mirrors in the focal plane of the fore-optics that separate (slice) the field into the corresponding number of sub-images. Each mirror is tilted with a different angle than the others so that the beam is reflected in a different direction toward the pupil mirror array. Each slicing mirror is curved to image the pupil on or near the pupil mirror array. This solves a vignetting problem from previous designs of slicers. Each beam from a slicing mirror hit a different pupil mirror which images the slice on the slit. All the slices are then imaged side-by-side on the slit with a small gap between them to avoid cross-talks. The gap is 5 pixel wide in the present design. Superimposed to each slice images is a slit mirror that reimages the pupil at the right place in the spectrograph.

Two different designs are presented here. In the first, the length of the slicer system is parallel to the telescope focal plane while it is parallel to the optical axis of the telescope in the second.

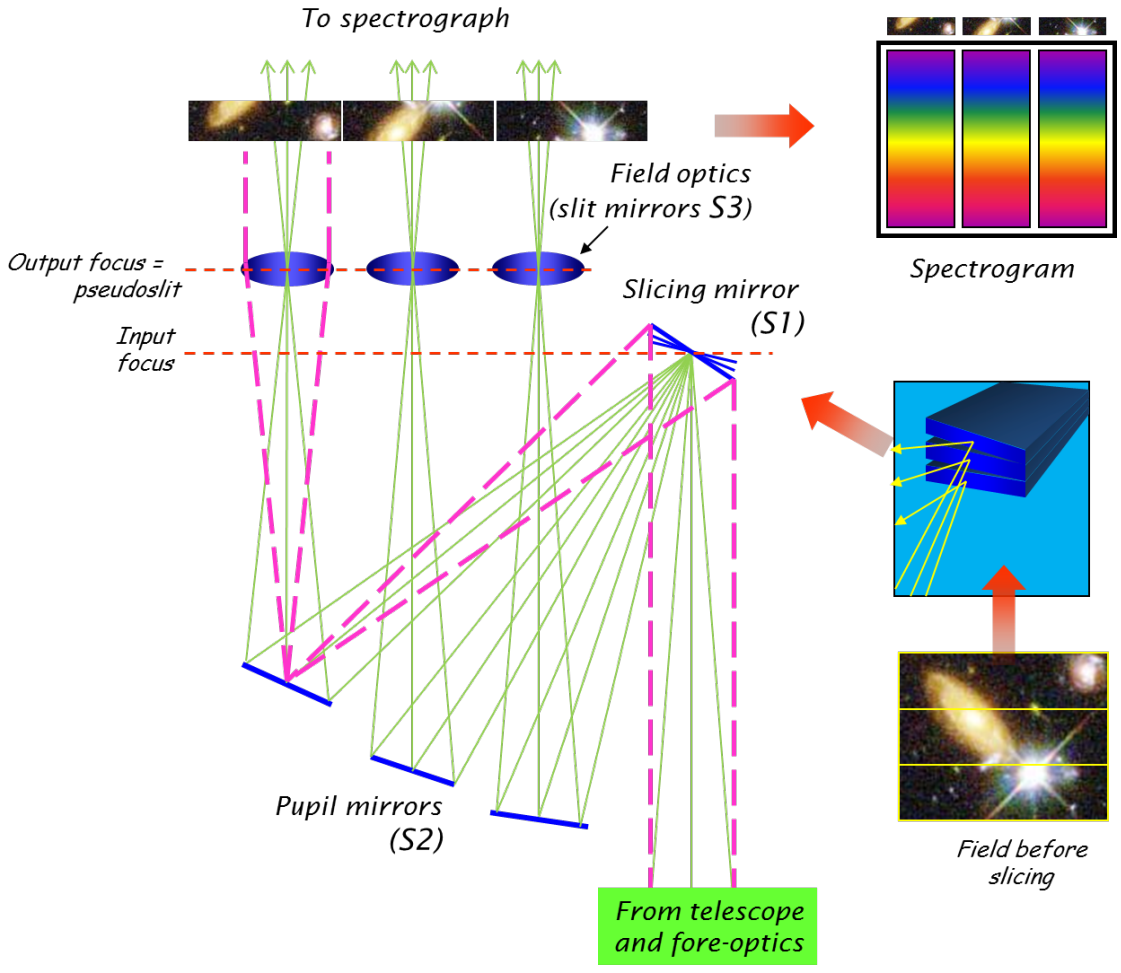

Figure 136 - Basic principle of the Advanced Image Slicer.

2.10.3. Length of slicer system along focal plane

In this configuration, a fold on or near the focal plane rotates the beam from the telescope by 90°. The light then bounces between mirrors following paths not far from parallel to the focal plane (Figure 137). The present design is based on the GNIRS slicer design. It uses 2 off-axis aspheric mirrors as fore-optics to reimage the input field on the slicer. They should not be expensive considering the actual cost of aspheres and the small size of the mirrors. Also, it may not be necessary to use complex aspheres depending on the needed image quality in the focal and pupil planes. There is a pupil image between the 2 mirrors where a cold stop could be placed after slightly modifying the design to leave more space around the pupil image. At the slit, the slit mirrors reflect the light at 90° into the spectrograph. They need to have a toroidal shape to give a sufficiently good pupil image quality. The slicing mirrors are all spherical with the same radius of curvature. The same is true for the pupil mirrors.

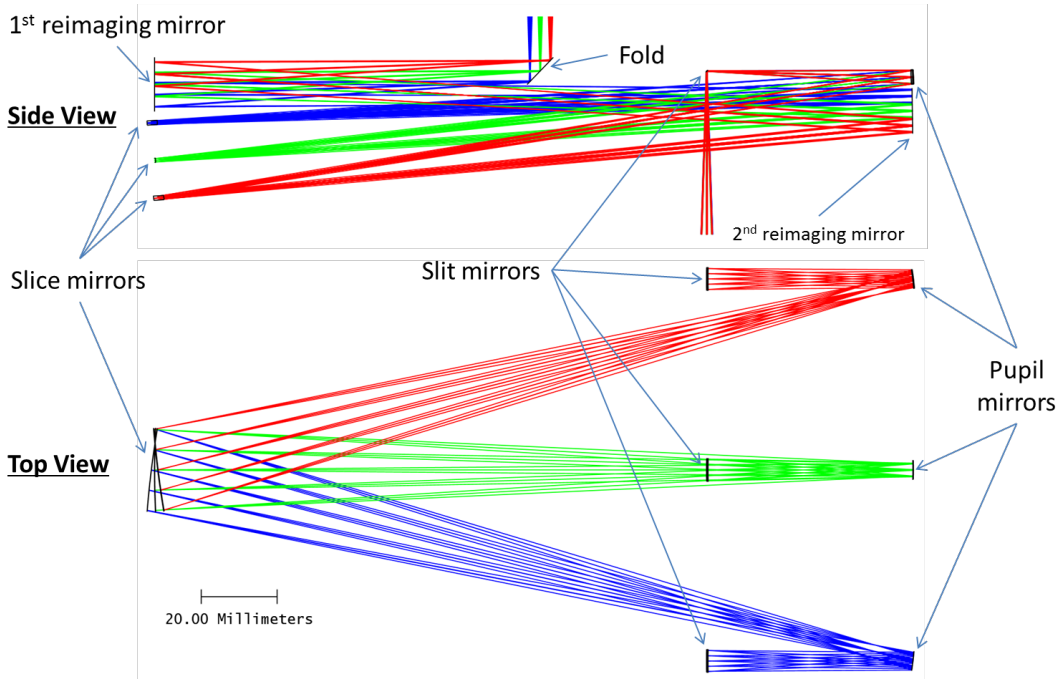

Figure 137 - Layout of the slicer system with length parallel to the focal plane. Only central and edge slices are shown.

2.10.4. Length of slicer system along optical axis

While there is less space along the optical axis than along the focal plane there is still enough room to put the slicer. In this case, there is no fold but there are three fore-optics mirrors instead of two (Figure 138). The second mirror is also used as a cold stop. The slit mirrors do not reflect the light at 90° but with only a shallow angle. This makes it possible to make them spherical although a small asphere improves the pupil image quality.

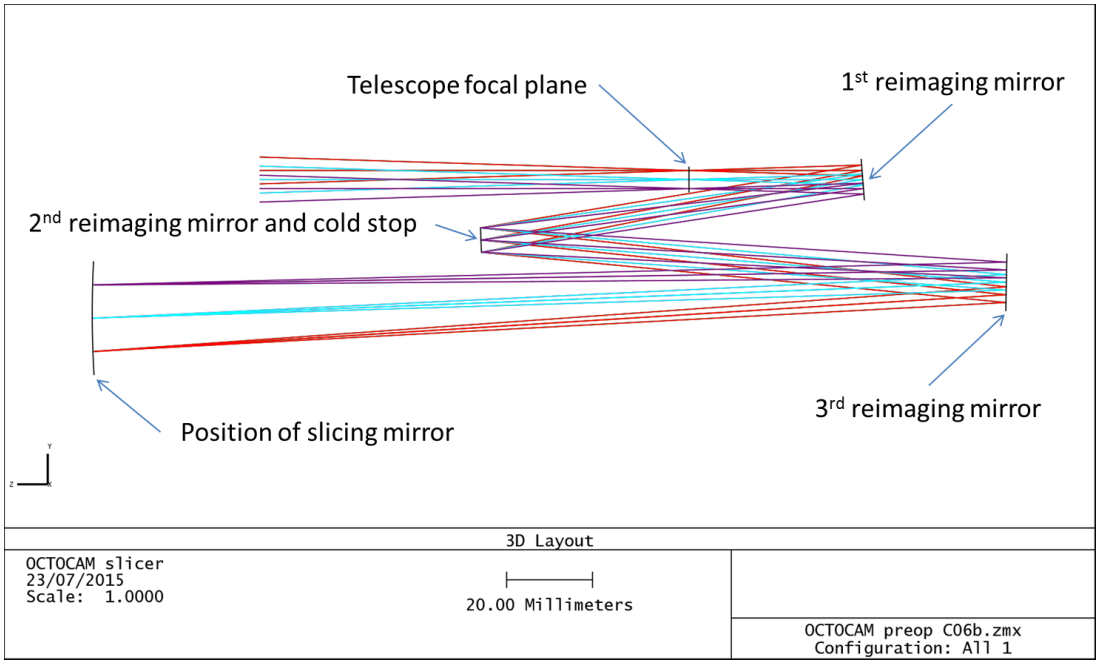

Figure 138 - Layout of the fore-optics of the slicer system with length parallel to the optical axis.

2.10.5. Other Slicer Systems

During the feasibility study we have considered two other slicer systems, as alternatives or possible add-ons to the OCTOCAM, although they are not included in the baseline design. One would maximize the field of view while the other would be for use with Adaptive Optics (AO).

Maximum field slicer:

This slicer would maximize the field of view by using the largest slice width that still gives sufficient spectral resolution in the NIR. A slit of 1.2" gives a spectral resolution of about 1800, which still gives more than 50% of the spectrum length covering the region between the lines. The slicer would have 10 slices of 1.2" x 16.5" for a total field of 12" x 16.5" and spaxels of 0.18" x 1.2".

Adaptive Optics slicer:

A slicer designed for AO would add that capability to OCTOCAM. It would be far more powerful than NIFS. The basic concept would be primarily for use with ALTAIR or GeMS so for the NIR spectrograph but a future more advanced AO system could extend the usable wavelength range to the VIS. The fore-optics would magnify anamorphically the field to make the spaxel width equal to the typical size of the ALTAIR PSF core, which is 0.08". This width would fit on 1 pixel in the spatial direction but the slices of 0.08" would be magnified on 2 pixel in the spectral direction to get the proper minimum spectral sampling. Also, the magnification reduces the beam size entering the spectrograph from F/16 to F/36 x F/72. This reduction permits the use a slit length 60% longer with almost no modifications to the spectrograph for the following reasons:

- Only less than half of the detector's width is normally used in the spatial direction so the detectors can accommodate a longer slit. The detectors would then be better used with this slicer system.

- The smaller beam permits the avoidance of vignetting except for the optics very much near the focal planes. Only the dichroic really needs an increase in diameter, which would be 15%. The last 2 lenses of the NIR cameras (the smallest of the design) may need up to 2 mm increase in diameter.
- The smaller beam reduces considerably the aberrations. Combined with the ability to focus each slice separately when designing the slicer system the image quality is excellent with a typical PSF width (GEFWHM) of less than 0.5 pixel even if the spectrograph is not designed for such a long slit.

The AO slicer on OCTOCAM would have 31 slices of 0.08" x 3.6" for a total field of 2.5" x 3.6". It would have many advantages over NIFS:

- At least all 4 NIR bands *Y*, *J*, *H* and K_S would be observed simultaneously at a spectral resolution of about 5000.
- The spaxel size of 0.08" by 0.08" would be a better fit to the ALTAIR PSF core of 0.08" than the NIFS spaxel size of 0.10" x 0.045" especially that a sampling of less than 1 pixel per FWHM can cause some undersampling problems even with dithering. With 2x2-images dithering the OCTOCAM AO slicer would give a full sampling of 2 spaxel per FWHM in both directions.
- The density of pixel per square arcsec is 1.4 times smaller which reduces the detector noise.
- While the field of view is the same as NIFS, the aspect ratio is better since a typical object would have a width and a length, not be circular or square. The longer length of 3.6" instead of the 3" of NIFS makes it more likely that an object would fit on the slicer.

As the cold stops in the cameras would be too large for the slower beam, the cold stop in the fore-optics would become the only cold stop. If optimized for GeMS, spaxels of 0.1", giving a larger field of 4.5" x 3.1", would be a better fit to the typical AO PSF. A field of view up to 30% larger in surface area could be obtained by using an even longer slit giving a field of up to 4.1" x 2.8" with 0.08" spaxels. Additional oversizing of the dichroic, the last 2 small lenses of each NIR camera and the 2 lenses following the first dichroic would however be necessary.

The slice width would be approaching the size of the diffraction limit at the longest wavelength. This causes diffraction in the spectral direction, which generates focal ratio degradation (FRD) of the beam. This problem was extensively studied for the GNIRS slicer. The pupil mirrors are consequently oversized. In the spectrograph, the beam is so slow (F/72) compared to the acceptance focal ratio of the spectrograph (F/16) that the additional FRD is negligible. NIFS and the JWST NIRspec slicers have demonstrated that slicers of sufficient surface quality can be manufactured to work near the diffraction limit.

2.10.6. Manufacturing

AAO would lead and coordinate all aspect of the fabrication assembly and testing of the IFU system. Fabrication of this device would follow that for the ESI-IFU (Sheinis 2003) and MUSE (at the VLT) (Henault et al 2004). Both of these devices are all-spherical with a toroidal surface, operate in the visible/NIR, and are fabricated from Zerodur. Both systems used standard optical fabrication

techniques with a high degree of polish. MUSE optics were polished in groups, while ESI-IFU optics were polished individually. The MUSE slicer elements were wrung together (molecular adhesion), while ESI-IFU were glued with UV curing cement in an alignment jig. Both methods can in principle be cooled down to cryogenic temperatures. The ESI-IFU was successfully tested for use in NIR instrument by being plunged in liquid nitrogen while molecular adhesion should remain unchanged with temperature since the material is the same. Both options will be explored in the preliminary design stage.

2.11. Spectropolarimeter

2.11.1. Goals & Requirements

By outfitting OCTOCAM with a full-Stokes polarimetric unit, it will become the most powerful medium-resolution spectropolarimetric instrument in the world, instantaneously combining the visible wavelength range covered by VLT/FORS (Bangulo et al. 2012 A&A, 538, 129) and the NIR range of Keck/LRISp (Harrington et al. PASP, in press). Moreover, its high-speed mode is truly unique, particularly when combined with polarimetry. OCTOCAM's spectropolarimetric mode can thus address a range of science cases from follow-up of SNe and GRBs to measure magnetic fields in a variety of stars across the H-R diagram, to characterize the surface structure of the atmosphereless bodies of the solar system and the composition of comet comae.

We specify the following requirements for the polarimeter. Please see Snik et al. (2013) for definitions for polarimetric performance parameters.

1. The polarimetric unit shall be installed on the slit/IFU insertion mechanism at the Cassegrain focal plane, without compromising the telescope controls due to an excessive demand for defocusing.
2. The amount of additional (cryo)mechanisms shall be as small as possible, i.e. one rotation mechanism for the polarization modulator.
3. The unit contains its own slit. Imaging polarimetry is therefore not supported.
4. Spectropolarimetric observations are supported for at least one (quasi-)point source and at least one sky reference aperture.
5. The polarimetric optics need to function under cryo-vacuum conditions.
6. The polarimeter furnishes full-Stokes spectropolarimetry: both linear (the fractional Stokes parameters Q/I and U/I) and circular polarization (V/I) shall be measured with efficiencies >80% of the maximum, for every wavelength.
7. The polarimetric mode shall cover a wavelength range of 370-2200 nm. Part of the K-band can be sacrificed as it is challenging to find strongly birefringent crystal materials with high transmission above 2.2 μm.
8. High polarimetric accuracy shall be achieved both in the spectral lines and in the continuum.
9. The polarimetric sensitivity shall be $<10^{-4}$, provided sufficient photon collection ($>10^{8}$ per resolution element).

10. The instrumentally induced polarization or spurious signal in the polarimetric data shall be $<10^{-3}$, after polarimetric calibration application.
11. The cross-talk between linear and circular polarization (and vice versa) shall be <2%, after polarimetric calibration application.
12. The modulator shall be reconfigurable to support a high time resolution mode (up to 100 Hz frame rate), if necessary with reduced polarimetric performance for continuum linear polarization only.

2.11.2. Design Choices

Generally, the polarimetric implementation for stellar spectropolarimetry consists of a polarizing beam-splitter to yield a dual-beam system, and a polarization modulator that sequentially converts the observable polarization states to the perpendicular linear polarization directions that are analyzed by the beam-splitter. This dual-beam implementation provides sufficient redundancy to cancel out systematic effects. The simultaneous recordings of perpendicular polarization states suppress spurious polarization signals due to seeing or variable sky transparency, while the temporal modulation reduces the polarimetric errors due to the differences between the two beams (i.e. transmission, aberrations, flat-fielding calibration residuals, etc.) (Bagnulo et al. 2009, PASP 121, 993). We therefore select a modulated dual-beam implementation to warrant a polarimetric *sensitivity* of $<10^{-4}$.

Polychromatic modulator

For relatively long exposure times, a rotating crystal-based modulator provides sufficient temporal bandwidth, while its detailed design permits the optimization for the measurement of all the Stokes parameters over a very wide spectral range. Classically, the modulator is either a half-wave plate for measuring linear polarization or a quarter-wave plate for measuring circular polarization. Both types of retarder can be made achromatic or super-achromatic by combining different crystals and/or several layers of birefringent elements at different angles Snik et al. (2013). Indeed, the super-achromatic 3x[quartz+MgF_2] modulator for Gemini's GPOL facility-level polarimetric system was designed and built to provide 0.50±0.02 waves of retardance over a wavelength range of 300-2500 nm (Hough et al. 2003, SPIE 4843, 200), but this project was discontinued. For OCTOCAM, such a solution cannot be considered, as a half-wave retarder provides no measurement efficiency for circular polarization. In theory, one could design an achromatized wave plate with 132° retardance to provide optimal modulation of all Stokes parameters (Sabatke et al. 2000, 25, 802). However, because the polarimetric observations are always wavelength-resolved, it is actually not necessary to achromatize the modulator; all that is required is that the modulation is optimal (del Toro Iniesta & Collados, 2000, AO, 39, 1637) for all Stokes parameters *at every individual wavelength*. This novel approach to spectropolarimetry is called "polychromatic modulation" (Tomczyk et al. AO, 49, 3580), and opens up new dimensions in the design space, for instance to cover the large instantaneous wavelength range of OCTOCAM. The main optimization parameters in the design process are the polarimetric efficiencies for the Stokes parameters *I* (the regular intensity) *Q, U* (denoting 2D linear polarization), and *V* (circular polarization).

Summarizing the thorough math of del Toro Iniesta & Collados (2000, AO 39, 1637), the polarimetric efficiencies describe to what extent the intensity recordings for n≥4 modulation states (i.e. sequential orientations of the modulator) are orthogonal, and therefore how well they can be demodulated to yield the complete Stokes vector. These efficiencies obey $\varepsilon_I \leq 1$; $\sqrt{(\varepsilon_Q^2 + \varepsilon_U^2 + \varepsilon_V^2)} \leq 1$ (del Toro Iniesta & Collados 2000, AO 39, 1637). The efficiency for Stokes I is equal to one, once its demodulation is fully independent from the incident polarization. If the modulator is a half-wave retarder, then the efficiency for measuring Stokes *V* is always zero. An optimal linear polarimeter with $\varepsilon_Q = \varepsilon_U = 1/\sqrt{2}$ is then obtained with modulation states (sequentially) filtering [0, 60, 120]° angle of linear polarization, or [0, 45, 90, 135]°, or indeed any equidistant sampling of 0-180°, as the definition of the polarimetric efficiencies is normalized by the amount of modulation states (del Toro Iniesta & Collados 2000, AO 39, 1637). The 132° retardance modulator of Sabatke et al. (2000, OL, 25, 802) yields $\varepsilon_Q = \varepsilon_U = \varepsilon_V = 1/\sqrt{3}$.

In previous work, we have already designed, analyzed, and successfully prototyped a polychromatic modulator for 300-2500 nm (Snik et al. 2012, SPIE, 8446, 844625, Skin et al. 2015, SPIE, 9613), which we adopt as our current baseline for OCTOCAM. For our polychromatic modulator we require $\varepsilon_I > 0.8$, and $\varepsilon_Q = \varepsilon_U = \varepsilon_V = 1/\sqrt{3}$ within a tolerance of 0.1. We choose 6 modulation states at sequential modulator orientations of [0, 30, 60, 90, 120, 150]°, to provide more degrees of freedom to the design process, and the polarimetric data-reduction process (see below). We optimized a stack of 4 quasi-order quartz retarders. Each retarder consists of two crossed quartz plates of which one has a thickness of 1 mm, and the other has a thickness of 1+*d* mm. In total, we have 8 free parameters to optimize the polychromatic retarder: 4 relative thicknesses *d*, and 4 orientations. The modulation matrix of the optimal solution is plotted in Figure 139. This matrix shows how every modulation state encodes a different linear combination of the polarized Stokes parameters onto the two split intensity spectra.

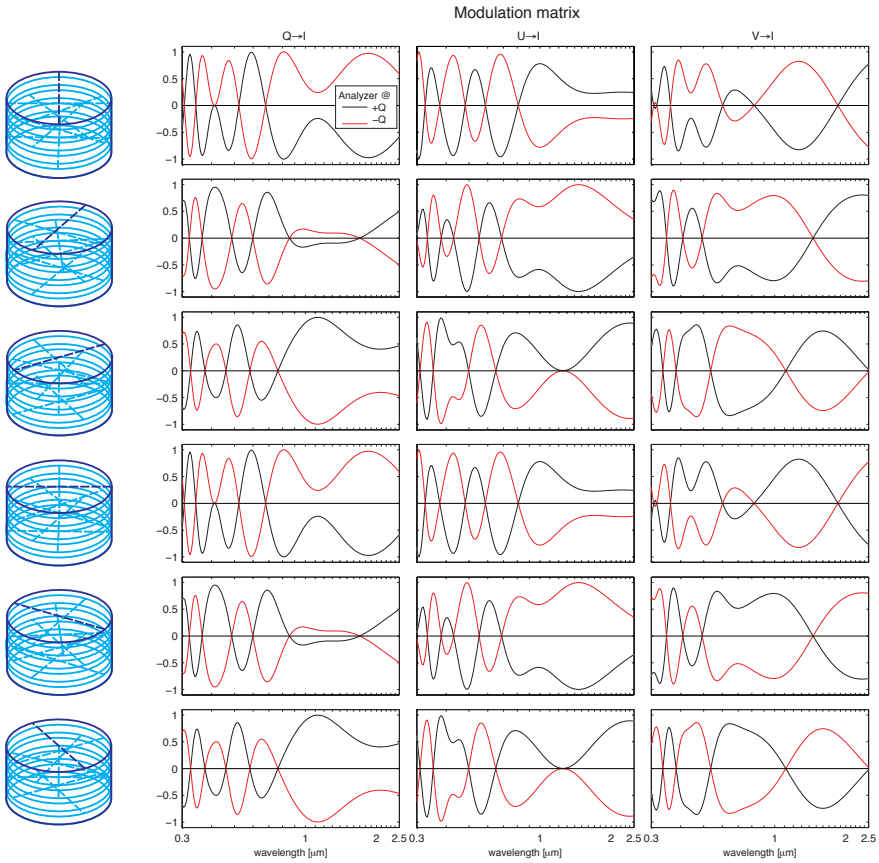

Figure 139 - Modulation matrix for the optimized polychromatic modulator consisting of 4x2 quartz plates that needs to be oriented at 6 incremental steps. Note that the first column of the matrix is omitted, as it is assumed that the transmission for the regular intensity is always 1, and assumed independent from the rotation of the modulator.

The 6 intensity recordings at every wavelength need to be demodulated to the Stokes parameters (*I, Q, U, V*). As this problem is overdetermined, there is an infinite amount of 6x4 demodulation matrices that fulfill this. Each beam is demodulated first, and then consequently combined (i.e. averaged). As is shown in del Toro Iniesta & Collados (2000, AO 39, 1637), the Moore-Penrose pseudo-inverse of the modulation matrix (in Figure 139) is the optimal choice in terms of propagation of random noise (i.e. predominantly photon noise). This optimal demodulation matrix also warrants the optimal polarimetric efficiencies, and therefore makes the most efficient use of the total exposure time. This is regardless of the number of modulation states, although the overheads due to detector read-out and the simultaneous rotation of the polarization modulator obviously do add up. The polarimetric efficiencies ε_I, ε_Q, ε_U, ε_V as a function of wavelength are plotted in Figure 140, and they clearly fulfill our requirements.

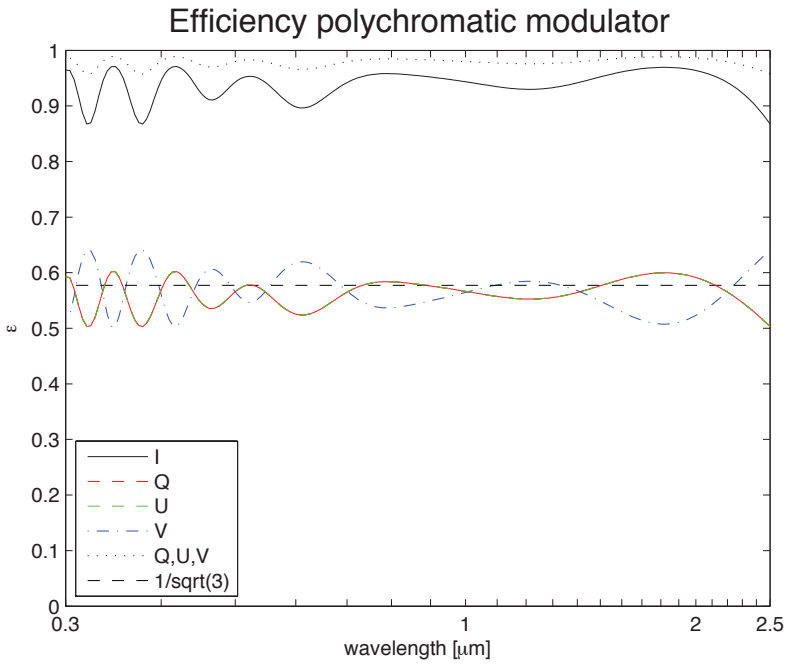

Figure 140 - The polarimetric efficiencies for the modulator presented in Figure 139.

Considering again the modulation matrix in Figure 139, it becomes apparent that for astrophysical cases where circular polarization can be ignored (Q, U >> V, e.g. for most scattering geometries), the full modulation is already achieved after the minimum number of 3 modulation states. The demodulation matrix then becomes a 3x3 matrix, which is the regular inverse of the truncated modulation matrix. For cases where Stokes V is dominant (e.g. magnetic field measurements using the Zeeman effect), the last column of the modulation matrix constitutes a true beam-exchange (Bagnulo et al. 2009, PASP, 121, 993), with the last three elements changing sign with respect to the first three.

Because the modulation matrix is overdetermined, we can also introduce a demodulation to the so-called "null spectra" (Bagnulo et al. 2009, PASP, 121, 993). By demodulating in a non-trivial way to the Stokes vector (I, 0, 0, 0) (Snik et al. 2015, SPIE 9613), we obtain fractional polarization spectra that for an ideal polarimeter only contain random noise, which can be used to determine the noise level in the data. In case of systematic errors (e.g. instrument flexures, see below), these null spectra can be used to flag bad data.

The design of the modulator presented in Figure 139 was also optimized in terms of acceptance angle, polarized spectral fringes, and temperature sensitivity (Snik et la. 2012, SPIE 8446, 844625). By using quasi-zero order quartz elements, the modulation matrix stays within tolerances for the maximum acceptance angles in an F/13 beam, and for temperature deviations of ±5°C. The individual plate thicknesses of ~1 mm makes that the polarized spectral fringes (due to polarization-dependent Fabry-Pérot etaloning) are sufficiently suppressed for spectral resolution as large as R_λ=10,000. We therefore conclude that this design is also applicable to the temperature-stabilized OCTOCAM instrument with R_λ≈4,000, when implemented at the F/16 Cassegrain focus.

Recently, we have successfully produced a prototype polychromatic modulator cf. the design in Figure 139, through an iterative manufacturing procedure in

close collaboration with B. Halle Nachfl. (Berlin) (Snik et al. 2015, SPIE 9613). After the production of each of the four quasi-zero order quartz stages, the design was re-optimized based on the measured thicknesses and birefringence dispersion. The preliminary performance of the prototype modulator therefore provides an excellent match with the theory (Snik et al. 2015, SPIE 9613). As this modulator was optimized for 300-2500 nm, the applied AR coating is necessarily a single layer of MgF2. For the reduced wavelength range of OCTOCAM, a more advanced AR coating shall be applied.

The current prototype modulator was developed for operation at room temperature (±5°C). For cryo-vacuum operation, the modulator needs to be slightly redesigned. First of all, because the refractive indices of quartz are a function of temperature, we need to design and test at the operating cryogenic temperature of OCTOCAM. Secondly, the 8 quartz plates of the prototype have been bonded with UV-transparent glue. A cool-down would most likely lead to shattering of the component, because of the differential CTE along the crystal axes. We will therefore investigate alternative mounting options (there is more flexibility in the selection of bonding material, as for OCTOCAM the glue only needs to be transparent above 370 nm).

Reconfigurable Modulator for Spectral Polarization Modulation

The implementation of high-speed detectors in OCTOCAM to yield observing modes with high time resolution (~100 Hz), in combination with the chromatic nature of our polychromatic modulator, leads us to develop a second unconventional polarimetric mode. It is obviously impractical to rotate the modulator in synchrony with the 100 Hz frame rate, but even at a single orientation the modulator does provide a polarimetric measurement. Considering any row in Figure 139, it is obvious that it imposes a quasi-sinusoidal polarization modulation in the *spectral domain*. For the current design, the spectral polarization modulation is already to a large extent orthogonal for *Q/I*, *U/I* and *V/I* (Snik et al. 2015, SPIE, 9613). To obtain the polarization modulation envelope independent from features in the intensity spectrum, the dual-beam implementation is crucial. While in the regular polychromatic mode either beam is first demodulated individually and then combined to suppress systematic effects, for the spectral modulation we immediately combine both spectra $S^+(\lambda)$ and $S^-(\lambda)$ to yield $(S^+(\lambda) - S^-(\lambda))/(S^+(\lambda) + S^-(\lambda))$. This spectral polarization modulation envelope can in turn be demodulated through linear algebra, Fourier, and/or χ^2 minimization techniques to yield the fractional polarization spectra $Q/I(\lambda)$, $U/I(\lambda)$ and $V/I(\lambda)$ (Snik et al. 2013; Snik et al. 2009, AO, 48, 1337). Obviously, the spectral information content of the observable polarization spectra needs to be at lower resolution than the typical modulation period. Hence, this technique is particularly suitable for continuum polarization. Our group has a lot of experience with such spectral polarization modulation techniques (Snik et al. 2009, AO, 48, 1337), and we have already demonstrated $\sim 10^{-3}$ absolute polarimetric accuracy with such a modulator (Rietjens et al., AO, in prep.). In fact, because the technique is intrinsically snapshot, it is not susceptible to the systematic effects that usually plague polarimetry. Once the typical sinusoidal modulation is observed, one can indeed be certain that a real polarization signal has been detected.

Because both spectrally modulated beams carry the full polarization information, we can use the redundancy in the data itself to correct for any potential transmission ratio drift between the two beams (van Harten et al. 2014, AO, 53, 4187). Furthermore, we can use this information to introduce an additional demodulation step at the full spectral resolution of the spectrograph (van Harten et al. 2014, AO, 53, 4187). In this way, we can even perform high-speed spectral linear polarimetry of spectral lines, provided the assumption can be made that the spectral line has the same polarization angle as the surrounding polarized continuum.

We therefore propose to make the polychromatic modulator reconfigurable, such that at a single orientation it furnishes high-speed linear spectropolarimetry of the continuum and (to some extent) spectral lines. Currently, the polychromatic modulator design would support ~6 spectral resolution elements for spectral polarization modulation. We aim to increase this number by abandoning the design approach with quasi-zero order quartz plates. By simply increasing the retardance order to >2 (in the infrared range) for each quartz plate combination to yield >~6 overall retardance in the polychromatic modulator design process, we obtain sufficient spectral polarization sampling in each of the 8 spectrograph channels. The merit function for the optimization then contains both the polarimetric efficiencies ε_{It}, ε_{Qt}, ε_{Ut}, ε_{Vt} for the temporal modulation at every wavelength, and the polarimetric efficiencies ε_{Q_λ}, ε_{U_λ}, for spectral modulation within every spectrograph channel.

Polarizing Beam-splitter

Although technically the polarization modulator and the polarizing beam-splitter (analyzer) could be separated, in this case the beam-splitter is to be implemented directly behind the modulator at the Cassegrain focus, as immediately after this focus the light is diverted to the 8 focal planes by means of dichroic beam-splitters. This means that the polarizing beam-splitter needs to effectuate a lateral splitting for all relevant wavelengths. A Savart plate (Snik et al. 2013) is then the only practical choice. Such a device consists of birefringent crystal plates that are cut such that the extraordinary axis points away at 45° from the entrance surface. Within the crystal, the incident light is then split up according to linear polarization directions in the ordinary ray and the extraordinary ray. While the ordinary ray for normal incidence just goes straight through, the extraordinary ray bends away at an angle that depends on the birefringence of the crystal. At the exit face, this ray bends back to its original direction, and the beams are split laterally. To ensure that both beams traverse the same path length, a Savart plate usually consists of two crystal plates with crossed orientations.

Because in our case we require the beams split along the slit direction, we need the two crystal plates to be oriented at ±45° in the plane of the entrance surface (while the extraordinary axes for both crystal plates also have an equal component in the direction of the optical axis, such that the maximum lateral splitting occurs). The amount of lateral splitting by the Savart plate needs to be larger than the typical PSF at the Cassegrain focus. This splitting is determined by the birefringence of the crystal and the thickness of the plates. To minimize this thickness, we select the crystal with the highest birefringence that can still

be acquired in relatively large substrates with high optical quality: calcite. Unfortunately, calcite becomes opaque at ~2.2 μm (Oliva et al. 1997, A&ASS, 123, 179), and therefore we will need to sacrifice part of the K band. Despite the large birefringence, we still need 2x 15 mm calcite plates to provide ~3 arcsec splitting along the slit direction. This number would be about ten times as large for quartz plates. It is impossible to build a Savart plate out of single calcite pieces to cover the entire 120 mm (=173 arcsec) FoV at the Cassegrain focal plane. We therefore design the polarimeter (modulator + Savart plate) for a single on-axis (quasi-)point source, plus two apertures for sky referencing at ±6 arcsec along the slit direction. To avoid overlapping between the two maps, we implement a slit-like aperture mask at the Cassegrain focal plane that consists of three apertures with ~0.5 arcsec width and <3 arcsec length, see Figure 141. If need be, this mask can be extended into a comb-like decker mask extending along the entire FoV, for which each group of 3-5 holes has its own Savart plate.

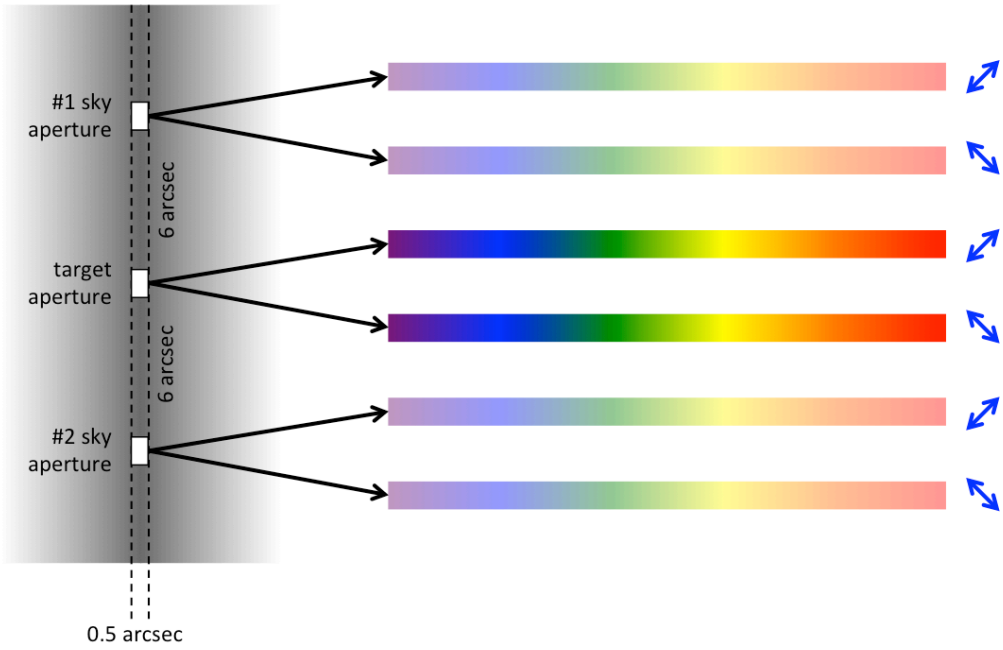

Figure 141 - Schematic overview of the focal plane mask in combination with the polarizing beam-splitting by the Savart plate.

As for the modulator, the bonding between the two calcite elements of the Savart plate needs to be investigated in the context of cryo-vacuum operation. Also, the AR coating on the calcite surfaces will require some research.

2.11.3. Optical Performance

We have modeled the optical performance of the proposed polarimetric implementation in ZEMAX. To investigate the impact of just the polarization optics on the image quality, we replaced the optical designs for the 8 arms with a single idealized optical relay that is used to analyze all wavelengths within the range simultaneously (see Figure 142).

It is clear that the allotted volume between the entrance window/ADC and the first dichroic is tight, but optically everything fits nicely. A complete mechanical design will need to demonstrate that also the required mechanisms for inserting the polarimeter (and also the slit and the IFU), and for rotating the modulator all fit within this volume without blocking the beam.

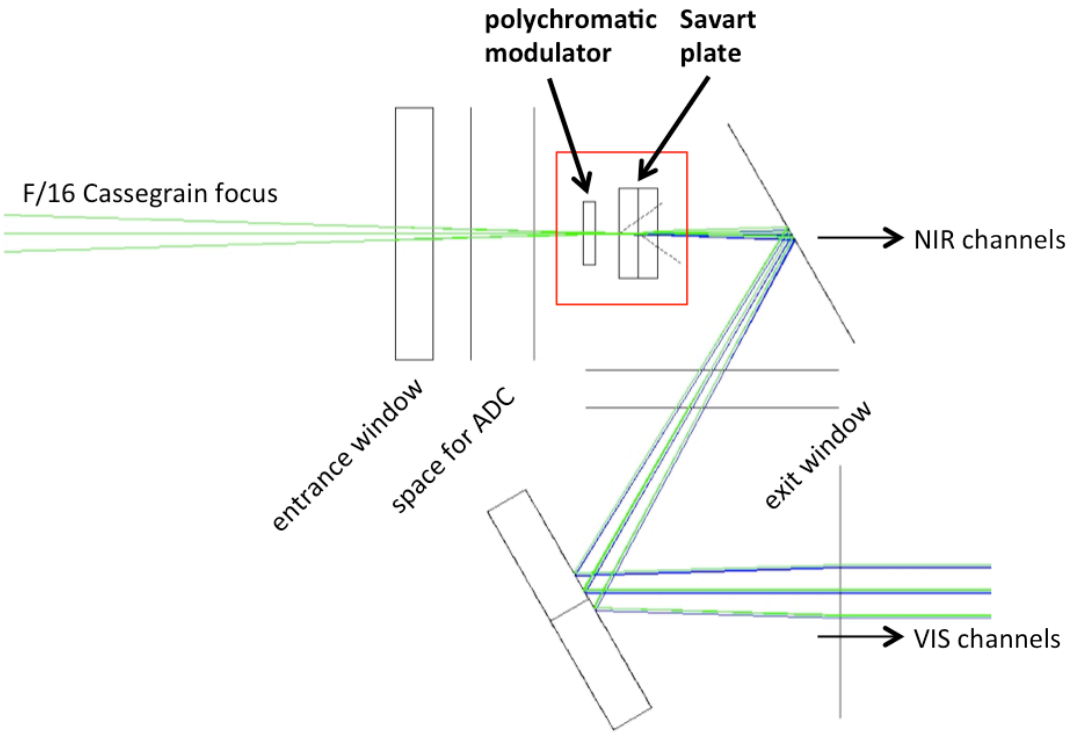

Figure 142 - Optical design for the polarimetric unit at the OCTOCAM Cassegrain focus.

Figure 143 shows the beam-splitting due to the Savart plate as a function of wavelength. Due to the dispersion of the birefringence of calcite, the splitting is a bit larger in the blue than in the IR. It is well known (Snik et al. 2013) that a Savart plate in a converging beam induces astigmatism, but fortunately that effect is very minimal for the F/16 beam.

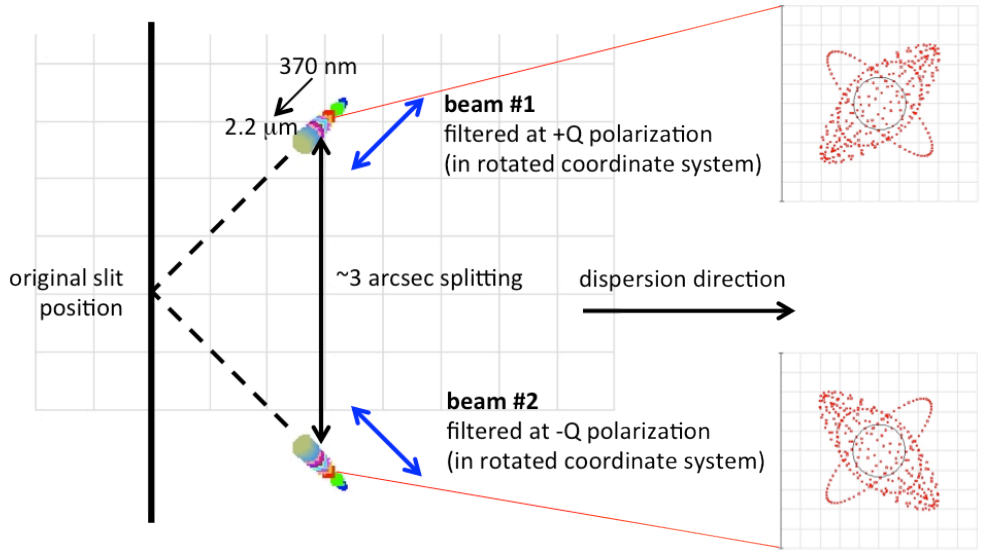

Figure 143 - Beam-splitting due to the Savart plate, evaluated at the virtual combined detector plane for all wavelengths. The insets show the aberrations (mostly astigmatism and spherical aberration) at 500 nm specifically due to the polarization optics in combination with the entrance window.

The inset spot diagrams in Figure 143 exhibit some spot elongation beyond the diffraction limit (in combination with some spherical aberration due to the entrance window). However, the elongation is fully symmetric for the two beams along the spectral direction, and will therefore barely impact the spectropolarimetric performance.

As is apparent in Figure 143, the beam-splitting also induces a small shift of the nominal slit position by ~1.5 arcsec.

For argument's sake, we have labeled the split polarization directions $\pm Q$, and align the Stokes coordinate system for the polychromatic modulator with respect to these polarization directions. Because the split polarization directions have polarization angles at ±45° with respect to the telescope's elevation axis, it may be more appropriate to rotate this coordinate system by 45° and call the split directions $\pm U$. However, in the end it would be preferable to connect the Stokes coordinate system to the equatorial sky coordinates. In that coordinate system the orientations of the polychromatic modulator need to be continuously updated according to the parallactic angle to convert the observable Stokes parameters on the (rotating) sky to the fix polarization direction as split by the Savart plate.

De/refocusing

There will be no focusing mechanisms associated with OCTOCAM itself. To accommodate the additional path length due to the polychromatic modulator (~10 mm of quartz) and the Savart plate (~30 mm of calcite), the telescope needs to refocused by moving the M2 backward by ~200 µm, which is just within the limitations imposed by the facility wavefront-sensing and guiding system.

As the focal plane mask needs to be positioned in front of the Savart plate, and the 8 detector focal planes cannot be refocused, the actual position of the

Cassegrain focal plane is shifted backwards by 11.5 mm with respect to the original focal plane position.

2.11.4. Mitigation of Instrumental Polarization Effects

The chosen dual-beam implementation suppresses many systematic effects related to seeing and variable atmospheric conditions, and to differences between the beams (transmission, aberrations, pixel gains, etc.). However, several effects still pertain that can create false polarization signals, and limit the polarimetric *accuracy*.

Induced Polarization

Any refraction or reflection at non-normal incidence introduces a few percent of linear polarization, even to a completely unpolarized beam. Hence, the rotationally symmetric Cassegrain focus is considered the ideal location for a polarimeter. Nevertheless, any optical component in front of the polarimeter can induce some instrumental polarization.

A main culprit will be the ADC, which necessarily contains an inclined surface inside both prisms, which are rotated with respect to each other as a function of zenith angle. Refraction at either of these surfaces creates instrumental polarization. The angle of this instrumental polarization is predictable by definition (inasmuch the two prisms are identical), while the induced degree of polarization as a function of wavelength depends on the refractive indices of the two glass pieces, and the properties of the interface.

This situation is seriously aggravated if OCTOCAM is mounted at a lateral Cassegrain port, i.e. behind an M3 at 45° incidence angle. The instrumental polarization due to this mirror is always oriented along the *S* orientation in the coordinate system of the reflection plane, but the polarization degree depends heavily on the mirror properties and potential contamination (Snik et al. 2013). Fortunately, Gemini's M3 polarization properties have already been extensively modeled and measured in the context of the GPI project (Wiktorowicz et al. SPIE 9147, 914783).

The instrumental polarization as a function of wavelength is best calibrated on-sky by observing unpolarized standard stars (which is most stars on the sky). At the straight-through port, with the two ADC prisms crossed, the induced polarized should be consistent with zero. These calibrations should lead to an instrument model for every observation such that instrumental polarization $I \rightarrow Q,U,V$ can be subtracted from Q/I, U/I, V/I data to better than 10^{-3}.

Polarization Cross-talk

In addition to inducing polarization do optical elements also *modify* the incoming polarization ($Q,U \leftrightarrow V$) from astrophysical targets. In case of transmission optics this is due to (thermal/mounting) stresses in the glass, which makes it slightly birefringent. In case of mirrors there is a fundamental phase shift between the polarization component along the *P* direction with respect to the component in the *S* direction.

For the cases of the entrance window and the ADC it is expected that both elements can be significantly birefringent with a retardance amount and orientation that are both unpredictable and variable. It is clear that the entrance

window will be under pressure, as it needs to maintain the vacuum. If the ADC's glass elements are glued, then thermal stresses will occur because of CTE differences. Also, the warm application of AR coatings can induce stress in the substrate glass. Finally, any glass substrate is intrinsically birefringent to some degree due to its production process. Therefore, both the entrance window and the ADC need to be carefully monitored for retardance at the 4 nm level (equivalent to 1% cross-talk in the blue) during all manufacturing steps. There is ample experience with this process from the CFHT instruments ESPaDOnS (Barrick et al. 2010, SPIE, 7735, 77354) and SPIRou (Parès et al. 2012, SPIE, 8446, 84462).

The cross-talk due to a putative M3 is exclusively related to the linear polarization components at ±45° with respect to the *S/P* directions. However, the amount of cross-talk as a function of wavelength again depends on the mirror properties.

If it is known that the amount of cross-talk is larger than the requirement (2%), it needs to be calibrated with observations of linearly polarized standard stars, that have known degree and angle of polarization in standard photometric bands (Heiles 2000, AJ, 119, 923; Whittet et al. 1992, ApJ 386, 562). Because the polychromatic modulator is full-Stokes, the cross-talk components are always measured, and can therefore always be generically corrected for. The same calibration observations will be used to measure/verify the performance of the modulator itself.

Flexure Issues

Although the dual-beam polarimetric implementation suppresses systematic effects to first order, any physical changes of the instrument configuration during the polarization modulation can induce false signals (Bagnulo et al. 2013, A&A, 559, 103). Cassegrain-mounted instruments are subject to flexures issues that may limit the accuracy of the measurements of the polarization of spectral lines. As detailed by Bagnulo et al. (2013, A&A, 559, 103), flexures occurring during an observing series (when a spectral line is recorded under different polarization states) may mimic Zeeman effect. Therefore, for polarimetry of spectral lines it is required that instrument flexures and guiding errors are limited to a tiny fraction of the FWHM of the line under investigation. Potential flexure issues may be identified using the null profiles (see Bagnulo et al. 2012), and because every modulation state furnishes snapshot spectral modulation, this additional domain could in theory be used to alleviate the stability requirements in the temporal domain.

3. Instrument performance and operations

3.1. Efficiency

In Table 43 and Table 44 we summarize the efficiency of the different elements of the instrument and telescope to give an idea of the expected performance of the instrument on sky (see also Figure 144).

Imaging								
Band	g	r	i	z	Y	J	H	K_S
Telescope	0.73	0.85	0.89	0.92	0.93	0.94	0.95	0.96
Optics	0.48	0.52	0.54	0.52	0.51	0.51	0.49	0.37
Detectors	0.83	0.91	0.92	0.66	0.85	0.83	0.83	0.83
O+Det	0.40	0.47	0.50	0.34	0.43	0.42	0.41	0.31
Tel+O+Det	0.29	0.40	0.44	0.31	0.40	0.39	0.39	0.30

Table 43 - Instrument efficiency in the imaging mode.

Spectroscopy								
Band	g	r	i	z	Y	J	H	K_S
Telescope	0.73	0.85	0.89	0.92	0.93	0.94	0.95	0.96
Optics	0.39	0.43	0.44	0.43	0.42	0.42	0.40	0.30
Detectors	0.83	0.91	0.92	0.66	0.85	0.83	0.83	0.83
O+Det	0.32	0.39	0.40	0.28	0.36	0.35	0.33	0.25
Tel+O+Det	0.23	0.33	0.36	0.26	0.33	0.33	0.31	0.24

Table 44 - Instrument efficiency in the spectroscopic mode.

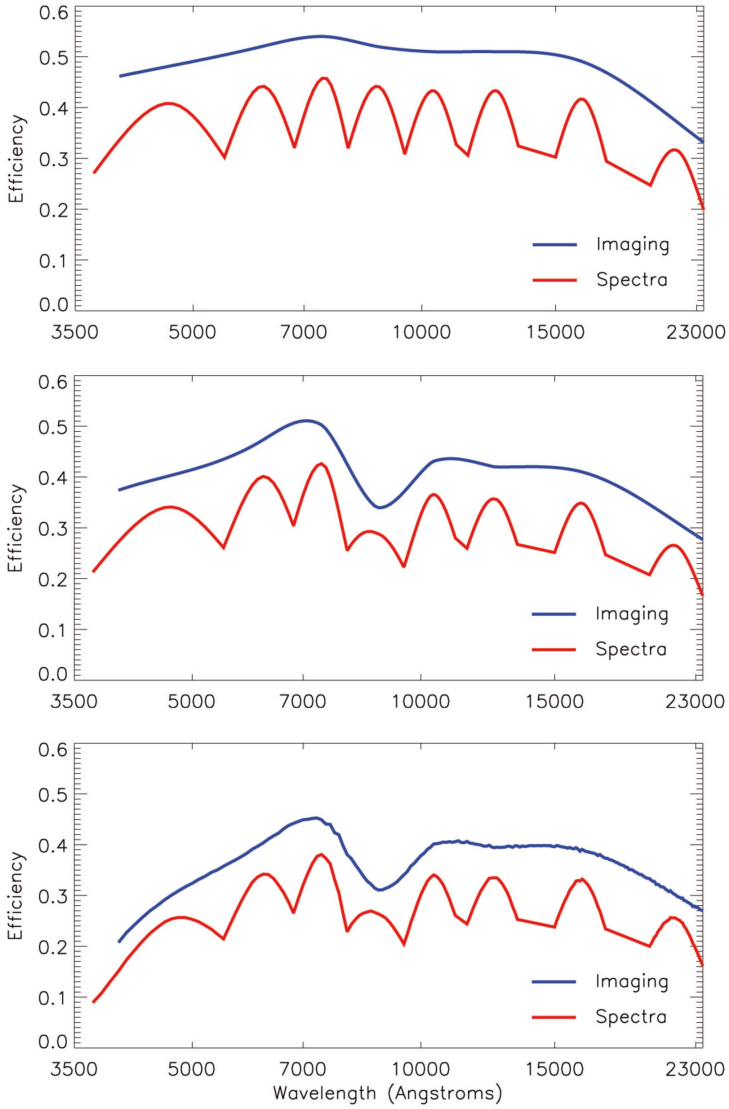

Figure 144 - Expected efficiency of OCTOCAM, including only optics (top), optics, and detectors (middle), and optics, detectors, and telescope mirrors with 3 refletions (bottom).

3.2. Limiting magnitude

Using the efficiency estimates of the telescope, optics, detectors and the absorption of the atmosphere we created an instrument performance simulator, based on the ESO exposure time calculators (UVES, FORS2, ISAAC). Table 45 and Table 46, as well as Figure 145 and Figure 146 show examples of limiting magnitudes that give an idea of the capabilities that OCTOCAM will have once installed on the telescope.

IMAGING (Airmass=1.2, seeing=0.8", 3 days from new Moon, $F_\nu \sim \nu^{-1}$)		
Band (central wavelength)	**Lim. Mag. (AB) (S/N=3, 1s)**	**Lim. Mag. (AB) (S/N=3, 1800s)**
g (480 nm)	23.0	27.5
r (615 nm)	22.8	27.1
i (745 nm)	22.6	26.9
z (875 nm)	22.1	26.2
Y (1035 nm)	21.3	25.5
J (1250 nm)	20.6	24.8
H (1630 nm)	19.8	24.0
Ks (2175 nm)	19.3	23.4

Table 45 - Limiting magnitudes (S/N=3) in imaging mode.

SPECTROSCOPY (Airmass=1.2, seeing=0.8", 3 days from new Moon, slit width=1", $F_\nu \sim \nu^{-1}$)		
Band (central wavelength)	**Lim. Mag. (AB) (S/N=10, 10s)**	**Lim. Mag. (AB) (S/N=10, 3600s)**
g (460 nm)	18.4	23.1
r (615 nm)	18.6	22.8
i (745 nm)	19.0	23.0
z (875 nm)	18.6	22.3
Y (1035 nm)	18.0	21.5
J (1250 nm)	17.8	21.0
H (1630 nm)	16.8	20.1
Ks (2175 nm)	16.2	19.4

Table 46 - Limiting magnitudes (S/N=10) in spectroscopic mode.

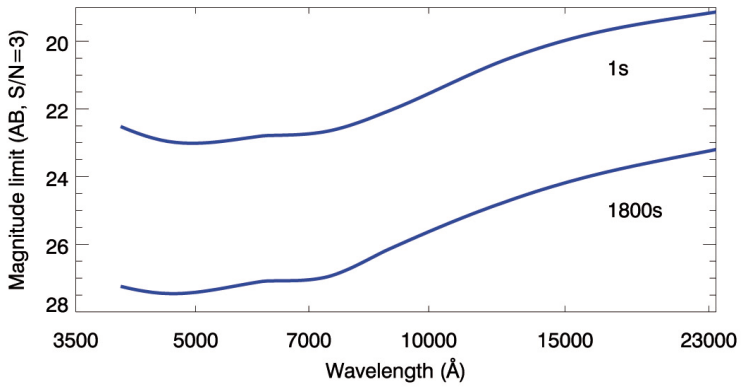

Figure 145 - Limiting magnitudes (S/N=3) in imaging mode. A power law spectrum Fν~ν-1, seeing of 0.8", an airmass of 1.2 and 3 days from the new Moon were assumed.

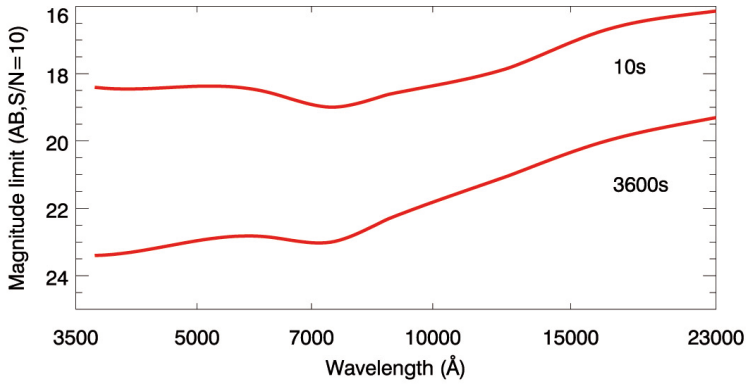

Figure 146 - Limiting magnitudes (S/N=10) of the continuum in the spectroscopic mode. A power law spectrum $F_\nu \sim \nu^{-1}$, seeing of 0.8", an airmass of 1.2, a slit of 1.0" and 3 days from the new Moon were assumed.

3.3. Spectral resolution

In Figure 147 we plot the expected spectral resolution for OCTOCAM, using the numbers displayed in Table 7. This shows the uniformity of the resolution across the spectral range, with slightly higher resolution in the NIR, which allows us to better resolve and observe in between the atmospheric emission lines. The thick line shows the maximum resolution using 3 pixel resolution elements corresponding to a slit of 0.54" on sky. This value is equivalent to the 70 percentile of the seeing in any of the two Gemini observatories in K_S-band[2]. We further plot the resolution for 0.7" and 0.85" slits (70 percentile seeing for *z*-band and *g*-band, respectively), and include the expected resolution for the IFU unit (0.4" slits).

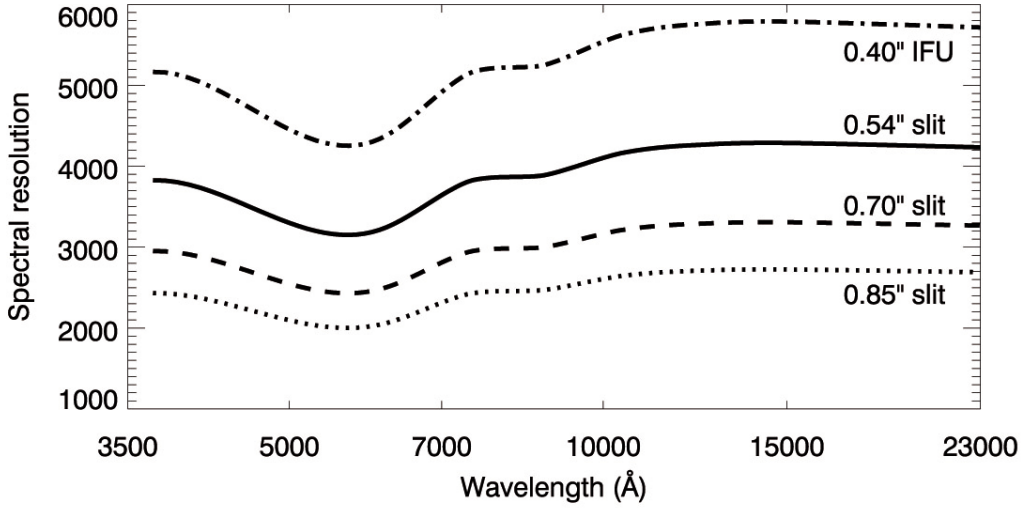

Figure 147 - Spectral resolution of OCTOCAM, considering a slit width of 0.54" (thick line, corresponding to the 70 percentile of the seeing in K_S-band for any of the two Gemini osbervatories) and a slit of of 0.7" (70 percentile in *z*-band). Also included is the expected resolution for the IFU (0.4" slices).

[2] https://www.gemini.edu/node/10781

3.4. Instrument operations

The observing modes of OCTOCAM are divided into two main groups, imaging and spectroscopy, which are then subdivided depending on the required time resolution. In the case of spectroscopy the observing modes are divided further in the long slit mode, integral field spectroscopy, or spectropolarimetry. Here we describe the characteristics foreseen for each of the observing modes of OCTOCAM. For the final instrument operation, an *observing tool* will be provided in order to configure the optimal camera settings for the needs of each individual observer. This is especially important when observing at time resolutions higher than 1Hz. The observing tool will take into account the available readout modes of each detector, the required exposure times and/or time resolutions and the observing strategy (i.e. if observations need to be simultaneous in the different arms, or if duty cycle is to be maximized independently in each arm).

3.4.1. Imaging modes

The exposure time, and hence the readout mode, of each channel is independent from the other channels. This means that the observer will have the flexibility to combine different observing modes for each detector. By default, the instrument will have two imaging modes, plus an extra one, which would be a customized imaging mode resulting from combining the two previous imaging modes. In cases where the observer makes use of a large amount of customized observing modes per night, Gemini might consider to provide calibrations during day-time exclusively to a limited number of observing modes.

Standard imaging mode (exposures of more than 5 seconds)

This would be the default-imaging mode for exposure times above 5 seconds when the 1x1 binning is used. For imaging OCTOCAM uses the central 1kx1k of each of the detectors. Given that the pixel scale is 0.18", most of the imaging observations will be performed using binning 1x1 to obtain an adequate sampling of the seeing at the observatory. Using the slowest readout speeds of the detectors used by OCTOCAM we will read out in 5.2 s for the VIS detectors and up to 8.4 s for the NIR. Hence, this "slow readout mode" will be recommended for all imaging observations with exposure times longer than roughly 5 s in normal seeing conditions.

High time-resolution mode (exposures of less than 5 seconds)

The fast imaging mode is thought for observations that require time resolutions of less than 5 s. This mode is designed for observers with a basic knowledge on the significance of dynamic range, read-out noise and exposure time, when the data start to be dominated by the detectors' readout performances. In full frame, the observer can reach time resolutions up to 13 ms in the *YJHK*-bands, and 93 ms in *griz*. Windowing would allow reducing this readout time.

Customized imaging mode (exposure times < 5 s and > 5 s, depending on the channel):

Given that the exposure time of each channel is independent, the observer may combine slow and high time resolution (HTR) imaging modes. This mode is thought for observations that require time resolutions beyond 5 s only in a certain number of channels, with the rest of the channels observing in slow mode (e.g. the object is only bright enough for fast photometry in some bands). The

possibility of performing windowing in a certain number of channels makes the possible setup combinations even larger.

An observing tool will be provided to automatically select the optimal observing mode for each user needs. The range of readout speeds, readout noises, and dynamic ranges in imaging mode for each arm is summarized in Table 47.

ARM	Readout time	Digital resolution	Readout noise (e^-)
VIS (*grist*-bands)	93-5250 ms	16 bit	8-3
NIR (*YJHK*$_S$-bands)	13-262 ms	12-16 bit	75-15

Table 47 - Readout characteristics of the different arms.

Note that the readout times of each of the four channels in VIS arm are independent. The same applies to each of the three channels in the NIR arm. Figure 148 shows the readout times of the eight channels in imaging mode.

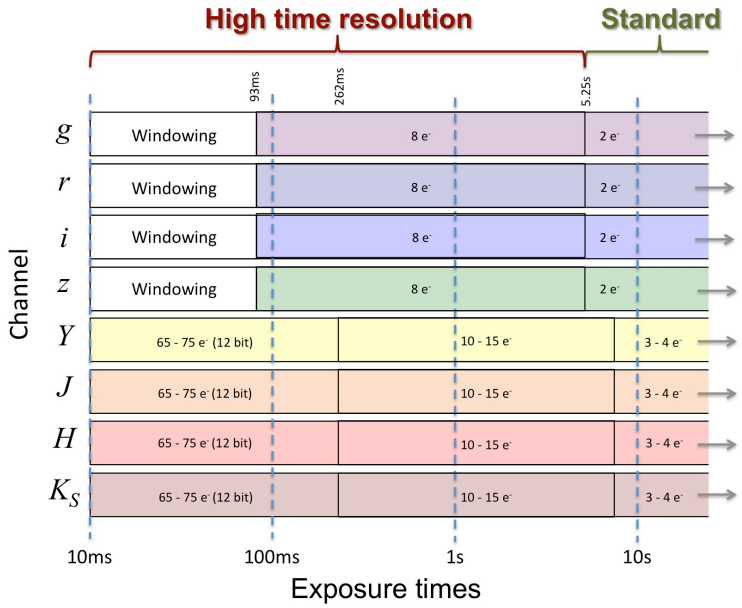

Figure 148 - Exposure time ranges available for each observing channel in imaging mode. For each band the readout noise (in e-) is indicated. The plot can be divided in two observing regimes; standard slow reading mode (exposure time > 5 s) and HTR mode (exposure time < 5 s). These two modes can be combined by the user in different channels.

3.4.2. Spectroscopic modes

As in the imaging mode, the readout of the spectral data is independently carried out in each channel, so a broad variety of combinations is possible. The spectroscopic observations can be performed with the long slit (LS), with the IFU or with the spectropolarimeter. Figure 149 shows the spectroscopic readout modes of all the channels for the LS mode. The spectroscopic modes can be divided in three groups similarly to the imaging mode: Standard slow reading, HTR and customized mode.

Standard slow reading spectroscopic mode (exposures of more than 10 seconds):

For typical seeing conditions the LS will be mostly used in unbinned mode. The IFU and spectropolarimeter are designed to be used in unbinned mode.

High Time Resolution Spectroscopic mode (exposures of less than 10 seconds):

The time resolution achieved in this mode for long slit observations can be as fast as 180ms in the optical and 13ms in the near-IR arm. For science cases requiring higher time resolutions the length of the slit on the detectors can be reduced through windowing.

Customized spectroscopic mode:

OCTOCAM allows combining standard slow reading and high-time-resolution modes. We do not foresee many science cases exploiting the combination of slow and HTR spectroscopic modes, but we keep this non-standard mode as an open possibility for any potential science case that might want to use it.

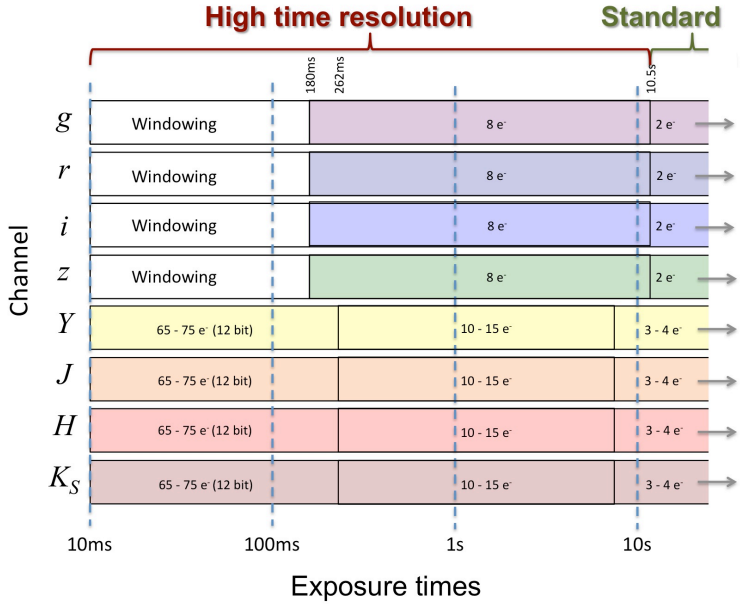

Figure 149 - Exposure time ranges available for each observing channel in spectroscopic mode. For each band the readout noise (in e-) is indicated. The plot can be divided into two readout modes; standard slow reading mode (exposure time > 10 s) and HTR mode (exposure time < 10 s). These two modes can be mixed by the user combining different channels.

3.4.3. Calibration plan

In this section we describe the standard calibration plan foreseen for OCTOCAM during regular operations. Standard calibrations and house keeping observations should be carried out during daytime at Gemini. In order to constrain the time allocated for calibrations, Gemini might consider imposing a limit in the number of modes to be used per night. However, thanks to the fast readout speed of the detectors, the calibration time per mode will be very small, thus allowing a quite flexible operation.

Imaging mode:

The OCTOCAM multi-channel capabilities allow to perform simultaneous imaging calibrations for all VIS and NIR arms. The dark current of all the detectors is negligible, however a monitoring of its value through dark frames of different exposure times would be highly desirable as a detector health check. In the case of the NIR arms ON-OFF dome flat frames could be provided depending on the observers' needs. Given the reduced field of view of OCTOCAM we do not foresee to take illumination frames to study the zero point variation across the field.

The HTR modes might require a more intensive (in terms of number of frames, exposure time sampling, windowing and readout modes) calibration program. The calibration tasks for the imaging mode are in given in Table 48.

OCTOCAM imaging calibration plan			
Calibration	**Number**	**Frequency**	**Purpose/ Comments**
Twilight flat fields	At least 1 set of 5 flat fields per channel and binning mode.	Daily.	Cheap to achieve given the simultaneous multi-channel capabilities.
Dome flat fields	For the UV and VIS arms, 1 set of 5 flat fields per channel. For the NIR arms, 1 set of 5 flats ON 1 set of 5 flats OFF.	Daily (optional, best effort basis).	Data reduction. Construction of bad pixel masks using a ramp of exposure times.
Photometric standard stars I	At least 1 star.	Daily	Monitor zero points.
Photometric standard stars II	At least 4 stars with highly different colors.	Every 6 months	Monitor color terms.
Photometric standard stars III	At least 4 stars at different airmasses.	Every 6 months	Monitor extinction coefficients.
Bias frames	10 frames for each observing mode used in the night. 10 frames binned 1x1. For VIS arms an additional set binned by 2x2.	Daily	Data reduction. Detector health check.
Dark frames	Exposure series of 0.1,1,10,100,1000s in UV and VIS arms. Exposure series of 0.1,1,10, 60s in NIR arm.	Weekly	Data reduction. Monitor dark current, fixed pattern noise, construction of bad pixel masks.
Astrometric calibration	At least 5 WCS calibrated frames.	Weekly	Monitor plate scale, distortions.
Parasitic light	1 hour 5 exposures in 2x2 bin and dome light off.	Monthly	Measure parasitic light levels (e-/hr/pix)

Table 48 - Imaging calibration plan.

Spectroscopic mode:

As in imaging mode, the multi-channel capabilities of OCTOCAM allow to carry out simultaneously the spectroscopic calibration plan of the VIS and NIR arms. The dark current of all the detectors is negligible, however a monitoring of its value through dark frames of different exposure times would be highly desirable. The spectroscopic calibration plan (see Table 49) is the same for the long slit and IFU, whereas the spectropolarimetry mode also requires the observation of polarization standards. The flat and arc lamp frames should be taken in combination with the different slits (including the IFU) used during the night. Halogen lamp flats would be mandatory, while sky flats are only taken on a best effort basis. OCTOCAM does not require the acquisition of new arc lamps as each channel has a large enough coverage to have a sufficient amount of calibration lines with the available lamps at Gemini.

OCTOCAM spectroscopic calibration plan			
Calibration	**Number**	**Frequency**	**Purpose/ Comments**
Halogen lamp flat fields (also for IFU and spectropolarimeter if used)	A set of halogen lamps to cover all the spectral range. 5 flat fields per channel.	Daily	Data reduction. Necessary to monitor the response function.
Twilight flat fields (also for IFU and spectropolarimeter if used)	At least 1 set of 5 flat fields per channel. The exposures would be variable to secure optimal count levels in each channel.	Daily (optional, best effort basis).	Data reduction. Cheap to achieve given the simultaneous multi-channel capabilities.
Spectrophotometric standard stars	At least 1 star	Daily	Flux calibration, response function.
Telluric standard star	At least 1 star	1 per target that requires it	Correction of telluric absorptions
Polarized standard star	At least 1 star	Daily (if polarizer is used)	Flux calibration, response function.
Unpolarized standard star	At least 1 star	Daily (if polarizer is used)	Flux calibration, response function.
Polatimetre: Telluric standard stars	At least 1 star	1 per target that requires it	Removal of telluric spectrum.
Bias frames	5 frames binned 1x1. For the UV and VIS arms an additional set binned by 2x2.	Daily	Data reduction. Detector health check.
Dark frames	Exposure series of 0.1,1,10,100,1000s in UV and VIS arms. Exposure series of 0.1, 1, 10, 60s in NIR.	Weekly	Data reduction. Monitor dark current, fixed pattern noise, construction of bad pixel masks.

Arc lamps	At least 2 sets of Arc lamps per channel at different intensities.	Daily	Dispersion solution, resolving power, study of flexures.
Slits + grisms alignment	Using flat field lamps to measure counts rates of trace.	Monthly	Slit trace detector position and orientation
Slicer + grisms alignment	Observation of a star to measure counts rates of slicer traces.	Monthly	Slit trace detector position and orientation

Table 49 - Spectroscopy calibration plan.

Both calibration plans rely on additional Gemini monitoring measurements such as CCD cryogenics, flat and arc lamp intensities, derotator alignment. Several products of the imaging calibration plan will be used for the spectroscopic one, e.g. bad pixel masks, parasitic light, or the detector health monitoring.

3.4.4. Overheads

The instrument overheads will be conditioned by the telescope acquisition and guiding unit, as the actual instrument overheads are very small (see Table 50). Telescope slewing and acquisition times are estimated according to the information provided by Gemini assuming that the guiding is performed by the telescope probe. If considered necessary, a custom guiding camera could be developed for OCTOCAM in a future phase.

Operation	Time	Comment
* Telescope pointing	1-3 min	
* Put probe follow mode, check pointing and close guide loop	1-3 min	
* Wait for astigmatism to converge	3-5 min	Observation may start before convergence in rapid response observations
Acquisition (automatic)	Exposure time + 5 s	This is the time the software takes to correct astrometry and localize the target. The telescope time to reposition the object is not considered here.
Acquisition (manual)	Exposure time + 120 s	The telescope time to reposition the object is not considered here.
Focal plane carriage setup (slits, IFU, polarimeter)	<5 s	
Grism/Filter setup	3 s	
Polarizing optics setup	< 5 s	
Readout	0.1 – 10.5 s	See Sections 2.6, 3.4.1, and 3.4.2. VIS detectors can read while exposing implying a duty cycle of ~100%

Table 50 – Estimated overheads of OCTOCAM. * Overheads due to the telescope.

3.4.5. A rapid response mode for Gemini?

Some of the key science cases of OCTOCAM such as gamma-ray burst observations or other newly discovered transient sources are expected to have fast decays in flux and/or rapid variability during the early minutes after their discovery, which requires very timely observations. We thus propose to implement a rapid response mode at Gemini similar to what is currently being used at ESO's VLT. This system would be especially useful for OCTOCAM but also interesting for all the other instruments at the telescope.

The rapid response mode system would receive alerts from authorized users with approved proposals, automatically interrupt ongoing observations and immediately point the telescope to the required field and start observations. With such a mode, observations could start as soon as a few minutes (5-10) after the alert is issued.

This mode would only operate if the telescope would already be observing with the requested instrument (OCTOCAM in this case but could be another), implying no further change in the observing configuration. The activation of the rapid response mode would need to be accepted by the telescope operator and would be blocked if the ongoing observations are time critical.